A PARALLELIZED, ULTRAHIGH-THROUGHPUT DROPLET MICROFLUIDIC PLATFORM FOR SINGLE-CELL ANTIMICROBIAL SUSCEPTIBILITY TESTING AND HETERORESISTANCE DETECTION

by

Carter Wade Hoffman

A dissertation submitted in partial fulfillment
of the requirements for the degree

of

Doctor of Philosophy

in

Chemical Engineering

MONTANA STATE UNIVERSITY
Bozeman, Montana

May 2025

DEDICATION

For Justin, my brother from another mother in this life and beyond. Rest in power.

ACKNOWLEDGEMENTS

Madie, thank you for everything. You are the light of my life, my sun and moon and my shelter from the storm. Mom & Dad, thank you for being so supportive and always having my back. I am only here because you guys always told me I could do it. Riley & Emma, thanks for being the best squad members a brother could ask for. I am made more powerful with you guys on my team. Marcos, Jake, Bobo, Burns, Mason, Rylie & Sebas—thanks for being such a great herd. Bozeman will always have my heart thanks to amazing people like you.

Thank you to Connie for sticking with me and bringing me to this crazy Mayo Clinic place. I am sorry for my problem child years, but look at me now! Mike and Kerry, thanks for the years of advising and patience. Thank you for being tough on me when you had to, and thank you as well for your level-headedness in the face of experimental failure. To Jen, thank you for helping me to become the person I wanted to become in grad school. You did something better than show me the way: you showed me how to find it myself. Thanks as well to Stephanie and Stephan for their support and advising throughout the years. I am the scientist that I am today, in no small part thanks to the guidance of these awesome committee members.

Thanks to the kind members of both iterations of the Chang Lab. Geoff, Humberto, Jake Shawna & Dimitri—thanks for creating such a good research atmosphere at MSU and taking me under your wings. Lydia, Maureen, Damon & Casper, thanks for making the Mayo iteration of our group so fun and enjoyable. And to my new friends in the Revzin, Peterson and Matveyenko groups (you know who you are), thanks for providing me a soft landing at the Mayo Clinic. This was a scary moment for me, and I felt much safer having you folks around.

TABLE OF CONTENTS

TABLE OF CONTENTS CONTINUED

TABLE OF CONTENTS CONTINUED

TABLE OF CONTENTS CONTINUED

LIST OF TABLES

Table Page

LIST OF FIGURES

Figure Page

LIST OF FIGURES CONTINUED

LIST OF FIGURES CONTINUED

LIST OF FIGURES CONTINUED

ABSTRACT

Antimicrobial resistance (AMR) is an immediate threat to global health, as the spread of resistant strains of pathogens has reduced the efficacy of many classical antimicrobial therapy routes. Antimicrobial susceptibility testing (AST) is a critical phase in clinical infection therapy, where the susceptibility profile of causative organisms is deduced empirically, and used to guide antimicrobial therapy. Standard AST techniques such as broth microdilution are population-level analyses, in which an entire culture of bacteria is analyzed. This results in long assay times on the order of 18-72 hours, as well as poor ability to detect resistant subpopulations within an infection, both of which phenomena can have negative effects on patient outcomes. In response, AST techniques based on single cell analysis have demonstrated promise in advancing AST capabilities. Single cell ASTs allow for sensitive detection of early cell divisions, possibly expediting AST results, as well as description of cell-cell heterogeneity.

Recently, drop-based microfluidics (DBMF) has emerged as a powerful tool for characterizing bacterial response to antibiotics with single-cell resolution. Despite this, DBMF has not seen wide-scale implementation toward AST and AMR-related problems. The presented research details three separate but related projects which aimed to increase DBMF capabilities for AST. The first project focused on the development of a robust platform for ultrahigh-throughput detection of assay signals from microfluidic droplets containing single cells. The assembled technology enables multiplexed droplet fluorescence detection at kHz rates, facilitating single-cell screening of large populations of cells. In the second project, we detail the development of a plate-interfacing parallel encapsulation (PIPE) chip, which rapidly emulsifies the contents of a microtiter plate into a multiplexed, barcoded droplet library. The PIPE chip provides advancements in conducting multiplexed experiments in droplets in parallel, an outstanding issue within the field. In the last project, we leverage the PIPE chip platform to conduct rapid droplet AST on single cells against a panel of antimicrobials, in parallel. The technique outputs quantitative susceptibility results by assaying ~150,000 single-cell antimicrobial responses, within a single working day. These results demonstrate advancements in developing single-cell screening technologies, and further the understanding of antimicrobial growth responses by bacteria.

CHAPTER ONE

INTRODUCTION

Antimicrobial resistance (AMR) is an immediate threat to global health, as the spread of resistant strains of pathogens has reduced the efficacy of many classical antimicrobial therapy routes. Antimicrobial susceptibility testing (AST) is a critical phase in clinical infection therapy, where the susceptibility profile of causative organisms is deduced empirically, and used to guide antimicrobial therapy. Standard AST techniques such as broth microdilution are population-level analyses, in which an entire culture of bacteria is analyzed. This results in long assay times on the order of 18-72 hours, as well as poor ability to detect resistant subpopulations within an infection, both of which phenomena can have negative effects on patient outcomes. In response, AST techniques based on single cell analysis have demonstrated promise in advancing AST capabilities. Single cell ASTs allow for sensitive detection of early cell divisions, possibly expediting AST results, as well as description of cell-cell heterogeneity. Among recent developments in single-cell technologies, drop-based microfluidics (DBMF) has emerged as a powerful tool for characterizing bacterial response to antibiotics with single-cell resolution. In DBMF, biological samples are compartmentalized into micron-scale water-in-oil emulsions, enabling ultrahigh-throughput analysis of single cells. This feature of DBMF has enabled the analysis of thousands of single cells within a population, enabling the description of phenotypic heterogeneities. The presented body of work adapts drop-based microfluidics to develop a multiplexed, ultrahigh-throughput platform for single-cell AST.

Funding and Collaborations

Funding for this research was provided by the Montana State University Alumni Foundation, National Science Foundation (NSF) CAREER Grant 1753352, Nation Institutes of Health (NIH) Grant 1R21Al151923, US Department of Agriculture (USDA) Grant NIFA-AFRI-007692. The research was conducted at the Center for Biofilm Engineering (CBE) at Montana State University (MSU) (Montana, USA) with *E. coli* studies in collaboration with the Franklin Lab at Montana State University (MSU) (Montana, USA).

Dissertation Outline

Five chapters and a series of appendices comprise the remainder of this dissertation. Chapter 2 reviews the current AMR crisis, the importance of single-cell technologies in mitigating AMR-related problems, and the potential of microfluidics as a body of single-cell tools which can be applied toward AMR problems. Chapter 3 details the development and optimization of equipment and techniques to assay multiplexed biological signals from microfluidic droplets at kHz rates. Chapter 4 presents a microfluidics device capable of parallel emulsification of experimental conditions from a well-plate into microfluidic droplets, for multiplexing droplet assays. In Chapter 5, the parallel encapsulation device is used to conduct multiplexed AST against single cells in droplets, enabling rapid AST and description of bacterial heterogeneity in antimicrobial response. Chapter 6 summarizes the results of this research within the context of the microfluidics AST community. The main body of this dissertation is followed by two appendices titled Appendix A and Appendix B. These sections encompass (A) supporting information for chapter 4 and (B) supporting information for chapter 5.

Chapter 2: "Microfluidic approaches for antimicrobial susceptibility testing"

Chapter overview: My dissertation encompasses the development of a droplet-based microfluidics platform for multiplexed testing of antimicrobial compounds against single bacterial cells, at ultrahigh-throughput. This platform was designed to enable parallel testing of multiplexed experimental conditions in droplets, provide susceptibility results over shorter timeframe than is typically possible, and concurrently describe cell-cell heterogeneities in antibiotic response. These advancements were motivated by the observations that (1) delays in susceptibility results can have negative effects on patient outcomes, (2) bacterial heterogeneity is implicated in reduced patient outcomes and the spread of antimicrobial resistance and (3) techniques and infrastructure to conduct multiplexed droplet experiments in parallel are generally poor. Here [in Chapter 2], I provide context of the wider antimicrobial resistance issue, the advantages of single-cell methods, and the current landscape of microfluidics-based solutions for these problems.

Chapter 3: "Development of a robust platform for ultrahigh-throughput analysis of multiplexed fluorescence signals from microfluidic droplets"

In this body of research, we developed a robust platform for fluorescence signal detection from microfluidic droplets, designed to enable multiplexed droplet bioassays. We report tutorials for (1) alignment of optical equipment, (2) reinjection of microfluidic droplets into detection devices, (3) use of a reference dye for monitoring droplet flow patterns, (4) data filtration processes for data quality assurance and (5) step-wise construction and optimization of a multiplexed droplet bioassay. It was hypothesized that droplet fluorescence detection assays can be optimized for robustness by the modulation of droplet detection variables available to the experimenter,

including but not limited to droplet reinjection protocol variables, data treatment steps, and electronics and detector settings.

Chapter abstract: Droplet-based microfluidics (DBMF) is a powerful technology for single-cell biological analysis, as it enables automated, high-throughput processing of individual cells. In DBMF, biological samples are partitioned into micrometer-scale, water-in-oil droplets, each acting as an isolated microreactor. This miniaturization converts a standard mL-scale sample into millions of discrete, single-cell experiments conducted in parallel. Maximal automation and throughput of emulsified droplet samples has been achieved by analyzing optical signals from flowing droplets. Despite this, signal analysis from flowing droplet samples presents several key challenges, including robust assembly of optical equipment to deliver optimized laser beams to the droplet sample, stable reinjection of emulsion samples, data quality assurance, and reliable acquisition of multiplexed droplet signals. In this thesis chapter, we detail the assembly of a robust platform for ultrahigh-throughput analysis of multiplexed fluorescence signals from microfluidic droplets, and provide tutorials for navigating these challenges.

Chapter 4: "Rapid parallel generation of a fluorescently barcoded drop library from a microtiter plate using the plate-interfacing parallel encapsulation (PIPE) chip"

In this work, we hypothesized that a microfluidic chip which integrates with a microtiter plate to directly emulsify the contents of the plate could facilitate multiplexed droplet-based experiments. This hypothesis was motivated by the need within the field for techniques and tools to conduct multiplexed droplet experiments in parallel.

Chapter abstract: In drop-based microfluidics, an aqueous sample is partitioned into drops using individual pump sources that drive water and oil into a drop-making device. Parallelization

of drop-making devices is necessary to achieve high-throughput screening of multiple experimental conditions, especially in time-sensitive studies. Here, we present the plate-interfacing parallel encapsulation (PIPE) chip, a microfluidic chip designed to generate 50 to 90 μm diameter drops of up to 96 different conditions in parallel by interfacing individual drop makers with a standard 384-well microtiter plate. The PIPE chip is used to generate two types of optically barcoded drop libraries consisting of two-color fluorescent particle combinations: a library of 24 microbead barcodes and a library of 192 quantum dot barcodes. Barcoded combinations in the drop libraries are rapidly measured within a microfluidic device using fluorescence detection and distinct barcoded populations in the fluorescence drop data are identified using DBSCAN data clustering. Signal analysis reveals that particle size defines the source of dominant noise present in the fluorescence intensity distributions of the barcoded drop populations, arising from Poisson loading for microbeads and shot noise for quantum dots. A barcoded population from a drop library is isolated using fluorescence-activated drop sorting, enabling downstream analysis of drop contents. The PIPE chip can improve multiplexed high-throughput assays by enabling simultaneous encapsulation of barcoded samples stored in a microtiter plate and reducing sample preparation time.

Chapter 5: "Automated, multiplexed antimicrobial susceptibility testing and quantitative heteroresistance determination in microfluidic droplets"

This work was motivated by the observations that (1) the ability to conduct multiplexed AST experiments in parallel in microfluidic droplets is an outstanding issue within the field, and that (2) droplet AST platforms typically treat growth as binary ("on" or "off"), a reductive approach which could be improved upon by the detection of single cells and estimation of biomass within

the droplet. We hypothesized that the parallel encapsulation chip developed in Chapter 4 could be used to facilitate multiplexed droplet AST, that signal detection of microfluidic droplets could be optimized for single-cell detection, and that these advances could be integrated into a single platform for high-resolution description of single-cell growth responses to multiplexed antimicrobial panels.

Chapter abstract: Antibiotic resistant bacteria are an immediate and growing threat to public health, responsible for millions of infections and tens of thousands of deaths annually in the US alone. In clinics, susceptibility profiles of offending microbes are assessed using techniques such as broth dilution, whereby samples of the infection are grown in the presence of antimicrobial dilution series and monitored for growth. These standardized techniques are invaluable to clinicians and society, however, suffer from long time-to-assay on the order of 18-72 hours, and fail to detect phenotypic heterogeneities present within an infection. Both of these limitations are related to the requirement of broth dilution to begin with 10^4-10^5 cells. Such a dense starting culture can result in long incubation periods before a detectable amount of growth has occurred, and can mask the presence of resistant subgroups if they are relatively infrequent. These shortcomings of standard susceptibility testing techniques have resulted in rampant misuse of antibiotics, compounding antimicrobial resistance (AMR)- related problems. As such, there is an urgent need of novel techniques to rapidly assess microbial antibiotic response with single-cell resolution. Among recent innovations, drop-based microfluidics (DBMF) has been used for ultrahigh-throughput examination of single-cell growth responses to antibiotics. However, current microfluidics techniques are hindered by experimental complexity, and limited ability to assay whole panels of antimicrobials in parallel, a necessary feature of AST. In this work, we present a

droplet-based AST platform that addresses these challenges. To solve the issue of multiplexing, we use a plate-interfacing, parallel encapsulation chip (PIPE chip) which emulsifies an entire panel of antimicrobials from a well plate, into a multiplexed library of single-celled droplets. The droplets are spectrally barcoded to enable parallel analysis of the droplet library. The assay readout module is a droplet laser-induced fluorescence (LIF) detector, which collects multiplexed fluorescence signals as droplets flow through a channel and encounter an excitation laser. During readout, droplet barcodes encoding experimental conditions, as well as droplet growth values, are recorded coincidentally at kHz rates. We demonstrate our platform by monitoring the growth response of single *E. coli* cells in droplets against a panel of 36 antibiotic conditions, comprising 6 antibiotics of varying class. In a single 8-hour working day we collect ~150,000 single-cell growth readings, and output quantitative metrics of population susceptibility and phenotypic heterogeneity in response to each of the 6 antibiotics. One of the major challenges in widescale heteroresistance and AMR surveillance is a technique which can rapidly assay many thousands of single cell replicates, against a multiplexed panel of antimicrobials; our platform represents an example solution to this challenge.

Chapter 6: “Conclusions and Outlook”

Chapter summary: The research presented in this thesis comprised three separate but related projects, during which a high-throughput, multiplexed microbial drug screening assay in microfluidic droplets was developed. The presented work contributes to the understanding of developing droplet-based single-cell assays, as well as heterogeneity in bacterial growth response to antimicrobials. Here, I will summarize the results of this work, provide context within the wider field of microfluidic AST, and comment on future work.

CHAPTER TWO

MICROFLUIDIC APPROACHES FOR ANTIMICROBIAL SUSCEPTIBILITY TESTING

Overview

My dissertation encompasses the development of a droplet-based microfluidics platform for multiplexed testing of antimicrobial compounds against single bacterial cells, at ultrahigh-throughput. This platform was designed to enable parallel testing of multiplexed experimental conditions in droplets, provide susceptibility results over shorter timeframe than the 18-72 hours typically required by standard susceptibility tests, and concurrently describe cell-cell heterogeneities in antibiotic response. These advancements were motivated by the observations that (1) delays in susceptibility results can have negative effects on patient outcomes, (2) bacterial heterogeneity is implicated in reduced patient outcomes and the spread of antimicrobial resistance and (3) techniques and infrastructure to conduct multiplexed droplet experiments in parallel are generally poor. Here [in Chapter 2], I provide context of the wider antimicrobial resistance issue, the advantages of single-cell methods, and the current landscape of microfluidics-based solutions for these problems.

The Antimicrobial Resistance Crisis and Antimicrobial Susceptibility Testing

Antimicrobial resistance.

Antimicrobial resistance (AMR) is an immediate threat to global health, as the spread of resistant strains of pathogens has reduced the efficacy of many classical antimicrobial therapy

routes. AMR arises from the misuse and overuse of antimicrobials in medicine, industry and agriculture. The development of novel antimicrobials has stagnated, rendering some common infections difficult, if not impossible, to treat. Antibiotic resistant bacterial infections were responsible for 1.27 million deaths globally in 2019, with forecasts predicting that this figure could rise to 8 million by 2050. In addition to global mortality, the AMR crisis also brings economic costs, with The World Bank estimating losses up to US$ 3.4 trillion in global gross domestic product (GDP) by 2030 [1-4].

Several notable pathogens exemplify the AMR crisis. The World Health Organization has compiled a 2024 Bacterial Priority Pathogens List which outlines key threats. Carbapenem-resistant *Acinetobacter baumannii* (CRAB), carbapenem-resistant Enterobacterales (CRE) and third-generation cephalosporin-resistant Enterobacterales (3GCRE) were among the highest-scoring threats. Other notable threats include *Salmonella*, *Shigella*, *Neisseria gonorrhoeae*, *Pseudomonas aeruginosa*, and methicillin-resistant *Staphylococcus aureus* (MRSA). These pathogens are associated with widespread prevalence in society, high transmissibility and concerning mortality rates [1, 2].

Gram-negative bacteria (GNB) are responsible for a significant component of the AMR crisis. Several pathogens marked by the WHO as high importance are part of this group, including Enterobacterales*, A. baumanii, Pseudomonas aeruginosa* and *Salmonella* spp. GNB are characterized by having two cell membranes, with a thin layer of peptidoglycan in the intermembrane periplasmic space. The name ‘gram-negative’ comes from the inability of GNB to retain the crystal violet stain during gram staining (their counterparts, gram-positive bacteria, possess a single cell membrane inside a thick peptidoglycan cell wall which retains the crystal

violet stain). The gram-negative outer membrane (OM) is structurally dynamic, and contributes to AMR phenotypes in gram-negative pathogens by impeding drug uptake [5, 6]. GNB possess numerous multidrug efflux pumps (MDEPs) which can evacuate drugs which are taken up by the cell [7-9]. Additionally, many GNB strains have acquired resistance through mobile genetic elements carrying genes such as MDEPs, and drug inactivation enzymes like extended-spectrum β-lactamases (ESBLs) or carbapenemases [5]. Notable examples include *Escherichia coli* and *Klebsiella pneumoniae*, which frequently harbor ESBL genes [10]. GNB have been shown to mediate AMR through all 4 of the AMR mechanistic groups, namely (1) drug inactivation, (2) limiting drug uptake, (3) drug target modification and (4) drug efflux [6, 11]. As treatment of infections by GNB and other AMR pathogenic strains is expected to continue increasing in difficulty, there is an urgent need for novel antibiotic therapy regiments and AMR surveillance techniques.

Antimicrobial susceptibility testing

Antimicrobial susceptibility testing (AST) is a critical phase in clinical infection therapy, where the susceptibility profile of a causative isolate is deduced empirically. Most AST techniques quantify the minimum inhibitory concentration (MIC) of a drug required to prevent microbial growth. The MIC is the standard metric for communicating the susceptibility level of an isolate, and can be compared to standardized breakpoint values such as those published by the Clinical & Laboratory Standards Institute (CLSI) [12], to classify an isolate as susceptible/intermediate/resistant (S/I/R). Standard techniques for measuring the MIC including agar dilution, antimicrobial gradient diffusion, disk diffusion and broth dilution all rely on monitoring changes in optical density (OD) of a bacterial colony in response to antibiotics,

sometimes by visual inspection [13-15]. To perform agar dilution, serial 2-fold dilutions of an antimicrobial are incorporated into molten agar, and poured into plates. The plates are then inoculated with a standardized inoculum of the isolate, and monitored for growth after incubation. Agar dilution presents advantages related to accuracy and ability to count colony forming units (CFU) in the presence of antimicrobial, however, suffers from high labor related to processing many agar plates. Gradient diffusion AST relies on the establishment of a gradient of antimicrobial concentrations within an agar plate. Perhaps the most well-known version of this test is the Etest (bioMérieux), which makes use of a plastic test strip impregnated with a gradient of antimicrobial. Up to 6 unique strips are placed radially onto an inoculated agar plate, and the zone of inhibition around each strip yields a quantitative susceptibility result. Etests are considered a useful option, as the organism can be assayed against many antimicrobial conditions on a single agar plate. However, Etests show biases toward higher or lower MIC values for certain microbe-antimicrobial combinations, and the interpretation of the result is subject to some variability based on operator error [14, 16]. In disk diffusion, a dense culture of bacteria (~10^8 CFU/mL) is inoculated onto an agar plate, and small disks impregnated with a single antimicrobial concentration are placed onto the plate. The zone of inhibition around the disk, which is measured in mm, is related to the susceptibility level of the isolate, as well as the diffusion of the antimicrobial compound through the agar. Disk diffusion is cheap, simple and easily conducted by any clinic, however it is considered qualitative, as it can classify organisms as S/I/R without quantifying a MIC. In broth dilution AST, serial 2-fold dilutions of antimicrobial are created in liquid broth, which is inoculated with a standardized inoculum and monitored for turbidity across an incubation period. Broth dilution is the most commonly used AST technique in clinics, due to its amenability to microtiter

plates and plate reading instruments which produce continuous turbidity readings (it is termed ‘broth microdilution’ when the reaction volume is µL-scale, as in the well on a microtiter plate). Current state-of-the-art AST platforms are automated broth microdilution assay machines. 4 are FDA approved and available in the US: VITEK-2 (bioMérieux), MicroScan WalkAway (Beckman Coulter), BD Phoenix (Becton Dickonson) and Sensititre ARIS (ThermoFisher Scientific) [15]. These systems have become commonplace because they reduce manual liquid handling steps and can produce MIC results, though limitations include cost and variable accuracy of susceptibility predictions. Notably, all the aforementioned techniques conduct AST against an entire population of bacteria at once, and therefore fail to detect phenotypic heterogeneities present within the isolate.

Whereas MIC measurements fall under the category of phenotypic AST, a number of molecular AST techniques, including PCR, MALDI-TOF MS, SERS and proteomics-based approaches have been developed to rapidly detect resistance markers in causative microbes [15, 17-19]. However, molecular AST approaches generally suffer from expensive reagents and/or high reaction volumes. Molecular AST approaches rely on detection of specific resistance-associated biomarkers, but this strategy is limited because many resistance phenotypes have not been directly linked to identifiable genetic markers [14, 17, 20]. For example, approximately 50% of carbapenem-resistant Enterobacteriaceae isolates in North America appear capable of carbapenemase production, based on PCR analysis [21]. Furthermore, phenotypic methods quantify susceptibility or resistance more accurately; as such, phenotypic AST has been the preferred form of AST in clinical settings and is poised to remain clinically relevant [14, 18, 19].

Much attention has been devoted in recent decades to reduce assay times in AST [22]. Manual AST techniques relying on broth dilution or agar plates have long time-to-assay readouts on the order of 18-72 hours. Automated broth microdilution platforms can produce MIC results moderately fast (~8-24 hours). Notably, all of these methods necessitate a standardized culture of the microbial infection prior to introduction into the assay, which requires agar plating over 24-120 hours [18, 19]. Thus, while the testing itself has seen significant speed improvements, AST results are often still not available until days after a patient sample is collected. AST results are critical for generating antibiograms to guide empiric therapy and provide treatments for specific infections. Delays in AST turnaround times can have negative effects on patient outcomes by delaying effective, patient-tailored care. Moreover, before susceptibility results are available clinicians apply broad-spectrum antibiotics, which can exacerbate antimicrobial resistance (AMR)-related problems by selecting for resistant strains. Thus, there is an urgent need for techniques to rapidly assess the susceptibility of bacterial isolates towards antibiotics.

Bacterial Phenotypic Heterogeneity, Heteroresistance and Single-Cell Analysis

Bacterial phenotypic heterogeneity

Bacterial phenotypic heterogeneity has become a subject of increasing interest as it is implicated in the spread of AMR and poor antibiotic therapy outcomes [23-30]. Resistant subgroups can evade eradication by antibiotics resulting in chronic, recurrent infections, and contributing to AMR. The presence of a resistant subgroup within a population of presumed isogenic, susceptible bacteria has been termed heteroresistance, and this phenotype has been documented in a variety of medically relevant pathogens [29, 31-34]. The reference standard assay

for detecting heteroresistance is population analysis profiling (PAP), which involves interrogation of the isolate by serial 2-fold dilutions of antimicrobial [35-37]. However, PAP is extremely labor- and time-intensive compared to the standard broth microdilution, as it relies on counting colonies on agar plates rather than multiplexing antibiotic dilution series using microtiter plates. Curiously, despite the concern over heteroresistance-related clinical complications, the relationship between heteroresistance and clinical outcome remains a matter of some debate [32, 34, 38]. The absence of a routine heteroresistance testing procedure has resulted in a dearth of heteroresistance data in the literature. Moreover, inconsistent definitions for heteroresistance have led to susceptibility misclassifications and confusion. The development of facile techniques to characterize bacterial heterogeneity in antimicrobial response could result in improved patient outcomes, by broadening the understanding of the clinical significance of heteroresistant bacterial infections.

A notable feature of heteroresistance is the transient nature of the resistance phenotype [39]. Heteroresistant isolates are regularly shown to revert to susceptibility after cessation of the antibiotic stress. Various mechanisms underlie the ability of an isogenic population of bacteria to produce heterogeneous responses to antimicrobial stress, without acquiring heritable genetic traits. Many of these mechanisms can be attributed to noise in genetic processes. For example, variable DNA topology in bacteria results in transcriptional noise, which in turn produces cell-cell heterogeneity and can result in persister cell phenotypes [30]. Heterogeneous gene expression can mediate heterogeneous susceptibility toward antibiotics [24], and stochastic partitioning of biomolecules at cell division produces daughter cells with heterogenous amounts of cellular machinery [40]. Spontaneous tandem gene amplifications contribute to a significant proportion of heteroresistance phenotypes [29]. Increased plasmid copy number and transposition of resistance

genes onto cryptic plasmids can also give rise to heteroresistance phenotypes, in a gene dosage-dependent manner [41]. These mechanisms contribute to bacterial adaptive resistance, a relatively under-explored form of resistance which allows bacteria to rapidly respond to environmental changes, over timescales much shorter than those required to acquire heritable resistance genes or mutations. It is understood that adaptive resistance phenotypes can be induced by environmental triggers, such as sub-lethal dosages of antimicrobial compounds [24, 42]. However, recent work has also demonstrated the presence of transiently resistant subpopulations of bacteria before the introduction of antimicrobial triggers [24, 29, 33, 39, 41]. Moreover, it has been shown that spontaneously resistant subpopulations can endure antibiotic exposure, while compensatory resistance mutations are generated [39]. Thus, adaptive resistance can contribute to the development of acquired, genetically-encoded resistance, which is then passed on vertically to daughter cells. These findings emphasize the deficiencies of using the MIC based on population-level analyses as the sole metric of bacterial susceptibility to antimicrobials. Furthermore, they emphasize the societal need for techniques to detect heteroresistance in bacterial isolates concurrently with AST analyses, so that such infections can be managed with tailored antimicrobial regiments.

Single-cell analysis in AST

Recently, AST techniques based on single-cell analysis have shown promise in advancing AST capabilities [43-47]. Analysis of growth responses of individual cells within a population presents obvious opportunities for characterizing cell-cell heterogeneity. Moreover, interrogation of single cells enables sensitive detection of early bacterial divisions and expedited AST results. Figure 2.1 shows images collected in our lab, of green fluorescent protein (GFP)-labeled *E. coli*

encapsulated into micron-scale emulsions. Bacterial growth is easily discerned after a 3-hour incubation period, implying that single-cell analyses could reduce AST turnaround times to the order of single working days. Tracking of individual bacterial divisions by optical microscopy has enabled AST results in as little as 30 minutes from bodily sample collection, including quantification of heterogeneous single-cell growth rates [48]. It has been posited [44] that the MIC measured in the limit of single cells (the single-cell MIC or scMIC) is a more meaningful metric of antimicrobial susceptibility than the MIC, as it eliminates the possibility of inoculum effects [49]. It has also been posited that AST on a single cell confined to a small volume could produce an inoculum effect, as the ratio of antimicrobial molecules to cells decreases with decreasing reaction volume [50]. These questions will doubtless be answered during the validation processes required to translate the results from emerging single-cell technologies.

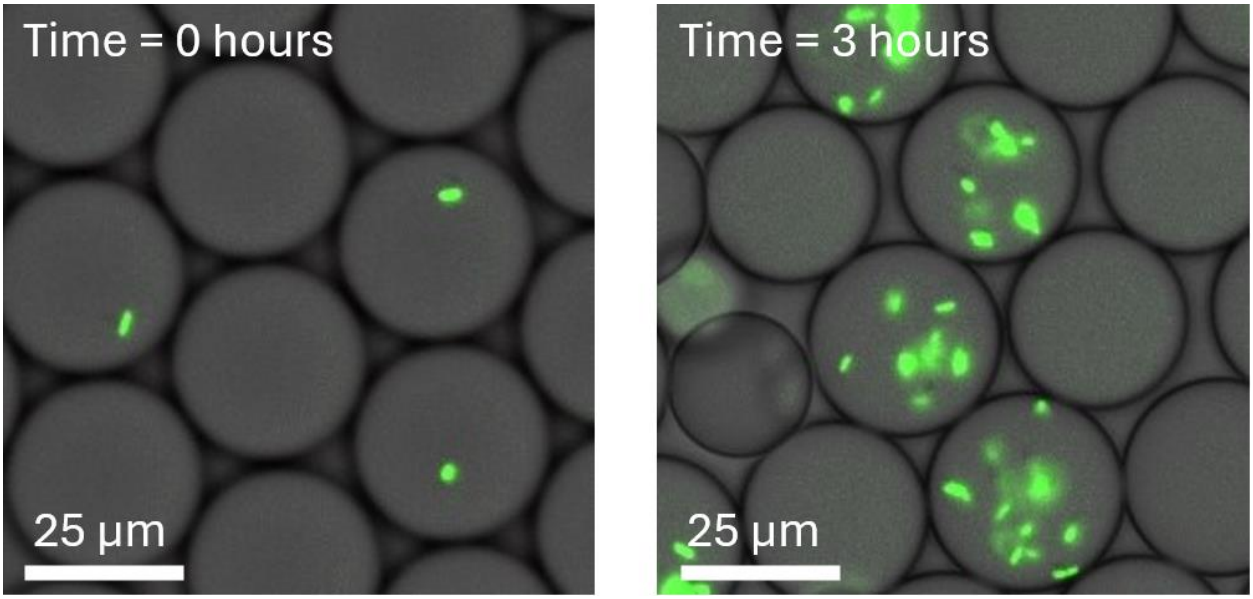

Figure 2.1. Analysis of single microbial cells allows expedited growth readouts. Images show green fluorescent protein-labeled E. coli cells encapsulated into microfluidic droplets at time = 0 hours (left) and 3 hours (right) of incubation. Growth is clearly discernible after a short incubation period, implying that single-cell analysis could expedite AST results.

Of the emerging platforms for single-cell AST, microfluidics devices are among the most commonly reported in literature. This is likely due to the ease with which microfluidic devices can navigate one of the primary challenges in developing a single-cell diagnostics platform: the isolation or compartmentalization of the single cell. Microfluidics is the scientific field in which fluidic flow is manipulated at the micro-scale. Microfluidics technologies are ideally suited to conducting single-cell biological analyses, as microfluidics devices generally consist of fluidic channels of 10^1-10^2 μm characteristic dimension—the scale of the cells themselves.

Microfluidics for AST

Microfluidic device fabrication.

Microfluidic devices are most commonly fabricated by casting silicone-based elastomers in molds fabricated by soft lithography, first presented by Whitesides et al. in 1998 [51]. SU-8 photoresist patterned onto silicon wafers are the most common mold materials [52]. To fabricate molds in this way, photoresist is spun onto the wafer substrate to a desired thickness. Then, the resist is exposed in the design of the microfluidic device, and un-exposed resist, washed away. The resulting mold is the negative mold of the microfluidic device, as a polymer cast and cured in the mold will contain cavities in the shape of the hardened photoresist. Cured polymer slabs are peeled from the mold, and plasma bonded to a glass microscope slide or another polymer slab to produce a sealed fluidic channel. Fabricated microfluidic devices are often termed ‘chips,’ in an intentional analogy meant to liken the microfabricated fluidic circuits to computer chip circuits.

Polydimethylsiloxane (PDMS) is the most commonly used elasteromeric material to cast microfluidic devices out of. PDMS has several notable advantages for biomicrofluidics, including (1) optically clear material suitable for microscopy techniques, (2) bio-compatible, and therefore

suitable for cell culture and bioassays, (3) facile surface modification, (4) excellent gas permeability, allowing aerobic conditions within microfluidic devices and (5) low-temperature curing over the course of ~hours.

Several techniques besides soft lithography have been used for microfluidic device fabrication, including 3D printing, hot embossing, injection molding, as well as mechanical techniques such as micro-cutting and CNC-based cutting techniques [53, 54].

Microfluidic flow characteristics

Flow through microchannels is almost exclusively realized in the laminar regime, owing to the small characteristic channel dimension of microfluidic devices. The long, narrow channels also result in flow which is characteristically uniaxial. In laminar uniaxial flow, individual fluid elements or layers do not mix as in turbulent flow. A key result of laminar uniaxial flow is therefore that all mass, momentum and heat transport in the direction normal to the flow is by diffusive mechanisms: molecular viscosity, molecular diffusivity, and thermal conductivity. Fluidic flow through microfluidic devices is generally pressure-driven, with pressure gradients created by pneumatic sources or syringe pumps. The achieved velocity profile is typical of Poiseuille flow, being parabolic with a maximum velocity in the channel center and minima at the channel walls [55, 56]. Together, these phenomena result in microfluidic devices which exhibit predictable fluid flow and reproducible device behavior. This is beneficial to the proliferation of microfluidic devices to end-users without microfluidics training.

Drop-based microfluidics

Drop-based microfluidics (DBMF) is the field of microfluidics which concerns the flow of multiple, immiscible fluidic phases which are segmented in a flow channel. Microfluidic droplets

function as micro-scale reaction compartments, which can contain components for biological assays, including single cells. Droplets are generated and assayed at kHz rates, enabling unprecedented high-throughput of experimental conditions. Moreover, droplets can be moved [57], immobilized [58], split [59], coalesced [60] and sorted [61] on-chip. Such precise manipulation of microfluidic droplets has enabled a variety of applications, including chemical synthesis [62], directed evolution [63], drug discovery [64] and antimicrobial susceptibility testing [50].

Droplet formation

To form microfluidic droplets, a stream of fluid A flows through a microfluidic channel and through an orifice, where it encounters a second, immiscible fluid phase B. The result is an emulsion of fluid A dispersed into fluid B, the latter of which is termed the continuous phase. The forces driving breakup of the stream of dispersed phase into droplets can be described with two dimensionless numbers, the Capillary (*Ca*) and Weber (*We*) numbers.

$$Ca = \frac{\mu v}{\Upsilon}$$

$$We = \frac{\rho v^2 l}{\Upsilon}$$

Where μ is dynamic fluid viscosity, v is characteristic fluid velocity, Υ is interfacial tension between two fluids, is ρ density and l is a length dimension, typically a channel diameter or hydraulic diameter. *Ca* describes the ratio of viscous shear forces to surface tension forces, and *We* describes the ratio of inertial forces to surface tension forces. Two prominent droplet formation regimes exist: dripping, where a forming droplet is broken up at the orifice into which the dispersed phase stream is forced, and jetting, where the dispersed phase stream forms a jet which extends

through the orifice, and droplet breakup occurs some distance downstream. Moreover, the relative values of the continuous phase Capillary number, Ca_{out} and the dispersed phase Weber number, We_{in}, have been shown to be predictive of the droplet formation regime (Figure 2.2). Drops formed in the dripping regime are highly monodisperse, therefore dripping is typically thought of as the more desirable of the two regimes. In the jetting regime, droplets are broken up at the end of the extended fluid thread due to Rayleigh-Plateau instabilities, which can result in polydisperse emulsions [65, 66].

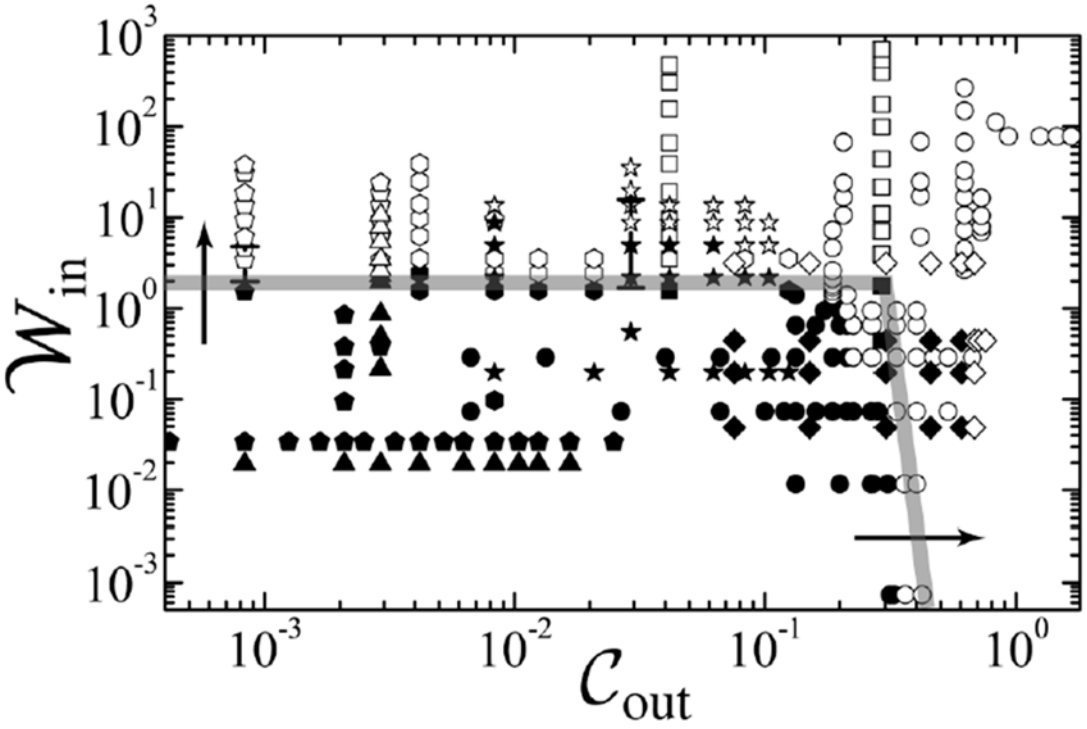

Figure 2.2. Dripping-to-jetting transition dependence on Ca_{out} and We_{in}. Filled symbols correspond to dripping regime, while empty symbols correspond to jetting. Each shape corresponds to a unique viscosity ratio, surface tension, or geometry. Reprinted figure with permission from A. S. Utada, A. Fernandez-Nieves, H. A. Stone, and D. A. Weitz, *Physical Review Letters*, **99**, 094502 (2007). Copyright (2007) by the American Physical Society.

Droplet formation junction geometry is a critical parameter which contributes to droplet formation characteristics [67, 68]. A common geometry for microfluidic droplet generation, which we used exclusively in this work, is a flow-focusing junction (Figure 2.3). A flow-focusing junction resembles a 4-way intersection, where a dispersed phase stream is intersected on two sides by continuous phase streams, which cause droplet pinch-off at the junction. A second common droplet formation junction is shown in Figure 2.4A, called a T-junction. Device geometry can influence the realization of a third droplet generation regime, which has been termed "squeezing." In squeezing, the nascent droplet bulges out from the orifice and obstructs the channel downstream of the orifice, restricting the flow of the continuous phase around it. This causes a dramatic increase in pressure upstream of the forming droplet, forcing droplet pinch-off [69].

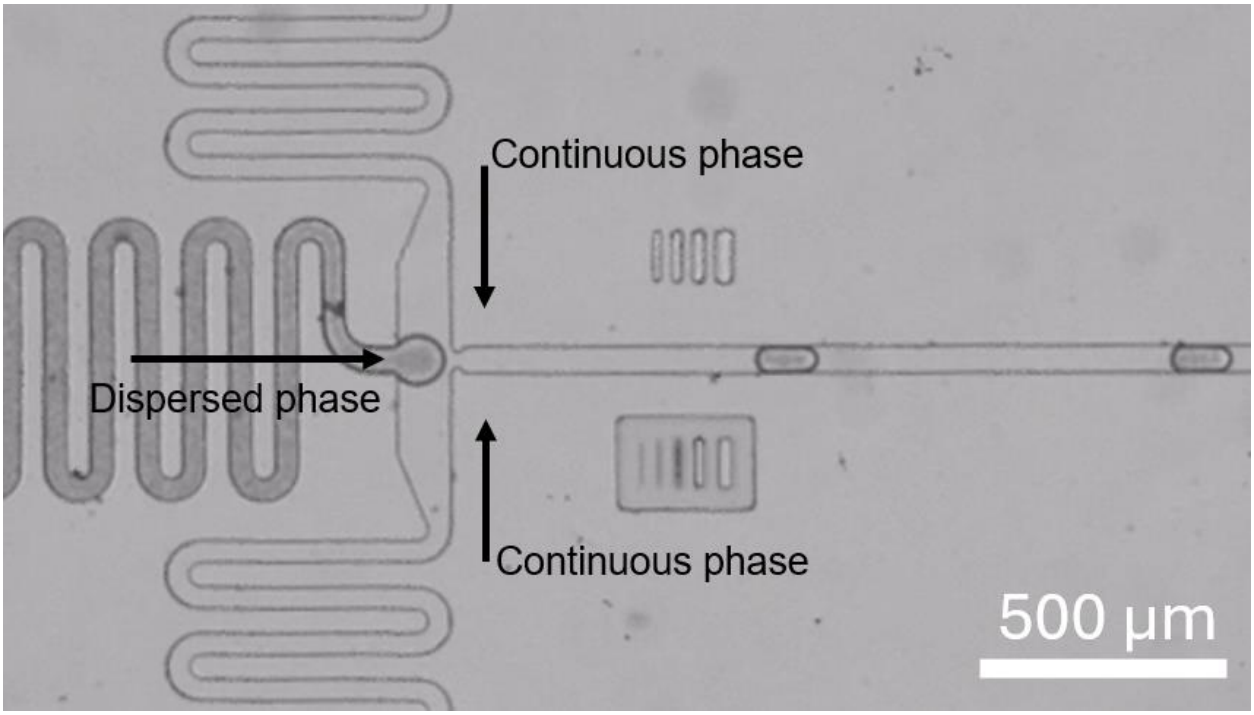

Figure 2.3. Flow-focusing droplet generation junction.

In practice, fluid flow rates and channel geometries can be tuned empirically to ensure desired, application-specific droplet production. Importantly, the results shown in Figure 2.2 were

generated using a co-axial flow device (Figure 2.4B), where the continuous phase stream is introduced concentrically around the dispersed phase stream. This 3D control over channel geometry is impractical in devices made by soft lithography and cast in PDMS, which explains the popularity of flow-focusing and T-junction devices. Therefore the results of the analyses in Figure 2.2 do not perfectly hold for 2-dimensional droplet formation devices, emphasizing the importance of empirical droplet generation observations [67].

The contents and surface chemistries of microfluidic droplets can be tuned for the specific application. To conduct biological assays, the droplets must consist of an appropriate biological media and be dispersed into an oil phase with good oxygen solubility, hence the common choice of fluorinated oils. Fluorinated oils also safeguard against the diffusion of reaction contents into the continuous phase, as fluorinated oils are very poor solvents for organic and hydrophilic molecules present in biological reactions. To prevent coalescence of the droplets, the droplets are stabilized with biocompatible surfactants. To prevent wetting of droplets onto channel walls, the channels are functionalized with fluorophilic molecules, which ensure that a sheath of continuous phase forms around droplets in the channel.

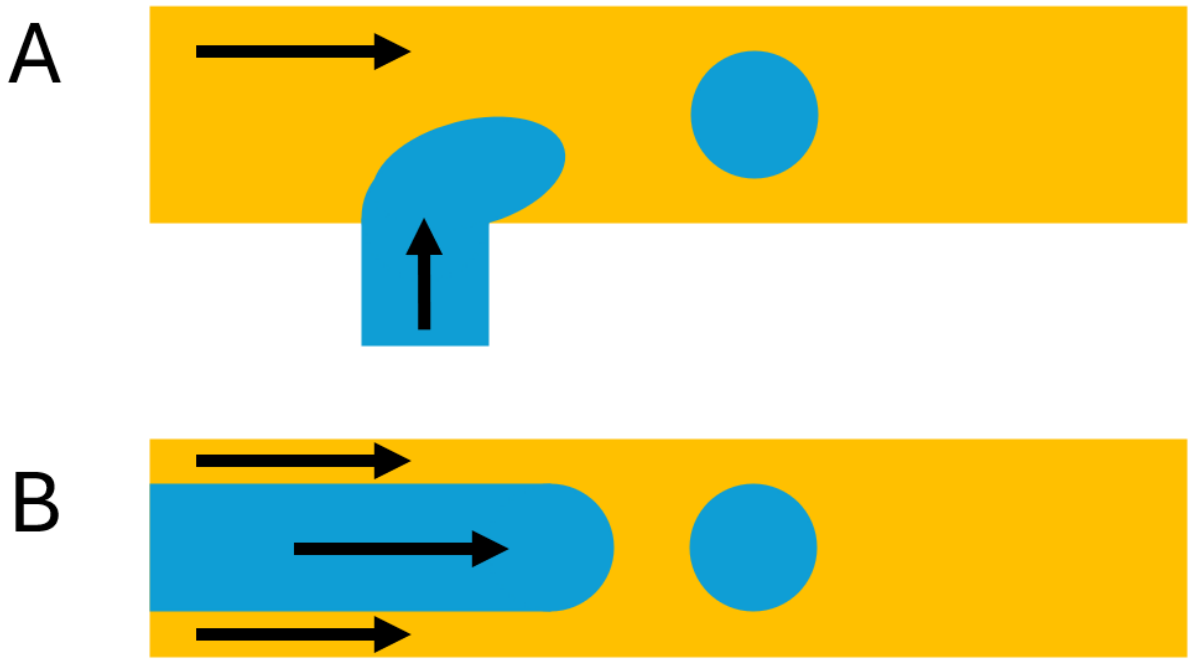

Figure 2.4. Common droplet generation junction geometries. A, T-junction geometry and B, co-axial flow geometry.

Droplet microfluidics for AST

DBMF has been used as a powerful tool for characterizing bacterial response to antibiotics with single-cell resolution [50, 70-73]. The principal advantage provided by microfluidic droplets is the automated encapsulation and subsequent analysis of thousands to millions of single-cell replicate experiments. AST analyses can be extracted from droplets arranged in static arrays [17, 64, 74-80] or from droplets flowing past a detector [42, 81-93]. Droplet array-style platforms promise superior precision of measurements by optical microscopy, enabling tracking of individual cell growth processes [77, 94]. However, microscopy-based readouts result in inherent throughput limitations, as the number of replicate experiments which can be conducted is related to the imaging field of view and the complexity of the image acquisition and analysis pipelines. Sabhachandani et al. reported a droplet docking array which enabled simultaneous monitoring of

bacterial growth in the presence of antibiotics in 1,000 droplets [17]. The authors conducted AST, as well as morphological and growth rate analysis using this platform. Researchers from the same group later updated this device design to incorporate 4 arrays of 8,000 docking sites each, increasing throughput and number of testable antimicrobial-pathogen combinations at once [80].

However powerful, the throughput demonstrated by droplet array platforms pales in comparison to analysis of flowing droplets, which can be analyzed at thousands of droplets per second. Analysis of flowing droplets is similar to flow cytometry (FC) as the analyzed particles pass through an interrogation region where droplet signals are collected. It should be noted that the advantages of flowing droplets come with reduced precision during readout. Flowing droplets do not allow for tracking of individual cell replication events by optical microscopy. However, processing data from flowing droplets is possibly more intuitive and translatable across labs and instruments, as the employed optical/electronic detectors generate quantitative data directly. This contrasts with microscopy-based methods, where image analysis pipelines are required to extract quantitative data from images, introducing a possible point of inter-lab or inter-instrument variability. Flowing droplet analysis is typically thought of as an end-point style assay, where the droplet sample is prepared, stored or incubated off-chip, and re-introduced into a signal detection device for assay readout.

Laser-induced fluorescence (LIF) is the most commonly used light signal in microfluidic droplets, as the vast array of fluorophores available provides experimental flexibility, and fluorescence promises superior signal-to-noise, as excitation and emission light can be separated spectrally. With droplet LIF, bacterial cells expressing a fluorescent protein [83], or encapsulated with a fluorescent metabolism indicator such as resazurin [81], can be used to produce a

fluorescence assay readout. Optical fibers have been integrated in so-called “optofluidic” devices to detect light scattered by microbial cells for AST applications [89, 90, 92, 95]. This latter droplet detection mode represents a promising label-free route toward droplet AST, which reduces the need for optical equipment.

Droplet-based AST platforms have enabled numerous biological discoveries. Scheler *et al*. used their platform to describe the distribution of heteroresistance phenotypes in an *E. coli* isolate, and showed that it is the relative amount of cefotaxime on a per-cell basis, not the concentration, which determines susceptibility [83]. Lyu *et al*. monitored the development of heteroresistance in a population of bacteria exposed to sub-inhibitory concentrations of antimicrobials, and detected resistance phenotypes comprising 10^{-6} of the total population [42]. Pacocha *et al*. demonstrated that the shape features of a viable fraction of cells vs. antibiotic concentration curve can inform about the species content within a droplet, including the presence of small colony variant phenotypes [92].

Parallelized microfluidics platforms

Infrastructure for multiplexing the testing of many antimicrobial conditions in microfluidics devices is generally lacking [50]. Certainly, it has lagged behind the industry standards set by automated broth microdilution systems, which test panels of 40-120 antimicrobials concurrently. This is a specific concern for microfluidic AST, as AST platforms must test entire panels of antibiotic dilution series in parallel to output a MIC and deduce a best therapy route over a reasonable timeframe. Several microfluidics platforms [77, 81, 87, 96] have navigated this by conducting breakpoint analyses, where one or a few specific antimicrobial conditions which correspond to clinical breakpoints are tested. By analyzing microbial growth at

a clinical breakpoint, the organism can be classified as S/I/R by the test AST platform. However, it is preferable to generate an antibiogram, where an entire dilution series of an antimicrobial is surveyed, so that a MIC can be output. Several reports have achieved parallelized testing of antimicrobials in microfluidic droplets, though only by way of complicated device and experimental designs, which prohibit proliferation of the techniques [80]. Kulesa *et al*. reported a droplet array-based technique, in which barcoded, antibiotic-laden droplets were randomly paired and coalesced in the array, allowing for pairwise testing of hundreds of combinations of antimicrobial compounds per chip [64]. However this platform was designed for drug discovery, not AST, and suffers from great complexity as it relies on pairwise merging of droplets and image analysis protocols. So far, the greatest degree of multiplexing in droplets for AST has been achieved by serial emulsification of individual experimental conditions [76, 81, 83, 91]. Computer-controlled, valve-operated sample mixing modules in microfluidic chips, and so-called "cascaded" device designs have automated some of these steps. However, in these platforms the problem of multiplexing is solved by the introduction of complexities elsewhere and it is difficult to envision their widespread use by untrained personnel. Kim *et al*. reported a method of parallel emulsification of an antibiotic dilution series, though it could only generate 8 droplet populations at once, and relied on mixing fixed cell and antibiotic inputs in varying proportions, and could thus be introducing unwanted inoculum effects [78]. Therefore, a facile technique to conduct multiplexed droplet AST would represent a significant advance in the field.

Continuous microfluidics

Continuous microfluidics (CMF) is the subcategory of microfluidics technologies which concerns the flow of a single fluidic phase through microfluidic devices. CMF is not the focus of

the present work, however, advancements in rapid AST have been made using CMF and will be briefly summarized here. The principal advantage provided by CMF is the ability to immobilize test organisms in a culture chamber for optical measurements. Indeed, several reported platforms have demonstrated rapid AST by leveraging the basic protocol of trapping cells in micro-scale chambers, followed by precise tracking of cell growth with optical microscopy [43, 46, 48, 97-100]. Notable advantages of culture chamber-style CMF devices include simplicity of sample preparation, non-complicated injection of samples into devices, and amenability to standard microscopy-based readouts. Increasing throughput in CMF devices presents issues though, as the number of experimental replicates which can be assayed in a single device (the number of micro-culture-chambers) is directly related to the device footprint. Opalski *et al*. reported a CMF-based device containing >1,000 individual microchambers, effectively addressing the throughput issue [99]. However, scale-up of numbers of microchambers necessitates increased complexity of the microscopy pipeline, as the microchambers must still be monitored optically. CMF devices also present issues in multiplexing of test conditions. The simplicity with which the bacterial sample is injected into the CMF device from a single inlet is one of the virtues of CMF, however, it provides poor control over chamber content. This issue has been addressed by non-contact printing of antibiotic conditions into microchambers [99], and with an integrated antibiotic multiplexing dilution module [43]. However, the complicated device design and experimental complexity of these platforms is expected to be an issue for their use by untrained personnel. A notable advance within continuous microfluidics pertains to the integration of electrodes, enabling impedance-based measurements on-chip for AST applications [101-104]. To our knowledge this label-free

biomass detection technique has not been applied to microfluidic droplets, suggesting a possible novel development route.

Commentary on commercialization of microfluidic AST platforms for clinical and point-of-care use

Given the ubiquity of a single type of AST platform in clinics (automated broth microdilution systems), it is tempting to envision the microfluidic AST solution as a singular master test, capable of all-in-one pathogen ID, phenotypic AST and heteroresistance detection against any bacterial species and from any bodily sample. This concept is appealing and would be well received by both the medical and research communities. Nevertheless, current evidence suggests that this vision is unlikely to be realized by a single platform. Rather, it seems more likely that a multitude of testing solutions will arise to address the multitude of bacterial infection-related problems. Each novel testing platform reported entails advantages and disadvantages, and allowing relevant platforms to specialize toward a specific problem allows for leveraging of the advantages and simultaneous navigating of the disadvantages. By contrast, a universal master solution will require the collectivization of its advantages and disadvantages. For example, a nanofluidics-based technology with European regulatory approvals recently received its first clinical evaluation, and demonstrated promising results [105]. This technology is currently only validated for urinary tract infections (UTIs), and leverages the fact that urine is a relatively uncomplicated bodily sample, which is amenable to rapid separation of contaminating bacteria from the sample matrix by mechanical filtration. AST with this platform using more complicated body samples such as bacteremic blood is expected to prove challenging. However, the technology is currently able to conduct AST on urine samples collected directly from the patient without pre-incubation steps, and outputs AST results for common UTI pathogens in 45 minutes from the time of urine

collection. Given that UTIs are the second-most common infectious disease in the world behind only respiratory tract infections [106], it would be detrimental to society to reject this technology on the basis of its specialization. On a different note, recent advances in rapid separation of bacteria from infected blood samples have resulted in rapid AST without the need for blood pre-culturing steps [107, 108]. The primary tradeoff between separation of bacteria from blood, and culture-amplification of bacteria from blood, is that the bacterial yield which can be used for subsequent testing is much greater from culture-amplification, though culture-amplification requires incubation for up to 24 hours. In theory, this is an issue that microfluidics platforms of all type are suited to address, *via* the miniaturization of AST reaction volumes. This result should extend to any bodily sample collected for suspected bacterial infection: microfluidics devices require lower reagent volumes and lower cell counts, and thus facilitate reduction or elimination of pre-culturing steps. It is therefore conceivable that separate microfluidics-based tests specifically designed to accommodate, for example, bacteria separated from blood cultures, bacteria minimally amplified from an abscess sample, or bacteria contained in whole urine, could all become commonplace. For point-of-care (POC) testing, it is possible that continuous microfluidics-based platforms hold an advantage over droplet-based platforms, as droplet generation is not required and whole infectious samples can be simply injected into the device. For example, a recent CMF device based on immunofluorescence demonstrated quantification of *E. coli* in synthetic urine, featuring smartphone camera-based readout [109]. This platform represents a powerful POC option which also navigates the general requirement of microscopy in CMF platforms. However, in a separate platform, bacterial encapsulation into droplets was driven by handheld syringe-vacuum, and viable bacteria were quantified by smartphone-based turbidity readings of the droplets [110]. Perhaps

then, the decision between droplets and continuous microfluidics should be related to the desired throughput. Droplet-based AST techniques come with complexities that are not present in CMF, however the trade-off is in their ability to assay many thousands of single-cell experiments. For example, in the future, in the case of recurrent infection or suspected heteroresistance, clinicians may opt for a droplet-based method with the goal of detecting a rare resistance phenotype, which could be used to inform the antimicrobial therapy route. Or, in the case of a multidrug resistant isolate, clinicians may need to rapidly identify a combinatorial drug treatment plan [111]. Recent microfluidic combinatorial AST platforms have leveraged on-chip drug mixing units with droplet sample generation to perform rapid, single-cell AST against a panel of combinatorial drug conditions [76, 86].

It is perhaps telling that most recently commercialized microfluidic AST systems rely on microscopy-based monitoring of a bacterial sample in a microchamber, in a single fluidic phase [105, 112-115]. Two commercial microfluidics-based AST options [116, 117] are available which rely on monitoring changes in resonant frequencies of cantilever sensors in response to microbial growth [118]. However, a recent platform based on pheno-molecular AST represents possibly the platform of greatest potential yet reported [45, 87]. This platform leveraged microfluidic droplets, as the effective concentration of bacteria from low-bacterial-load urine is immediately and dramatically increased when the cell is encapsulated into a 4 pL droplet. This phenomenon, combined with detection and quantitation of bacterial 16S rRNA enabled simultaneous ID and AST of common uropathogenic bacteria, in 30 minutes directly from patient urine. Questions about the ability of untrained personnel to conduct this experiment remain, as it relies on complicated equipment and device design—perhaps this explains why this platform has not been

commercialized yet. Nevertheless, simultaneous pathogen ID and AST directly from patient sample is something of a holy grail in AST.

CHAPTER THREE

DEVELOPMENT OF A ROBUST PLATFORM FOR ULTRAHIGH-THROUGHPUT ANALYSIS OF MULTIPLEXED FLUORESCENCE SIGNALS FROM MICROFLUIDIC DROPLETS

Abstract

Droplet-based microfluidics (DBMF) is a powerful technology for single-cell biological analysis, as it enables automated, high-throughput processing of individual cells. In DBMF, biological samples are partitioned into micrometer-scale, water-in-oil droplets, each acting as an isolated microreactor. This miniaturization converts a standard mL-scale sample into millions of discrete, single-cell experiments conducted in parallel. Maximal automation and throughput of emulsified droplet samples has been achieved by analyzing optical signals from flowing droplets. Despite this, signal analysis from flowing droplet samples presents several key challenges, including robust assembly of optical equipment to deliver optimized laser beams to the droplet sample, stable reinjection of emulsion samples, data quality assurance, and reliable acquisition of multiplexed droplet signals. In this thesis chapter, we detail the assembly of a robust platform for ultrahigh-throughput analysis of multiplexed fluorescence signals from microfluidic droplets, and provide tutorials for navigating these challenges.

Introduction

Droplet-based microfluidics (DBMF) has enabled unprecedented throughput in single-cell assay screening [42, 70, 73]. In DBMF, a biological sample is compartmentalized into micron-

scale water-in-oil emulsions, converting a standard mL-scale sample into thousands or millions of single-cell technical replicate experiments. Each microfluidic droplet is equivalent to a well on a microtiter plate, and the droplets are generated using automated platforms at kHz rates. As microfluidic droplets contain picoliter to nanoliter volume, each droplet is 10^3 to 10^6 times smaller than the minimum required volume on a well plate, which is on the scale of microliters.

Maximal automation and throughput of emulsified droplet samples has been achieved by analyzing optical signals from flowing droplets [119]. Detection of light signals from droplets is similar to flow cytometry (FC) as the analyzed particles pass through an interrogation region where signals such as fluorescent, scattered or transmitted light are emitted from the droplets and analyzed by detectors. Then, the signals are evaluated against pre-determined criteria. Laser-induced fluorescence (LIF), in which droplets flow past a laser beam which excites fluorescence signals from the droplets, is the most commonly used light signal in microfluidic droplet detection. The vast array of fluorophores available provides experimental flexibility, and fluorescence promises superior signal-to-noise, as excitation and emission light can be separated spectrally.

While FC is a mature technology, providing such benefits as superior throughput, integrated FC instruments and at some institutions, institutional FC cores, there are several analyses which are only enabled by the compartmentalization of the cell into a discrete volume as in DBMF. Microfluidic droplets contain an entire reaction so reaction products like secreted molecules, extracellular metabolites or daughter cells can be analyzed and linked to the original seeded cell. This is in contrast to FC, in which sample components are not discretized, and are free to mix throughput the process. This feature of droplets enables ultrahigh-throughput, flow based analyses which are impossible by analyzing flowing cells on a flow cytometer [120].

In Chapters 4 and 5 of this thesis, we use a droplet fluorescence detection platform to conduct multi-color LIF, enabling parallelized microfluidics and single-cell analyses. The assembly of the equipment required to conduct LIF on microfluidic droplets has been detailed in the literature [121, 122]. In this thesis chapter, we will provide information on the equipment used in our detection stand, as well as the optimization procedures conducted on our unit which enabled the applications detailed in later chapters. The optimization protocol will be detailed in order of most global to most specific variables, beginning with the shaping of the laser beam and droplet detection basic procedures, and ending with the optimization of individual fluorescence channels and their combination, to produce a multiplexed droplet LIF application.

Droplet LIF detection working principle and equipment.

In our detection stand, a microchannel device containing a flowing droplet sample is first mounted onto a microscope stage. A microscope objective focuses a multi-color laser onto the flow channel, which excites fluorophores in the flowing droplets. Fluorescence signals are collected by the microscope objective and propagate toward an array of photomultiplier tubes (PMTs) at the rear of the microscope. The fluorescence signals are separated by color using dichroic mirrors before signal amplification by the PMTs. Each color channel has a laser and PMT specific to the channel; thus, in our 4-color setup, there are 4 laser diodes of unique wavelength, and 4 PMTs uniquely gated to accept channel-specific wavelengths of fluorescent light. Each PMT outputs a voltage proportional to the incident fluorescent light from an excited droplet. We use a custom script in LabView 2015 and a National Instruments PCIe-7852 data acquisition card (NIDAQ) to record PMT voltage signals, apply PMT gains, and write datafiles during droplet fluorescence detection phases (Figure 3.1).

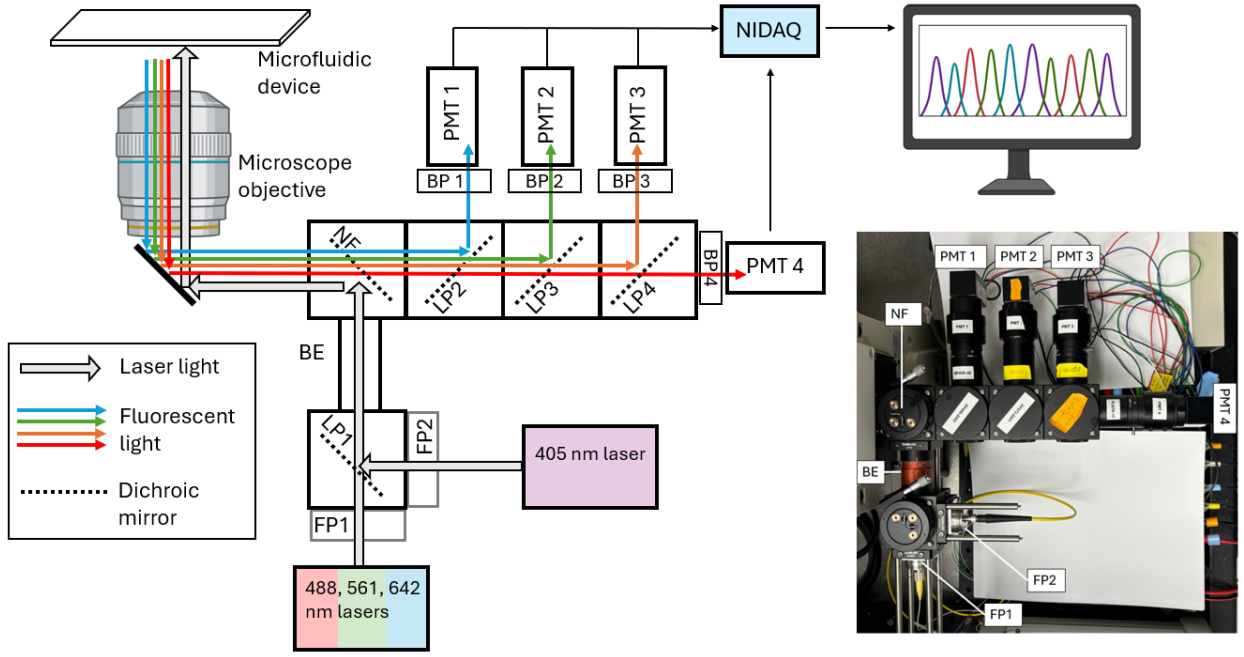

Figure 3.1. Schematic of optical train used for droplet laser induced fluorescence. Picture bottom right taken of the optical train integrated with the microscope.

Component	Part number	Manufacturer	Purpose
FP1	PAF2-A4A	Thorlabs	RGB laser coupling into free-space
FP2	PAF2S-7A	Thorlabs	405 nm laser coupling into free-space
LP1	DMLP-425	Thorlabs	Redirect 405 nm laser onto optical axis
BE	GBE02-A	Thorlabs	2x magnification beam expander
NF	Di01-R405/488/561/635	SemRock	Reflect laser beams while transmitting fluorescent light
LP2	FF495-Di03	IDEX H&S	Direct blue fluorescent light into PMT 1
LP3	FF573-Di01	IDEX H&S	Direct green fluorescent light into PMT 2
LP4	FF652-Di01	IDEX H&S	Direct orange fluorescent light into PMT 3 and transmit red-far red light into PMT 4
BP1	MF-445/45	Thorlabs	Filter fluorescent light prior to PMT
BP2	FB530-10	Thorlabs	Filter fluorescent light prior to PMT
BP3	FB620-10	Thorlabs	Filter fluorescent light prior to PMT
BP4	FL 670-10	Thorlabs	Filter fluorescent light prior to PMT
PMT 1-4	H10723-20	Hamamatsu	Amplify fluorescent light signals

Table 3.1. Optical components used in the droplet LIF optical train.

Laser excitation and droplet fluorescent light are propagated along an epifluorescence configuration, meaning the same microscope objective which delivers the laser beam to the sample is used to collect the fluorescent light. Epifluorescence provides superior background signal reduction, as the excitation light source does not point directly into the photodetectors. Epifluorescence also supports multi-channel fluorescence collection, with the use of in-line optical filters to separate multi-wavelength light signals by color.

Fluorescence-based biological applications are commonly multiplexed using up to 4 color channels which are simultaneously detected from a sample. The 4 most common color channels used coincidentally correspond to DAPI (exc/em 360/460 nm), FITC (497/520 nm), TexasRed (595/615 nm) and Cy5 (645/665 nm) stains, owing to their minimal spectral overlap, availability of filter sets and appropriate laser diodes, and compatibility with existing instrumentation. Our multichannel droplet LIF platform was designed to reflect this arrangement of fluorophores. As such we implement 405, 488, 561 and 642 nm lasers to excite fluorophores in channels roughly corresponding to DAPI, FITC, TexasRed and Cy5 bandwidths.

The optical train used to arrange excitation and emission light signals is detailed in Figure 3.1. The order of operations, beginning with the introduction of laser beams and ending with the amplification of fluorescence signals by PMTs, is as follows:

(1) 488, 561 and 642 nm lasers are delivered to the optical train in a single optical fiber and coupled into free-space using fiberport 1 (FP1, Thorlabs part no. PAF2-A4A). These three laser beams are combined into a single beam using a fiber laser combiner (Thorlabs part no. RBG50HF) upstream of FP1, not shown in Figure 3.1. This 3-color combined laser will be referred to as the RGB (red-green-blue) laser. The 405 nm laser

is delivered to the optical train in a separate fiber, coupled into free-space using FP2 (Thorlabs part no. PAF2S-7A).

(2) Dichroic mirror LP1 reflects the 405 nm laser beam into coalignment with the RGB laser. The RGB laser is transmitted through LP1.

(3) A beam expander (BE, Thorlabs part no. GBE02-A) expands the beam waist two-fold.

(4) The 4-color laser is reflected off the notch filter (NF, Semrock part no. Di01-R405/488/561/635) and travels to the microscope objective to excite fluorescence. The notch filter reflects laser light while transmitting Stokes-shifted fluorescent light.

(5) Flowing droplets are excited by the multicolor laser focused onto the microfluidic channel. Droplets emit fluorescence isotropically. Fluorescent light is collected by the microscope objective and propagated along the epifluorescence path in the reverse direction as the laser beam, toward the optical train.

(6) Emitted fluorescent light is transmitted through the notch filter. Any laser light reflected back along the same path as the emitted fluorescent light is prevented from reaching the PMT array by the notch filter.

(7) LP2 reflects blue light into PMT 1 and transmits longer wavelength light.

(8) LP3 reflects green light into PMT 2 and transmits longer wavelength light.

(9) LP4 reflects orange light into PMT 3 and transmits red-far red light into PMT 4.

Beam shaping considerations

Focusing a laser beam onto a microfluidic droplet sample through a microscope objective requires directing the beam from an external laser diode source, through the microscope body and to the objective's rear aperture. The beam must also be shaped and aligned in order to produce an

optimized beam spot within the microfluidic device for droplet LIF applications. For optimal performance, the laser beam delivered to the back aperture of the microscope objective should be collimated, concentric with and parallel to the central axis of the objective, and should over-fill the back aperture [123]. A collimated beam allows the microscope objective to focus the laser to its smallest possible spot size, enabling one droplet at a time to be irradiated by the laser. A non-collimated beam can reach a focus in a different plane than the focal plane of the microscope objective, and can also produce spherical aberrations in the beam spot. If the beam is delivered off-axis, this can produce aberrations such as astigmatism or coma, or could even result in beam vignetting if the microscope objective's apertures clip the beam [124, 125]. Filling the back aperture of the microscope objective allows the microscope objective to focus the laser beam using its entire numerical aperture, producing a higher-resolution, smaller beam spot.

Methods, Results & Discussion

Laser beam collimation.

We use optical fibers to guide the laser beams from external diode sources to the optical train for safety and setup flexibility reasons. Optical fibers are the safest way to propagate a laser as the beam is contained within the fiber, preventing stray laser beam hazards. Moreover, optical fibers are flexible and can guide a laser beam in any direction without reflective mirror optics. However, the laser beam must be coupled into free-space before it can be propagated through a microscope. When a laser exits an optical fiber into free-space, it diverges according to the numerical aperture (*NA*) of the fiber:

$$NA = n_0 * \sin(\theta)$$

Where n_o is the refractive index of the medium into which the laser exits from the fiber (air, in the case of coupling into free-space), and θ is the half-angle of the cone of light that defines the laser beam shape (Figure 3.2). This contrasts with the requirement for a collimated beam, which is a bundle of light rays with parallel direction of propagation, to be delivered to the microscope objective.

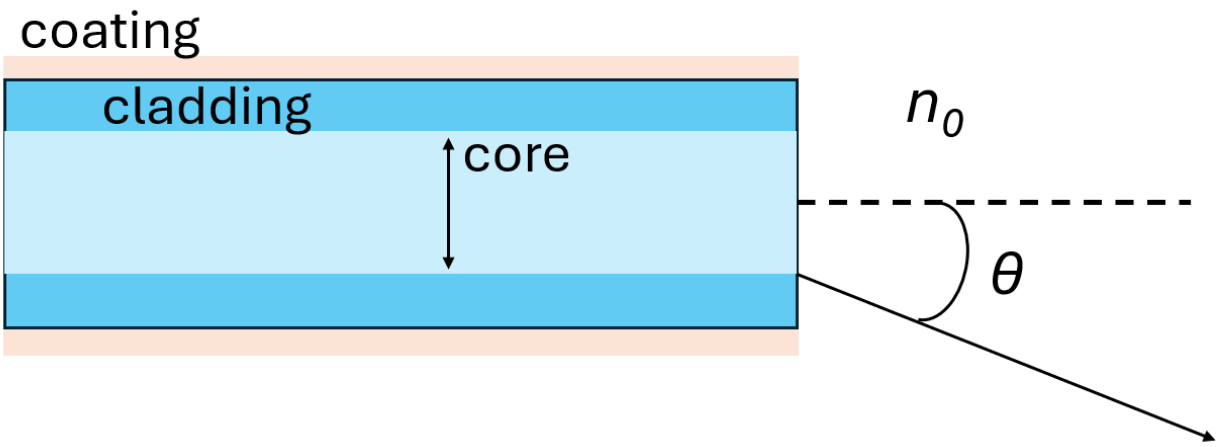

Figure 3.2. A laser beam exiting an optical fiber diverges according to the numerical aperture of the fiber.

To mediate laser beam coupling into free-space and beam collimation, we deployed Thorlabs FiberPort collimator/couplers (FP1 and FP2, Figure 3.1). The fiberport fulfills two primary functions: first, as an optomechanical device, it positions the optical fiber centrally and perpendicular to a cube in the optical train's cage system. This is an essential crude beam positioning step, in which the beam is positioned to within manufacturing tolerances of the optical axis, so that it may later be moved onto the axis. Second, each fiberport contains an aspheric lens element for beam shaping which can be used to collimate the beam. The shaping lens can also be

used to translate and tilt the beam, though it is recommended that these functionalities be implemented sparingly, to prevent the introduction of beam aberrations.

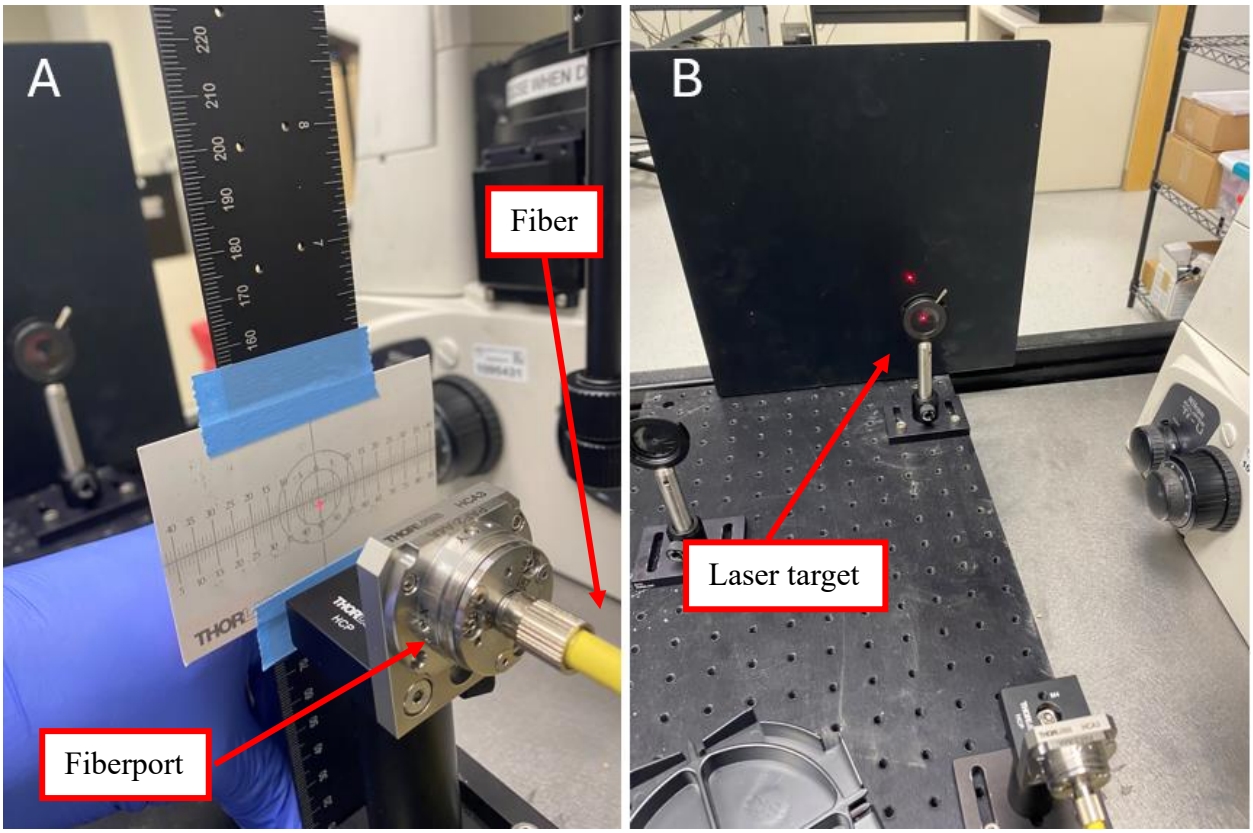

Figure 3.3. Optical fiberport mounted on an optical post for laser beam visualization and shaping.

To collimate the beam output by the shaping lens, it is necessary to visualize changes in the beam waist as a function of distance from the lens element. A collimated beam will have a constant waist, regardless of distance from the lens element. By contrast, the beam waist of a converging or diverging beam will show dependence on distance from the lens. To visualize the beam waist-distance relationship, the fiberport was mounted on a post and the fiber was integrated (Figure 3.3). The beam was visualized on a notecard. During visualization, the black laser screen shown in Figure 3.3B was removed. This allowed visualization of the beam spot up to 10 meters from the lens element, which can be approximated as infinity in optical terms, as it is many times

the focal length of the lens elements (effective focal length, EFL <7.5 mm for each fiberport). A divergent beam will show increasing beam spot size with distance from the lens element; oppositely, a convergent beam will show decreasing beam spot size with increasing distance. Importantly, a convergent beam will diverge after it reaches its focus, so the user must take care to document the correct deviation from collimation, if present. A well-collimated beam will maintain constant beam waist across many focal lengths. Thus for best results, the beam waist should be visualized while walking the visualization card as far away as is feasible within the lab space.

We found that both of our laser-fibers were convergent after mating with their respective fiberports. In each case when visualizing the beam on a notecard, the laser spot decreased in diameter for the first ~2 meters of free-space propagation, then began to diverge after the focal point. To collimate the beams, the three "Zθ" screws on the fiberports were adjusted one eighth-turn at a time, until the beam waist maintained constant diameter over the length of the microscopy room. The Zθ screws must be adjusted equally, or else a tilt will be imposed onto the lens element which will produce aberrations in the final laser beam [126]. If the beam is divergent, the lens element is too close to the fiber, and the Zθ screws must be tightened to move the lens element away from the fiber; the opposite adjustment is required if the beam is convergent.

Beam alignment

While laser beam collimation ensures that every ray within the beam is propagating in the same direction, the direction of the beam as a whole must also be aligned to the system of optics. It is conventional to use cylindrical coordinates in optics, as lens systems are most often composed of individual elements which are sections of spheres, arranged concentrically. The optical axis is the z-axis in cylindrical coordinates terminology. In most laser beam alignment procedures

including the present application, the goal is to position the beam so that it is concentric with and parallel to the optical axis. Henceforth we will refer to such a beam as on-axis. Moreover, the co-alignment of laser beams originating in two separate optical fibers presents an additional design constraint (Figure 3.1).

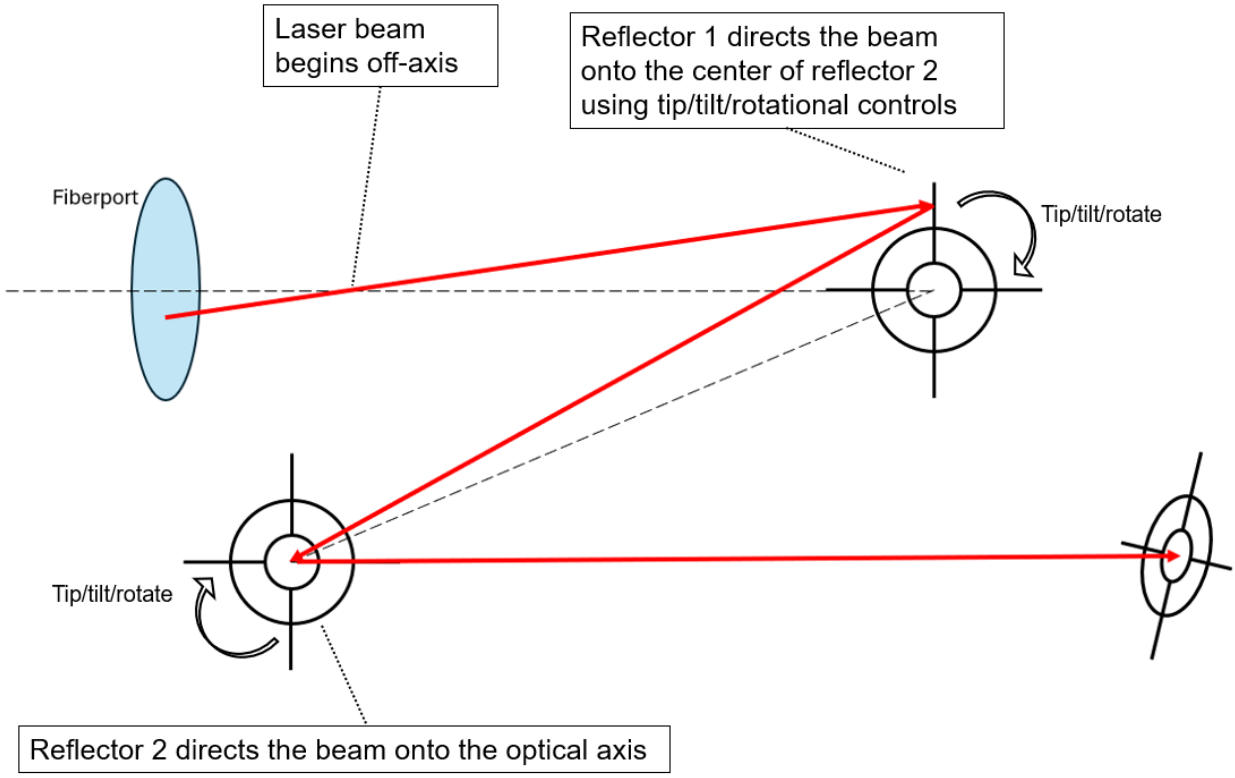

Figure 3.4. Procedure for walking a laser beam onto the optical axis using two reflective optics.

405 nm laser beam alignment

FP2, containing the collimated 405 nm laser fiber, was mounted onto the optical train in its final position for alignment using reflective optics. A collimated beam will maintain its collimation through any number reflective events. Furthermore, two reflectors with complete tip/tilt/rotational control provide sufficient degrees of freedom to walk a laser beam onto any desired path. Thus, a step-wise laser alignment procedure was conducted to walk the 405 nm

laser beam onto the optical axis. In the step-wise approach, the first reflector was adjusted to position the laser spot centrally on the second reflector, then the second reflector was fine-tuned to direct the beam precisely onto the desired path (Figure 3.4).

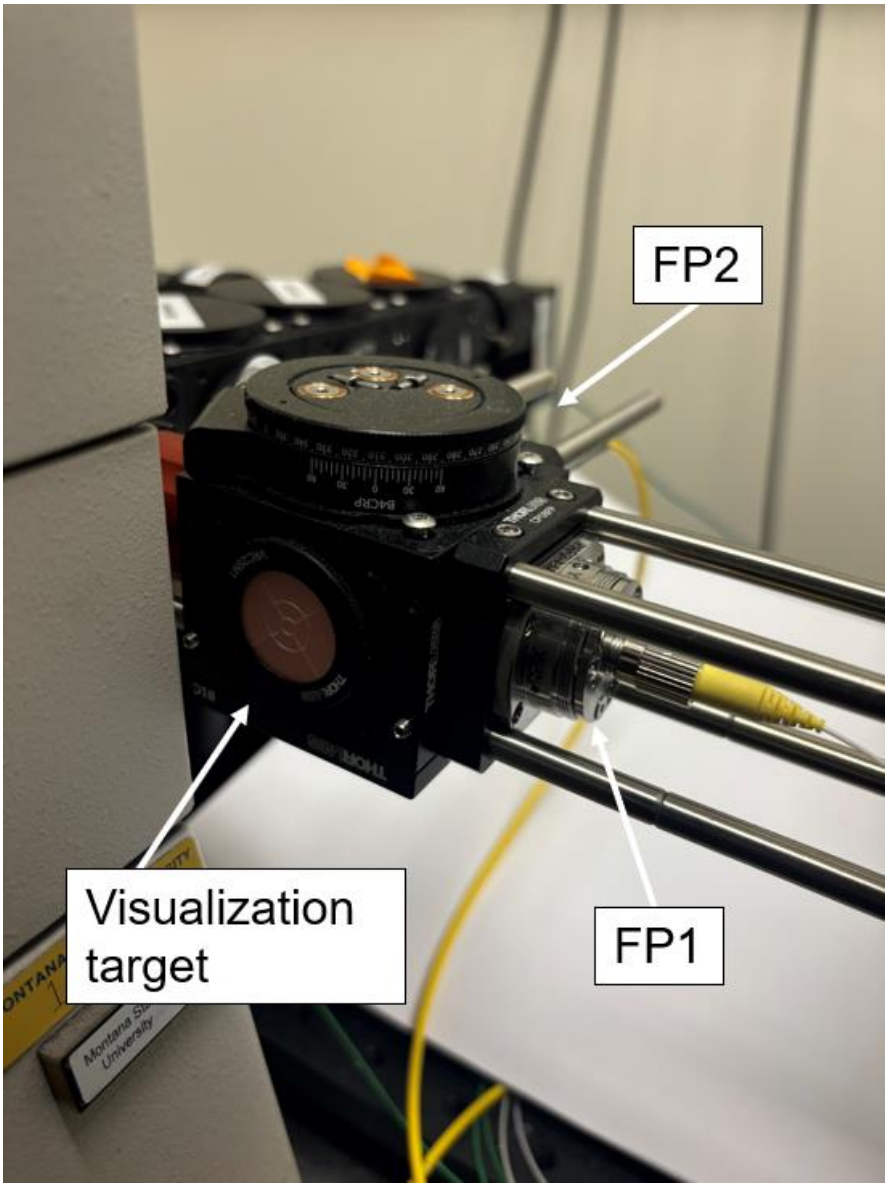

Figure 3.5. Laser visualization target mounted opposite FP2 for crude alignment of the 405 nm laser beam.

A laser visualization target (Thorlabs part no. VRC2SM1) was threaded onto the optical cage face directly opposite FP2 (Figure 3.5). We observed that the laser beam exiting the shaping lens was not initially centered on the visualization target. This is an artifact of the manufacturing tolerances of optomechanical components. To adjust the beam position, the X-Y translational limiting screws on the fiberport were adjusted until the beam spot had translated onto the center of the visualization target. At this point the laser beam was also visualized on a notecard while modulating the distance from the fiberport, to ensure the X-Y translational adjustments had not introduced any aberrations. This first alignment step guaranteed that the laser beam intersected the optical axis at a point near the first reflective element, LP1. LP1 was then put in place to reflect the beam further downstream in the optical train. To ensure tip/tilt/rotational control, all dichroics were held in position by Thorlabs B4CRP kinematic rotation platforms, which mediated the control over dichroic orientation.

The visualization target was then moved to directly opposite FP1 (Figure 3.6) in the same cube as NF. The orientation of LP1 was modulated using its tip/tilt/rotational controls until the 405 nm laser spot reflected off LP1 was centered on the visualization target. Last, the visualization target was moved to a microscope objective lens port, and the notch filter was replaced. The tip/tilt/rotational controls modulating the notch filter orientation were adjusted until the laser spot was centered on the visualization target in the microscope turret. Very little adjusting was required during this last step, due to the preceding alignment steps.

In this way, the 405 nm laser beam was made to propagate on-axis. Documenting a laser beam's position at any two points in space produces its propagation vector. Forcing the two points to both be on the optical axis using tip/tilt/rotational controls ensures on-axis propagation. The

reflection by LP1 toward NF guaranteed that the laser beam intersected the optical axis in the plane of NF. Then, the reflection by NF to another point on the optical axis, discerned as the center of the visualization target in the microscope turret, ensured on-axis propagation.

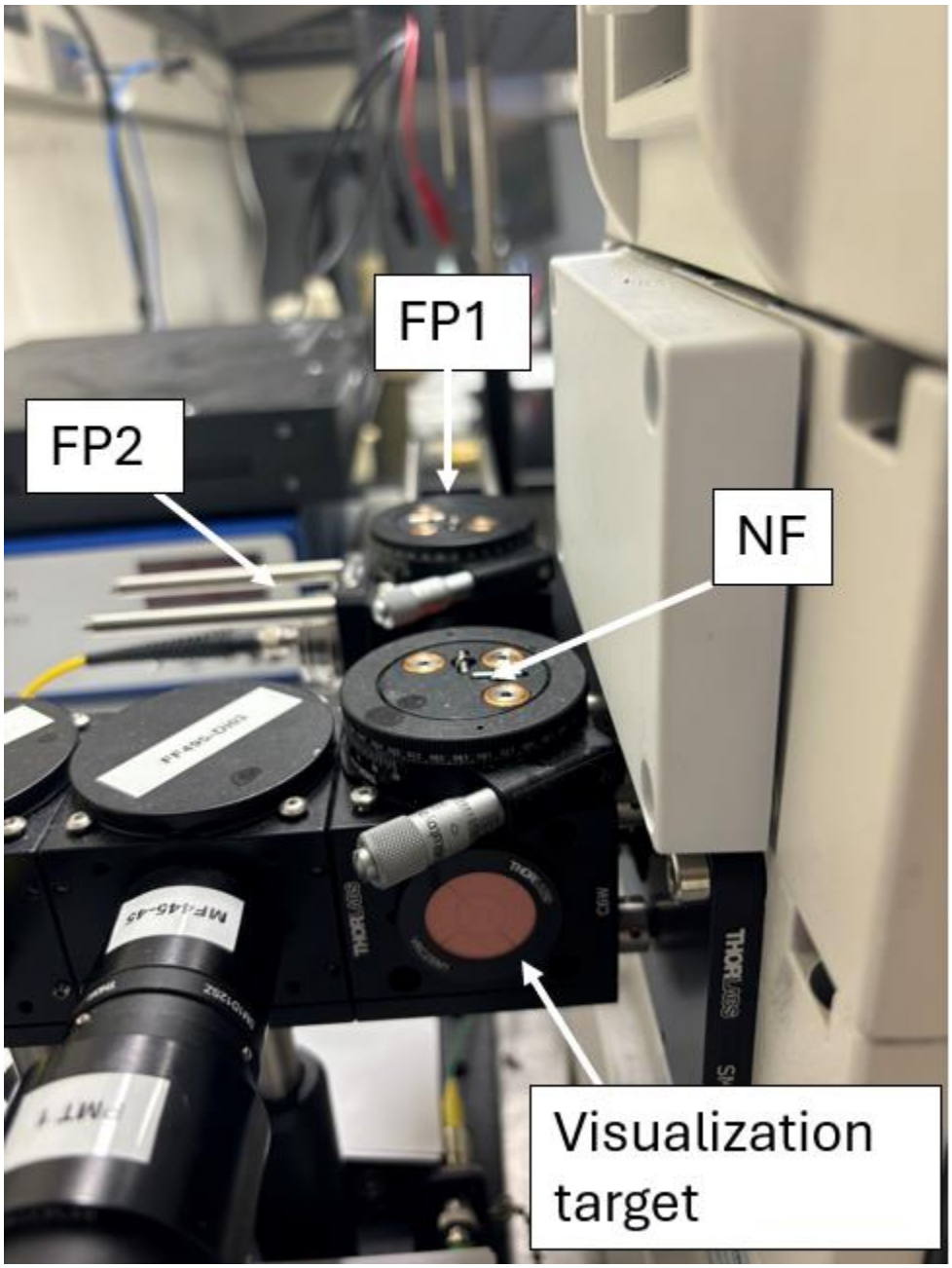

Figure 3.6. Laser visualization target mounted opposite FP1, in the same cube as NF, for laser beam alignment.

RGB laser beam alignment

FP1, containing the collimated RGB laser fiber, was mounted onto the optical train in its final position for alignment by reflective optics. The laser visualization target was threaded opposite FP1 in the same cube as NF (Figure 3.6). Of note, the RGB laser will transmit through LP1 so this dichroic was left in place. Again, we observed that this laser beam was not centered on the visualization target and centered it using the X-Y translational limiting screws on FP1. The introduction of new beam shape aberrations was ruled out by visualizing the RGB beam spot on a notecard while modulating distance.

At this stage, it was possible that the RGB and 405 nm lasers intersected at the visualization target opposite FP1, while propagating at different angles. If this were the case, NF would reflect the two beams along different trajectories and two beam spots would be visible on the visualization target in the microscope objective lens port. This was not the case as only a single beam spot was visible on the microscope turret visualization target. This indicated that the two initially separate laser beams had been coaligned to the optical axis. To verify their co-alignment, we propagated the 642 and 405 nm laser beams through a microscope objective and onto the ceiling of the microscope room and observed concentricity of the two beam spots, confirming successful co-alignment. In a second experiment to test for co-alignment of the lasers, we detected fluorescence from droplets containing dissolved AlexaFluors 405, 488, 568 and 647, each at 1.0 μM. Figure 3.7A shows a close up of a single fluorescence peak in the live LabView detection window, confirming simultaneous fluorescence detection in all 4 channels. If the lasers were not co-aligned

at this point, individual fluorescence color peaks would appear at slightly different points in time, as in Figure 3.7B.

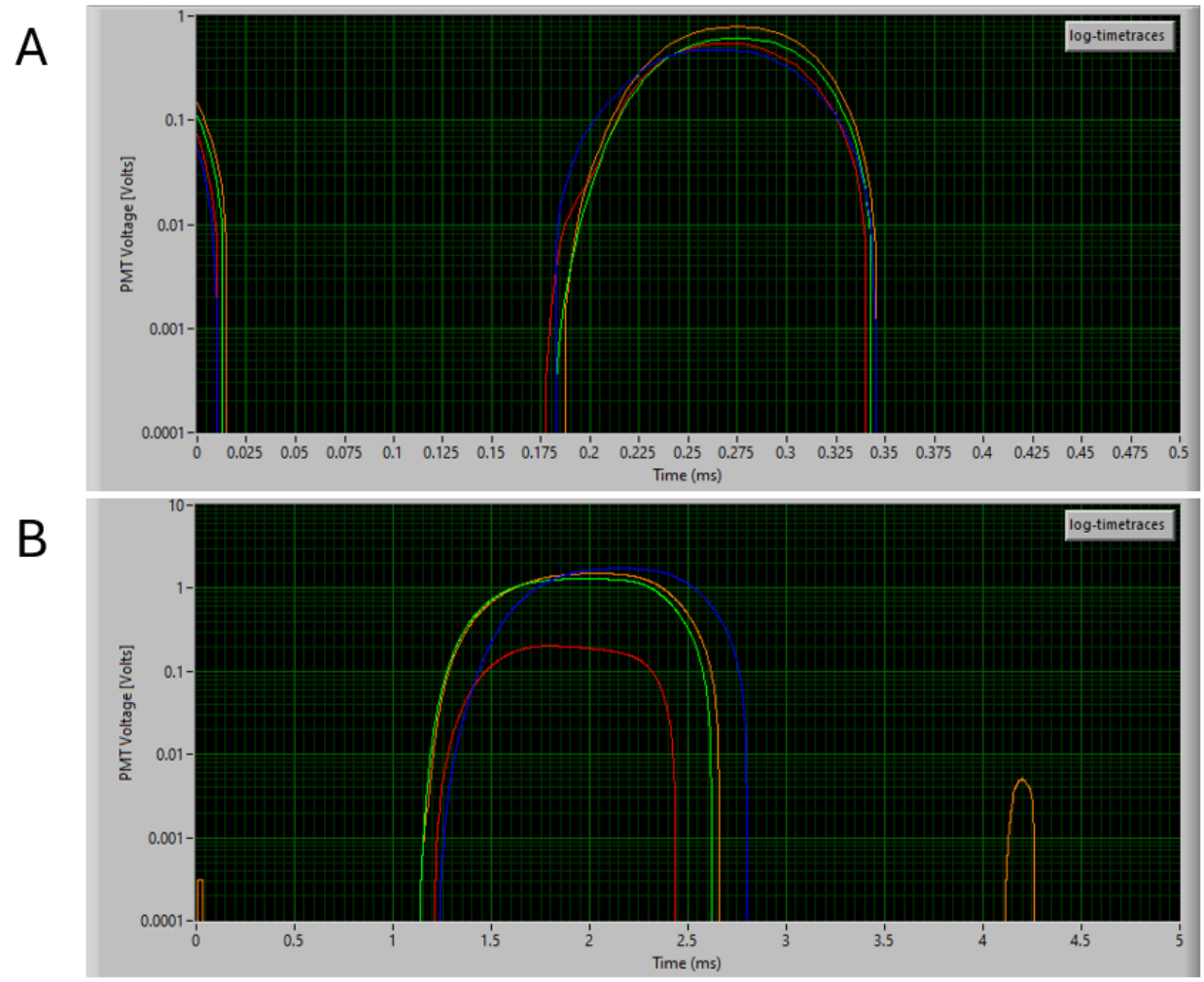

Figure 3.7. Visualization of laser beam alignment by 4-color droplet fluorescence detection in LabView. A shows aligned laser beams producing different color peaks which are aligned in time. B shows the result of a misaligned laser, and individual color peaks which are not temporally aligned.

Of note, the RGB laser was aligned with only a single reflective optic. This was a fortunate occurrence; all optical and optomechanical components are subject to manufacturing variability, and can occasionally show good alignment within an optical system as manufactured. In the case that the RGB laser could not be centered using the X-Y adjusters, or if these adjusters introduced

beam aberrations, the beam could be aligned by introducing an extra right-hand turn as done for the 405 nm laser. In this scenario, the RGB laser would be introduced parallel to the 405 nm laser, and would reflect 90^{o} off a dichroic mirror upstream of LP1. This extra reflective event would provide the degrees of freedom required to walk the RGB laser beam onto the optical axis, without use of the X-Y translational adjusters.

Beam expansion

With the preceding steps, the delivery of an on-axis, collimated, 4-color laser beam to the rear aperture of the microscope objective was ensured. At this stage, a laser beam expander should be added if the laser beam does not over-fill the rear aperture of the microscope objective. The laser beam spot size in the plane of the microscope objective rear aperture can be visualized with the visualization target used for alignment. Beam expanders such as Thorlabs' line of Galilean beam expanders (for example, part no. GBE02-A) are designed to intake a collimated, on-axis beam and expand its waist by a specified magnification, without introducing unwanted effects on the collimation or direction of beam propagation.

Stable reinjection of emulsion samples for flow-based analysis.

The power of high-throughput droplet microfluidics comes from its amenability to flow-based detection schema in which droplets, acting as individual bioreactors, are analyzed automatically at kHz rates. However, achieving reliable droplet flow regimes is a challenge. Droplets are composed entirely of liquids, and are only stabilized by the surfactant layer adsorbed onto the liquid-liquid interface of the droplet [127]. As droplets flow through a device, any droplet deformation causes momentary fluctuations in the density of surfactant in the adsorbed layer [69].

If droplets flow too quickly past microfluidic device structures or suspended particles such as contaminant dust, they are susceptible to coalescence or shear [128]. Indeed, droplet deformation by flowing past microfluidic structures has been used as a mechanism to induce coalescence [129]. Sometimes droplet samples are polydisperse even in the absence of destabilizing effects, which can result in irregular flow patterns, possibly obfuscating droplet detection signals.

Several theoretical treatments of droplet coalescence are available [69, 130-132], none of which are a stand-alone substitute for lab-specific optimization of a droplet reinjection protocol to avoid emulsion instabilities. Much of the theoretical and experimental work on coalescence has considered idealized systems, such as the coalescence of two droplets freely suspended in a fluid, or droplets confined in a model channel geometry [69, 131, 133]. While these treatments are useful and informative, in practice, microfluidic devices used for bioassays generally present deviations from these idealized systems. For example, the use of various surfactants to stabilize droplets of varying content, and confined to flow channels of varying geometry, are factors which cannot always be accounted for in a theoretical treatment of coalescence.

When preparing microfluidic devices, care should be taken to avoid the introduction of dust from the outset. Reinjection devices should be designed with filtration structures which can catch dust and other contaminants without damaging droplet samples. The injected emulsion should be close-packed. Close-packing can be achieved by removing as much of the continuous phase as possible [128], for example, by positioning the syringe or tube holding the emulsion upright, and allowing the continuous phase to drain out while the emulsion floats to the top. Upon introduction to the microfluidic device, inter-droplet contact forces will order the close-packed emulsion [128, 133], and the droplets will flow through the device regularly. In our group, we pre-

lubricate microfluidic tubing lengths used for reinjection with continuous phase, and treat the tubing with an anti-static gun, to prevent electrostatic coalescence in the tubing.

Even during reinjection of a stable, monodisperse emulsion, the droplets flowing in the detection channel must be adequately spaced to avoid simultaneous detection. This is generally achieved by introducing an additional stream of continuous phase, which intersects the reinjected droplets and spaces them. The theoretical minimum distance between two droplets in sequence, Δx, required to prevent their co-detection by LIF is defined by the laser beam diameter, d. If $\Delta x < d$, two sequential droplets will be irradiated by the laser coincidentally. The spot size of a laser in a diffraction-limited system, d_o, can be calculated using the Airy Disc Diameter formula:

$$d_o = 1.22 * \frac{\lambda}{NA}$$

Where λ is the wavelength of the laser beam and NA is the numerical aperture of the microscope objective [134]. However, the laser beam will reach this minimum spot size at the focal plane of the microscope objective, and will assume a conical beam of greater waist diameter before and after its focal point [123]. Moreover, most microfluidics labs do not contain sophisticated optical equipment required to reach the diffraction limit, so deviations from a diffraction-limited optical system should be prepared for. As such, we suggest empirical observation of the relationship between emulsion injection flow rates, droplet spacing and discrete droplet detection. For example, the diameter of the diffraction-limited airy disk produced by the NA = 0.6 microscope objective used in our setup ranges from 900 nm for λ = 405 nm, and 1,200 nm for λ = 642 nm. However, as we will show in the later section, *Fluorescence intensity and time inside measurements collected*

by droplet LIF are correlated, practical data from droplet fluorescence detection suggest that the region of laser illumination is on the order of 10^1 μm diameter. Laser beam spots smaller in diameter than the droplet in the flow channel could result in failure to detect particles of interest, such as cells or colloidal particles, if the particles are positioned outside the beam waist during detection.

Robust detection of flowing microfluidic droplets using reference dyes.

To facilitate robust detection of microfluidic droplets we developed a method to impart each droplet with a standardized fluorescence signature, enabling visualization of droplet spacing and differentiation from noise, coalescence, and sheared emulsions. We dubbed this standard fluorescence signature the reference dye, in an intentional analogy to the reference dyes used in qPCR applications. The inclusion of a reference dye in the dispersed phase means that the entire droplet is fluorescently stained. Thus, abnormally sized droplets can be discerned as fluorescence peaks of larger or smaller than average width, due to the droplet residence time underneath the laser. Figure 3.8 shows a screenshot of the live detection window in LabView, during detection of droplets stained with a red reference dye, and containing green-fluorescent *E. coli* cells loaded at ~20% rate. Each droplet, as well as its adequate spacing from neighboring droplets, can be clearly discerned. Moreover, the yellow boxed panel labeled *Detection Parameters* contains user-programmable controls to define a set of criteria required to trigger a droplet detection event. The criteria can be defined as a range of fluorescence peak amplitudes and widths, for a specific fluorescence channel. These controls provide a means to program the LabView software to record signals from droplets and exclude noise or incorrectly sized droplets. For example, high-frequency, low-amplitude noise can be observed in channel 4 (red) in Figure 3.8. To gate this signal from

recorded datasets, the controls in the *Detection Parameters* panel are programmed to only record signals in channel 4 which are greater in amplitude than 0.1 V and wider than 0.01 ms.

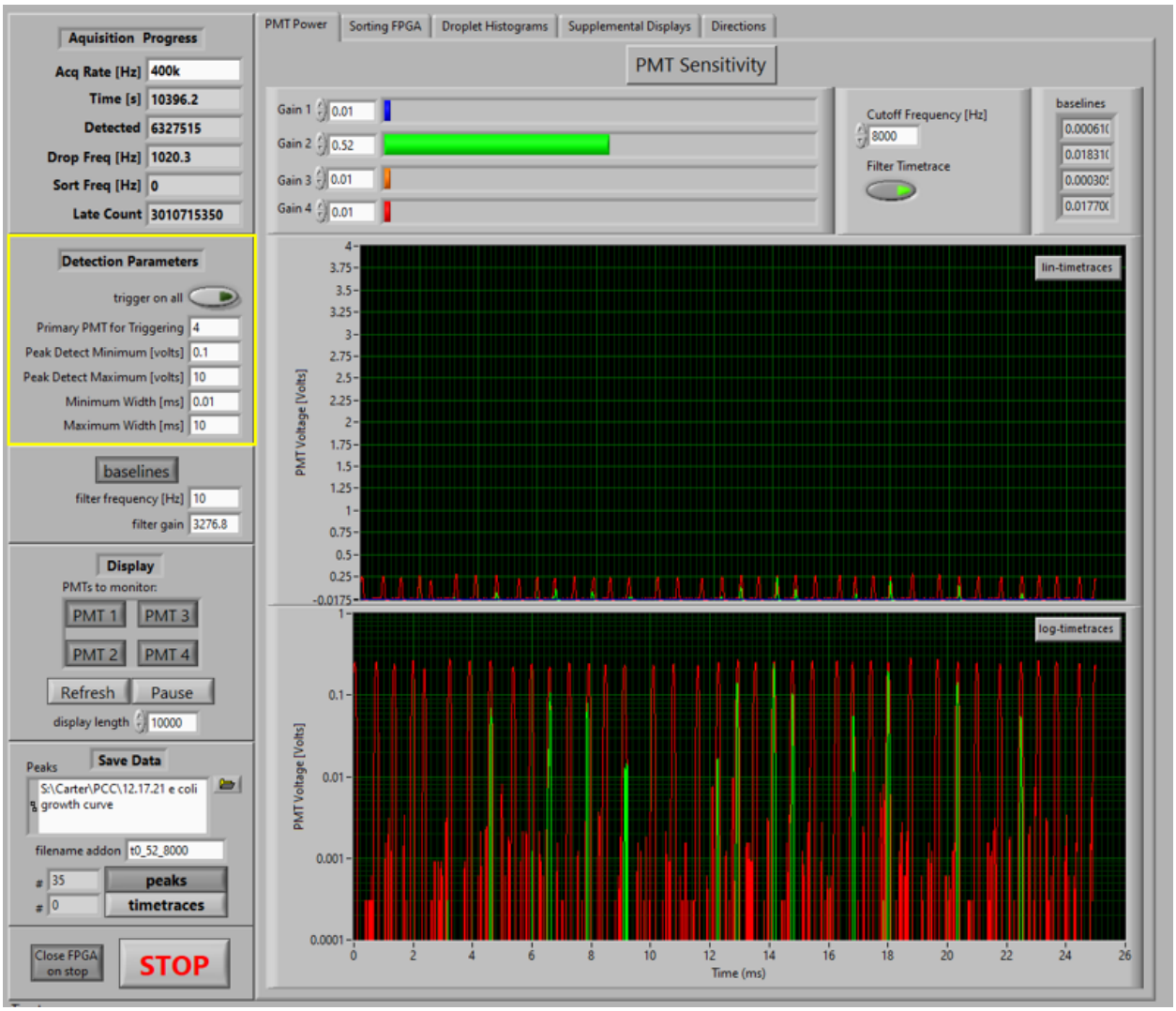

Figure 3.8. Screenshot of LabView live detection window showing LIF detection of droplets stained with red fluorescent dye and loaded with green fluorescent *E. coli* cells at approximately 20% rate.

The reference dye has the added benefit of staining and detecting droplets which did not receive a fluorescent particle of interest, for example fluorescent cells. In the absence of a reference dye, only the droplets loaded with a fluorescent particle are detected. Thus, a reference dye is a requirement for applications such as cell counting or digital drop polymerase chain reaction

(ddPCR), in which the desired readout is an enumeration of the fraction of droplets loaded with an analyte of interest.

We use AlexaFluor dyes as reference dyes. AlexaFluor dye carboxylic acid conjugates can be dissolved into water or biological media and thus stain the entire droplet, facilitating its detection by LIF. We have tested AlexaFluors 405, 488, 568 and 647, all of which proved functional as reference dyes at 100 nM final concentration. However, for complex, multi-fluorescence-channel applications, we primarily used AlexaFluor 405, a DAPI-channel dye. This is because channel cross-talk in multi-color fluorescence applications typically moves upward in wavelength, meaning that cross-talking fluorophores will appear in off-target channels of higher wavelength, but not lower wavelength. Using the lowest-wavelength fluorescence channel for reference dye detection thus safeguards against cross-talk into the reference dye channel, ensuring its robustness.

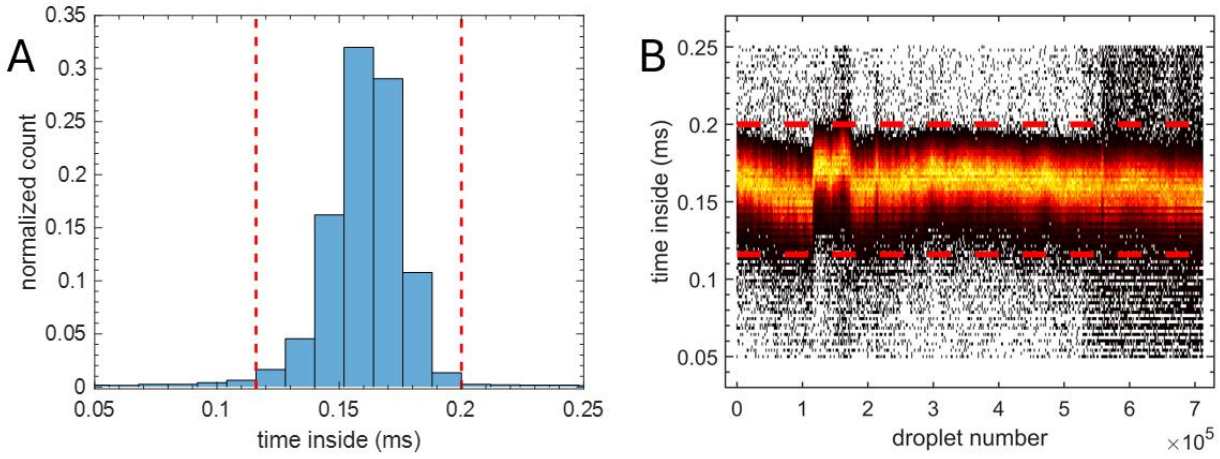

Figure 3.9. Data filtration using fixed gates to eliminate incorrectly sized droplets, discerned by droplet time inside measurements. Data with time inside measured between the red dashed lines are kept, and all other data are eliminated. The red dashed lines are drawn at the same time inside value in both figures.

In Figures 3.9 and 3.10 we show tutorials for size- and reference dye signal-based data filtration, to eliminate data from droplets of incorrect size or reference dye signals. The procedures we will describe herein are the same for filtration based on droplet size and reference dye signal. The LabView script records a residence time measurement, called 'time inside,' for each droplet recorded in the data set. Data filtration of the dataset using time inside can be easily conducted by visualizing the time inside distribution as a histogram, and eliminating incorrectly sized drops which fall outside of fixed gates, as shown in Figure 3.9A. However, a plot of time inside vs droplet number in chronological order, such as the heatmap in Figure 3.9B, reveals that fixed gating is inappropriate if any variability in droplet flow is present. Flow variations can result, for example, in the case of fluidic pump fluctuations or developing flow. From Figure 3.9B, it can be seen that the y-axis data are normally distributed for a small window of time, but the center of the distribution oscillates slightly up and down with flow variations. This allows some data which should be eliminated to pass through the fixed data filtration gates, which are plotted on the same time inside value in Figure 3.9B as in Figure 3.9A. Thus, a dynamic gating method is required to move the data filtration gates in response to flow variations.

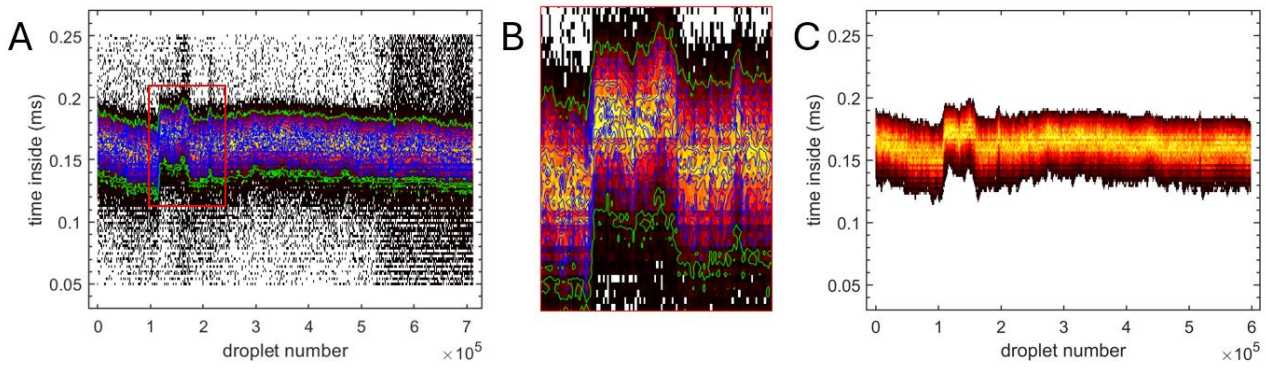

Figure 3.10. Dynamic data gating in MATLAB. (A) The dynamic gating program draws contour lines on a plot of time inside vs. droplet number, corresponding to data density. The outermost green contour defines the dynamic gate. Only data that falls within the perimeter of the green contour will be kept. (B) Zoom of boxed region in A. (C) Plot of time inside vs droplet number for the filtered dataset.

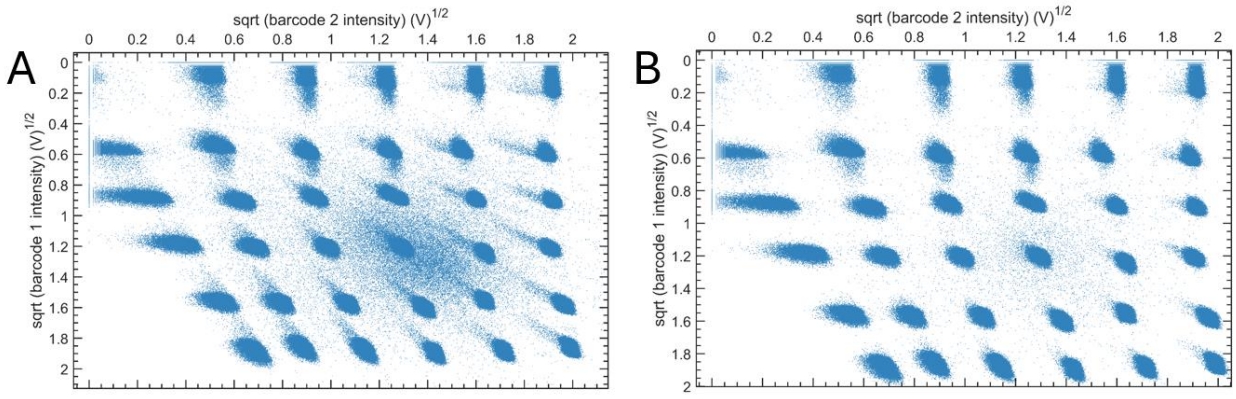

Figure 3.11. Scatter plots of fluorescence barcode data before (A) and after (B) data filtration by time inside. The data filtration process effectively eliminates coalesced and broken up droplets, discerned as data which falls between fluorescence clusters in (A).

The dynamic gating MATLAB program we developed is shown in Figure 3.10. The program plots time inside or reference dye signal against droplet number in chronological order as a heatmap. Then contour lines are generated around the heatmap based on data density (Figures 3.10A and 3.10B). The contour lines are analogous to elevation contours on a topographic map, where regions of high data density are analogous to regions of greater elevation. The user inputs a normalized data density, as a percentage, and the data filtration gate is drawn as a contour to include every region of equal or greater data density. For example in Figure 3.10 the normalized data density was specified as 8%, and the green contour line was drawn to include every region of data density $\geq$ 8% of the maximum observed data density value. The filtered data are shown in Figure 3.10C, and it can be seen that the dynamic gating method effectively eliminates all incorrectly sized droplets, while preserving the desired data. The effect of the data filtration on data quality is shown in 3.11, which shows two scatter plots of fluorescence data from droplets generated with unique fluorescence signatures, before (Figure 3.11A) and after data filtration (Figure 3.11B). In the absence of coalescence or other forms of droplet instabilities, the data should cluster into 36

unique clusters based on fluorescence signature. However, droplet instabilities were present during detection of this droplet sample. Unwanted data from sheared or coalesced emulsions registered fluorescence signatures between the unique data clusters, and were effectively eliminated by the data filtration process.

A low-pass filter reduces detector noise and smooths over droplet fluorescence signal pulses.

The PMT output voltage is represented by a waveform: the voltage rises as the PMT is excited and converts incident light into photocurrent (which is transformed into a voltage at the output), and falls to a ground state in the absence of incident light. Background detector noise can also be represented by a waveform, generally consisting of high frequency, low-amplitude signals. The total waveform output by the PMT corresponds to a composite signal comprised of noise and fluorescence signal, and these individual components can be separated on the basis of frequency. While droplet signal pulses typically have durations on the order of 10^{-1}-10^{0} ms and frequencies of occurrence on the order of 10^{2}-10^{3} Hz, the character of the PMT noise is typically much higher in frequency, on the order of 10^{4}-10^{5} Hz.

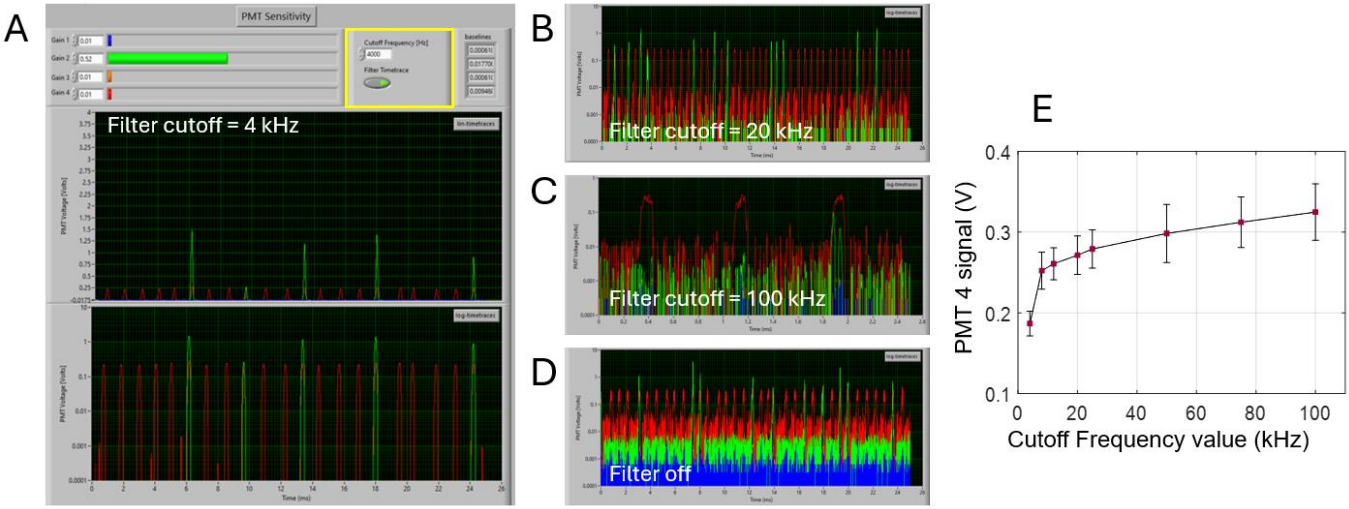

Figure 3.12. Demonstration of the noise filter in LabView. A-D, screenshots of the LabView window taken at various cutoff frequency values. E, PMT signal maximum amplitude vs cutoff frequency value, showing signal attenuation at low filter values.

The LabView script contains a user-programmable parameter called *Cutoff Frequency* (Figure 3.12A, boxed yellow) which defines a low-pass filter to reduce high-frequency signal above the cutoff value. The noise filter can be applied to produce clean, easily discernible fluorescence pulses. However, its use must be optimized in an application-dependent manner. For this purpose, we treated the noise filter as an independent variable during fluorescence channel optimization phases. The functionalities of this parameter which we have learned from empirical testing, will be described here.

The low-pass noise filter is applied to the voltage waveform output by the PMT by specifying a frequency, in Hz, at which to process the waveform. When applied, signal content of higher frequency than the specified cutoff frequency is filtered from the waveform recorded by the NIDAQ. Figures 3.12 A-D show screen shots during LIF detection of a droplet sample flowing at approximately 1 kHz occurrence frequency, while modulating cutoff frequency to demonstrate its effect. There are three primary effects on droplet signal collection which result from application

of the noise filter. Most notably, the filter will effectively reduce most or all of the noise, if the cutoff frequency is set to ≤12 kHz. A higher cutoff frequency can be thought of as a more "relaxed" filter, which will allow more components of the total waveform to pass. Secondly, the noise filter is a smoothing function. Unfiltered droplet signal pulses will be composed of high-frequency components oscillating on top of the low frequency signal waveform (Figure 3-12C). Elimination of the high frequency components produces the smooth, sinusoidal peaks observed in Figure 3.12A. However, elimination of high frequency signal content also produces the third effect, which is signal attenuation. The data in Figure 3.12E were collected from the same droplet sample as in Figure 3.12A-D. These data demonstrate that the amplitude of the PMT signal is a function of filter cutoff value, with signal attenuation especially prominent at low cutoff values near the frequency of droplet occurrence. As we will show later in *Optimization of channel 2, GFP-E. coli cell density,* setting the cutoff frequency too low can entirely eliminate the signals from single fluorescent cells in droplets. The optimized filter cutoff value is therefore one which balances noise elimination and peak smoothing with signal attenuation. We have found through empirical observation that a cutoff

frequency value equal to 4-5 times the expected droplet frequency of occurrence, for droplet frequencies of occurrence of 1-4 kHz, is an acceptable rule of thumb.

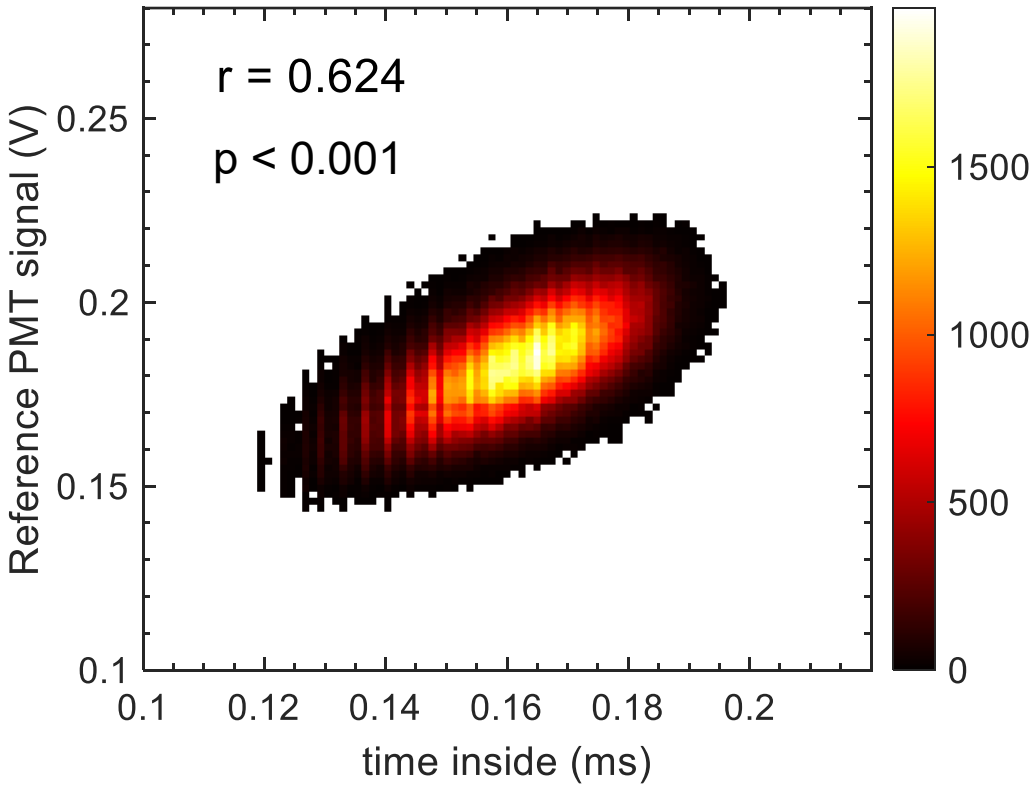

Figure 3.13. Time inside measurements correlate with reference dye PMT signal. Pearson correlation coefficient, r = 0.624 with p-value < 0.001 indicates moderate positive correlation with statistical significance. Color bar indicates number of droplets.

Fluorescence intensity and droplet size measurements collected by droplet LIF are correlated

A notable observation we have made regarding the use of reference dyes as a droplet signature, is that in our system, time inside measurements correlate with the amplitude of the reference dye fluorescence peak (Figure 3.13). The data shown in Figure 3.13 are from LIF detection of a population of droplets generated by emulsion of a fluorescent dye sample in a single emulsification generation procedure. The variation in time inside and fluorescence signature therefore represents the natural variability of a single population of droplets, which will always

assume a narrow distribution of sizes and fluorophore concentrations. For these data, we calculated a Pearson correlation coefficient, $r = 0.624$ with p-value < 0.001, indicating moderate positive correlation with statistical significance.

We proposed two hypotheses to explain, causatively, the correlation between time inside and PMT signal amplitude. In hypothesis 1, larger drops result in greater PMT output voltages. The rationale behind this hypothesis relies on geometric constraints imposed on droplets during flow. The LIF flow channel was designed to squeeze droplets vertically and from the sides, so that they elongate in the direction of flow (Figure 3.14). Larger droplets will elongate further, and experience a longer residence time underneath the laser beam. This increased residence time naturally results in a greater time inside measurement. Plausibly, greater residence times could result in greater perceived fluorescence intensity if the PMT circuit conducts some form of time-integration over the duration of the fluorescence signal pulse. In this scenario, the rate of fluorescence emission by two droplets is constant as they have equal fluorophore concentration, but a larger droplet will emit more photons by residing longer underneath the laser beam. Alternatively, the observed correlation could suggest that the area illuminated by the laser beam in the flow channel is greater than the area assumed by a typical droplet. If the beam spot is large enough to illuminate whole droplets regardless of droplet size, then the larger droplets will result in greater instantaneous illuminated volume when encompassed entirely inside the laser beam. This in turn produces a greater rate of fluorescent photon emission and higher-amplitude PMT signal pulse for the larger droplets.

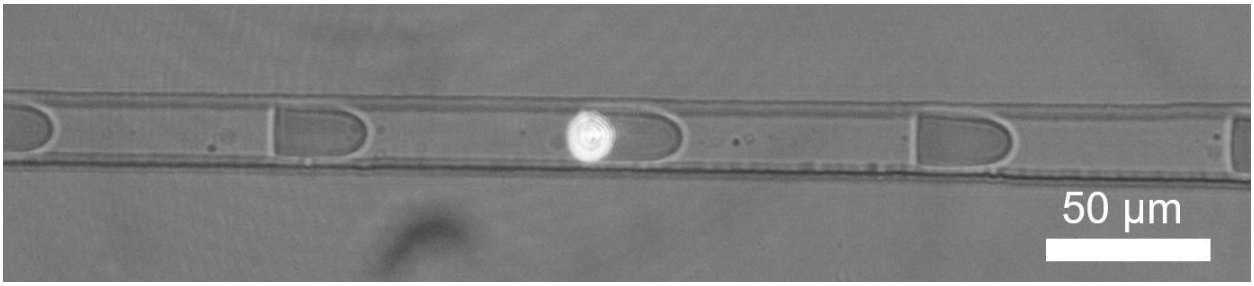

Figure 3.14. Detection devices were designed to squeeze flowing droplets vertically and from the sides, so they elongate in the direction of flow.

In hypothesis 2, natural variations in fluorescence signals from droplets of equal size produce perceived variations in time inside measurements. The rationale behind hypothesis 2 can be explained by describing droplet detection as a threshold-governed process. According to this hypothesis the PMT must experience a photonic input signal which is greater than a certain threshold value, in order to output a non-zero, noise filter-conditioned voltage and initiate a detection event by the NIDAQ. The rate of photon emission by the droplet is a function of the droplet's illuminated volume, which is itself a function of droplet position relative to the laser, and therefore time. Possibly, the detection threshold is crossed as soon as an infinitesimally small volume of the droplet is illuminated by the laser, and the first photon of the droplet excitation event reaches the PMT. Alternatively, the threshold might only be crossed once a finite volume of the droplet is illuminated and the droplet has emitted relatively many photons. In this latter scenario a droplet which was, by chance, loaded with an above-average number of fluorophore molecules will cross the detection threshold at an earlier point in the droplet illumination process than a droplet of equal size and typical fluorophore content. Thus the droplet of greater fluorescence intensity due to natural variation will produce a greater time inside measurement, despite being of typical size. We note that variations in the photocurrent generated by the PMT can also arise from detector shot noise [135]. Shot noise is a form of noise inherent to PMTs and is related to the

particle nature of light. In this scenario, a droplet of typical size and fluorophore content might cross the detection threshold earlier than average, if a chance upward variation in detector noise produces an abnormally large photocurrent from a standard photonic input.

We designed parallel experiments to test these hypotheses. In experiment 1, designed to test hypothesis 1, a single dropmaker was used to generate two populations of fluorescent droplets of different size, by varying the flow rates during emulsification. The two populations were identical in fluorophore concentration, as they originated from the same syringe containing dissolved AlexaFluor dyes, yet were bimodal in size (Figure 3.15A). The two subpopulations were then mixed and detected by LIF to probe for size-related effects on fluorescence intensity. Figure 3.15B shows the distribution of droplet diameters as measured by microscopy, confirming the bimodal size distribution. Figure 3.15C shows a screenshot of the live LIF detection window in LabView, where fluorescence peaks from two droplets in sequence show different peak heights and widths. Figure 3.15C and 3.15D show the measured time inside and PMT 2 signal distributions, respectively, where bimodality is again captured. Last, in Figure 3.15E, PMT 2 signal is plotted against time inside as a heatmap. The two droplet populations and their respective bimodal signals are clearly visible, as is their correlation. For these data, we calculated a correlation coefficient, $r = 0.985$ with p-value <0.001, indicating near-perfect positive correlation with statistical significance.

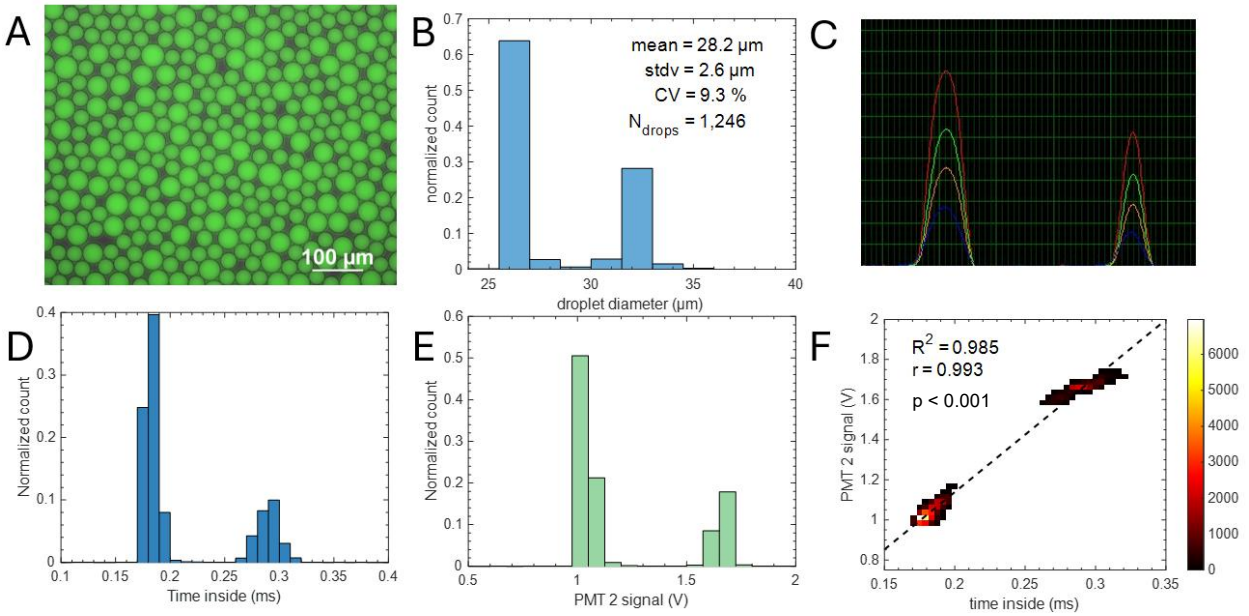

Figure 3.15. Increased droplet diameter produces fluorescence intensity measurements of greater magnitude. A, fluorescence image of a mixed population of droplets containing droplets of two different diameters and equal fluorophore concentration. B, droplet diameter distribution measured by microscopy. C, screenshot of LabView LIF detection window depicting two droplets in sequence registering fluorescence peaks of bidisperse amplitude and width. D, time inside distribution measured by LIF detection of the mixed droplets. E, PMT signal intensity distribution measured by LIF. F, PMT 2 signal vs time inside for the mixed droplet sample. r = 0.993 with p-value < 0.001 indicates near perfect correlation with statistical significance.

This result led us to accept hypothesis 1, that larger droplets produce greater PMT output voltages in our system. However, the mechanism by which this causative relationship arises is not yet confirmed. The PMT datasheet [136] indicates that the output signal pulse is not produced by a summation over the signal pulsewidth. Our results therefore suggest the second mechanism by which larger droplets might produce greater PMT voltages: by illuminating whole droplets, regardless of size. This further indicates that the area illuminated by the laser in the flow channel is tens of microns in diameter. To confirm this mechanistic explanation of the observed correlation, a similar experiment should be conducted in which a variety of fluorescent droplet sizes are detected coincidentally, with the goal of observing at least one subpopulation which assumes a

larger area than can be covered by the laser beam. If this mechanism correctly explains the observed correlation, the increase in PMT voltage should plateau once the droplets cannot be fully covered by the laser beam, as increasing droplet size no longer results in increased illuminated droplet volume. This experiment would also yield a more rigid estimate of the laser beam waist in the flow channel. This experiment was not conducted in the present work.

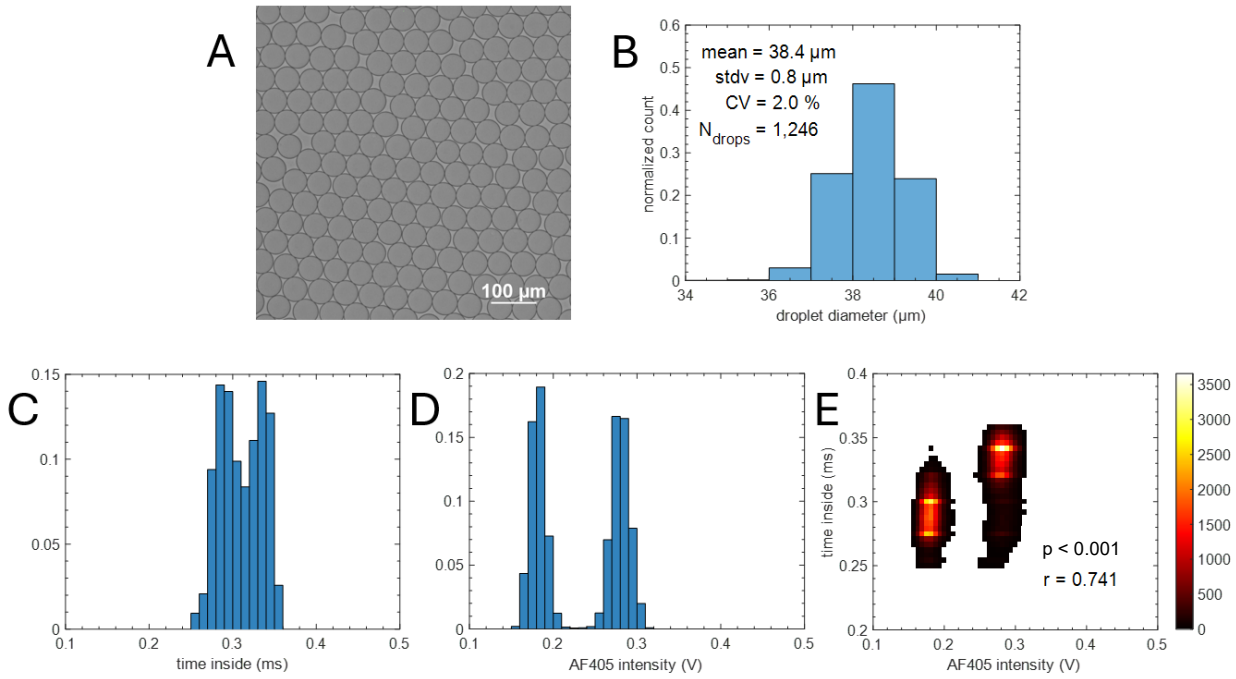

Figure 3.16. Fluorophore concentration effect on time inside measurement. A, micrograph of a mixed population of droplets of equal diameter and bidisperse fluorophore concentrations. B, droplet diameter distribution measured by microscopy. C, time inside distribution measured by droplet LIF. D, channel 1 fluorescence intensity distribution measured by droplet LIF. E, time inside vs. channel 1 PMT signal. Pearson correlation coefficient = 0.741 with p-value <0.001 indicates strong linear correlation with statistical significance.

In experiment 2, designed to test hypothesis 2, two droplet populations were generated, of equal size and with two distinct fluorophore concentrations. The two populations, which contained 100 nM and 250 nM AlexaFluor 405, were then mixed and detected by LIF to probe for effects of fluorophore concentration on measured time inside. The results are shown in Figure 3.16. Figure

3.16A and 3.16B show a brightfield image of the mixed droplet sample, and the droplet diameter distribution as counted by microscopy, respectively. By these methods, the sizes of the two droplet types in the mixed droplet sample are indistinguishable. Yet, as shown in Figure 3.16C, the measured time inside distribution is bimodal. Furthermore, as expected, the distribution of fluorescence intensities detected from the mixed droplet sample is bimodal (Figure 3.16D) and correlates to the time inside measurements (Figure 3.16E).

This result led us to accept hypothesis 2, that droplets can register greater time inside measurements by containing more concentrated fluorophore. It also supports the existence of a droplet fluorescence emission threshold, below which, a noise filter-conditioned PMT voltage will be recorded as zero and a detection event will not occur. The conditioning of the PMT voltages by the noise filter is likely a critical parameter affecting the detection threshold. The raw PMT signal voltage never has an amplitude truly equal to zero, as it always outputs some background dark current. However, the noise filter can condition very low amplitude and/or high frequency voltages to be recorded as zero values. Later in *Optimization of channel 2, GFP-E. coli cell density,* we will show that increasing the noise filter cutoff value permits a greater proportion of single-celled droplets to register PMT signals > 0 V in amplitude.

Together these results demonstrate that, in our droplet LIF system, the relationship between measured time inside and fluorescence signal amplitude is bidirectionally causative. Larger droplets can produce fluorescence signal pulses of greater amplitude, and droplets of greater fluorophore concentration can produce greater droplet time inside measurements. These findings have implications in designing droplet LIF-based assays, as they demonstrate that the signal pulse amplitude and width can be influenced by factors which do not intuitively relate to these

measurements. For example, in a hypothetical droplet qPCR assay, two droplets containing equal concentrations of fluorescent reporter dye, proportional to PCR product accumulation, might be measured as having different fluorescence intensities if they are of different size. Moreover, in some applications it might be suitable to use the average or summed value of a fluorescence signal pulse as the assay readout. These measured values are directly related to the pulsewidth, which we have shown can be influenced by the fluorescent content of the droplet.

Allocation of fluorescence channels in a multiplexed microbial growth assay

We sought to use our droplet fluorescence detection setup to develop a multiplexed microbial growth assay in droplets using multicolor fluorescence signals. A single fluorescence channel is required for assay readout. We therefore hypothesized that 2 additional fluorescence channels could be used in a spectral barcoding technique [64, 83, 137] to encode multiplexed experimental conditions contained within the droplets. Spectral barcoding of microfluidic droplets involves imparting unique optical signatures, such as fluorescence spectra, onto droplets during emulsion generation, enabling identification and tracking using their distinct fluorescence signatures.

A green fluorescent protein (GFP)-labeled strain of *E. coli* was made available to us, in a kind gift from Dr. Michael Franklin of Montana State University. We therefore reserved channel 2 which detects green fluorescence from droplets as the cell growth channel, and sought to develop the spectral barcoding method using channels 1, 3 and 4. We purchased AlexaFluor dyes for barcoding based on reports in literature [64], and readily observed that AlexaFluor dyes can be used to impart unique fluorescence signatures onto droplets in all 4 of our fluorescence channels (Figure 3.17).

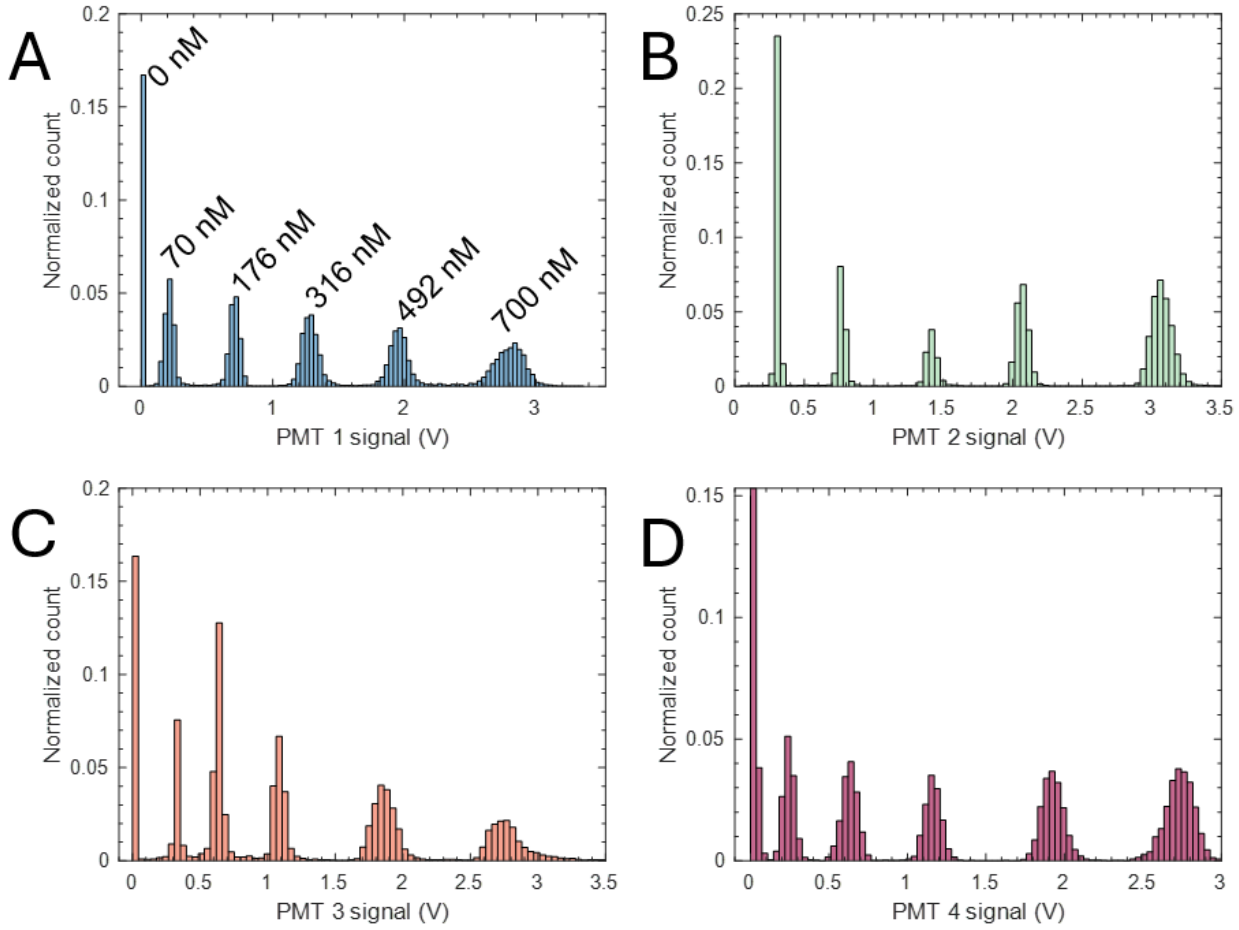

Figure 3.17. AlexaFluor dyes are suitable for spectral barcoding of microfluidic droplets. Each plot shows a histogram of PMT signals from droplet LIF detection of a population of droplets containing unique AlexaFluor concentrations. A-D correspond to detection in PMT 1-4, using AlexaFluor 405, 488, 568 and 647, respectively. The concentrations of dye used are indicated by the text in Figure 3.17A.

In initial experiments, we tried using AlexaFluor 647 in channel 4 as the reference dye. We speculated that, as this channel is filtered by the narrowest bandpass filter, it would be robust against spectral cross-talk from neighboring channels. We further speculated that the highest wavelength channel would have more room for parametric flexibility to optimize detection in that channel, as it does not have an upwards neighbor into which it can exhibit channel cross-talk. However, it was immediately observed that droplets barcoded with AlexaFluor 568 dye in channel

3 will produce cross-talk into channel 4 in a concentration-dependent manner. This resulted in droplet populations emitting a variety of reference dye signals into channel 4, which depended on the fluorescent content in channel 3 (Figure 3.18). This was deemed untenable, and we opted to proceed with channel 1 as reference dye, channel 2 as assay readout, and channels 3 and 4 for spectral barcoding channels.

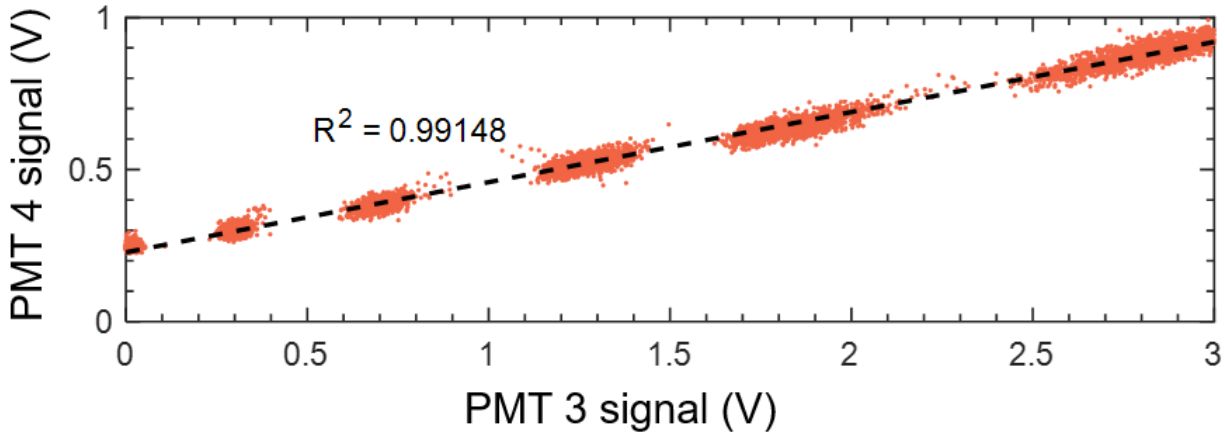

Figure 3.18. Channel 3 fluorescence barcodes produce cross-talk into channel 4. The data shown were collected from a population of droplets containing 6 unique AlexaFluor 568 conditions which fluoresce in channel 3, and each subpopulation of droplets contained a fixed concentration of AlexaFluor 647 which fluoresces in channel 4.

Overview of optimization protocol for multichannel fluorescence detection.

Fluorescence channel cross-talk is a major challenge which must be overcome in multichannel fluorescence applications [137]. In fluorescence microscopy, spectral overlap can be mitigated by collecting fluorescence from multiple channels, sequentially. For example, the iris to the FITC detector is only opened after the DAPI signal has been collected and the 405 nm excitation light is turned off, preventing light emitted by DAPI-channel fluorophores from reaching the FITC channel detector. However this is less feasible in flowing droplet applications which use a single microscope objective to excite fluorophores in all channels coincidentally.

We hypothesized that user-programmed detection variables controlling individual fluorescence channels could be optimized, so that each channel performs its specific function, while preserving the functionality of neighboring channels. An individual fluorescence channel has *N* variables which can be modulated to affect the performance of the channel, for example but possibly not limited to, laser power and PMT gain. Each channel thus has an inherent parameter space, which is a *N*-dimensional matrix, where each node of the matrix is a combination of variables set to specific values. In a multichannel fluorescence application consisting of *M* channels, the sheer scale of the available parameter space becomes infeasible to examine exhaustively, as the multichannel parameter space is a *D*-dimensional matrix, where

$$D = \sum_{i=1}^{M} N_i$$

For example, in a 4-channel fluorescence application, if each channel has 3 channel variables which can be set to 5 unique values, the 4-channel parameter space is a 12-dimensional matrix, containing 2.44×10^8 unique combinations of parameters.

To address this optimization problem, we further hypothesized that the parameter spaces of individual fluorescence channels, being much smaller than the multichannel parameter space, could be systematically scanned for regions of channel functionality. Parameter space regions of non-functionality could then be eliminated to produce a smaller viable parameter space for each channel, which we called the functional parameter space. When the individual channel functional parameter spaces are then combined to create the multichannel parameter space, it is of lesser complexity, and the individual channel functionalities, in isolation, have already been guaranteed.

To develop a 4-channel droplet fluorescence detection application, we therefore implemented an optimization protocol beginning with optimization of individual channels, followed by channel co-optimization. In the first phase, each individual channel's parameter space was assessed for regions of desired functionality, producing functional parameter spaces for each channel which are reduced in scale compared to the total available parameter spaces. In the second phase, we combined channels pairwise to ensure that their functionalities were maintained despite the presence of neighboring fluorophores. In the final phase we combined all 4 fluorophores to demonstrate the simultaneous detection of 4-channel fluorescence in droplets for a multiplexed microbial growth application.

Optimization of individual fluorescence channels

To systematically test the channel's performance at each node of its parameter space is to characterize every possible performance level for the individual channel. Therefore, an individual channel's performance can be optimized by first establishing a performance criterion for the channel, and assessing its performance relative to the criterion at each node of the channel's parameter space. To construct each channel's parameter space, we varied the laser power, channel gain, and noise filter. In a multichannel application, the noise filter is applied to every channel in unison. However, we treated it as an individual channel variable during individual channel optimizations. Thus, from the outset, a 3D parameter space for each fluorescence channel was constructed, consisting of 140 to 288 unique combinations of parameters, depending on the channel. Of note, the power of the 405, 488 and 642 nm laser diodes is input as a current in mA on our laser module. Therefore, for these lasers we report the laser current, which is proportional to the realized laser power.

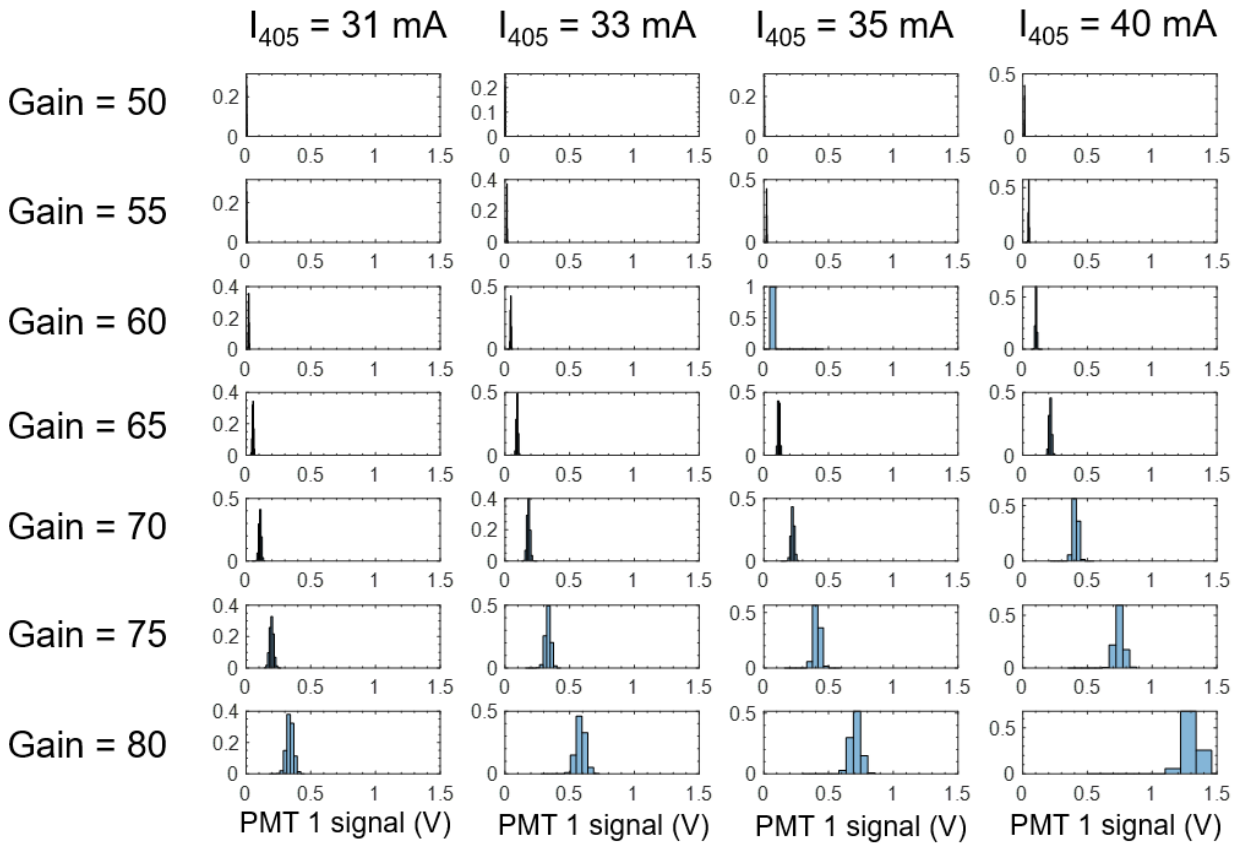

Figure 3.19. Channel 1 reference dye PMT signals as a function of PMT gain and 405 nm laser current, for a fixed noise filter value. I405, 405 nm laser current.

Optimization of channel 1, reference dye.

The reference dye's primary function is to register a fluorescence signature of any value, so long as it is readily distinguishable from the noise floor, and provides proxy measurements of droplet size. When used in channel 1, the reference dye has the added constraint of minimizing cross-talk into the GFP channel, channel 2. Conceivably, excessive cross-talk from channel 1 to 2 could mask the fluorescence signals from single microbial cells, which would hinder the growth assay. This constraint is particularly challenging to navigate, as bacterial undefined media such as Luria broth (LB) and cation-adjusted Mueller-Hinton broth (CAMHB) show significant autofluorescence in the violet-green range of the visible spectrum. As increasing the current

supplied to the 405 nm laser diode produces increased media autofluorescence into channels 1 and 2, we sought minimize the 405 nm laser current while optimizing channel 1.

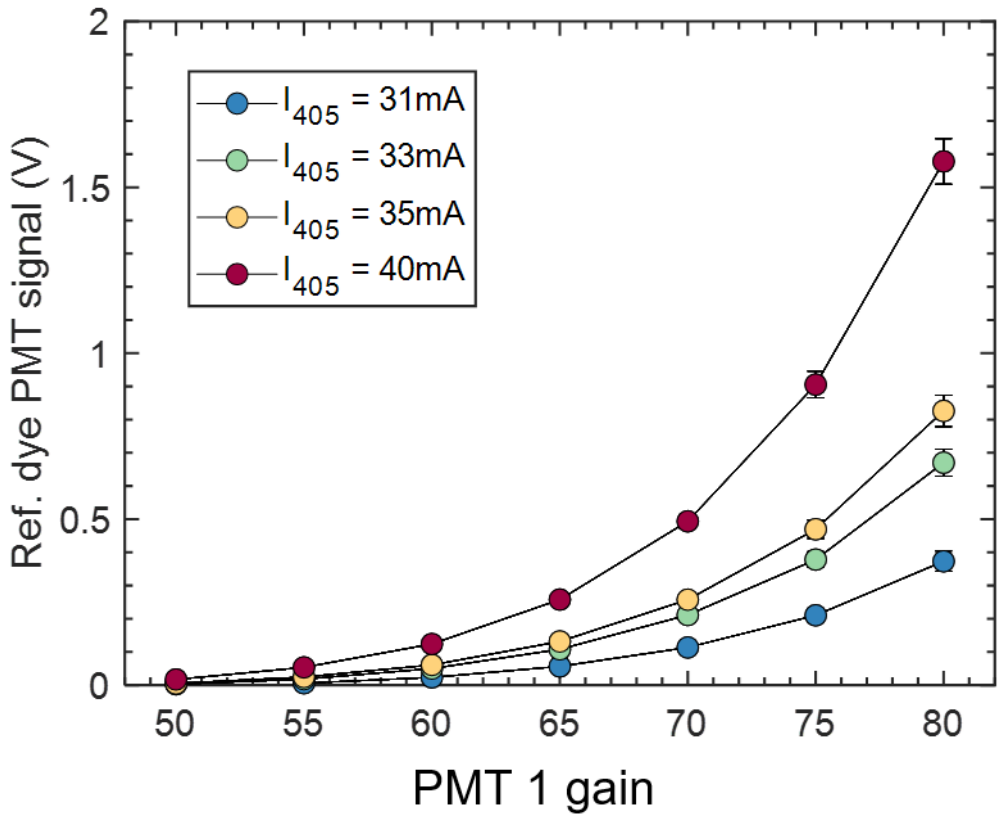

Figure 3.20. Reference dye PMT signal vs PMT gain for several different 405 nm laser current settings.

To optimize the detection of reference dye signals in channel 1, we detected fluorescence signals from droplets containing 100 nM AlexaFluor 405 dissolved into cation-adjusted Mueller-Hinton broth (CAMHB), to mirror a microbial growth assay. We surveyed 4 laser currents at the low end of the laser current range, 7 PMT gain values and 5 noise filter values, producing a 140-node parameter space. Figure 3.19 shows an array of histograms of reference dye signal intensities for a single noise filter value, arranged as a grid of laser current and detector gain conditions. The region of higher gain and laser current naturally produces reference dye signals of greater

amplitude. These data are shown as mean PMT 1 signal vs PMT gain in Figure 3.20. There are several regions where the reference dye distribution cannot be adequately discerned, namely gain = 50, 55 and parts of 60, for all 4 laser powers. These nodes were therefore eliminated from the functional parameter space for channel 1. For channel 1 optimization, we found that the noise filter had a negligible effect on the performance of the channel, and therefore included all noise filter values in the functional parameter space.

Optimization of channel 2, GFP-*E. coli* cell density

As the biological readout of the designed assay, channel 2 presented the most stringent requirements. Single-cell detection was required, which requires a high ratio of GFP fluorescence signal to background noise. It was also required that droplets exhibiting full microbial growth show good separation from non-growth droplets in terms of PMT signal. These two requirements are opposing: to increase fluorescence signal from microbial cells, channel 2 laser power, gain and noise filter cutoff are increased, which can in turn introduce background noise and obfuscate single-cell fluorescence signals.

In early attempts at optimization, it was found that the channel 2 parameter space can be divided into two regimes, based on PMT gain and noise filter. In the first regime, background signal originating from cross-talk and detector noise is completely eliminated by the noise filter, and empty droplets register a true zero signal in channel 2 (Figure 3.21A). In the second regime, background signal produces a non-zero PMT 2 signal in every droplet, but cells in droplets are still discernible by their heightened channel 2 signal (Figure 3.21B). In regime 2, increased PMT gain and noise filter values result in significant background signals which are permitted through the noise filter.

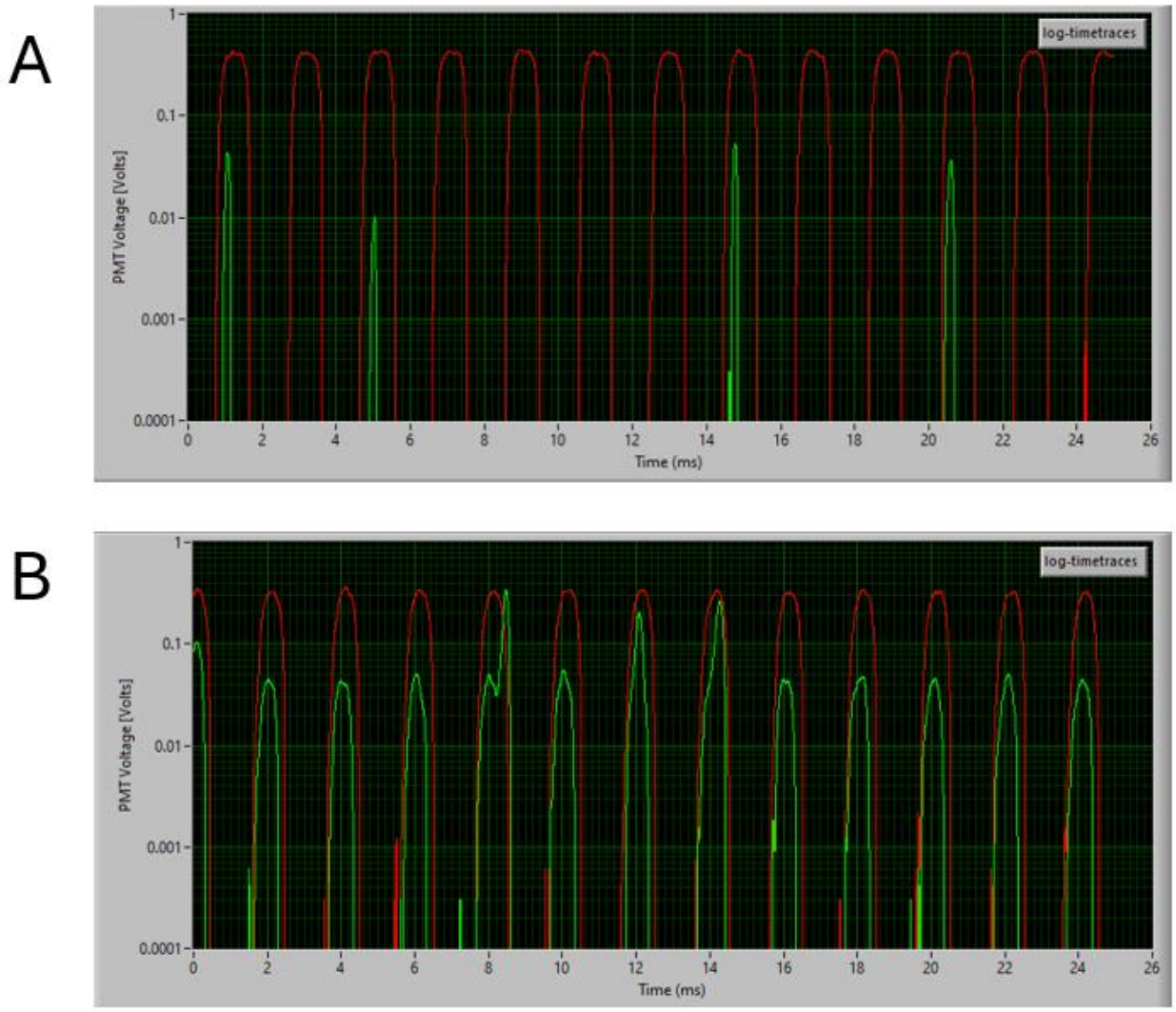

Figure 3.21. Two regimes for detection of cellular fluorescence. A, regime 1, in which detector gain and noise filter values are low, abiotic droplets register 0 values in PMT 2 (green) and biotic droplets register a sharp peak in the green channel. B, regime 2, in which PMT 2 gain and noise filter values are high, and background signal results in every droplet registering a non-zero PMT 2 voltage.

Regime 1 provides straightforward identification of biotic droplets, as abiotic droplets register zero values in channel 2. For this reason, we initially defined the functional parameter space for channel 2 as the set of parameters that produce regime 1. This corresponds to the region of maximum gain = 52, noise filter ≤10 kHz and all 488 nm laser currents. To assess the

functionality of channel 2 in this region of the parameter space, a population of droplets was generated containing CAMHB media, 100 nM AlexaFluor 647 as reference dye, and single GFP-*E. coli* cells loaded at ~8% rate. LIF was conducted on this droplet sample before and after a 5-hour incubation period, while sweeping the available parameter space. It was observed that in this parameter space which consists of low gain and noise filter values, the separation between growth and non-growth droplets is poor (Figure 3.22).

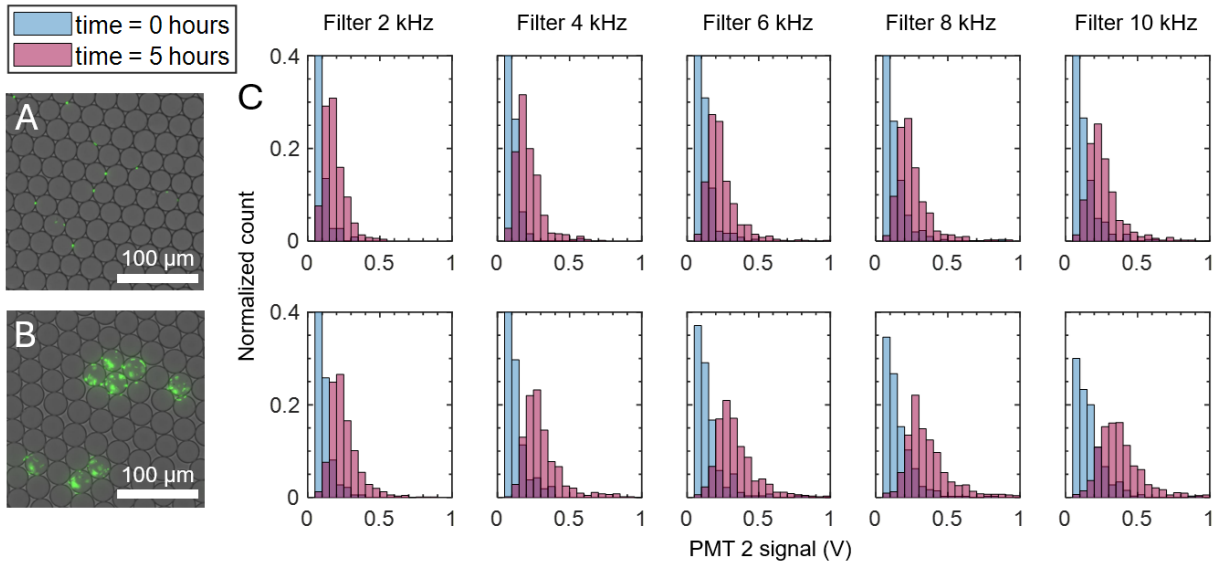

Figure 3.22. Detection of droplet GFP signals in PMT 2 regime 1. A, representative fluorescence image of droplets at time = 0 hours. B, representative fluorescence image of droplets at time = 5 hours, showing growth in droplets. C, PMT 2 signal distributions from LIF detection at time = 0 (blue) and time = 5 hours (red) at an array of detection parameters which produce regime 1. Top row, PMT 2 gain = 50, bottom row, PMT 2 gain = 52. Noise filter values are indicated above histograms.

It was also observed that, in PMT 2 regime 1, a significant portion of single cells evade detection by LIF. Figure 3.23 shows a plot of the biotic fraction of droplets observed by LIF vs noise filter value, with gain and laser set to the highest values available in this parameter space. To calculate the biotic fraction, we enumerated the fraction of droplets with channel 2 PMT signal > 0 V. The green shaded region corresponds to the biotic fraction of cells counted by analyzing

fluorescence images of the same droplet population, +/- 95% confidence interval. The biotic fraction calculated from image analysis was used as a positive control value, to assess the single-cell detection performance by LIF. These data demonstrate that, when channel 2 variables are set to produce detection regime 1, a significant portion of single cells go undetected by LIF in a noise filter-dependent manner. The observed dependence on noise filter corroborates the previous suggestion that the noise filter can errantly condition target fluorescence signals to be recorded as zero values. A plausible explanation for this observation is that, at low detector gain, a portion of single cells produce a low amplitude or high frequency PMT voltage which is susceptible to elimination by the noise filter. Incrementally relaxing the noise filter by increasing the cutoff frequency then decreases the proportion of single cell signals eliminated by the filter.

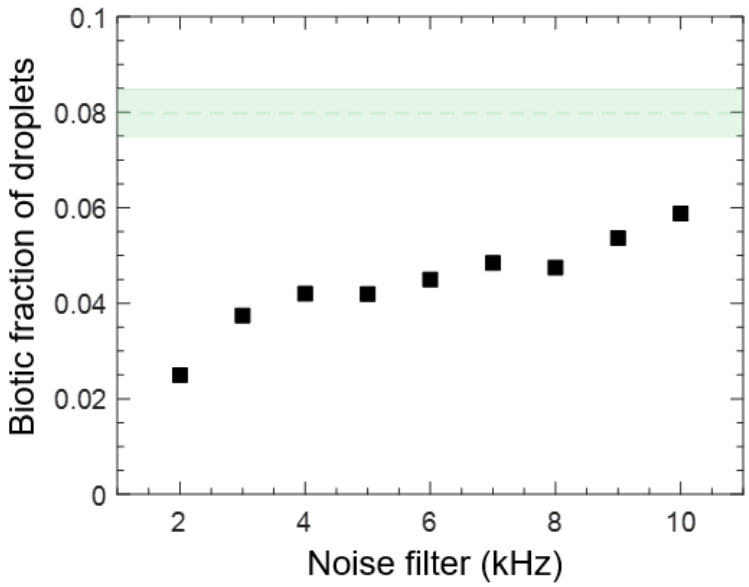

Figure 3.23. Detection of single cells in regime 1 is poor. Biotic fraction of droplets detected by LIF vs noise filter value is shown for a population of droplets containing single cells. Green shaded region corresponds to the biotic fraction enumerated by image analysis of the same population of droplets. For LIF data, biotic fraction was equal to the fraction of droplet data with PMT 2 signal > 0 V.

During preliminary optimization experiments, it was also observed that the background green fluorescence signal due to media autofluorescence is not a function of the 488 nm laser current (Figure 3.24). This result indicated that cellular GFP fluorescence signals could be increased by increasing the 488 laser current, without incurring any additional background signal. As such the channel 2 parameter space was truncated to include only a single laser current, the maximum current, I_{488} = 76 mA.

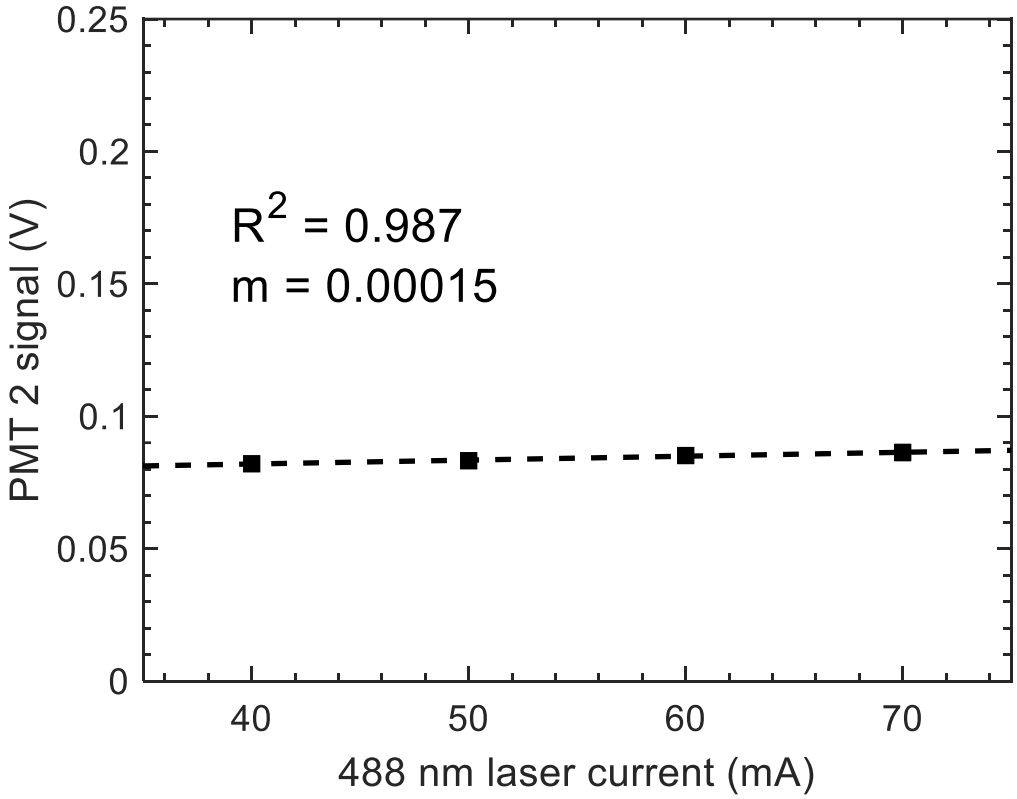

Figure 3.24. PMT 2 background signal from media autofluorescence is not a function of 488 nm laser current. Data collected during LIF detection of droplets containing media and channel 1 reference dye. m, slope of fit curve.

In subsequent experiments, the channel 2 parameter space corresponding to regime 2 was assessed. Regime 2 promises superior signal from fluorescent cells as it corresponds to the region of high detector gain and noise filter. However, in this regime, every droplet registers a non-zero

channel 2 PMT signal, thus, a method to separate biotic from abiotic data was required. To address this issue, we explored a method to divide datasets binarily using a fixed cutoff value. In this method, any droplet registering a channel 2 signal below the cutoff value was eliminated as noise. The efficacy of the cutoff value was then assessed by comparison of biotic data counts to an image analysis control, as done previously in Figure 3.23. The cutoff value thus represents an additional dimension to channel 2's parameter space. Figure 3.25 shows the result of a channel 2 optimization experiment, in which we conducted LIF on droplets loaded with single cells, before (Figure 3.25A) and after (Figure 3.25A) a 5-hour growth period. In this experiment we surveyed a 288-node parameter space consisting of 6 channel gain values, 6 noise filter values and 8 binary cutoff values, while keeping the laser current set to its max. In Figure 3.25C, each of the 8 plots is specific to a channel 2 binary cutoff value for abiotic data elimination. Each plot shows two surfaces, a lower surface corresponding to channel 2 LIF signals at time = 0 hours, and an upper surface corresponding to channel 2 LIF signals at time = 5 hours of incubation. The GFP fluorescence signals in channel 2 function as the assay readout, and are plotted on the z-axis against gain and noise filter. Each individual data point on a surface is the mean PMT 2 signal from a subset of droplet LIF data collected at that node in the parameter space, after abiotic data elimination. It can be seen that separation of growth from non-growth values is superior in the region corresponding to gain = 58-60 and noise filter = 8-12 kHz, as discerned by the superior separation of the two surfaces in this region. Moreover, the effect of the increasing cutoff value can be discerned: in the first row of plots, the cutoff value is too low for some conditions in the parameter space, and the time = 5 hours surface appears crumpled. This is due to the errant inclusion of abiotic data in the final dataset, which have low GFP signal and reduce the average channel 2 signal. Figure 3.26

shows a comparison of biotic data counts between image analysis and LIF data with binary cutoff applied, from the same experiment as Figure 3.25. Each column of plots is specific to a timepoint, with channel 2 binary cutoff value increasing across successive rows within the column. Each individual plot shows the calculated biotic fraction against PMT 2 gain, and the green shaded region again corresponds to the biotic fraction enumerated by image analysis, +/- 95% confidence interval. Thus, the regions where black data intersect the green shaded region indicate agreement between the two biotic data counting techniques, and accurate elimination of abiotic data by binary cutoff division. It is notable that so many more conditions produce agreement between the biotic data counting techniques for time = 5, than for time = 0. This is likely because at time = 5 hours, the average biotic droplet has become filled with GFP-producing *E. coli*, and is readily distinguishable from an abiotic droplet at a variety of nodes within the channel 2 parameter space. With these results, we defined the channel 2 functional parameter space as the region corresponding to gain = 58-60, noise filter = 8-12 kHz, I_{488} = 76 mA and channel 2 binary cutoff = 0.02 – 0.05 V.

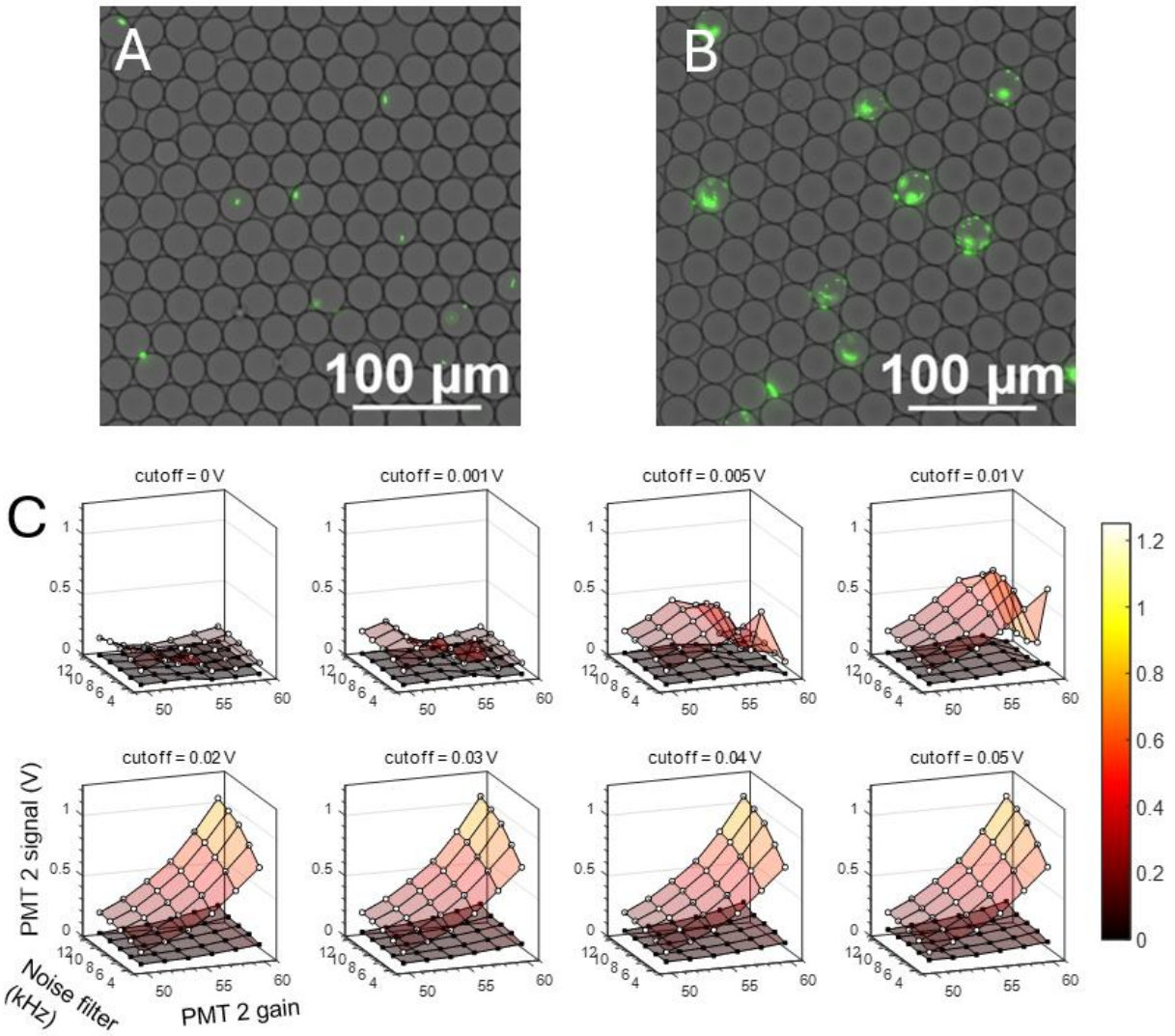

Figure 3.25. Channel 2 optimization in regime 2. A and B, representative fluorescence images of droplets at time = 0 and 5 hours, respectively. C, droplet LIF data in channel 2 as a function of noise filter, PMT 2 gain and channel 2 binary cutoff value. Each of the 8 plots is specific to a cutoff value. Upper surface, time = 5 data, lower surface, time = 0 data. Each point on a surface corresponds to the mean value of the dataset collected at that node of the parameter space, with abiotic data eliminated according to the specific cutoff value.

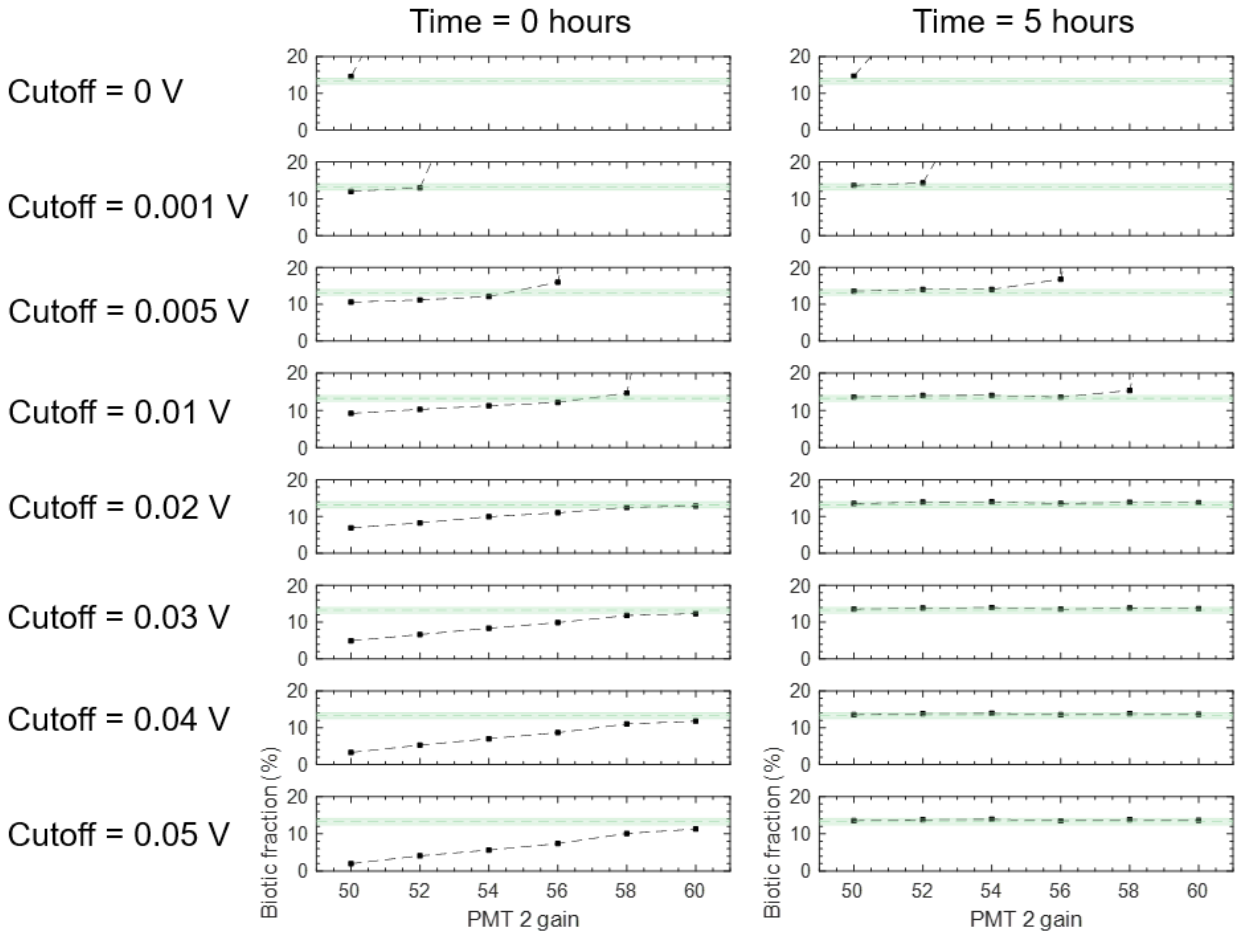

Figure 3.26. Assessment of binary cutoff value efficacy. Each individual plot shows the biotic fraction detected vs PMT 2 gain, for the binary cutoff value listed left. Left column, time = 0 LIF data, right column, time = 5 hours. Green shaded region indicates the biotic fraction enumerated by image analysis, thus, accuracy of binary division of LIF data is indicated when the black data intersects the green region.

Channel 1 and 2 co-optimization

The previous experiments concerning channel 2 optimization were conducted with a red, channel 4 reference dye, so that channel 2 could be optimized before the introduction channel cross-talk by the reference dye. To co-optimize channels 1 and 2, we conducted a similar experiment to the channel 2 individual optimization, with a multichannel parameter space of greater complexity. The multichannel parameter space was 4-D, consisting of dimensions

corresponding to 405 nm laser current, channel 2 gain, noise filter, and channel 2 binary cutoff value. However, each dimension was drastically reduced in number of values, owing to previous single-channel optimization phases. In this experiment we generated droplets containing CAMHB media, 100 nM AlexaFluor 405 reference dye, and single GFP-*E. coli* cells at ~10% loading rate. Fluorescence signals in channels 1 and 2 were detected coincidentally from the droplet samples, before and after a 5-hour growth period. During LIF detection, we collected data at each node of the 4D multichannel parameter space, to probe for regions of preserved functionality in the two channels once they were combined.

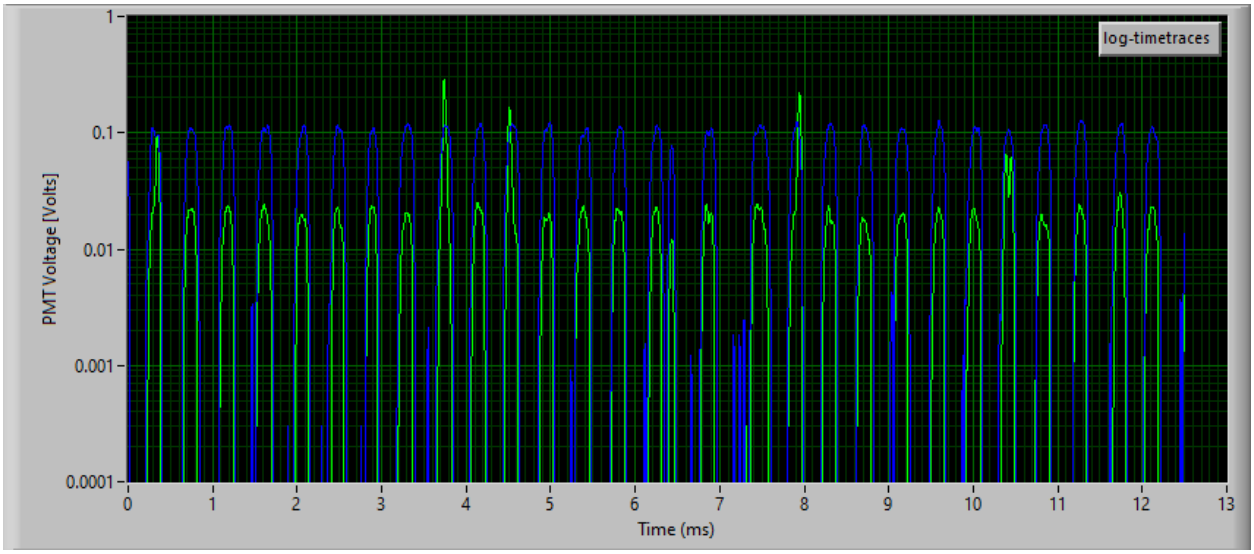

Figure 3.27. Screenshot of LabView LIF detection window during channel 1 (blue) and 2 (green) co-optimization, showing background fluorescence signal in channel 2. Droplets containing a single bacterial cell can be discerned as high-amplitude green peaks, while empty drops all contain a background level of green fluorescence signal.

Figure 3.27 shows a screenshot of the LabView detection window during LIF. Regular blue reference dye peaks as well as green background fluorescence peaks in every droplet, are clearly discernible. Moreover, biotic droplets are easily distinguished by their increased GFP signal. Figure 3.28 contains surface plots of the time = 0 and 5 hours GFP channel intensities, as a function

of PMT 2 gain and noise filter value. As in Figure 3.25, the lower surface corresponds to time = 0 hours, and each plot is specific to a channel 2 binary cutoff value. As expected, the separation of time = 5 from time = 0 growth data is again best in the region of high gain and noise filter. Moreover, the accurate elimination of abiotic data was maintained, as can be seen in Figure 3.29. We note that the range of viable cutoff values increased slightly in value upon the introduction of a reference dye in channel 1, from 0.02 – 0.05 V to 0.04 – 0.06 V. This makes sense intuitively: increasing the amount of background signal in channel 2 by increasing the fluorescent content of channel 1, should result in a higher binary division value to separate background signals from assay signals. At this stage we elected to control the noise filter value, to simplify proceeding optimization experiments in channels 3 and 4. Of the available range, 8-12 kHz, we opted for the median value, 10 kHz.

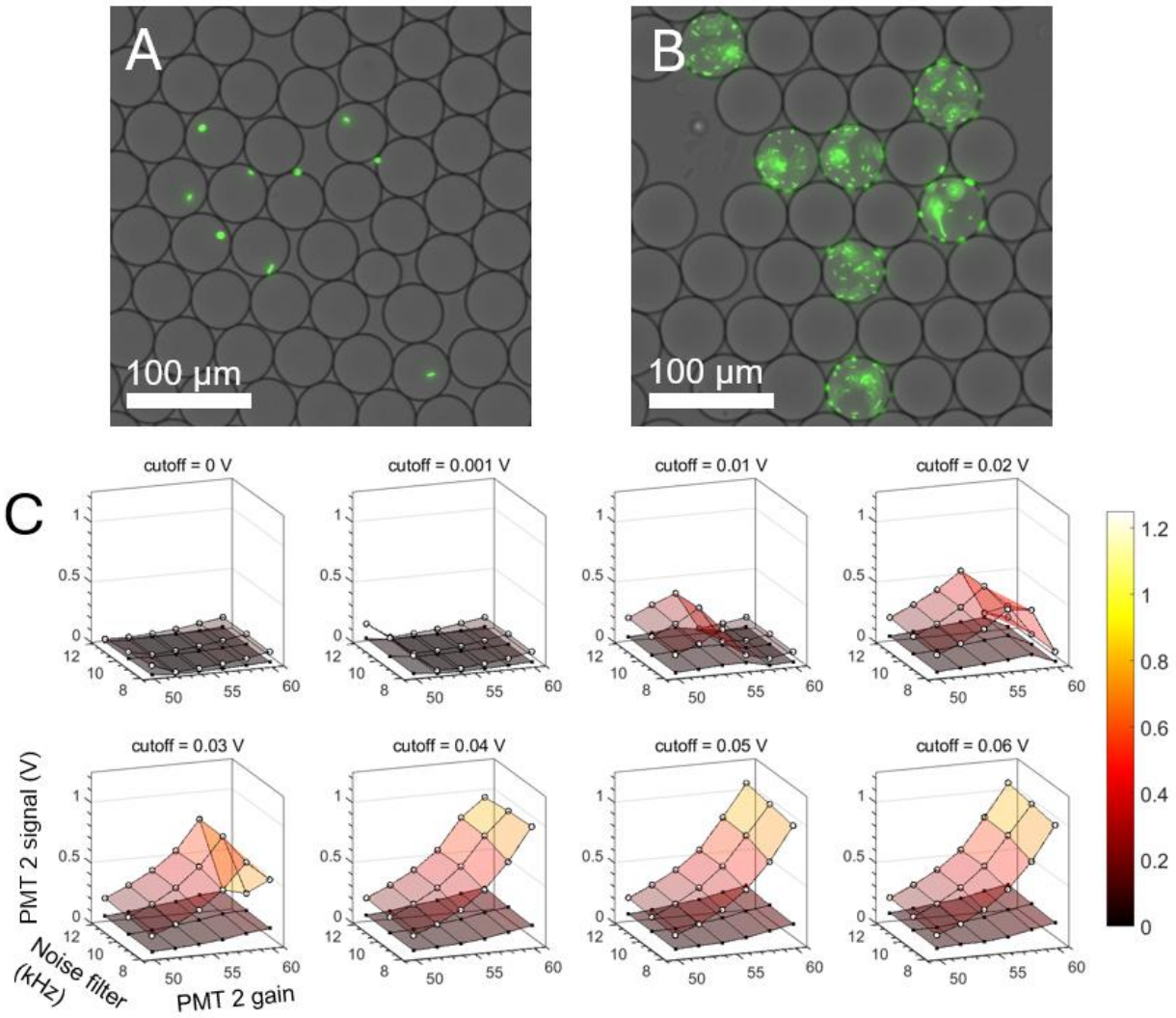

Figure 3.28. Channel 1 and 2 co-optimization. A, B, representative fluorescence images of droplets at time = 0 and 5 hours, respectively. C, droplet LIF data in channel 2 as a function of noise filter, PMT 2 gain and channel 2 binary cutoff value. Each of the 8 plots is specific to a cutoff value. Upper surface, time = 5 data, lower surface, time = 0 data. Each point on a surface corresponds to the mean value of the dataset collected at that node of the parameter space, with abiotic data eliminated according to the specific cutoff value. As expected, separation of growth from non-growth values is maintained at high laser and gain values after channels 1 and 2 were combined.

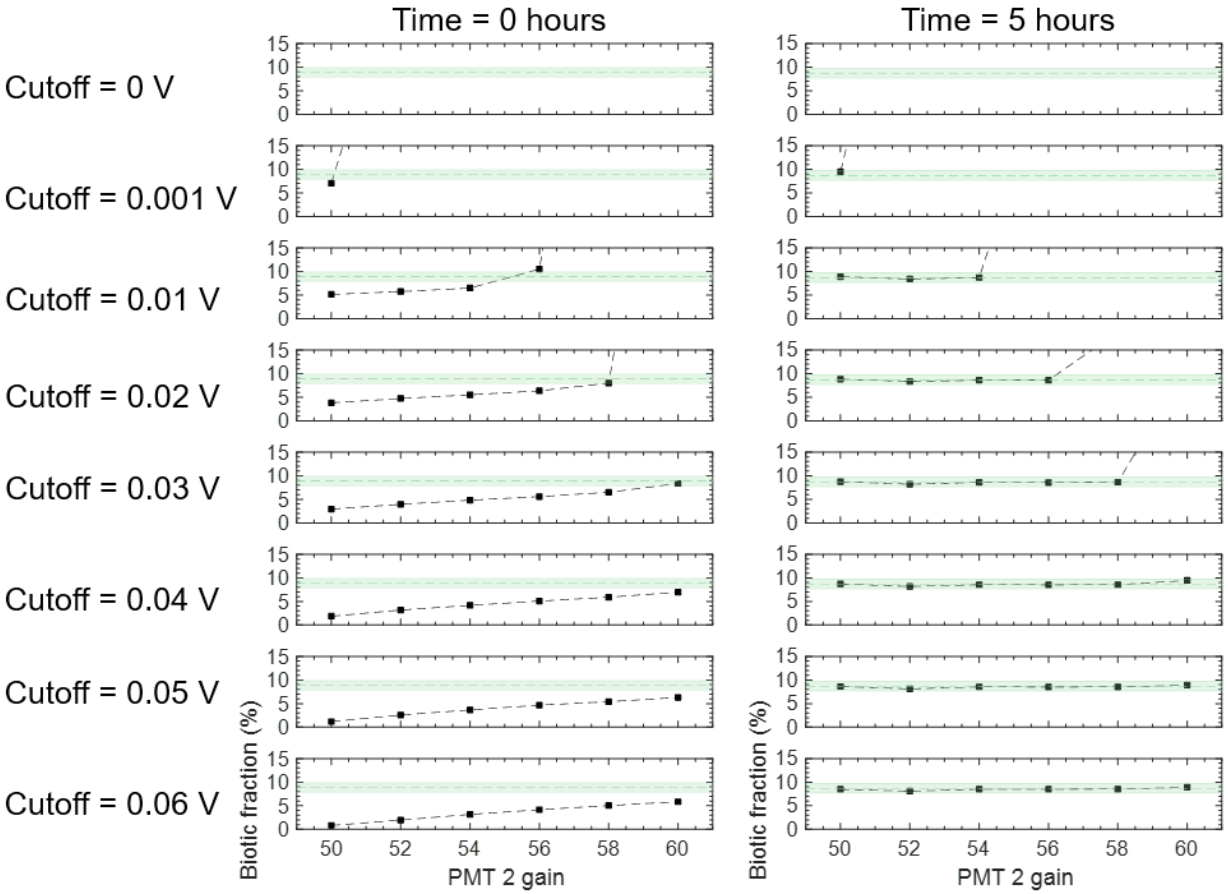

Figure 3.29. Assessment of binary cutoff value efficacy after channels 1 and 2 were combined. Each individual plot shows the biotic fraction detected vs PMT 2 gain, for the binary cutoff value listed left. Left column, time = 0 LIF data, right column, time = 5 hours. Green shaded region indicates the biotic fraction enumerated by image analysis, thus, accuracy of binary division of LIF data is indicated when the black data intersects the green region. These data indicate that accurate elimination of abiotic data was maintained after combination of channels 1 and 2.

Channel 3 optimization

Channels 3 and 4 were used for a spectral barcoding channel, which represents an application of moderate requirements. For each barcoding channel, we aimed to generate 6 barcodes by loading droplets with a single AlexaFluor dye in 6 concentrations. In this way, 36 barcodes can be generated by pairwise combination of the two dyes in 6 concentrations each. Thus the requirements of each spectral barcoding channel were that the 6 unique fluorescence signatures are readily distinguishable from each other, with good separation between barcoded data clusters.

In early attempts to impart fluorescence barcodes onto droplets, it was observed that unique fluorescence signatures are readily distinguishable when the entire range of the detector is utilized. This result was reproduced during channel 3 optimization experiments. In these experiments, a parameter space consisting of 3 laser powers and up to 5 gain settings was explored. A mixed droplet sample was generated, consisting of 6 subpopulations of droplets, containing 0, 70, 176, 316, 492 and 700 nM AlexaFluor 568, with channel 1 reference dye. To optimize detection of the 6 unique barcode signatures, we conducted LIF on the mixed droplet population while scanning the individual channel parameter space. Figure 3.30 shows the results of this examination. By visual inspection, it can be discerned that the 6 individual data clusters are more easily distinguished in the region of higher laser power and gain. To demonstrate facile clustering of the data into 6 clusters based on AlexaFluor 568 signal, we conducted DBSCAN data clustering [138] on the dataset corresponding to P_{561} = 30 mW, gain = 74 and noise filter = 10 kHz (Figure 3.31). Figure 3-31A shows the non-clustered, raw barcode channel histogram of PMT signals, and Figure 3.31B shows the clustered result. The DBSCAN clustering algorithm accurately identifies the 6 barcoded clusters of data, and less than 2% of the total data is eliminated as noise.

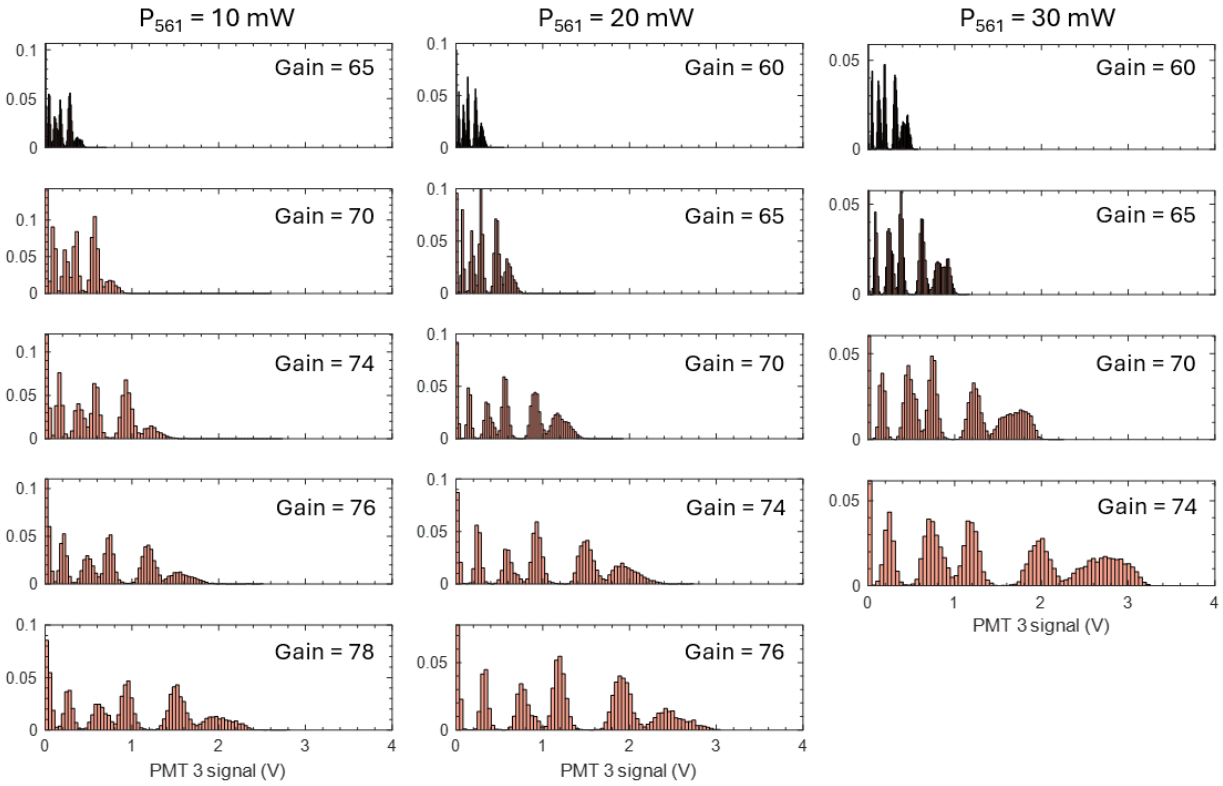

Figure 3.30. Channel 3 optimization. A droplet sample consisting of 6 subpopulations of unique AlexaFluor 568 concentration was detected by LIF while varying detection parameters controlling channel 3. By visual inspection, 6 unique fluorescence barcodes are most readily distinguishable at high gain and laser powers.

Rather than establish a functional parameter space for this channel, it was instead decided that the channel 3 and 4 co-optimization phase should be conducted first, to establish if an individual functional parameter space was necessary. The most likely problem to arise would be cross-talk from channel 3 fluorophores into channel 4. During attempts to use channel 4 as a reference dye, it was observed that channel 3 to 4 cross-talk is considerable (Figure 3.19). However, this is of greater concern if channel 4 is used as a reference dye, than if it is used as a barcoding dye. In experiments prior to this work, we have managed cross-talk between channels in a two-color barcoding schema by background subtraction, and it was expected that this same

treatment could be applied here. Thus, we planned to use the combination of parameters shown in Figure 3.31B in the proceeding co-optimization phase, and proceeded to channel 4 optimization.

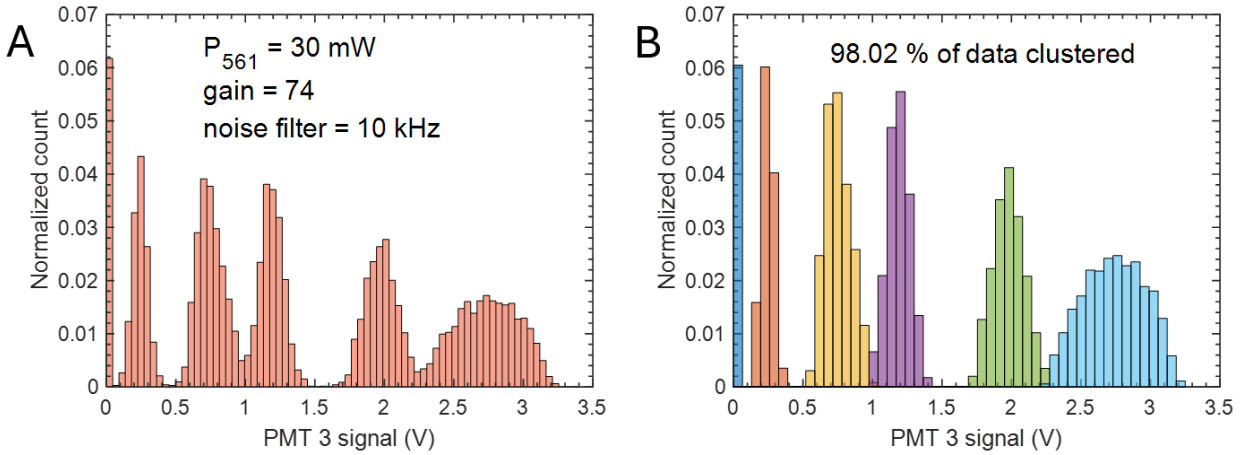

Figure 3.31. DBSCAN clustering analysis of AlexaFluor 568 barcodes in droplets. A, raw PMT signal histogram for a single dataset from channel 3 optimization experiment. B, same dataset as A, grouped by cluster identified by DBSCAN analysis.

Channel 4 optimization

The procedure to optimize channel 4 was identical to the procedure used to optimize channel 3. However, channel 4 was reduced in constraints, as it has no neighboring channel of higher wavelength into which to cross-talk. Thus, it was expected that maximum laser and gain settings could be used to promote separation of barcoded data clusters, without cross-talk penalty.

As expected, the regions of channel 4 parameter space corresponding to high gain and laser setting produced readily distinguishable barcode clusters (Figure 3.32). To demonstrate facile clustering of the data into 6 clusters based on AlexaFluor 647 signal, we conducted DBSCAN data clustering on the dataset corresponding to the highest gain and laser settings. The results are shown in Figure 3.33, where the raw barcode channel histogram shown in Figure 3.33A was accurately clustered into the 6 subpopulations shown in Figure 3.33B, and less than 1% of data was eliminated

as noise. Rather than establishing a functional parameter space, we instead planned to use these highest gain and laser settings in the co-optimization phase.

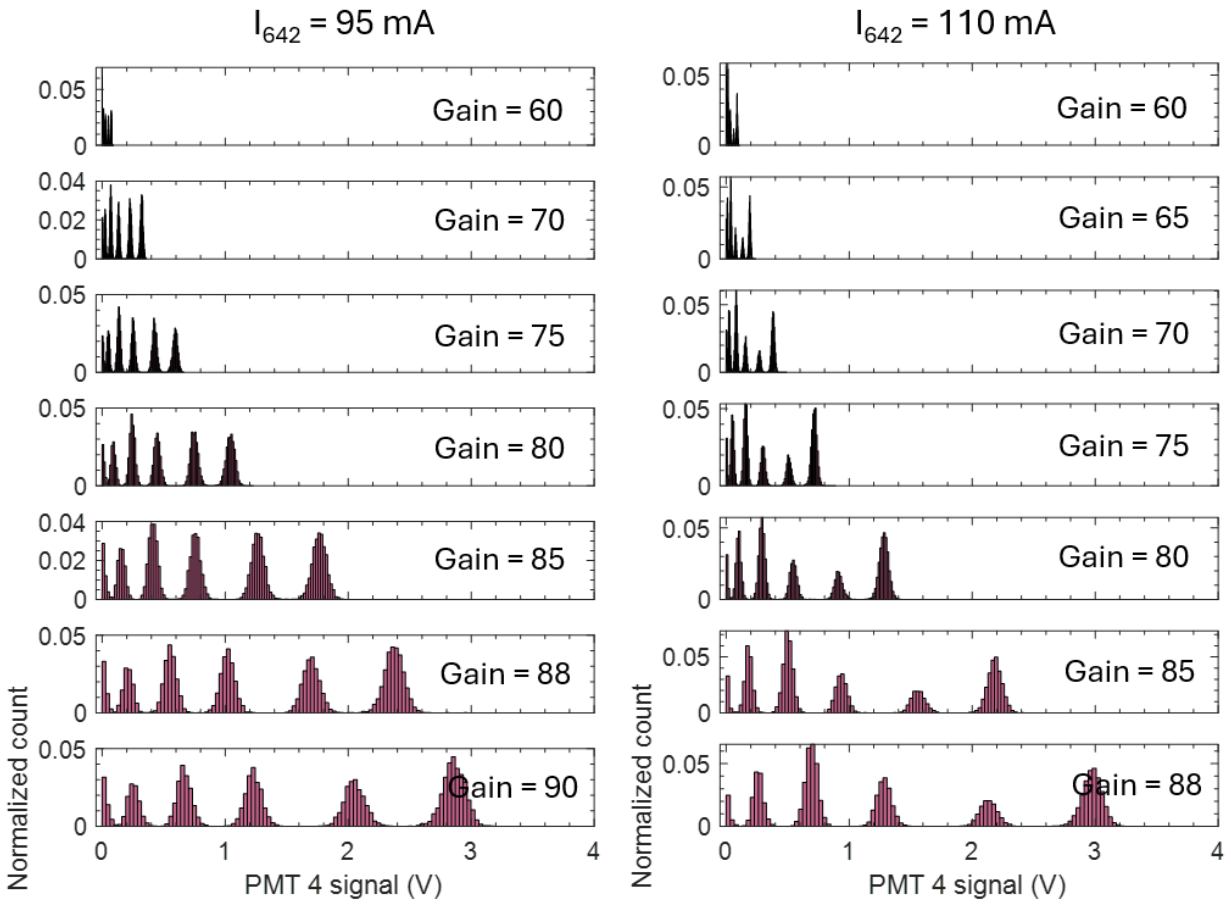

Figure 3.32. Channel 4 optimization. A droplet sample consisting of 6 subpopulations of unique AlexaFluor 647 concentrations was detected by LIF while varying detection parameters controlling channel 4. 6 unique fluorescence barcodes are most readily distinguishable at high gain and laser powers.

Channel 3 and 4 co-optimization.

The procedure to establish working conditions to detect AlexaFluor 568 and 647 barcoding dyes coincidentally was not so much an optimization procedure, as an experiment to verify maintained functionality in both channels once combined. For this experiment, the barcoding dyes in 6 concentrations each were combined pairwise to generate 36 unique 2-color fluorescence

barcodes. A library of droplets was generated which consisted of 36 uniquely barcoded subpopulations, and LIF was conducted on the droplet library. Prior to the experiment, a 4D multichannel parameter space was constructed, with dimensions corresponding to 561 nm laser power, 642 nm laser current, and both channel gains. However, it was found that channel bifunctionality is preserved by the conditions identified during individual channel optimizations corresponding to maximum laser and gain settings. Thus, the 4D multichannel parameter space was not examined. The results of this experiment are shown in Figure 3.34. Figure 3.34A shows a fluorescence image of the droplet library in both barcoding channels, and Figure 3.34B shows a scatter plot of the raw PMT signals in the barcoding channels. The cross-talk from channel 3 to 4 can be discerned, as the PMT 4 signal is a function of PMT 3 signal. However, the discrimination of 36 unique barcode clusters was not affected by this cross-talk. Figure 3.34C shows the result of DBSCAN clustering, in which 36 unique clusters comprising over 99% of the total data were identified. Data which were not clustered are plotted as red X's.

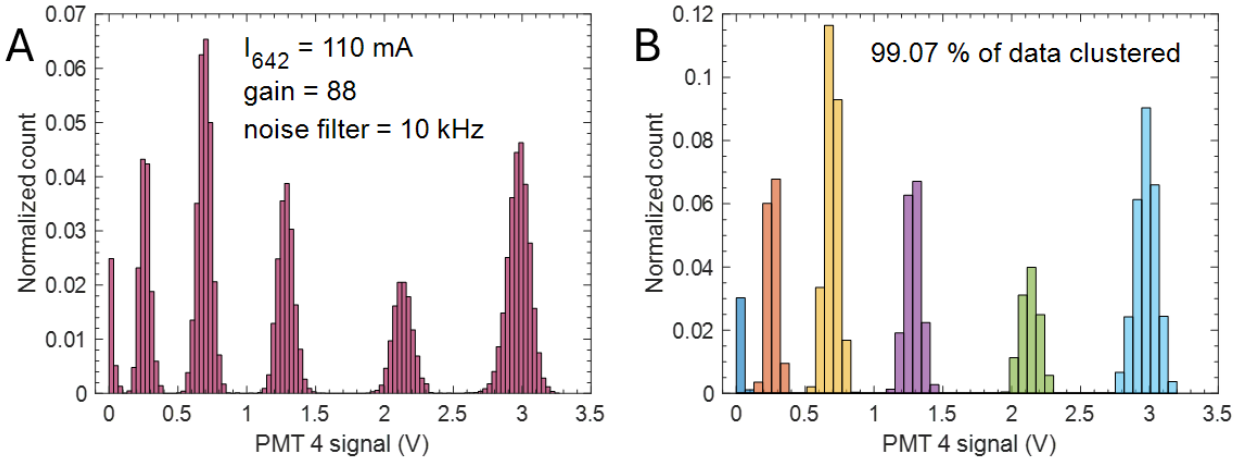

Figure 3.33. DBSCAN clustering analysis of AlexaFluor 647 barcodes in droplets. A, raw PMT signal histogram for a single dataset from channel 4 optimization experiment. B, same dataset as A, grouped by clusters identified by DBSCAN analysis.

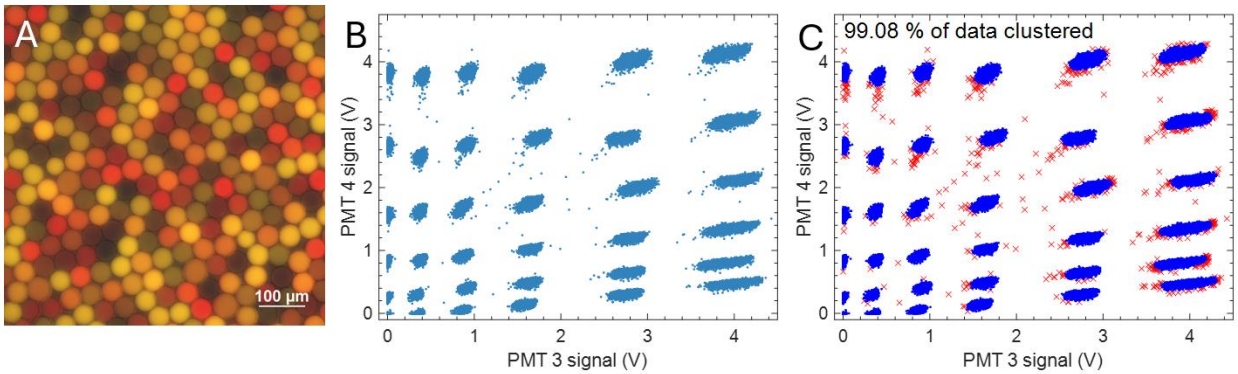

Figure 3.34. Detection of 2-channel fluorescence barcodes. Two barcoding dyes in 6 concentrations each were combined pairwise to generate 36 unique 2-color fluorescence barcodes in droplets. A, fluorescence image of the droplet library. B, scatter plot of PMT signals in the two barcoding channels. C, DBSCAN clustering analysis of the same data in B. The clustering algorithm readily identifies 36 subpopulations of droplets comprising over 99% of the total data. Non-clustered data plotted as red X's.

Simultaneous 4-color fluorescence detection of microfluidic droplets enables a multiplexed microbial growth assay.

We designed a multiplexed droplet microbial growth assay, to show proof-of-concept of the utility of our multicolor droplet fluorescence detection setup. In this assay, single microbial cells were loaded into a library of droplets encoded with 2-color fluorescence barcodes, and LIF was conducted on the droplet library at time = 0 and 5 hours of incubation. The resulting datasets contain data from a mixture of abiotic and biotic droplets, from all 36 barcoded subpopulations. Below, we will demonstrate the data processing procedures implemented to assay microbial growth across 5 hours, for each of the subpopulations of droplets.

Figure 3.35 shows the data quality filtration process based on droplet time inside, for the time = 0 (Figure 3.35A-C) and time = 5 hours (Figure 3.35D-F) datasets. Figures 3.35A and 3.35D show time inside vs droplet number in chronological order for the whole, unfiltered datasets. Coalesced and sheared droplets are discernible as the regions of low data density above and below

(respectively) the central bands of greatest data density. In Figures 3.35B and 3.35E, the dynamic gating MATLAB program has been applied to draw the data density contour lines. The outermost green contour defines the dynamic gate; droplet data which falls outside this perimeter was eliminated from the dataset. Figures 3.35C and 3.35F show time inside vs droplet number of the filtered datasets. This filtration process was repeated on the once-filtered datasets, using reference dye signal as the filtration criterion (Figure 3.36). Figure 3.36A-C correspond to time = 0 hours and Figures 3.36D-F correspond to time = 5 hours datasets. As seen in Figures 3.36A and 3.36D, which show plots of reference dye PMT signal vs droplet number from the once-filtered dataset, a significant amount of undesired data was already eliminated by filtration based on time inside. As in Figure 3.35, Figures 3.36B and 3.36E show the reference dye vs droplet number heatmaps with dynamic gating program applied, and Figures 3.36C and 3.36F show the same plot, from the filtered datasets. The double filtration process resulted in the elimination of 11.52% and 14.24% of total data points, from the time = 0 and 5 hours datasets, respectively.

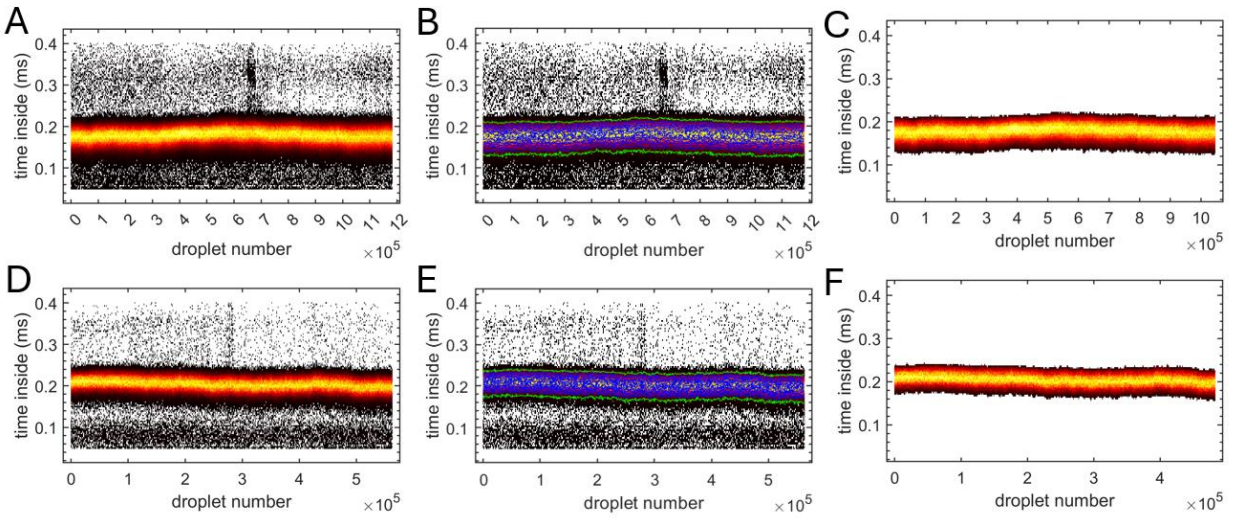

Figure 3.35. Data filtration based on time inside measurements, of whole mixed datasets. Top row corresponds to time = 0 hours data, bottom row, time = 5 hours. A, D, time inside vs droplet number in chronological order. B, E, the dynamic gating MATLAB program applied to the same plots as in A and D, to define the data quality gate. C, F, time inside vs droplet number for the filtered datasets.

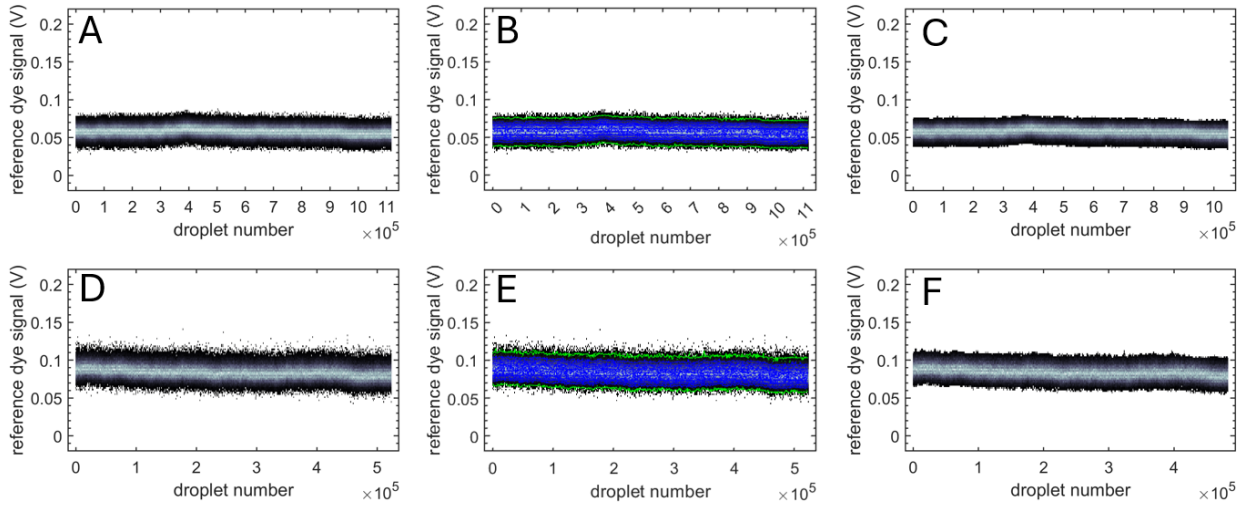

Figure 3.36. Reference dye-based filtration of mixed datasets. Top row corresponds to time = 0 hours data, bottom row, time = 5 hours. A, D, reference dye signal vs droplet number in chronological order. B, E, the dynamic gating MATLAB program applied to the same plots as in A and D, to define the data quality gate. C, F, reference dye signal vs droplet number for the filtered datasets.

The elimination of abiotic data from the twice-filtered datasets is detailed in Figure 3.37. Figures 3.37A and 3.37C show histograms of PMT signals in the cell growth channel, with representative fluorescence images of the droplets shown in the insets. The channel 2 binary division value was established by visual inspection of the histograms. Each histogram contains several bins near 0 on the x-axis which account for approximately 80% of the dataset. Moreover, these bins occupy the region of PMT 2 signal = 0 – 0.05 V, which corresponds to the range of PMT 2 signals from abiotic droplets established during the channel 2 optimization phase. As such, we speculated that abiotic data could be eliminated from the datasets by elimination of the abnormally tall bins. The binary division value is shown in Figures 3.37B and 3.37E, which show a zoomed in region of the same histograms in Figures 3.37A and 3.37D, respectively. A red dashed line is plotted along the binary division values for each dataset, which corresponded to PMT 2 signal = 0.03 and 0.04 V for time = 0 and 5 hours, respectively. The accuracy of this binary division process is reported in Figure 3.37C and 3.37F. In each figure, the difference between the biotic fraction, F_+, counted by image analysis and binary division of LIF datasets is reported as $\Delta F_+ = F_{+,\,image} - F_{+,\,LIF}$, as a raw percentage. The error bar corresponds to the 95% confidence interval calculated for the image analysis control value. This result indicates excellent agreement between the two F_+ counting methods, and accurate elimination of abiotic data using the binary division method.

Clustering of the filtered, biotic datasets into 36 subpopulations based on fluorescence barcode signatures is demonstrated in Figure 3.38. Scatter plots of PMT signals in channels 3 and 4 are shown in Figures 3.38A and 3.38C, for time = 0 and 5 hours, respectively. Figures 3.38B and 3.38D show the results of the DBSCAN-based clustering in MATLAB. In each case, the clustering

algorithm identifies 36 clusters based on fluorescence signature, comprising over 97% of the data. Data which were not clustered, and subsequently were eliminated as noise, are plotted as red X's.

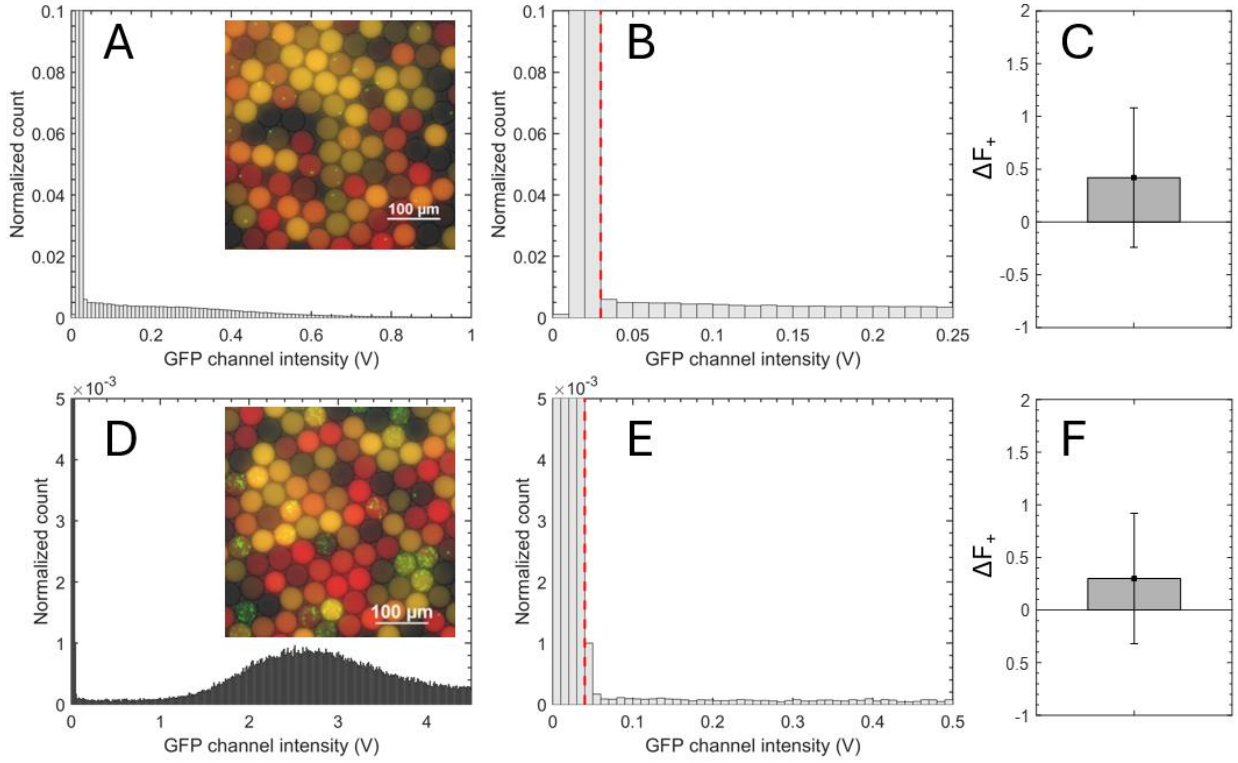

Figure 3.37. Elimination of biotic data by binary division. A, D, GFP fluorescence histograms for time = 0 and 5 hours, respectively. Insets show representative fluorescence images of the droplets. B, E, zoom of A and D, respectively. Red dashed line indicates the binary division value. Droplets with PMT 2 signal less than the division value were marked as abiotic and eliminated from the datasets. C, F, assessment of binary division accuracy. Difference in biotic fraction, ΔF+, enumerated by image analysis and by droplet LIF with binary division. $\Delta F_+ = F_{+,\,\text{image}} - F_{+,\,\text{LIF}}$. Error bar corresponds to 95% confidence interval calculated for the image analysis control value.

In Figure 3.39, we show endpoint growth analysis for each of the 36 subpopulations of droplets. Each subplot in Figure 3.39 is specific to one of the 36 barcoded subpopulations of droplets, and histograms of cellular GFP fluorescence are shown for time = 0 (blue) and time = 5 hours (red). As established during channel 2 optimization, excellent separation of growth from non-growth values can be discerned. In this proof-of-concept assay, the same experimental growth

condition was encapsulated into each of the 36 subpopulations of droplets, namely, growth media. However in the future, this platform could be used to assay a panel of 36 unique experimental conditions in droplets, such as antimicrobial dilution series.

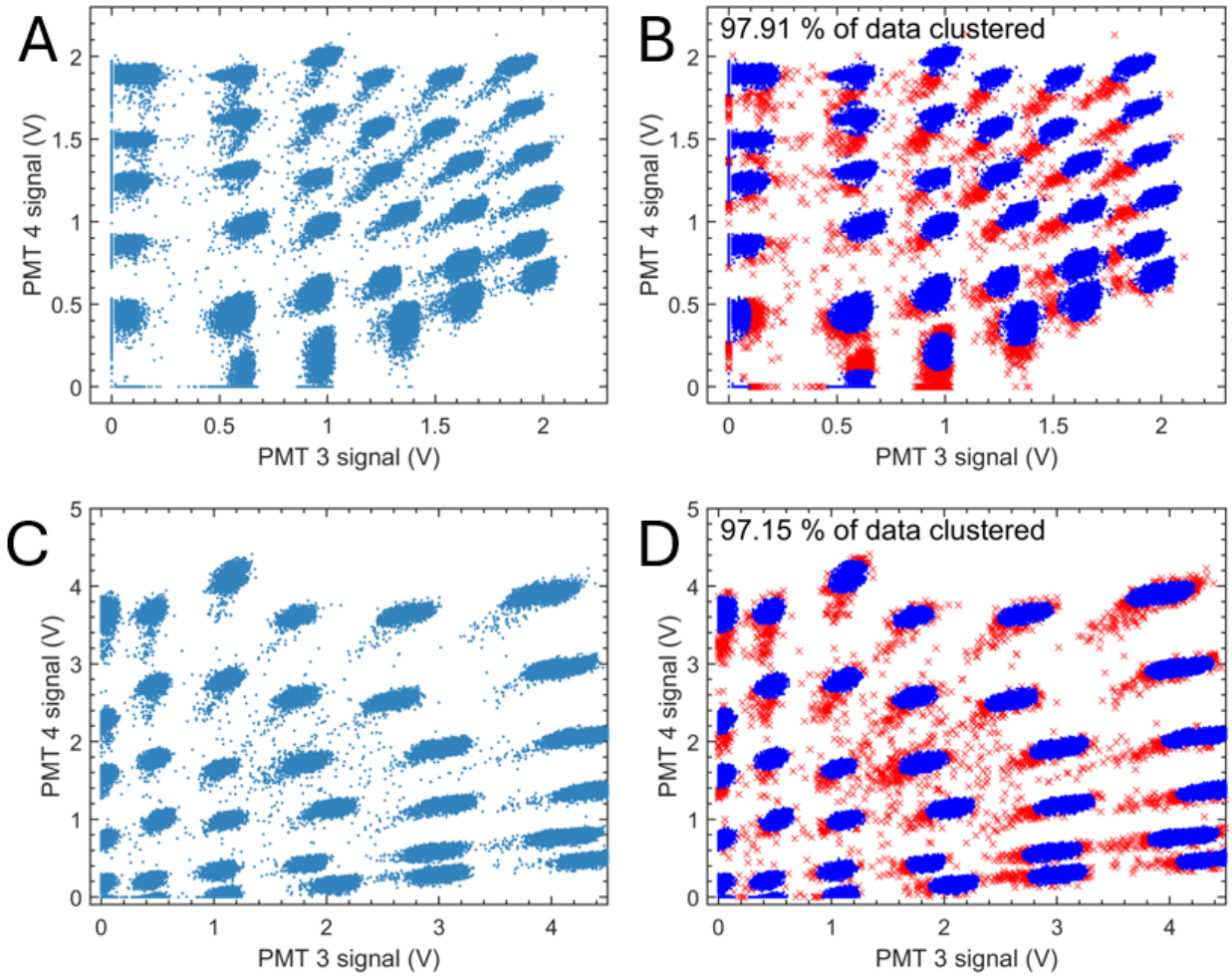

Figure 3.38. DBSCAN clustering of droplet the droplet library at time = 0 (top row) and 5 hours (bottom row). A, C, scatter plots of PMT signals in the two barcoding channels. B, D, results of DBSCAN clustering. Non-clustered data are plotted as red X's.

The assay shown here represents the culmination of the procedures developed in this thesis chapter: from mixed, multi-channel droplet fluorescence datasets, we (1) eliminated noise using dynamic gating of time inside and reference dye measurements, (2) eliminated data corresponding to abiotic droplets using a channel 2 binary division value, (3) clustered the data into 36

subpopulations based on 2-color barcode signals, and (4) conducted endpoint growth analysis on each of the 36 subpopulations of droplets. We achieved simultaneous detection of droplet reference dye, cell growth, and 2-color fluorescence barcode signals, which was only made possible by the step-wise optimization procedures detailed previously.

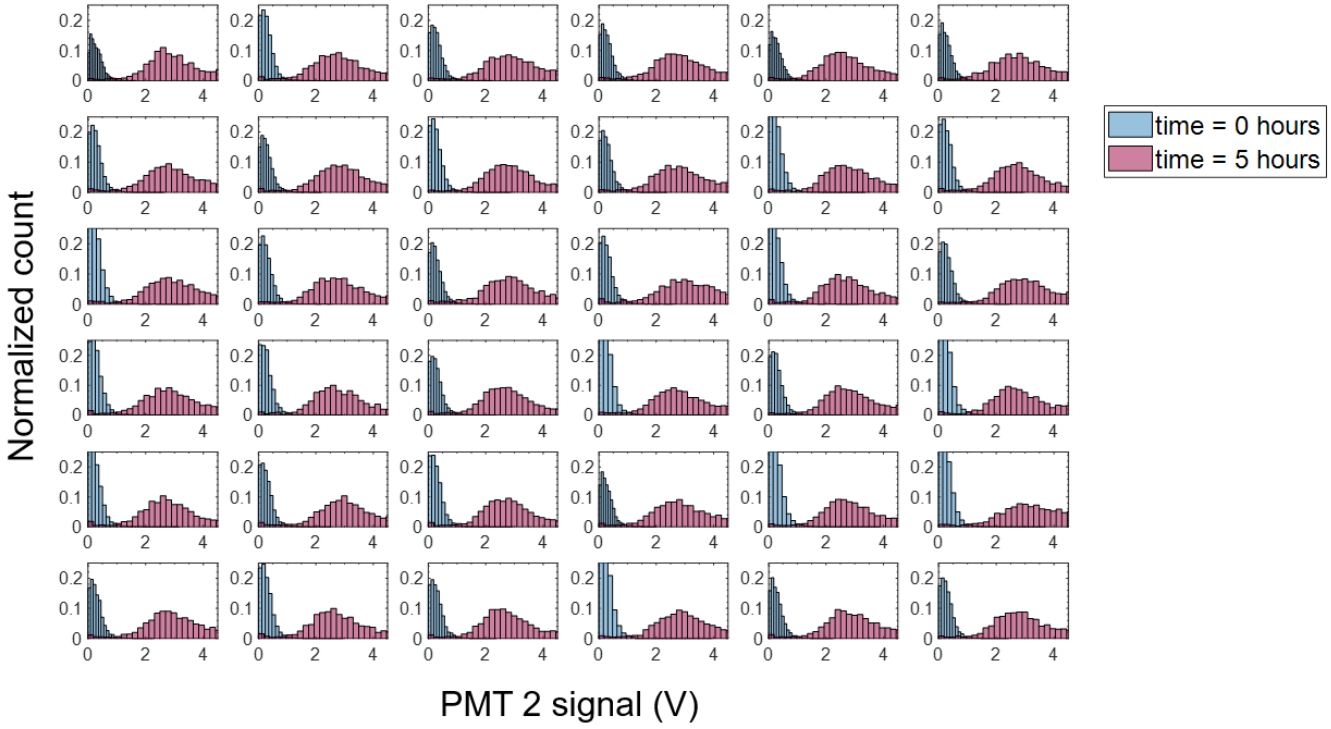

Figure 3.39. Endpoint growth analysis of the 36-plexed droplet library. Each plot shows histograms of PMT signals for time = 0 hours (blue) and 5 hours (red), for each of the 36 barcoded subpopulations of droplets, with abiotic data eliminated. In this proof-of-concept assay, there is no difference in the test condition of each subpopulation. In the future, experimental conditions such as antimicrobials could be tested in parallel using this technique.

Conclusions

The power of droplet microfluidics is realized in flowing droplet LIF assays, in which microfluidic droplets, acting as single-cell microreactors, are analyzed at ultrahigh-throughput. However, the analysis of flowing droplet samples presents several key challenges, including robust assembly of optical equipment to deliver optimized laser beams to the droplet sample, stable

reinjection of emulsion samples, data quality assurance, and reliable acquisition of multiplexed droplet signals. In this thesis chapter, we provided tutorials for navigating these challenges.

The first step in any droplet LIF application is the delivery of a laser beam to a flowing droplet sample. Without requisite alignment and beam shaping operations, the laser beam which exits a microscope objective might contain aberrations. The possibilities for deterioration of droplet LIF are myriad: simultaneous detection of two droplets in sequence, spatiotemporally separated beam spots of different laser wavelength, reduction in fluorescence signal by attenuated laser beam power or off-axis excitation of droplets, to name a few. To safeguard against these artefacts, we developed and outlined here a stepwise procedure to shape and align laser beams before delivery to the microscope objective. The procedures are robust, and can be conducted with off-the-shelf optical components by persons without prior optical training.

Reinjection of emulsion samples for flow-based analysis is a known point of droplet-based experimental failure [128]. Even when droplet reinjection has been optimized to reduce droplet instabilities, some degree of low-level droplet coalescence and/or breakup is virtually inevitable. In response to this, we detailed a method to encode microfluidic droplets with a standardized fluorescent reference dye condition, which can be used as a data quality signature. We reported tutorials on how to use this standard fluorescence signature to conduct data quality control by eliminating data corresponding to droplets of incorrect size or reference dye intensity. Moreover, we reported on non-intuitive factors which influence measurements of droplet size and fluorescence intensity in our system. The techniques reported are facile and could facilitate the acquisition of high-quality droplet data by future experimenters.

Last, we outlined a rational method to optimize the detection of multiplexed fluorescence signals from flowing droplets. In theory, the method could be used to optimize the use of any fluorophore as an assay readout. The process of identifying performance criteria and establishing an available parameter space, followed by systematic assessment of performance within the parameter space, enabled step-wise, bottom-up construction of a multiplexed droplet bioassay. The method can serve as a blueprint for future experimenters hoping to detect biological assays at ultrahigh-throughput from microfluidic droplets.

Droplet microfluidics can enable impactful discoveries *via* ultrahigh-throughput single cell biological analyses. Therefore, society stands to benefit greatly from the continued proliferation of microfluidics-based techniques. As microfluidic methods spread further from microfluidics-specific laboratories, the translation of existing biological assays into microfluidics-based assays is a challenge which must be addressed. Taken together, this chapter serves as a step-by-step guide to developing flow-based bioassays in microfluidic droplets. It is our hope that this thesis chapter might facilitate the development of novel assays conducted in microfluidic droplets.

CHAPTER FOUR

RAPID PARALLEL GENERATION OF A FLUORESCENTLY BARCODED DROP LIBRARY FROM A MICROTITER PLATE USING THE PLATE-INTERFACING PARALLEL ENCAPSULATION (PIPE) CHIP

Contribution of Authors and Co-Authors

Manuscript in Chapter 4

Author: Geoffrey K. Zath

Contributions: G. K. Z. designed research, performed research, analyzed data, and wrote the manuscript

Co-Author: Ralph A. Sperling

Contributions: R. A. S. designed research, performed research, analyzed data, and wrote the manuscript

Co-Author: Dimitri A. Bikos

Contributions: D. A. B. wrote the manuscript

Co-Author: Carter W. Hoffman

Contributions: C. W. H. performed research and wrote the manuscript

Co-Author: Reha Abbasi

Contributions: R. A. performed research

Co-Author: Adam R. Abate

Contributions: A. R. A. designed research

Co-Author: David A. Weitz

Contributions: D. A. W. designed research

Co-Author: Connie B. Chang

Contributions: C. B. C. designed research and write the manuscript

Manuscript Information

Geoffrey K. Zath, Ralph A. Sperling, Dimitri A. Bikos, Carter W. Hoffman, Reha Abbasi, Adam R. Abate, David A. Weitz, Connie B. Chang

Lab on a Chip

Status of Manuscript:
☐ Prepared for submission to a peer-reviewed journal
☐ Officially submitted to a peer-reviewed journal
☐ Accepted by a peer-reviewed journal
☒ Published in a peer-reviewed journal

Royal Society of Chemistry

Lab on a Chip

ROYAL SOCIETY OF CHEMISTRY

PAPER

View Article Online
View Journal | View Issue

Cite this: Lab Chip, 2022, 22, 4755

Rapid parallel generation of a fluorescently barcoded drop library from a microtiter plate using the plate-interfacing parallel encapsulation (PIPE) chip†

Geoffrey K. Zath, ‡[ab] Ralph A. Sperling, ‡[da] Carter W. Hoffman, [abc] Dimitri A. Bikos, [ab] Reha Abbasi, [ab] Adam R. Abate, [f] David A. Weitz [dg] and Connie B. Chang *[abc]

In drop-based microfluidics, an aqueous sample is partitioned into drops using individual pump sources that drive water and oil into a drop-making device. Parallelization of drop-making devices is necessary to achieve high-throughput screening of multiple experimental conditions, especially in time-sensitive studies. Here, we present the plate-interfacing parallel encapsulation (PIPE) chip, a microfluidic chip designed to generate 50 to 90 μm diameter drops of up to 96 different conditions in parallel by interfacing individual drop makers with a standard 384-well microtiter plate. The PIPE chip is used to generate two types of optically barcoded drop libraries consisting of two-color fluorescent particle combinations: a library of 24 microbead barcodes and a library of 192 quantum dot barcodes. Barcoded combinations in the drop libraries are rapidly measured within a microfluidic device using fluorescence detection and distinct barcoded populations in the fluorescence drop data are identified using DBSCAN data clustering. Signal analysis reveals that particle size defines the source of dominant noise present in the fluorescence intensity distributions of the barcoded drop populations, arising from Poisson loading for microbeads and shot noise for quantum dots. A barcoded population from a drop library is isolated using fluorescence-activated drop sorting, enabling downstream analysis of drop contents. The PIPE chip can improve multiplexed high-throughput assays by enabling simultaneous encapsulation of barcoded samples stored in a microtiter plate and reducing sample preparation time.

Received 28th September 2022,
Accepted 26th October 2022

DOI: 10.1039/d2lc00909a

rsc.li/loc

Introduction

Drop-based microfluidics technology reduces assay times and increases sample throughput by rapidly creating and analyzing picoliter-sized drops.[1,2] Drop-based microfluidics has recently been applied towards combinatorial drug discovery,[3] massively multiplexed nucleic acid detection,[4] and antibiotic susceptibility screening.[5] In these assays, 10^3 to 10^6 drops are tracked by a unique identifier in each drop, called a "barcode". This is commonly achieved using one of two barcode types: DNA barcodes introduced to tag drop contents as part of a next generation sequencing pipeline;[6–9] or fluorescent dyes and particles used to label drops for fluorescence-based assays, such as enzyme activity or dose–response screening.[3–5,10–14] DNA barcoding can provide upwards of 10^7 unique identifiers, enabling large-scale single-cell transcriptomics, but requires coalescing the drop emulsion before sequencing.[6–9] Though an advantage in single cell sequencing, drop coalescence prohibits ultrahigh-throughput experiments in which drop contents are assayed

[a] Center for Biofilm Engineering, Montana State University, Bozeman, MT, USA. E-mail: conniebchang@gmail.com
[b] Department of Chemical and Biological Engineering, Montana State University, Bozeman, MT, USA
[c] Department of Physiology and Biomedical Engineering, Mayo Clinic, Rochester, MN, USA
[d] Department of Physics, School of Engineering and Applied Sciences, Harvard University, Cambridge, MA, USA
[e] Fraunhofer Institute for Microengineering and Microsystems IMM, Mainz, Germany
[f] Department of Bioengineering and Therapeutic Sciences, University of California, San Francisco, CA, USA
[g] Wyss Institute for Biologically Inspired Engineering at Harvard University, Boston, MA, USA

† Electronic supplementary information (ESI) available: Detailed device fabrication and additional experimental details. See DOI: https://doi.org/10.1039/d2lc00909a

‡ Authors contributed equally.

over time. Fluorescent labeling allows the barcode and fluorescent assay output to be measured simultaneously without coalescing the drops. The resulting collections of either DNA or fluorescent barcodes in drops, known as "libraries", enable multiplexed or combinatorial readouts of the unique components encapsulated within the drops.[10–13]

A typical method for creating a barcode within a drop library is to emulsify a fixed sample volume of that barcode contained within a microtiter plate well or microcentrifuge tube using a single drop-making device. The process rapidly becomes labor- and time-intensive when a single drop-making device is used to generate increasingly large numbers of barcoded drops that are subsequently pooled together. Individual microfluidic drop makers can be run in parallel, but this requires multiple pump sources to emulsify each sample. Alternatively, liquid handling machines or autosamplers can be programmed to sequentially load individual samples from a microtiter plate into a microfluidic device;[14–17] however, these technologies are costly and cannot create multiple different barcodes simultaneously, which may be necessary for time-sensitive experiments. For example, all samples must be emulsified and processed in parallel to accurately capture the time-sensitive kinetics needed for performing comparative rapid enzymatic reaction screening studies.[18,19] Thus, to perform parallel encapsulation of multiple different barcodes, specialized microfluidic devices actuated using vacuum[20] or positive pressure[7,8] and containing multiple drop makers have been designed to interface with wells on standard microtiter plates. In prior work from Rotem *et al.*, such a device was used to encapsulate DNA barcodes to perform single-cell chromatin profiling.[7,8] In this prior work, however, the fabrication of the device was not described in detail, nor was the device used to create fluorescently barcoded libraries. Extending the utility of this device for fluorescent barcoding would enable multiplexed assaying, wherein a barcoded signal is simultaneously measured along with an assay output. Additionally, fluorescently barcoded drops enable sample isolation and enrichment of a particular sample using fluorescence-activated drop sorting.[21,22] To allow for longer term storage of the drop libraries, fluorescent particles may be used in the place of dyes[3,11] to prevent diffusion of barcode labels between drops.[23]

Here, we detail the fabrication of a microfluidic device comprised of 96 simultaneously operating drop makers called the plate-interfacing parallel encapsulation (PIPE) chip that directly interfaces with 96 wells of a standard 384-well microtiter plate. The PIPE chip is operated within a pressure chamber, a modified commercial pressure cooker, wherein pressurized air drives parallelized drop formation across the 96 drop makers on the device. Parallelization enables rapid creation of drop libraries at a total drop throughput of approximately 300 kHz, approximately two orders of magnitude larger than serial drop generation using a single drop-making device, creating a total of approximately 3.6×10^7 drops in 2 min. Drop sizes produced by the PIPE chip are described using a simple drop scaling law, which allows for fine-tuning of drop diameters ranging from approximately 50–90 μm. The PIPE chip is used to create two types of optically barcoded drop libraries using two-color combinations of either microbeads or quantum dots (QDs). A quarter of the 96 drop makers on the PIPE chip was used to create a drop library consisting of 24 fluorescent microbead combinations. The PIPE chip was also used twice to create a drop library consisting of 192 QD combinations. Fluorescence from each barcoded drop was measured at high speed using a flow-based detection method[22] to create a two-color scatter plot for each type of barcode library. A data clustering method, density-based spatial clustering of applications with noise (DBSCAN),[24] is used to identify uniquely barcoded concentrations and minimize the signal overlap between the combinations. The dominant sources of noise influencing the fluorescence signal overlap between barcode populations arise from Poisson loading for drops containing fluorescent microbeads approximately 1 μm in diameter and shot noise of the photodetector for drops containing QDs approximately 10 nm in diameter. The effect of these noise sources when designing barcode label concentration can be accounted for by scaling the barcode particle concentration with a quadratic function, thereby allowing for quick prototyping of barcode library labels. Finally, we demonstrate the utility of the PIPE chip by sorting and isolating a single fluorescently barcoded sample from a drop library of 24 different barcode combinations.[21,22] The ability to sort a specific barcoded sample from a drop library enables further analysis of drop contents using downstream techniques such as PCR amplification and genetic sequencing.[25–27] Drop libraries created with the PIPE chip can help to streamline existing multiplexed assays, such as combinatorial drug screening[3] or high-throughput assaying of protease activity,[12] by enabling simultaneous encapsulation of barcoded samples stored in a well plate.

Materials and methods

PIPE chip design

The PIPE chip was fabricated from three separate approximately 5 mm thick layers of polydimethylsiloxane (PDMS) plasma bonded on top of one another to form a 3-dimensional network of channels. The top layer of the device (Fig. 1a, i) is comprised of a narrow strip of PDMS containing two long channels that function as a common oil inlet and drop outlet for all three layers. Oil inlet and drop outlet channels run perpendicular to the channels in the remaining two PDMS layers, thereby allowing oil and drops to flow throughout the device from a single inlet and outlet, respectively. The oil inlet channel (Fig. 1a, i, blue) and drop outlet channel (Fig. 1a, i, yellow) are connected to the rest of the device through a total of nine via holes punched in the middle layer (Fig. 1a, ii), five for oil distribution and four for drop collection, providing a pathway for fluids from the top layer through to the bottom layer (Fig. 1a, dashed black lines). The middle layer contains oil distribution and drop collection

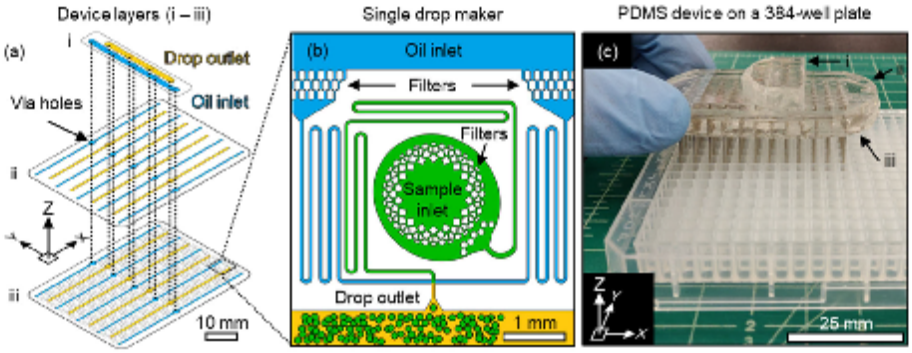

Fig. 1 PIPE chip design and assembly. (a) The PIPE chip was assembled from three layers: (i) a top layer containing oil distribution (blue) and drop collection (yellow) channels connected to a single inlet and outlet, respectively; (ii) a middle layer which reduces fluidic resistance by providing additional height to the oil and drop collection distribution channels on the bottom layer; and (iii) a bottom layer which contains an array of 96 drop makers (eight rows of twelve drop makers) with channels for oil distribution (five rows, blue) and drop collection (four rows, yellow). (b) Detailed view of one of the 96 drop makers positioned on the bottom layer. Colors are used to distinguish oil inlet (blue), aqueous sample inlet (green), and drop outlet (yellow) channels. (c) Image of a completed device interfaced with i of a 384-well plate. Each layer (i–iii) of the fully assembled device from part (a) is indicated using black arrows. Stainless steel sample inlet capillary tubes are visible extending into the microtiter plate wells below.

channels that pass the oil phase to the drop makers and collect produced drops. The bottom layer (Fig. 1a, iii) contains 96 drop makers (Fig. 1b), each connected to oil distribution and drop collection channels. Drop maker inlet holes are spaced 4.5 mm apart to match the standard pitch of a 384-well microtiter plate, enabling the PIPE chip to interface directly to i of a 384-well microtiter plate.

PIPE chip fabrication

Each of the PDMS layers i–iii (Fig. 1a) was cast from a unique master mold and bonded following standard techniques in soft lithography (see ESI† PIPE chip fabrication for details).[22] Short lengths (22.5 mm) of SAE 304 stainless steel capillary tubes (0.71 mm OD, 0.41 mm ID, Vita Needle) were fitted into the sample inlet holes of the device to provide a path for fluids from each microtiter plate well to the sample inlet of each drop maker (Fig. 1b). For encapsulating barcoded samples, the device was manually positioned above i of a standard 384-well microtiter plate such that each of the stainless steel inlet capillaries nearly extended to the bottom of a different well (Fig. 1c).

Pressure chamber

The barcoded samples contained in the wells of the microtiter plate were simultaneously driven into each of the 96 drop makers of the PIPE chip under the uniform pressure within the sealed aluminum interior chamber of a 6-quart pressure cooker (Fig. 2a). Compressed air (approximately 60 psig) supplied both the oil reservoir pressure P_{oil} and chamber pressure P_{water}, both adjusted from 0–15 psig using manual regulators (McMaster-Carr 6745 K32 0–25 psi) and analog gauges (McMaster-Carr 3850 K2 0–15 psi). The oil reservoir was comprised of a pressure-rated glass bottle (Sigma Duran Z674397) and a cap fitted with ports for compressed air and oil inlet tubing. Custom-drilled ports in the pressure chamber allowed the passage of oil inlet tubing and drop outlet tubing (Fig. 2a, side view). The ports were sealed with silicone sealant (DAP Kwik Seal Plus). A viewport was created using a 1.5 mm-thick transparent polycarbonate sheet that was affixed and sealed to a fabricated opening in the pressure chamber lid, allowing device operation to be monitored or recorded (Fig. 2a, top view). A strip of white LEDs (Ledmo SMD 2835) was mounted to the inside of the chamber to provide illumination.

Drop encapsulation

Barcoded samples were pipetted into individual wells of a 384-well microtiter plate and then placed into the pressure chamber apparatus. The PIPE chip was connected to the oil inlet and drop outlet tubing and positioned with the inlet capillaries extending into the wells of the microtiter plate containing barcoded samples (Fig. 2b). An oil reservoir was pressurized by house air and was regulated at pressure P_{oil} to control the oil flowrate. The oil reservoir contained Novec 7500 fluorinated oil (3 M) with 1.5% w/w of a Krytox-PEG surfactant that was synthesized in-house following a previously published protocol incorporating Jeffamine ED900 (Huntsman) as the hydrophilic portion of the PTFE–PEG–PTFE triblock perfluorosurfactant.[28] The water flowrate was controlled by a second regulator which adjusted P_{water} within the chamber, driving barcoded samples from each microtiter plate well into the PIPE chip to be encapsulated into drops. Barcoded drops were passed through the wall of the pressure chamber before reaching a collection tube to form a library of

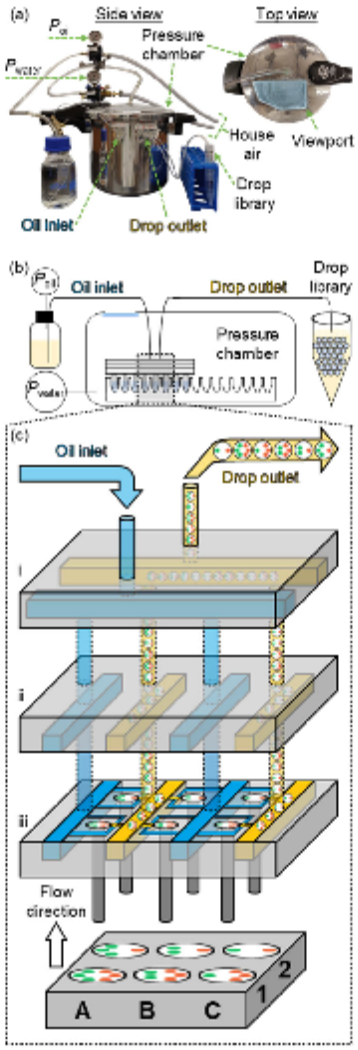

Fig. 2 PIPE chip operation and barcoded drop library production. (a) Side view and top view profiles of the PIPE chip apparatus and components. (b) PIPE chip operation schematic for the encapsulation of 96 wells from a 384-well microtiter plate. Pressure P_{oil} is applied to an external oil reservoir to provide oil to the device within the pressure chamber while a second pressure P_{water} applied to the chamber pushes fluid from sample wells into the microfluidic device. Barcoded drops travel through tubing past a sealed opening in the wall of the chamber for collection in a drop library. (c) Detailed schematic of the internal channels and flows within the PIPE chip. Samples in wells (indexed A-C and 1-2) barcoded with different concentrations of green and red microbeads are encapsulated in layer (iii), collected in large drop channels (yellow) formed from both layers (ii) and (iii) where they are transported to perpendicular drop collection channels in layer (i). The barcoded drops flow out of the device in a shared drop outlet.

drops, each indexed to a unique sample well. Drop collection continued for 2–3 min, or until air bubbles were observed in the outlet tubing, indicating sample wells were empty.

A detailed schematic summarizes barcoded drop encapsulation within the PIPE chip where barcoding is represented by a unique combination of green and red fluorescent microbead concentrations in each well (Fig. 2c). The encapsulation process is the same when quantum dots are used. Pressurization of the chamber pushes the fluid from these wells into the bottom PIPE chip layer (Fig. 2c, iii) where drops are formed at individual drop makers. The drops are then collected in shared drop outlet channels formed from the union of channels in the middle and bottom layer (Fig. 2c, ii and iii, yellow). These shared channels are connected to a perpendicular collection channel on the top layer (Fig. 2c, i) through via holes where drops subsequently flow and are collected in a common drop outlet. The flow of oil is the reverse of the flow of drops; a common oil inlet is distributed in the top layer (Fig. 2c, i) to perpendicular channels (Fig. 2c, ii and iii, blue) through via holes until oil reaches the drop makers (Fig. 2c, iii).

Drop size measurements

To characterize drop formation, the PIPE chip was placed on a petri dish filled with 10 mL of sterile-filtered deionized water (0.2 μm filter) within the pressure chamber and the oil reservoir was filled with 100 mL of Novec 7500 (3 M) oil with surfactant[2,8] added at 1.5% w/w. Drops were collected across a range of water P_{water} and oil P_{oil} inlet pressure combinations (2–3, 2–6, 2–12, 4–3, 6–3, 6–6, 6–12, 8–9, and 8–12 psig, where combinations are denoted as $P_{water} - P_{oil}$). Approximately 10 μL of drops were placed on an 8-well Teflon printed slide (Electron Microscopy Sciences, Cat. #63422-06) and imaged under an inverted brightfield microscope (Nikon TE2000). The height of the Teflon well was larger than the drop diameter, as drops regularly formed a bilayer during imaging. A custom image processing script in MATLAB (R2019a) was used to measure drop diameter D_{drop}. To convert the water and oil pressure ratios P_{water}/P_{oil} to volumetric flowrate ratios Q_{water}/Q_{oil}, we measured the volumes V of the oil and water phases after t = 0.5–2.5 min of collection for each water and oil pressure condition. In this case, surfactant was not added to the oil phase to allow for drop coalescence and phase separation of oil and water. The volumetric flowrates of each phase were calculated using $Q_i = \frac{V}{t}$ and plotted as Q_{water}/Q_{oil} as a function of P_{water}/P_{oil} (Fig. S1†).

Real-time drop formation within the PIPE chip was visualized through the viewport on the pressure cooker using a high-speed camera (Phantom VEO 710 L, Vision Research) attached to a tube lens (Model CFM, ISCO-OPTIC) mounted with a 10× objective (NA 0.25). The underside of the PIPE chip was illuminated by a liquid light guide routed through the side of the pressure cooker and attached to an LED light source (SugarCUBE, Ushio America).

Fluorescent microbead barcodes

Microbead barcodes consisted of unique two-color combinations of approximately 1 μm diameter green and red microbeads (Thermo Scientific Fluoro-Max G0100 ex. 468/em. 508 nm and R0100 ex. 542/em. 612 nm). Green and red microbead (stock of 1% solids, approximately 2.5×10^7 microbeads per μL) barcode labels were made from five dilutions in water (5.1×10^5, 1.3×10^6, 2.3×10^6, 3.6×10^6, 5.1×10^6 beads per μL). The five dilutions of each microbead color were mixed equally in a combinatorial manner to create a total of 24 barcode labels. The concentration combinations are detailed in Table S1.† Four concentrations of blue microbeads (Thermo Scientific Fluoro-Max B0100 ex. 412/em. 473 nm, 5.1×10^5, 1.3×10^6, 2.3×10^6, 3.6×10^6 microbeads per μL from a stock of 1% solids, approximately 2.5×10^7 microbeads per μL) were randomly spread across 24 microbead-barcoded wells and used as a mock assay signal. For microbead barcoded drop experiments, the oil pressure was set to 3 psig (P_{oil}) and the chamber pressure was set to 2 psig (P_{water}). For the purpose of collecting 24 samples instead of 96, a modification to the PIPE chip was made to allow drop outlet tubing to be directly connected to the drop collection channels of the second layer of the device. This modification provided separate collection from each quadrant of drop makers on the device where each quadrant is comprised of 24 drop makers. A confocal image of the microbead barcoded drops captured in a drop array device[29] is shown in Fig. S2.† The drop library was collected and re-injected into a secondary device for use with a custom drop fluorescence detection system (see ESI† Barcoded drop detection and Fig. S3 and S4 for details).[22] The photomultiplier tube (PMT) gain control voltage was set to 0.32 V for microbead barcoded drop detection.

Quantum dot barcodes

QDs of two colors (Thermo Scientific QD625 and QD705) were used as barcode labels by preparing 12 QD625 (1.15×10^4, 9.68×10^3, 8.00×10^3, 6.48×10^3, 5.12×10^3, 3.92×10^3, 2.88×10^3, 2.00×10^3, 1.28×10^3, 7.20×10^2, 3.20×10^2, 8.00×10^1 pM) and 16 QD705 (1.02×10^4, 9.00×10^3, 7.84×10^3, 6.76×10^3, 5.76×10^3, 4.84×10^3, 4.00×10^3, 3.24×10^3, 2.56×3, 1.96×10^3, 1.44×10^3, 1.00×10^3, 6.40×10^2, 3.60×10^2, 1.60×10^2, 4.00×10^1 pM) dilutions in 10 mM sodium borate buffer pH 9 containing 0.5 mg mL^{-1} bovine serum albumin (BSA). The 12 and 16 dilutions were mixed equally in a combinatorial manner to create a total of 192 barcode labels. The concentration combinations are detailed in Table S2.† For drops containing QD barcodes, the oil pressure (P_{oil}) was set to 8 psig while the chamber pressure (P_{water}) was set to 5 psig. The PIPE chip was operated twice to create 192 barcodes (96 × 2). The PMT control voltage was set to 0.45 V for QD barcoded drop detection.

Two-channel fluorescence-activated drop sorting

Barcoded drops were injected into a microfluidic drop sorting device[22] at a flowrate of 40 μL h^{-1} and spacer oil (Novec 7500) without surfactant was injected at a flowrate of 800 μL h^{-1}. A sorting electrode driven by a high voltage amplifier (Trek Model 2220-CE) and controlled by a custom LabVIEW program was used to pull drops into a collection channel. The sorting electrode provided a 400 μs pulse of a 25 kHz, 400 V square wave signal when the drop fluorescence signal fell within the threshold values set for a specific barcode (1–1.2 V green channel, 0.15–0.25 V red channel).

Results and discussion

Drop formation characterization

Drops were generated with the PIPE chip under a range of pressures for P_{water} and P_{oil} to identify combinations that produce uniformly-sized drops. We measured D_{drop} and its distribution, as quantified by the coefficient of variation (CV) of D_{drop}, at each pressure combination (Fig. 3a). To observe drop formation across the range of pressures tested, high speed videos of drop formation in the PIPE chip were captured at four extreme water and oil pressure combinations. The four combinations are labeled with corresponding symbols in Fig. 3a–c: high water pressure (■, P_{water} = 6 psig and P_{oil} = 3 psig), low combined pressure (▼, P_{water} = 2 psig and P_{oil} = 3 psig), high combined pressure (▲, P_{water} = 8 psig and P_{oil} = 12 psig) and high oil pressure (♦, P_{water} = 2 psig and P_{oil} = 12 psig). Representative images of Videos S1a–d† are presented in Fig. 3b. At high water pressure (■), the greater water volume fraction led to each drop filling the full length of the exit channel and partially extending into the collection channel before drop break-up occurred, a phenomenon not seen with the other three combinations. As drop formation is no longer fully constrained by the flow focusing junction, this extension of the drop into the collection channel may explain the greater polydispersity at this condition, where D_{drop} = 83.9 ± 12.5 μm. At low and high combined pressure conditions (▼, ▲, both at P_{water}/P_{oil} = 0.67), drop formation occurred within the exit channel, creating smaller, more uniform drops at the high pressure condition (▲, D_{drop} = 56.2 ± 2.6 μm) than the low pressure condition (▼, D_{drop} = 68.8 ± 5.0 μm). Drop uniformity did not improve with a higher oil volume fraction (♦, CV = 6.0%) when compared to the high combined pressure condition (▲, CV = 4.6%). As the oil volume fraction was increased, drop formation was limited by the 50 μm width of the exit channel, a characteristic of drop formation in the dripping regime.[30,31] The dripping regime forms highly uniform drops, whose diameters are largely determined by the flowrates and the width of the flow focusing junction.[30,32,33] For all the conditions observed, drop break-up occurred at the flow-focusing junction which indicates that drop formation was in the dripping regime.[30,32]

The size of drops formed in the dripping regime can be described by a drop scaling law,[34] thereby providing a predictive drop formation model for the PIPE chip. A drop scaling law[34] developed for T-junction geometries, and shown to be applicable for flow focusing geometries,[35] is fit to the data and defined as:

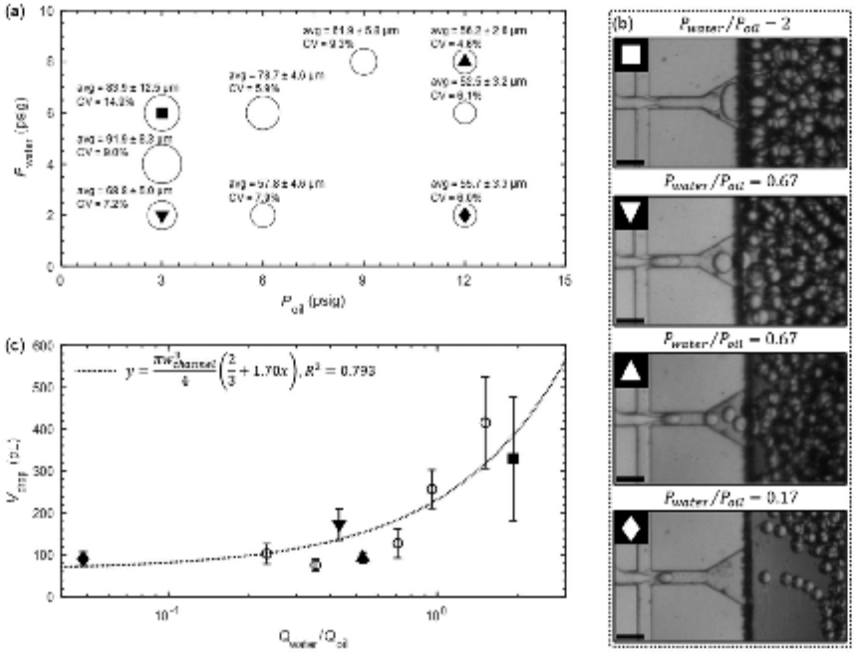

Fig. 3 Characterization of drop sizes produced by the PIPE chip. (a) Drop diameter average, standard deviation, and CV at various water pressures P_{water} and oil pressures P_{oil}. For additional visualization, the relative size of each open circle corresponds to the relative mean drop diameter measured. Solid shapes indicate conditions used for high-speed image capture in (b). (b) High-speed image capture of drop formation, ordered by descending D_{drop} for high water pressure (■, P_{water} = 6 psig and P_{oil} = 3 psig, P_{water}/P_{oil} = 2), low combined pressure (▼, P_{water} = 2 psig and P_{oil} = 3 psig, P_{water}/P_{oil} = 0.67), high combined pressure (▲, P_{water} = 8 and P_{oil} = 12 psig, P_{water}/P_{oil} = 0.67), and high oil pressure (♦, P_{water} = 2 psig and P_{oil} = 12 psig, P_{water}/P_{oil} = 0.17) conditions. Scale bars = 100 μm. (c) Corresponding drop volumes V_{drop} versus the volumetric flowrate ratio Q_{water}/Q_{oil} (open circles or solid shapes). V_{drop} scales with Q_{water}/Q_{oil} following a drop scaling law (dotted black line).[34] Error bars represent one standard deviation from the mean.

$$\frac{L_{drop}}{w_{channel}} = 1 + \alpha\frac{Q_{water}}{Q_{oil}} \quad (1)$$

where L_{drop} is defined as the length of a drop in the channel measured end to end, $w_{channel}$ is the width of the channel (50 μm), Q_{water}/Q_{oil} is the volumetric flowrate ratio, and α is a geometric constant of order 1. To apply the scaling law to our data, pressure ratios are converted to flowrate ratios using a standard curve (Fig. S1†). We converted L_{drop} from eqn (1) to drop volume V_{drop} by approximating the shape of the drop as a capsule geometry when drops are elongated within the microfluidic channel (see ESI† PIPE chip drop formation characterization for details). The best fit of the drop scaling law with V_{drop} plotted as a function of Q_{water}/Q_{oil} is presented as a dotted line in Fig. 3c with α = 1.70 and an R^2 = 0.793.[34] Drops produced using the PIPE chip can be adjusted by tuning the pressures applied to the oil and aqueous phases, thereby adjusting Q_{water}/Q_{oil} and enabling the generation of drops within a desired range of diameters (≈50–90 μm).

Drop size distribution improved from a CV of 14.9% to 4.6% as Q_{water}/Q_{oil} was decreased from 2 to 0.17 (Fig. 3c). When $Q_{water}/Q_{oil} < 1$, further reductions in Q_{water}/Q_{oil} have diminishing effects on V_{drop}. In this case, the minimum drop volume (65 pL, correlating to D_{drop} = 50 μm) is reached as $Q_{water}/Q_{oil} \to 0$ due to the 50 μm width of the drop channel ($L_{drop} \approx w_{channel}$ according to eqn (1)). Interestingly, despite the low and high combined pressure conditions having the same pressure ratio and similar measured flowrate ratios (Q_{water}/Q_{oil} = 0.43 or 0.53, respectively), they produced drops with different V_{drop}, from 173 ± 37 pL to 94 ± 13 pL. The difference in V_{drop} for similar Q_{water}/Q_{oil} at higher oil flowrates may be attributed to an increased oil phase capillary number Ca which represents the ratio of the viscous drag to surface tension forces acting on a drop. A higher oil phase Ca corresponds to increased drag at the drop formation junction which leads to faster break-up, resulting in a decreased V_{drop}.[34,35]

Optimizing barcode discrimination in drop libraries

Drop libraries barcoded with fluorescence-based barcodes have recently reached a label count of 1050 unique combinations with the use of four dye colors.[4] Lanthanide nanophosphors

are capable of creating up to 1023 unique labels with a six-color combination, but have yet to be used in drop libraries.[36] However, using a large number of barcode colors may not be advantageous, as the overlap of emission spectra between the fluorescent reporters can limit the practical number of colors that can be used in an assay.[37,38] Simply reducing the number of barcode colors to one or two and varying their concentrations can greatly expand the range of usable reporters. Thus, the PIPE chip was used to generate two fluorescently barcoded drop libraries from two-color combinations of either microbeads or QDs. Fluorescent particles were used to prevent diffusion of the barcode labels between drops.[23] The libraries were prepared by mixing different ratios of each color to form distinct combinations on a microtiter plate (see Materials and methods). The polystyrene microbead drop library was comprised of 24 barcodes made from ratios of green and red fluorescent polystyrene microbeads while the QD drop library was comprised of 192 barcodes made from ratios of QDs with peak emissions at 625 and 705 nm. The PIPE chip was used to simultaneously encapsulate all the barcoded contents of the plate in 2 min, creating approximately 3.75×10^5 drops (D_{drop} = 50 μm) per barcode. Barcoded drops were reinjected into a microfluidic device for analysis using a laser-induced fluorescence detection system.[23] Drop fluorescence was measured as the drops flowed past a laser at approximately 300 Hz.

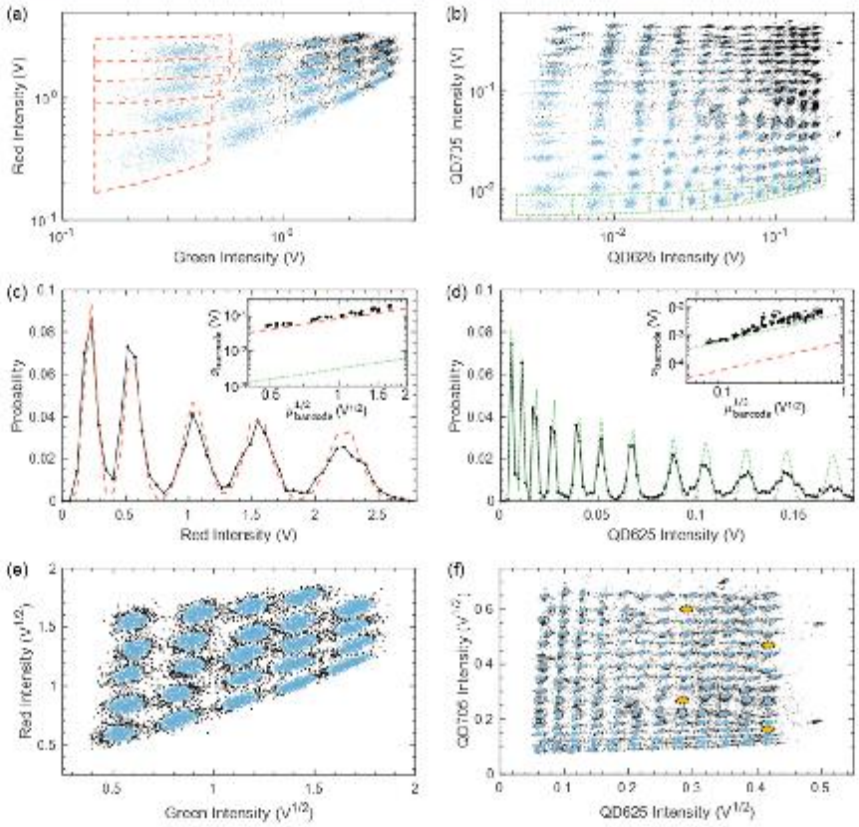

Fig. 4 Analysis of microbead and QD barcoded drop libraries. Scatter plots of (a) microbead and (b) QD fluorescence intensity in the drop library. Clusters identified by DBSCAN are indicated in blue while noise is in black. Probability distributions of (c) five red microbead barcoded drop populations (black dots) plotted against the particle loading noise estimate (dashed red line, R^2 = 0.931) and (d) twelve QD625 barcoded drop populations (black dots) plotted against the shot noise estimate (dotted green line, R^2 = 0.852). Solid black lines guide the eye for the measured microbead and QD625 data. Inset (c and d): standard deviations of each barcode $\sigma_{barcode}$ (black dots) plotted against $\mu_{barcode}^{1/2}$ with estimates for $\sigma_{particle}$ (dashed red line) and σ_{shot} (dotted green line). Scatter plots of (e) microbead and (f) QD drop library data scaled by $V^{1/2}$. Clusters identified by DBSCAN are indicated in blue while noise is in black. Missing clusters in (f) are due to two clogged channels in the PIPE chip and are indicated by dotted yellow ovals.

Contributions from spectral crosstalk and sources of noise limit the number of barcodes that can be identified after library reinjection. The narrow emission spectra of QDs leads to less spectral crosstalk between each barcoding color compared to the microbeads. This can be observed in the raw data of the 24 microbead fluorescence intensities (Fig. 4a) compared to the 192 QD fluorescence intensities (Fig. 4b). Due to the wide emission spectra of the microbeads, the emission of the green microbeads overlaps with the red microbeads. This causes barcodes with high green intensity to appear more red, skewing the data to the upper right (Fig. 4a). The effect of spectral crosstalk also skews the QD data (Fig. 4b), but due to the narrow emission spectra of the QDs, the effect is lower in magnitude compared to the microbeads.

We applied a clustering algorithm, Density-Based Spatial Clustering of Applications with Noise (DBSCAN), to identify and separate "clusters" of specific barcoded drops within the libraries.[24] Densely packed data points are assigned to clusters by DBSCAN while outlier data points in low-density regions are marked as noise. When the data are graphed on a linear plot, DBSCAN was able to group 70% of the 1.31×10^4 drops containing microbeads into 24 clusters (Fig. 4a, blue dots) and 30% as noise (Fig. 4a, black dots), with a mean of 399 ± 201 drops per barcode (CV = 50.4%). However, DBSCAN was not able to completely identify clusters in the QD raw data (Fig. 4b, blue dots). Of the clusters identified, DBSCAN grouped 76% of the 1.27×10^5 drops containing QDs with a range of 15 to 6033 drops per barcode (mean of 508 ± 478 drops and CV = 94.1%). A significant number of clusters were mislabeled as noise (Fig. 4b, upper right black dots) due to the large variability in cluster density.

To better understand the variability between barcode clusters, we identify two major sources of variation in our data, both a direct consequence of particle size: Poisson loading for microbeads and shot noise for QDs. The loading of approximately 1 μm diameter fluorescent microbeads into drops is dependent upon Poisson statistics. The fluorescence signal obtained from drops containing microbeads follows a Poisson distribution due to the discrete nature of particle loading in drops.[22] The Poisson distribution is described by the equation:

$$P = \frac{\lambda^k e^{-\lambda}}{k!} \quad (2)$$

where P is the probability distribution of drops that contain k number of particles with a mean number of particles per drop λ. Variability inherent to Poisson loading[22] is represented by the standard deviation of the number of particles in drops $\sigma_{particle} = \lambda^{1/2}$. We plot a representative subset of five red microbead barcodes (Fig. 4c, black dots) corresponding to the clusters in Fig. 4a (dashed red boxes). The subset is compared to estimated Poisson distributions centered around the microbead loading concentrations λ = 33, 83, 149, 232, and 333 beads/drop where λ is converted to voltage using an experimentally verified linear standard curve relating PMT output voltage to microbead concentration (beads/drop, λ) (Fig. S7a†). The probability of microbead distributions (Fig. 4c, dashed red line) closely tracks the PMT voltage measurements of the red microbead data (Fig. 4c, black dots) with $R^2 = 0.931$.

When the particle size is far below the objective resolution, for example in the case of QDs that are approximately 10 nm in diameter, the variability in drop fluorescence is no longer a function of the number of discrete particles in drops, but is instead governed by the shot noise of the PMT. Shot noise is inherent to counting photons with a PMT and contributes to the fluorescence signal in low light environments such as high-speed detection of drop fluorescence.[39,40] We plot the signal distributions of a 12 QD625 barcode subset of the QD barcoded library (Fig. 4d, black dots) corresponding to the clusters outlined in Fig. 4b (dashed green boxes). The Schottky equation approximates shot noise[40,41] in which the standard deviation of the PMT voltage σ_{shot} is proportional to the square root of the mean PMT voltage $\mu_{intensity}$ (see ESI† Schottky equation for details). The subset of QD data is compared to normal distributions defined by $\mu_{intensity}$ and σ_{shot} for each QD barcode. The value of $\mu_{intensity}$ is determined by an experimentally verified linear standard curve relating PMT output voltage to QD concentration (nM) (Fig. S7b, eqn (S1)†). The probability of QD distributions (Fig. 4d, dashed green line) closely tracks the PMT voltage measurements of the QD625 data (Fig. 4d, black dots) with $R^2 = 0.852$.

To demonstrate that the remainder of the experimental microbead and QD barcode data follow either Poisson loading or shot noise, barcode clusters are manually grouped and compared to theoretical estimates of $\sigma_{particle}$ (Fig. 4c and d, inset, dashed red line) and σ_{shot} (Fig. 4c and d, inset, dotted green line, see ESI† Calculation of noise for details). Drop library fluorescence data are manually grouped by drawing lines around each cluster by eye (Fig. S8†) to isolate individual barcode signal populations for each PMT channel. The mean $\mu_{barcode}$ and standard deviation $\sigma_{barcode}$ of the manually-segmented 24 microbead and 192 QD signal distributions are calculated for each PMT channel, yielding 48 and 384 values of $\mu_{barcode}$ and $\sigma_{barcode}$. The $\sigma_{barcode}$ is plotted against $\mu_{barcode}^{1/2}$ for each grouped microbead and QD barcode population (Fig. 4c and d, inset, black dots). The experimental $\sigma_{barcode}$ of the microbeads closely follows the theoretical estimate of particle loading noise $\sigma_{particle}$ (Fig. 4c, inset, dashed red line). The $\sigma_{barcode}$ is approximately an order of magnitude greater than the theoretical estimate of shot noise σ_{shot} (Fig. 4c, inset, dotted green line). Therefore, across all drops, the discrimination of microbead barcode signals is limited by particle loading noise as the dominant source of variation. By contrast, the experimental $\sigma_{barcode}$ of the QDs closely follows the theoretical estimate of shot noise σ_{shot} (Fig. 4d, inset, dotted green line) and is approximately an order of magnitude greater than the estimate of particle loading

noise $\sigma_{particle}$ (Fig. 4d, inset, dashed red line), indicating the data is shot noise-limited. The narrow emission spectrum of the QDs results in a 1–2 log decrease of σ_{shot} compared to $\sigma_{particle}$. This enables an 8× increase in unique barcode concentrations obtained with QDs compared to microbeads (192 *versus* 24).

As signal variation depends upon Poisson loading for microbeads ($\sigma_{particle} \propto \lambda^{1/2}$) and shot noise for QDs ($\sigma_{shot} \propto \mu^{1/2}$), scaling the intensity data for both barcode libraries by a square root function linearizes the noise. This scaling spaces each barcode grouping as shown in Fig. 4e and f (Fig. S5 and S6†). When DBSCAN is applied to the scaled data, the increased spacing allows for improved clustering of each barcode compared to the unscaled raw data (Fig. 4a and b). Of the 1.31×10^4 microbead barcoded drops detected, DBSCAN was able to group 74.8% of the data into 24 clusters (Fig. 4e, blue dots) and identify 25.2% as noise (Fig. 4e, black dots) with a mean of 408 ± 62 drops per barcode (CV = 15.2%). The CV of clustered square root scaled data is greatly reduced from 50.4% with the linearly scaled data (Fig. 4a) to 15.2% with the square root scaled data (Fig. 4e). Additionally, a square root scaling of the QD data allows DBSCAN to correctly identify 188 out of the 192 of barcoded drop populations where the missing four populations are due to two clogged drop makers on the PIPE chip and are indicated by the yellow ovals (Fig. 4f). Of the 1.27×10^5 QD barcoded drops detected, DBSCAN was able to group 85.4% of data into 188 clusters (Fig. 4f, blue dots) and identify 14.6% as noise (Fig. 4f, black dots) with a mean barcode cluster size of 576 ± 88 drops (CV = 15.3%). Once again, the CV is greatly reduced from 94.1% with the linearly-scaled quantum dot data to 15.5% with the square root-scaled data.

Previous examples of drop libraries using one or two fluorescence dye colors have realized up to eight[10] or sixteen[11] unique labels. Using the PIPE chip, we achieved a total of 188 discrete barcodes with two-color combinations of QDs. To our knowledge, this is the largest two-color fluorescent barcode combination in drops to date. Additionally, the effect of particle size on signal noise can be described empirically and used for future experiments to inform the selection of barcode concentrations.

Sample isolation using fluorescence-activated drop sorting

To demonstrate the utility of the PIPE chip, fluorescence-activated drop sorting[21,22] was performed to isolate drops of a single barcode population within a drop library of 24 green and red microbead combinations spiked with four concentrations of blue microbeads. We verify that the desired green and red barcode combination was isolated by detecting a single concentration of the blue microbeads. A barcode from the drop library was chosen by designating a box with upper and lower fluorescence intensity bounds in the green and red fluorescence channels (Fig. 5a, red box). Recovery of

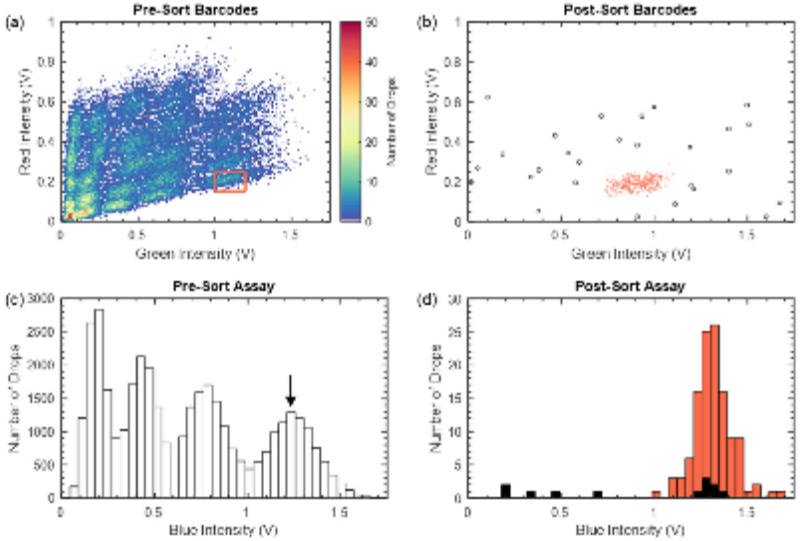

Fig. 5 Fluorescence-activated drop sorting of a microbead-barcoded drop library. (a) Fluorescence intensity of barcoded drops before sorting. The sorted region is indicated by the red box. (b) Fluorescence intensity of barcoded drops after sorting. DBSCAN is used to separate the outlier data points (open black circles) from the target barcode population (red dots). (c) Distribution of four concentrations of blue microbead drops within the drop library. (d) Distribution of blue microbeads in the sorted barcoded drop population shows a single peak corresponding to the largest concentration of blue microbeads. DBSCAN is used to separate the outliers (black bars) from the target sorted population (red bars).

the desired barcode population is confirmed by performing flow-based fluorescence detection on the sorted drops, yielding an isolated barcode cluster with intensity bounds close to those originally chosen in the green and red channels (Fig. 5b). However, there is an observed shift in fluorescence signal distribution from pre- to post-sort (Fig. 5a and b) where the post-sort data has shifted by ≈0.2 V along the *x*-axis. This shift is likely caused by run-to-run variation arising from the positioning of the laser in the device channel. Post-processing of the sorted drop data using DBSCAN provides a clear distinction between the target barcode population (Fig. 5b, red dots) and the outlier data points (Fig. 5b, open black circles). The outlier points comprise 7.5% of the drop data.

The four populations of blue microbead-barcoded drops were detected in the pre-sort drop library (Fig. 5c). Fluorescence detection of the sorted drops yielded a single blue microbead population with few outliers (Fig. 5d), matching the highest blue microbead concentration (Fig. 5c, arrow). DBSCAN clustering of corresponding green and red fluorescence identifies these outliers (Fig. 5d, black bars) and the target sorted population (Fig. 5d, red bars). The outliers comprise 5.9% of the sorted population, in close agreement with the data corresponding to the green and red barcoded drops (Fig. 5b). These results demonstrate the ability to isolate a single barcoded population from a drop library created using the PIPE chip, critical for performing downstream assays.

Conclusions

Here we have demonstrated tunable parallel production of 50 to 90 μm diameter drops containing upwards of 96 different loading conditions from a microtiter plate, improving upon the previously published limit of 24.[20] By scaling the signal noise with the square root of the intensity, barcoded drop libraries comprised of 24 microbead barcodes or 192 QD barcodes are distinguishable using DBSCAN.[24] Barcode number is ultimately limited by microbead or QD signal resolution. As a function of size, signal resolution between larger microbeads was limited by Poisson loading noise while the signals from the smaller QD barcodes were limited by shot noise. This empirical relationship found between signal noise and barcode concentration can be used to quickly prototype barcode label concentrations for future experiments. Utilizing two-color combinations of QDs, we achieved a total of 188 discrete barcodes, the largest two-color fluorescence barcode combination in drops published to date. The addition of a third QD color, offering up to 16 unique concentrations, would enable QDs to easily index multiple 384-well microtiter plates using as many as 3072 unique barcodes (12 × 16 × 16), far surpassing what has been achieved with four color combinations (1050 labels).[4] Furthermore, we have shown that barcoded populations can be selectively sorted with minimal error (5.9–7.5%), demonstrating that downstream analysis of a specific sample population is possible. By reducing sample encapsulation time and enabling rapid, parallel generation of a barcoded library directly from a microtiter plate, we envision that the PIPE chip will further advance multiplexed assaying in applications including combinatorial drug screening,[3,10] DNA microarray analysis,[11] or enzyme activity screening.[12]

Author contributions

G. K. Z., R. A. S., A. R. A., D. A. W. and C. B. C. designed research; G. K. Z., R. A. S., C. W. H., and R. A. performed research; G. K. Z. and R. A. S. analyzed data; and G. K. Z., R. A. S., C. W. H., D. A. B., and C. B. C. wrote the manuscript.

Conflicts of interest

There are no conflicts to declare.

Acknowledgements

This work was supported by Defense Advanced Research Projects Agency (DARPA) grant W911NF-17-2-0034, National Institutes of Health (NIH) 1R21AI151923, and National Science Foundation (NSF) CAREER DMR-1753352 (to C. B. C). The work at Harvard was supported in part by the NSF through the Harvard MRSEC (DMR-2011754 to D. A. W). We thank, Joshua Ricouvier, Stan Cotreau for help with machining, and Betsey Pitts for help with confocal imaging. R. A. S. gratefully acknowledges financial support from the German Research Foundation (DFG), grant SP 1282/1-1. G. K. Z. acknowledges financial support from Montana State University Office of the Provost.

References

1 J. J. Agresti, E. Antipov, A. R. Abate, K. Ahn, A. C. Rowat, J.-C. Baret, M. Marquez, A. M. Klibanov, A. D. Griffiths and D. A. Weitz, *Proc. Natl. Acad. Sci. U. S. A.*, 2010, **107**, 4004–4009.
2 M. T. Guo, A. Rotem, J. A. Heyman and D. A. Weitz, *Lab Chip*, 2012, **12**, 2146–2155.
3 A. Kulesa, J. Kehe, J. E. Hurtado, P. Tawde and P. C. Blainey, *Proc. Natl. Acad. Sci. U. S. A.*, 2018, **115**, 6685–6690.
4 C. M. Ackerman, C. Myhrvold, S. G. Thakku, C. A. Freije, H. C. Metsky, D. K. Yang, H. Y. Simon, C. K. Boehm, T.-S. F. Kosoko-Thoroddsen and J. J. N. Kehe, *Nature*, 2020, 1–6.
5 O. Scheler, K. Makuch, P. R. Debski, M. Horka, A. Ruszczak, N. Pacocha, K. Sozański, O.-P. Smolander, W. Postek and P. J. S. R. Garstecki, *Sci. Rep.*, 2020, **10**, 1–8.
6 A. M. Klein, L. Mazutis, I. Akartuna, N. Tallapragada, A. Veres, V. Li, L. Peshkin, D. A. Weitz and M. W. J. C. Kirschner, *Cell*, 2015, **161**, 1187–1201.
7 A. Rotem, O. Ram, N. Shoresh, R. A. Sperling, A. Goren, D. A. Weitz and B. E. Bernstein, *Nat. Biotechnol.*, 2015, **33**, 1165–1172.
8 A. Rotem, O. Ram, N. Shoresh, R. A. Sperling, M. Schnall-Levin, H. Zhang, A. Basu, B. E. Bernstein and D. A. Weitz, *PLoS One*, 2015, **10**, e0116328.

9 E. Z. Macosko, A. Basu, R. Satija, J. Nemesh, K. Shekhar, M. Goldman, I. Tirosh, A. R. Bialas, N. Kamitaki and E. M. Martersteck, *Cell*, 2015, **161**, 1202–1214.

10 E. Brouzes, M. Medkova, N. Savenelli, D. Marran, M. Twardowski, J. B. Hutchison, J. M. Rothberg, D. R. Link, N. Perrimon and M. L. Samuels, *Proc. Natl. Acad. Sci. U. S. A.*, 2009, **106**, 14195–14200.

11 A. R. Abate, T. Hung, R. A. Sperling, P. Mary, A. Rotem, J. J. Agresti, M. A. Weiner and D. A. Weitz, *Lab Chip*, 2013, **13**, 4864–4869.

12 C. H. Chen, M. A. Miller, A. Sarkar, M. T. Beste, K. B. Isaacson, D. A. Lauffenburger, L. G. Griffith and J. Han, *J. Am. Chem. Soc.*, 2013, **135**, 1645–1648.

13 J. Kehe, A. Kulesa, A. Ortiz, C. M. Ackerman, S. G. Thakku, D. Sellers, S. Kuehn, J. Gore, J. Friedman and P. C. Blainey, *Proc. Natl. Acad. Sci. U. S. A.*, 2019, **116**, 12804–12809.

14 O. J. Miller, A. El Harrak, T. Mangeat, J. C. Baret, L. Frenz, B. El Debs, E. Mayot, M. L. Samuels, E. K. Rooney, P. Dieu, M. Galvan, D. R. Link and A. D. Griffiths, *Proc. Natl. Acad. Sci. U. S. A.*, 2012, **109**, 378–383.

15 T. S. Kaminski, S. Jakiela, M. A. Czekalska, W. Postek and P. Garstecki, *Lab Chip*, 2012, **12**, 3995–4002.

16 T. D. Rane, H. C. Zec and T.-H. Wang, *J. Lab. Autom.*, 2012, **17**, 370–377.

17 J. Clausell-Tormos, A. D. Griffiths and C. A. Merten, *Lab Chip*, 2010, **10**, 1302–1307.

18 M.-P. N. Bui, C. A. Li, K. N. Han, J. Choo, E. K. Lee and G. H. Seong, *Anal. Chem.*, 2011, **83**, 1603–1608.

19 J. Lim, O. Caen, J. Vrignon, M. Konrad, V. Taly and J.-C. Baret, *Biomicrofluidics*, 2015, **9**, 034101.

20 L. A. Bawazer, C. S. McNally, C. J. Empson, W. J. Marchant, T. P. Comyn, X. Niu, S. Cho, M. J. McPherson, B. P. Binks, A. deMello and F. C. Meldrum, *Sci. Adv.*, 2016, **2**, e1600567.

21 J. C. Baret, O. J. Miller, V. Taly, M. Ryckelynck, A. El-Harrak, L. Frenz, C. Rick, M. L. Samuels, J. B. Hutchison, J. J. Agresti, D. R. Link, D. A. Weitz and A. D. Griffiths, *Lab Chip*, 2009, **9**, 1850–1858.

22 L. Mazutis, J. Gilbert, W. L. Ung, D. A. Weitz, A. D. Griffiths and J. A. Heyman, *Nat. Protoc.*, 2013, **8**, 870–891.

23 P. Gruner, B. Riechers, B. Semin, J. Lim, A. Johnston, K. Short and J.-C. Baret, *Nat. Commun.*, 2016, **7**, 1–9.

24 M. Ester, H.-P. Kriegel, J. Sander and X. Xu, *A density-based algorithm for discovering clusters in large spatial databases with noise*, Portland, OR, 1996.

25 S. W. Lim, T. M. Tran and A. R. Abate, *PLoS One*, 2015, **10**, e0113549.

26 H. Zhang, S. K. Cockrell, A. O. Kolawole, A. Rotem, A. W. Serohijos, C. B. Chang, Y. Tao, T. S. Mehoke, Y. Han and J. S. Lin, *J. Virol.*, 2015, **89**, 7722–7734.

27 Y. Tao, A. Rotem, H. Zhang, S. K. Cockrell, S. A. Koehler, C. B. Chang, L. W. Ung, P. G. Cantalupo, Y. Ren and J. S. J. C. Lin, *ChemBioChem*, 2015, **16**, 2167–2171.

28 C. Holtze, A. C. Rowat, J. J. Agresti, J. B. Hutchison, F. E. Angile, C. H. Schmitz, S. Koster, H. Duan, K. J. Humphry, R. A. Scanga, J. S. Johnson, D. Pisignano and D. A. Weitz, *Lab Chip*, 2008, **8**, 1632–1639.

29 C. H. Schmitz, A. C. Rowat, S. Köster and D. A. Weitz, *Lab Chip*, 2009, **9**, 44–49.

30 T. Cubaud and T. G. Mason, *Phys. Fluids*, 2008, **20**, 053302.

31 J. D. Tice, A. D. Lyon and R. F. Ismagilov, *Anal. Chim. Acta*, 2004, **507**, 73–77.

32 D. Funfschilling, H. Debas, H.-Z. Li and T. Mason, *Phys. Rev. E: Stat., Nonlinear, Soft Matter Phys.*, 2009, **80**, 015301.

33 P. Garstecki, H. A. Stone and G. M. Whitesides, *Phys. Rev. Lett.*, 2005, **94**, 164501.

34 P. Garstecki, M. J. Fuerstman, H. A. Stone and G. M. Whitesides, *Lab Chip*, 2006, **6**, 437–446.

35 A. Abate, A. Poitzsch, Y. Hwang, J. Lee, J. Czerwinska and D. Weitz, *Phys. Rev. E: Stat., Nonlinear, Soft Matter Phys.*, 2009, **80**, 026310.

36 H. Q. Nguyen, B. C. Baxter, K. Brower, C. A. Diaz-Botia, J. L. DeRisi, P. M. Fordyce and K. S. Thorn, *Adv. Opt. Mater.*, 2017, **5**, 1600548.

37 M. Han, X. Gao, J. Z. Su and S. Nie, *Nat. Biotechnol.*, 2001, **19**, 631.

38 H. Lee, J. Kim, H. Kim, J. Kim and S. Kwon, *Nat. Mater.*, 2010, **9**, 745–749.

39 A. Huebner, M. Srisa-Art, D. Holt, C. Abell, F. Hollfelder, A. Demello and J. J. C. C. Edel, *Chem. Commun.*, 2007, 1218–1220.

40 R. L. McClain and J. C. Wright, *J. Chem. Educ.*, 2014, **91**, 1455–1457.

41 W. Schottky, *Ann. Phys.*, 1918, **362**, 541–567.

CHAPTER FIVE

AUTOMATED, MULTIPLEXED ANTIMICROBIAL SUSCEPTIBILITY TESTING AND QUANTITATIVE HETERORESISTANCE DETERMINATION IN MICROFLUIDIC DROPLETS

Contribution of Authors and Co-Authors

Manuscript in Chapter 5

Author: Carter W. Hoffman

Contributions: C. W. H. designed research, performed research, analyzed data, and wrote the manuscript

Co-Author: Evan Martin

Contributions: E. M. performed research

Co-Author: Kerry S. Williamson

Contributions: K. S. W. designed research, performed research, analyzed data, and wrote the manuscript

Co-Author: Michael J. Franklin

Contributions: M. J. F. designed research and wrote the manuscript

Co-Author: Connie B. Chang

Contributions: C. B. C. designed research and wrote the manuscript

Manuscript Information

Carter W. Hoffman, Kerry S. Williamson, Evan Martin, Michael J. Franklin, Connie B. Chang

Status of Manuscript:

☒ Prepared for submission to a peer-reviewed journal

☐ Officially submitted to a peer-reviewed journal

☐ Accepted by a peer-reviewed journal

☐ Published in a peer-reviewed journal

Abstract

Antibiotic resistant bacteria have emerged as a critical and growing challenge for public health systems, responsible for millions of infections and tens of thousands of deaths annually in the US alone. In clinics, susceptibility profiles of offending microbes are assessed using techniques such as broth dilution. These standardized techniques are invaluable to clinicians and society, however, suffer from long time-to-assay on the order of 18-72 hours, and fail to detect phenotypic heterogeneities present within an infection. These shortcomings have resulted in rampant misuse of antibiotics, compounding antimicrobial resistance (AMR)- related problems. As such, there is an urgent need of novel techniques to rapidly assess microbial antibiotic response with single-cell resolution. Among recent innovations, drop-based microfluidics (DBMF) has been used for ultrahigh-throughput examination of single-cell growth responses to antibiotics. However, current microfluidics techniques are hindered by experimental complexity, and limited ability to assay whole panels of antimicrobials in parallel, a necessary feature of AST. In this work, we present a droplet-based AST platform that addresses these challenges. To solve the issue of multiplexing, we use a plate-interfacing, parallel encapsulation chip (PIPE chip) which emulsifies an entire panel of antimicrobials from a well plate, into a multiplexed library of single-celled droplets. The droplets are spectrally barcoded to enable parallel analysis of the droplet library. Droplet barcodes encoding experimental conditions, as well as droplet growth values, are recorded coincidentally at kHz rates on a flow-based, laser-induced fluorescence (LIF) assay readout module. We demonstrate our platform by monitoring the growth response of single *E. coli* cells in droplets against a panel of 36 antibiotic conditions, comprising 6 antibiotics of varying class. In a single 8-hour working day we collect ~150,000 single-cell growth readings, and output quantitative metrics

of population susceptibility and phenotypic heterogeneity in response to each of the 6 antibiotics. One of the major challenges in widescale heteroresistance and AMR surveillance is a technique which can rapidly assay many thousands of single cell replicates, against a multiplexed panel of antimicrobials; our platform represents an example solution to this challenge.

Introduction

Antibiotic resistant bacteria are an immediate threat to global health [139, 140]. The US Centers for Disease Control and Prevention (CDC) reports approximately 3 million infections caused by antibiotic resistant bacteria annually in the US, resulting in over 48,000 deaths; this death toll is predicted to rise to 10 million annually by 2050 [141]. In clinical settings, antimicrobial susceptibility testing (AST) is conducted by monitoring changes in optical density (OD) of a bacterial colony in response to antibiotics, using techniques including broth dilution, agar dilution, and disk diffusion [14, 139]. Importantly, these techniques output the minimum inhibitory concentration (MIC) of antimicrobial required to prevent growth, which has become the standard in communicating the susceptibility level of an isolate. These techniques suffer from long assay time on the order of 18-72 hours, which can produce negative effects on patient outcomes by delaying effective, patient-tailored care. Before susceptibility results are available, clinicians apply broad-spectrum antibiotics which can exacerbate antimicrobial resistance (AMR)-related problems by selecting for resistant strains.

Standard AST techniques are population-level analyses which fail to capture phenotypic heterogeneities present at the single-cell level [142, 143]. Bacterial phenotypic heterogeneity has become a subject of increasing interest within the field of AST as it is implicated in the spread of AMR and poor antibiotic therapy outcomes [23-30]. Resistant subgroups can evade eradication by

antibiotics resulting in chronic, recurrent infections, and contributing to AMR. The presence of a resistant subgroup within a population of presumed isogenic, susceptible bacteria has been termed heteroresistance, and this phenotype has been documented in a variety of medically relevant pathogens [31-34]. The reference standard assay for detecting heteroresistance is population analysis profiling (PAP), which involves interrogation of the isolate by serial 2-fold dilutions of antimicrobial [35-37]. However, PAP is extremely labor- and time-intensive compared to standard broth dilution, as it relies on counting colonies on agar plates, rather than multiplexing antibiotic dilution series using microtiter plates. Curiously, despite the concern over heteroresistance-related clinical complications, the relationship between heteroresistance and clinical outcome remains a matter of some debate [32, 34, 38]. The absence of a routine heteroresistance testing procedure has led to limited data on heteroresistance in the literature. Moreover, inconsistent definitions for heteroresistance have led to susceptibility misclassifications and confusion. The technological shortcomings of standard AST and heteroresistance assaying techniques have resulted in repeated misuse of antibiotics in society. As such, there is an urgent need for rapid, precise AST techniques which can also assay heteroresistance.

Recently, AST techniques based on single-cell analysis have shown promise in advancing AST capabilities [43-46, 50, 99]. Interrogation of single cells enables sensitive detection of early bacterial divisions and expedited AST results, as well as description of cell-cell heterogeneities. Among many recent technological advances, drop-based microfluidics (DBMF) has emerged as a powerful tool for characterizing bacterial response to antibiotics with single-cell resolution [50, 70-74, 77, 81, 83-85, 89, 91-93, 144]. In DBMF, biological samples are compartmentalized into micron-scale water-in-oil emulsions, enabling ultrahigh-throughput analysis of single cells. This

feature of DBMF has enabled the analysis of thousands of single cells within a population, enabling the description of phenotypic heterogeneities. However, infrastructure for multiplexed droplet experiments is poor. This is a specific concern for microfluidic AST, as AST platforms must test entire panels of antibiotic dilution series in parallel to output a MIC and deduce a best therapy route over a reasonable timeframe. Several reports have achieved parallelized testing of antimicrobials in microfluidic droplets, though only by way of complicated device and experimental designs, which prohibit proliferation of the techniques [80]. So far, the greatest degree of multiplexing has been achieved by serial emulsification of individual experimental conditions [76, 81, 83, 91]. Computer-controlled, valve-operated sample mixing modules in microfluidic chips, and so-called "cascaded" device designs have automated some of these steps. However, in these platforms the problem of multiplexing is solved by introducing complicated device and/or experimental designs, which could impede their widespread use by untrained personnel. Kim *et al*. reported a method of parallel emulsification of an antibiotic dilution series, though it could only generate 8 droplet populations at once, and relied on mixing fixed cell and antibiotic inputs in varying proportions, and could thus be introducing inoculum effects [78].

To avoid multiple-cell-encapsulation events, single-cell bioassays are typically conducted in droplets by encapsulating cells at approximately 10-20% rate. This loading process is governed by Poisson statistics, and produces droplet samples of mostly abiotic droplets, so that the biotic fraction of droplets are primarily single-celled [146]. This can present a problem during data analysis if the delineation between biotic and abiotic data is unclear. In many droplet AST platforms, only vigorous-growth droplets are detectable, and abiotic droplets are classified together with single- and few-celled droplets [83, 89, 91, 92]. In other cases, a biotic droplet is identified

by the fluorescent signal of a metabolism indicator such as resazurin, and all such droplets are classified together as growth droplets [74, 81, 84, 85]. These assay schemas constitute digital assays in which droplets are binned binarily as positives (1's) or negatives (0's), and the readout is an enumeration of the positive droplets. The utility of digital AST platforms comes from the quantification of the viable fraction within the analyzed sample, but information regarding cell-cell growth heterogeneity is generally lost. By contrast, growth of individual bacterial cells has been shown to be a stochastic process, where single seeded cells grow dynamically along a path from 0 to 1 [147, 148]. To reduce a droplet AST assay to digital is to ignore these growth dynamics entirely. Lu *et al*. demonstrated an automated approach to counting fluorescent cells in flowing microfluidic droplets, but it relied on acquiring a fluorescent image of the droplets concurrent with droplet fluorescence detection, and was not used to assay growth [146]. Kim *et al*. used their platform to detect heterogeneous growth in response to antibiotics in droplets [78]. However, it relied on an image analysis pipeline, and their method only allowed for ternary binning of growth readings as growth, non-growth or intermediate.

Here, we present a droplet-based approach to AST and heteroresistance assaying which achieves multiplexing with facile techniques and devices, and automatically detects single cells in droplets, enabling high-resolution description of growth values. This work was driven by our hypotheses that (1) a microfluidics chip which directly emulsifies biological samples arranged in a microtiter plate could facilitate multiplexed droplet susceptibility testing, (2) that signal detection from microfluidic droplets could be optimized to detect single cells and (3) these technological advances could be combined into an integrated platform, enabling high-resolution measurements of single-bacterial-cell growth responses against a multiplexed panel of drugs, at ultrahigh-

throughput. We use our previously reported plate-interfacing, parallel encapsulation chip (PIPE chip) to rapidly emulsify antibiotic dilution series from a well plate, into a multiplexed library of droplets [137]. We implement a spectral barcoding method [64, 75, 83] to encode the experimental condition of each droplet, allowing parallel analysis of the entire droplet library. Biotic droplets, even single-celled droplets, are identified from mixed datasets programmatically, allowing high-resolution description of heterogeneous growth response and growth processes in droplets. Droplet signals are detected in an automated, flow-based data collection module, which relies detection of photonic signals from droplets, rather than image analysis pipelines. Thus, the only manual operations are the pipetting of reagents into the microtiter plate for emulsion preparation, and injection of the droplet library into the data collection module. In this work, we generate AST results after a 5-hour sample incubation, though our results suggest that as little as 1 hour will be sufficient in the future. We demonstrate our platform by monitoring the growth response of single *E. coli* cells in droplets against a panel of 36 antibiotic conditions, comprising 6 antibiotics of varying class. In a single 8-hour working day we collect ~150,000 single-cell growth readings, conduct AST and calculate MIC values for each of the 6 antibiotics, and output quantitative metrics of heteroresistance. One of the major challenges in widescale heteroresistance and AMR surveillance is a technique which can rapidly assay many thousands of single cell replicates, against a multiplexed panel of antimicrobials. Our platform represents an example solution to this challenge, and will facilitate high-resolution characterization of heterogeneous bacterial responses to antimicrobials.

Materials & Methods

Microfluidic chip fabrication.

Microfluidic devices were cast in polydimethylsiloxane (PDMS) mixed 10:1 with curing agent. Microfluidic molds were fabricated using standard techniques in soft lithography [51, 121]. Cured PDMS slabs were plasma bonded in a Harrick PDC-001 plasma cleaner with O_2 plasma at $P_{operating}$ = 500 mtorr. The PIPE chip is composed of 3 unique PDMS layers bound together as previously reported [137]. The chip used for droplet detection was based on the design by Sciambi et al. [119], and was fabricated by plasma bonding to a glass microscope slide. All microfluidic devices were functionalized by flowing 1% vol/vol trimethoxy(1*H*,1*H*,2*H*,2*H*-tridecafluoro-*n*-octyl)silane (CAS 85857-16-5, Tokyo Chemical Industry) dissolved in Novec HFE 7500 through the channels of the device by manual pushing through a syringe. The silane mixture was allowed to react at room temperature for 30 minutes before evaporation in a 65^{o}C oven.

Cell culture.

The night before experimentation, *E. coli* HB101(pMF230) was inoculated into 1x CAMHB supplemented with 100 μg/mL ampicillin for plasmid maintenance. On the day of experimentation, 100 μL of overnight culture was inoculated into 10 mL fresh CAMHB with no antibiotic and allowed to reach exponential phase for 90 minutes. After 90 minutes, the exponential phase culture was diluted to OD_{600} = 0.02 as measured on a PG Instruments T60 Spectrophotometer and pipetted onto the well plate for emulsification by the PIPE chip.

Microtiter plate preparation.

All antibiotics and AlexaFluor barcoding dyes were purchased from Thermo-Fisher in powdered form and diluted in sterile MilliPure water. Stocks were prepared at 100x so that working concentration could be achieved by pipetting 1 uL of antibiotic or AlexaFluor stock into 100 uL total volume on a well plate. Each well received 98 μL OD 0.02 exponential phase *E. coli* suspension in CAMHB, 1 μL antibiotic stock and 1 μL barcode dye stock. The working concentrations of chemicals prepared in the wells of the plate are identical to the final concentrations contained within the emulsion.

PIPE chip operation

PIPE chip operation protocols were described in previous work [137]. Briefly, the PIPE chip was connected to a sample-prepped 384-well plate via its stainless steel capillaries, and the plate-chip assembly was placed inside the pressure chamber. The continuous phase, Novec HFE 7500 with 1.5% w/w PFPE-PEG-PFPE fluorosurfactant (RAN Biotechnologies), was pressurized in an external vessel. The pressures applied to the fluids, P_{chamber} and P_{oil}, were ramped according to Table B.1. Once at operating pressure, the droplet collection tubing was fed into a waste stream for 2 minutes to ensure stable, developed flow. After equilibration, the droplet library sample was collected for 3 minutes into an Eppendorf tube or syringe.

Droplet laser-induced fluorescence detection.

Droplet samples were reinjected into the detection channel and spaced by recycled HFE 7500 with surfactant. Droplets and spacer oil were injected at 300 μL/hr and 700 μL/hr, respectively. The 4-color excitation laser was focused onto the flowing droplets by first focusing a 40x microscope objective onto the PDMS-glass interface, then shifting the focal plane upwards by half of the channel height. In this schema, the laser is focused on the vertical center of the

detection channel. Multi-color fluorescence signals from flowing droplets were collected through the microscope objective and directed through the rear epi port of the microscope, where the signals were split into 4 channels according to color, by dichroic mirrors. Four photomultiplier tubes (PMTs), one for each color channel, amplified the fluorescence signals, and output a voltage proportional to the incident fluorescent light. PMT voltages were digitized using a National Instruments PCIe-7852 FPGA card, and recorded by a custom LabView script. All fluorescence signals reported in this work correspond to the peak height of the output PMT voltage.

Gaussian mixture modelling of mixed biotic and abiotic droplet datasets.

The Gaussian mixture model (GMM) MATLAB script was programmed to process whole datasets containing data from both biotic and abiotic droplets of all 36 barcoded subpopulations. Datasets were imported into MATLAB and visualized as a histogram of GFP intensities. GMMs were generated with MATLAB's fitgmdist function with full, non-shared covariance matrix, and regularization value = 10^{-5}. To eliminate abiotic data, we first assumed that the biotic droplets emit greater GFP fluorescence than abiotic droplets. The GFP dataset was then sorted by descending GFP signal and divided binarily according to the proportions of the two subpopulations specified by the GMM.

GFP fluorescence antibiograms and MIC calculations.

Individual droplet GFP fluorescence intensities were first normalized by the average GFP fluorescence intensity observed in the no-antibiotic control (NABC). Then, 6 antibiograms (one for each antibiotic) were plotted as the mean normalized GFP intensity of each barcoded subpopulation against its natural log-transformed antibiotic concentration. Each antibiogram also

received a datapoint corresponding to the NABC and the time = 0 distribution. As these data do not have inherent antibiotic concentrations, we set the NABC equal to 0.1x the lowest concentration tested, and the time = 0 datum equal to 10x the highest concentration tested, for each individual antibiogram (Figure 4 white triangles and white circles, respectively). Then, a Gompertz function (Equation (1)) defined as:

$$Equation\ (1):\ \ y = A + Ce^{-e^{B(x-M)}}$$

was fit to the antibiogram data using MATLAB's lsqcurvefit function. The only boundary imposed on the fit curve was to the lower asymptote. As fully inhibitory antibiotic conditions still contain fluorescent cells, they register as non-zero PMT signals, so the lower asymptote of each fit sigmoid was bounded to be ≥ the lowest mean normalized GFP value observed in the dataset. R^2 values for the curve fits were > 0.9 in all cases, and >0.98 in most cases.

scMIC PDF and heteroresistance calculation.

The scMIC PDF, f '(x), is the derivative of the curve fit to a plot of normalized viable fraction vs antibiotic concentration, f (x) [83]. To categorize individual droplets binarily as viable or non-viable, we defined a cutoff value equal to the mean normalized GFP signal at time = 0, plus two standard deviations. We assessed the validity of this cutoff value by applying it to the NABC population from all 10 biological reps and confirming its effect by visual inspection. In each experiment there is a small population (~1%) of cells that do not proliferate, even in absence of antibiotics. For all biological reps, dividing the NABC dataset according to the defined cutoff marked the proliferating droplets as viable, and the non-proliferating droplets as non-viable. A sigmoid was fit to the normalized viable fraction vs antibiotic concentration curves, defined as:

$$Equation\ (2): \quad f(x) = \frac{1}{1 + \left(\frac{x}{a}\right)^{b} + c\left(\frac{x}{a}\right)^{2b}}$$

where x is the antibiotic concentration and a, b, and c are the fit parameters which are iteratively solved for in MATLAB. Once the normalized viable fraction vs antibiotic concentration was fit, f '(x) was solved for numerically, rather than analytically, as

$$Equation\ (3): \quad f'(x_i) = \frac{f(x_{i+1}) - f(x_{i-1})}{x_{i+1} - x_{i-1}}$$

Last, the probability of observing a scMIC greater than or equal to a given concentration, *c,* is given by the definition of a probability density function:

$$Equation\ (4): \quad P(scMIC \geq c) = \int_{c}^{\infty} f'(x)\, dx$$

Results & Discussion

PIPE chip platform overview.

The PIPE chip platform enables parallel analysis of a multiplexed panel of antibiotic conditions, against single microbial cells in microfluidic droplets. We tested our platform on *E. coli* HB101, a K-12 derivative, labeled with plasmid-encoded, constitutively-expressed green fluorescent protein (GFP) for detection of growth signals. The plasmid pMF230 contains *ampR,* a transcriptional regulator conferring resistance against *β*-lactams, to allow selection with ampicillin [149-152]. As such, the strain is expected to show varying degrees of resistance toward *β*-lactams, and unchanged physiology in response to other classes of antimicrobials.

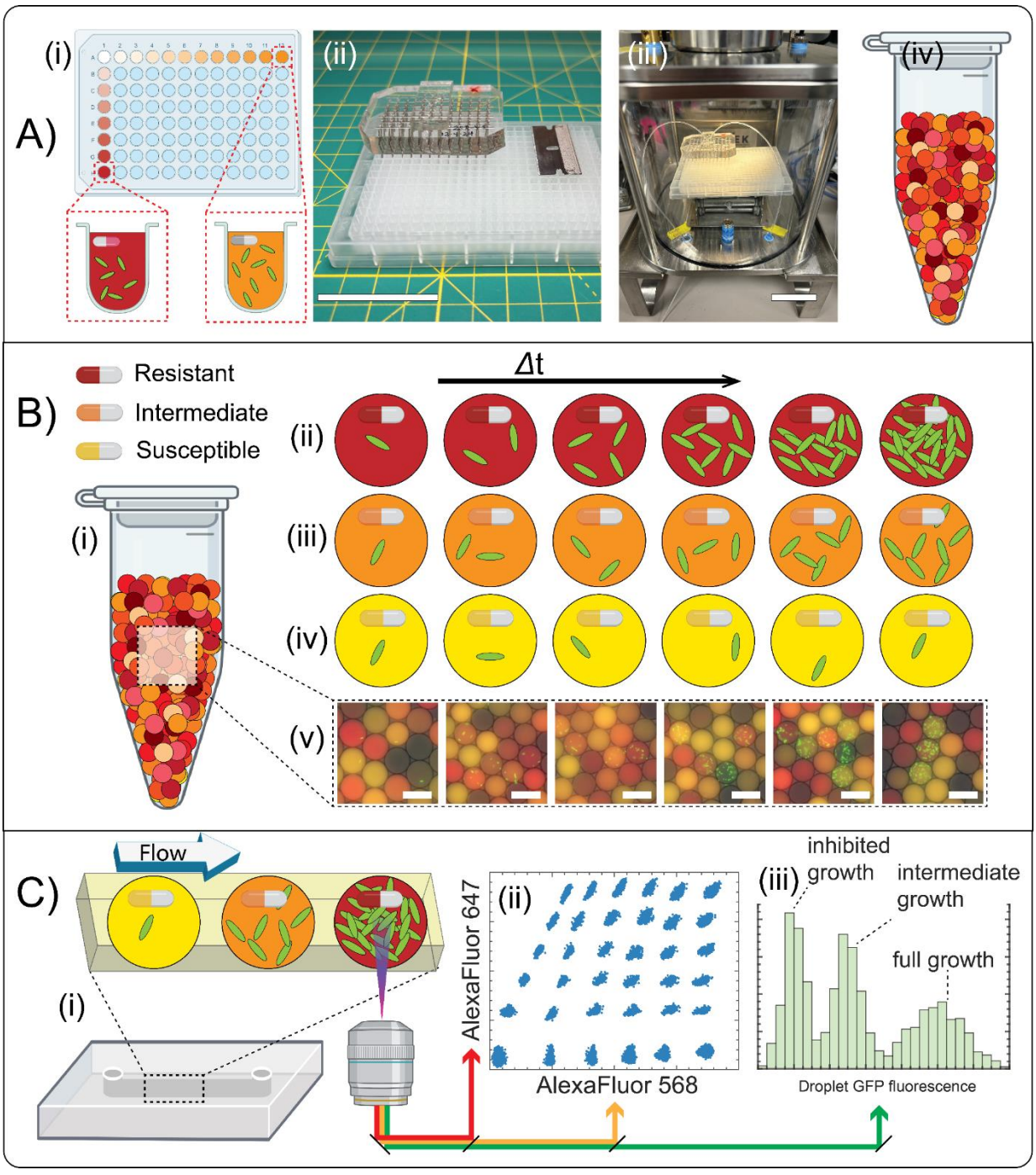

Figure 5.1. PIPE chip platform overview. A) Droplet library generation. (i) Barcoded antibiotic solutions are prepared by pipetting into wells of a microtiter plate, along with a bacterial cells in media. (ii) The PIPE chip interfaces with the well-plate. (iii) the chip-plate assembly is placed in a pressure chamber, to drive fluidic flow from the wells into the device. HFE carrier oil used as the continuous phase is pressurized in an external vessel (not shown) (iv) In less than 10 minutes, a barcoded droplet library of $\approx 10^7$ individual droplets is generated. Scale bars, 50 mm. B) Droplet

growth processes. (i) The droplet library incubates in a syringe or Eppendorf tube for up to 5 hours to allow microbial growth to proceed in droplets. (ii) – (iv) Example growth processes. Over the course of a few hours, a seeded cell will exhibit (ii) vigorous growth if it is resistant to the antibiotic in its droplet, (iii) intermediate growth if it has intermediate resistance and (iv) no growth if it is susceptible to the antibiotic. (v) Fluorescence images from a no-antibiotic growth control, representative droplets seeded with single cells and allowed to incubate for 0-5 hours. Scale bars, 50 μm.C) Multiplexed growth readout. (i) The incubated droplet library is reinjected into a flow channel, where the droplets pass under an interrogation laser in single-file. (ii) Fluorescence barcodes and (iii) GFP growth signals are detected from each droplet coincidentally, at over 2 kHz.

The panel of experimental conditions to be emulsified into droplets is first prepared in the wells of a 384-well plate. Each well receives (1) a culture of exponential phase bacteria diluted to appropriate concentration in cation-adjusted Mueller-Hinton broth, (2) a unique antibiotic condition and (3) a unique fluorescence barcode composed of a 2-color combination of AlexaFluor 568 and AlexaFluor 647 fluorescent dyes (Figure 5.1A, i). The PIPE chip contains an array of microfluidic dropmakers, which are fluidically connected to the wells of the microtiter plate by capillary tubes [137]. Upon mating the PIPE chip with the well-plate (Figure 5.1A, ii), the plate-chip assembly is placed inside a custom-built pressure chamber (Figure 5.1A, iii), and the pressurized atmosphere of the chamber drives fluidic flow from the wells, upwards into the dropmaker array. During operation, the PIPE chip forms microfluidic droplets at approximately 10^5 Hz. Using these procedures, we generate a library of $\approx 10^7$ individual droplets, each containing one of 36 uniquely barcoded antibiotic conditions (Figure 5.1A, iv), in approximately one hour starting from a flask culture of bacteria. The droplets are 29-32 μm in diameter, with CV ranging from 1-4% (Figure 5.2A, B), and are loaded with cells at 10-20% loading rate, so that most droplets contain only a single microbial cell.

Due to the artificial concentration of analytes provided by microfluidic droplets [84], microbial growth in droplets is easily discernible within a few hours. The formed droplet library

is first collected into an Eppendorf tube and incubates at 37°C, during which time microbial growth processes occur in droplets. Microbial growth and droplet GFP fluorescence signal correlate inversely to the susceptibility level of the seeded cell (Figure 5.1B, ii - iv). Fluorescence images taken hourly across a 5-hour growth process, using the model organism and in absence of antibiotics, are shown in Figure 5.1B, v.

For laser-induced fluorescence (LIF) assay readout [61], the droplets are reinjected single-file into a microfluidic flow channel, where they encounter an interrogation laser (Figure 5.1C, i). During LIF, individual droplet barcodes and growth readings are collected coincidentally, at approximately 2.1 kHz. The data are first grouped according to antibiotic condition, using the fluorescence barcode signatures of the droplets (Figure 5.1C, ii). Then during data analysis, we use a custom MATLAB script to programmatically discriminate between empty (abiotic) and celled (biotic) droplets. After elimination of abiotic droplet data, the growth response of each of the 36 sub-populations of cells toward their individual antibiotic conditions, is assessed (Figure 5.1C, iii). In an average data collection phase, we generate >4,000 single-cell growth readouts, for each of the 36 barcoded antibiotic conditions, within a 15-minute detection period.

The PIPE chip rapidly emulsifies antibiotic dilution series
into a monodisperse droplet library.

We use an iteratively-optimized pressurization protocol to generate droplet samples using the PIPE chip (Table B.1). We found that immediately jumping the two pressurized vessels from atmospheric pressure to operating pressure can result in undesired flow regimes and polydisperse droplet samples. Thus, a key feature of the operating protocol is the ramping to operating pressures over a few minutes. We found that the combination of final pressures, P_{chamber} = 2 PSI_g and P_{oil} =

3.5 PSI_g, will produce the desired monodisperse, 29-32 μm diameter droplet library (Figure 5.2A, B). At operating pressures, the PIPE chip produces a $\approx 10^7$-droplets sample (Figure 5.1A, iv) in 3 minutes. The device can produce monodisperse droplet samples up to 40 μm in diameter at higher pressure ratio ($P_{ratio} = P_{chamber} / P_{oil}$). However, we found that generating droplet populations smaller than 30 μm comes at the expense of monodispersity. For example, we have operated the chip at $P_{ratio} = 1/3$ to produce 25 μm droplets, with CV = 10%.

As reflected elsewhere in literature [119], we find that monodispersity of the droplet sample is a critical feature for reliable droplet LIF. In a flow channel used for droplet fluorescence detection, a small droplet will catch up to a larger droplet, possibly resulting in their co-detection and obfuscating droplet signals. By contrast, a monodisperse droplet sample will flow monotonously down a detection channel, with equal spacing between droplets and stable droplet frequency. We find that droplets of different size emit different fluorescence signals from dissolved barcoding dyes, with fluorescence signal magnitude correlating directly to droplet size (Figure B.1). Our data show correlation, not causation, though it is conceivable that this phenomenon arises from geometric constraining of droplets in the flow channel: a larger droplet will be squeezed and elongate along the direction of flow, and experience a larger residence time ("exposure") underneath the excitation laser. Also of note, a polydisperse droplet sample will have variable cell loading rates, with loading rate correlating directly to droplet size, given a fixed input bacterial concentration. This could produce unwanted inoculum effects in the larger, higher-loading-rate droplet populations. While these effects are minimized in a monodisperse droplet sample, achieving monodispersity from tens of individual dropmakers is a major challenge. A solution, which we implemented in the PIPE chip, is to design the chip such that the fluidic

resistance of the fluid distribution channels is negligible compared to the resistance of the individual dropmaker units [153]. If designed otherwise, the fluid distribution channels impart a pressure drop onto fluid phases *en route* to the dropmaker units, and the individual dropmakers will operate with different flow rates, producing a polydisperse sample.

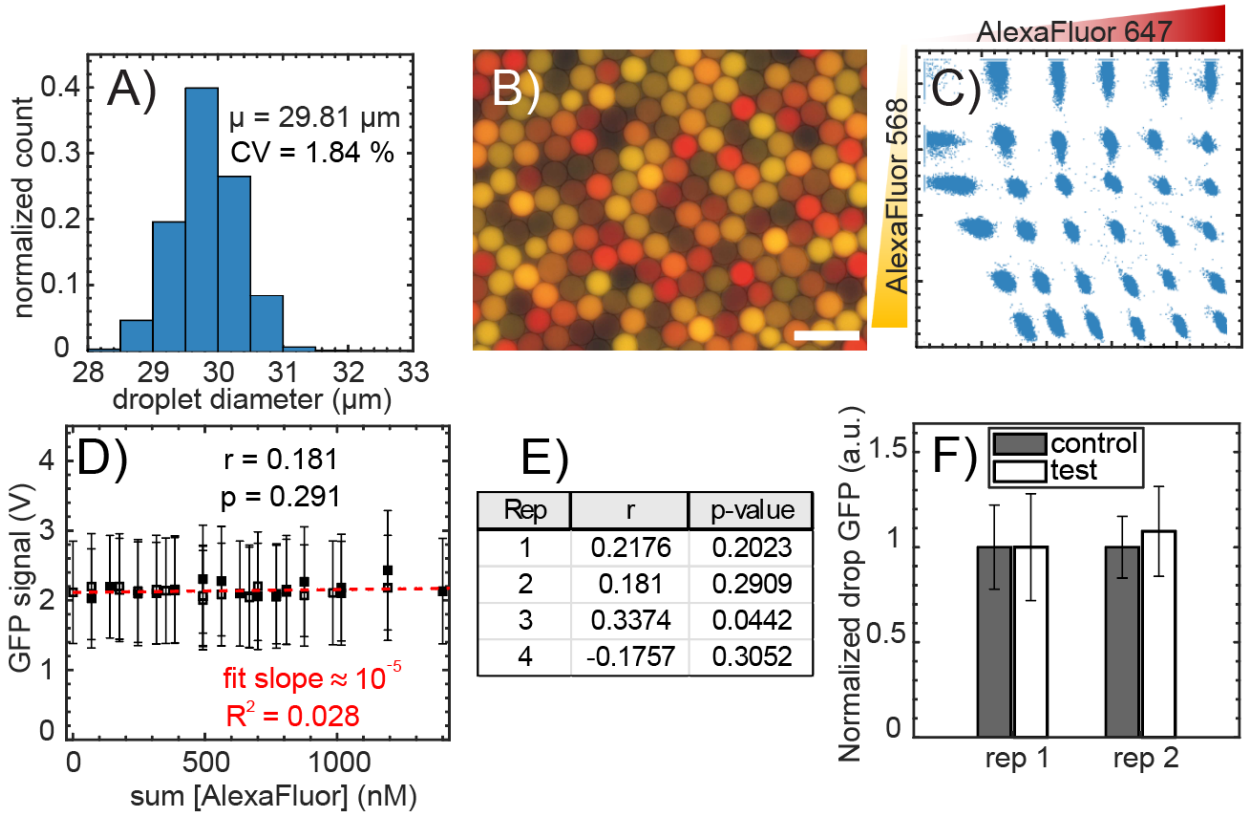

Figure 5.2. PIPE chip performance metrics. A) Histogram of droplet diameters measured by microscopy after PIPE chip droplet library generation. Data from a single, representative experiment. B) Fluorescence image of barcoded droplets generated by the PIPE chip, taken from a representative experiment. C) 2D barcode scatter plot. On average, 92-99% of data are clustered into a barcode group by DBSCAN clustering algorithm. D) Average time = 5 GFP signal vs. barcode concentration from a representative AlexaFluor dye growth control experiment. Individual barcoded clusters show some variability after 5 hours growth, but it is random and unrelated to barcode condition. E) Pearson correlation statistics, r, and associated P-values for 4 biological reps of AlexaFluor dye growth control. F) Duplicate testing for interdrop transport of the multiplexed antibiotic panel. For the control value, reporter drops were incubated next to bacterial media drops. For the test value, reporter drops were incubated next to the multiplexed panel of antibiotic droplets. Alignment of test and control values after 4 hour growth period indicates negligible interdrop transport of antibiotics.

Two-color AlexaFluor dye barcodes encode experimental conditions in microfluidic droplets.

To assay a panel of antibiotic conditions in microfluidic droplets in parallel, we implement a method to spectrally encode each droplet according to its antibiotic condition. Each spectral barcode is a 2-color combination of AlexaFluor 568 and AlexaFluor 647 dyes in predetermined concentrations. To barcode droplets, the barcoding dyes are simply diluted to working concentration into microwells during the microtiter plate preparation step. The dye concentrations of droplets formed from a particular well are identical to the concentrations prepared in the well. To generate 36 fluorescence barcodes, each individual dye is present in 6 unique concentrations: 0, 70, 176, 316, 492 and 700 nM. We combine the two dyes in pairwise fashion to create a square 6 x 6 panel of 36 barcodes (Figure 5.2B, C). Notably, the dilution series does not follow any linear or fold-dilution pattern. The variance of the fluorescence barcode distributions increases with signal magnitude, thus, the spacing between barcode concentrations must increase with concentration [137]. Using a dilution series which is finer than 2-fold allows us to fit more barcodes into a given range of dye concentrations. During data processing, we use the DBSCAN clustering algorithm in MATLAB to group data clusters according to their barcode signal. Typically, between 1-8% of data falls outside of barcode clusters, and is eliminated from the dataset.

To verify that AlexaFluor barcodes do not interfere with biological assays in droplets, we conducted microbial growth experiments in the presence of barcoding dyes. For these experiments, we prepared a droplet library containing the panel of 36 barcodes dissolved in bacterial media, and GFP-*E. coli* cells loaded at 10-20% rate. We allowed the droplet library to incubate for a 5-hour growth period, and detected growth signals from the droplets at the endpoints (time = 0 and 5

hours) to probe for dye-related growth effects. We found that there is some variability in growth between barcoded droplet populations, however it is random and not related to the barcoding dye concentration (Figure 5.2D, data from single representative experiment). For 4 biological repetitions of this experiment, we calculate a Pearson correlation coefficient, r, to test for statistical correlation between barcoding dye and microbial growth in droplets (Figure 5.2E). For 3 repetitions, we found $r < 0.3$ indicating negligible correlation, with non-significant P-statistic ($P > 0.05$). Intriguingly, for 1 of the 4 biological reps, we found $r = 0.3374$ indicating very low correlation, with statistical significance ($P = 0.0442$). However, the line fit to these data to assess their linear relationship follows a line of slope $\approx 5 \times 10^{-5}$, and we conclude that this is negligible. Together, these results demonstrate that the AlexaFluor barcodes used in this work do not produce any growth effects on *E. coli* grown in droplets.

Interdrop transport of the multiplexed panel of antibiotics is negligible.

Transport of dissolved chemicals between microfluidic droplets is a documented phenomenon which poses potential challenges in droplet AST [154-158]. Droplets in an emulsion system may receive unintended chemical antibiotic inputs from neighboring droplets, compromising the accuracy of growth readings taken from the droplets. Recently, it was shown that the transport of antibiotics between droplets stabilized by PFPE surfactants is influenced by the solubility of the antibiotic [157]. Specifically, greater water solubility is associated with minimal transport between aqueous droplets. We selected the panel of antibiotics used in this work based on this knowledge. However, we further hypothesized that multiple water-soluble antibiotics, which individually show only trace interdrop transport, could synergize in off-target drops to produce non-negligible growth effects in a multiplexed assay. To test this hypothesis, we

conducted experiments resembling those implemented by Ruszczak et al. [157]. This approach utilizes droplets containing bacterial cells as reporter drops, to detect the transport of antibiotics from neighboring droplets. In these experiments, antibiotic transport from neighboring droplets is indicated by reduced growth in the reporter droplets. As the test condition, we incubated reporter drops alongside a droplet library containing the entire 36-plexed panel of antibiotics; as a control condition, we incubated reporter droplets with droplets containing bacterial media. After a 4-hour growth period, we quantified GFP fluorescence from fluorescence images of the droplet samples. The data (Figure 5.2F), show minor differences in growth signals between test and control populations, indicating negligible interdrop antibiotic transport, for the panel of antibiotics selected and for our model organism.

These experiments allowed us to evaluate potential synergistic effects from a mixture of antibiotics, which individually show negligible transport between droplets. This positive result suggests that in the future, panels of antimicrobials could be pre-vetted for retention in drops, and specifically designed for implementation in multiplexed droplet experiments. Unfortunately, there are entire classes of antimicrobials which are poorly soluble in water and expected to be incompatible with droplet AST, including macrolides, fluoroquinolones, tetracyclines, and some penicillins. Fortunately, those expected to be compatible with droplet AST are some of the most important classes of antibiotics to society, including aminoglycosides, cephems and carbapenems [157]. Moreover, recent advances in tuning the chemistry and spatial geometries of fluorosurfactant polar head groups have resulted in stable emulsions which exhibit minimal small-molecule interdrop transport [159, 160]. Further advances within this field could open the door to the deployment of all antibiotic classes in droplet AST applications, regardless of water-solubility.

Interestingly, in this work we showed that colistin, an antibiotic predicted by Ruszczak et al. to leak from droplets and be incompatible in droplet AST assays [157], does not leak appreciably at the concentrations tested. This observation emphasizes empirical testing for antibiotic leakage as a necessary prerequisite control experiment to droplet AST.

Gaussian mixture modelling of mixed datasets enables programmatic discrimination of biotic and abiotic droplet signals.

To detect high-resolution growth signals from droplets, we built a custom MATLAB program to identify subpopulations of biotic and abiotic data within mixed droplet fluorescence datasets. The program generates a gaussian mixture model (GMM) of the dataset, which reliably identifies biotic and abiotic subpopulations in correct proportions, and bins the data accordingly. With this data treatment step, we can distinguish droplets containing even a single fluorescent cell from abiotic droplets. Zhang et al. presented a novel approach to susceptibility assessment, which also utilized a gaussian mixture model to bin droplets binarily. However, the method was not detailed, and did not allow for identification of biotic, non-proliferating droplets and thus was not used to describe heteroresistance phenomena [81]. Our method is automated, and acts on datasets collected in massively parallel, scalable designs. The ability to specifically extract biotic data from mixed droplet datasets will enable novel studies of bacteria in droplets, as well as improve on insights gained from phenotypic droplet AST studies.

The GMM program was optimized during the AlexaFluor dye growth control experiments discussed in the previous section. For each of 4 biological replicates at time = 0 and 5 hours, we collected fluorescence images of the multiplexed droplet samples, and enumerated the biotic fraction, F_+. On average, we counted 3,163 +/- 817 droplets per timepoint per experiment, to ensure

statistical significance of the image counts. In this way, we use the sample of fluorescence images as a positive control to assess the performance of programmatic counting of F_+ by the GMM program in MATLAB. Figure 5.3 shows a demonstration of the counting program, as well as performance assessment. Representative fluorescence images of cell-laden droplets are shown at time = 0 hours (Figure 5.3A) and after a growth period at time = 5 hours (Figure 5.3D). Figures 5.3B and 5.3E show histograms of LIF detection data from the same droplets at time = 0 and 5 hours, respectively. The GMM generated for each dataset is overlaid onto each histogram; at both timepoints, the model identifies two subpopulations corresponding to biotic and abiotic fractions, that agree strongly in proportion. Discrepancy between the two counting methods is shown in Figures 5.3C and 5.3F, for time = 0 and 5 hours respectively. For each timepoint and for all 4 biological repetitions, the data are plotted as $\Delta F_+ = F_{+,\,\mathrm{image}} - F_{+,\,\mathrm{GMM}}$, such that a value of 0 indicates perfect agreement between the two F_+ counting methods. Error bars show the binomial 95% confidence interval of the control, image counting method. While there is some discrepancy between the two counting methods, the magnitude of the discrepancy is always reasonably close to 0. Moreover, the 95% confidence interval of the image count method, which is a measure of uncertainty of the control method, is generally greater than the magnitude of error. These analyses demonstrate the robustness of our programmatic biotic data identification method, and indicate

that the program can be used to eliminate abiotic data points from mixed droplet fluorescence datasets in AST assays.

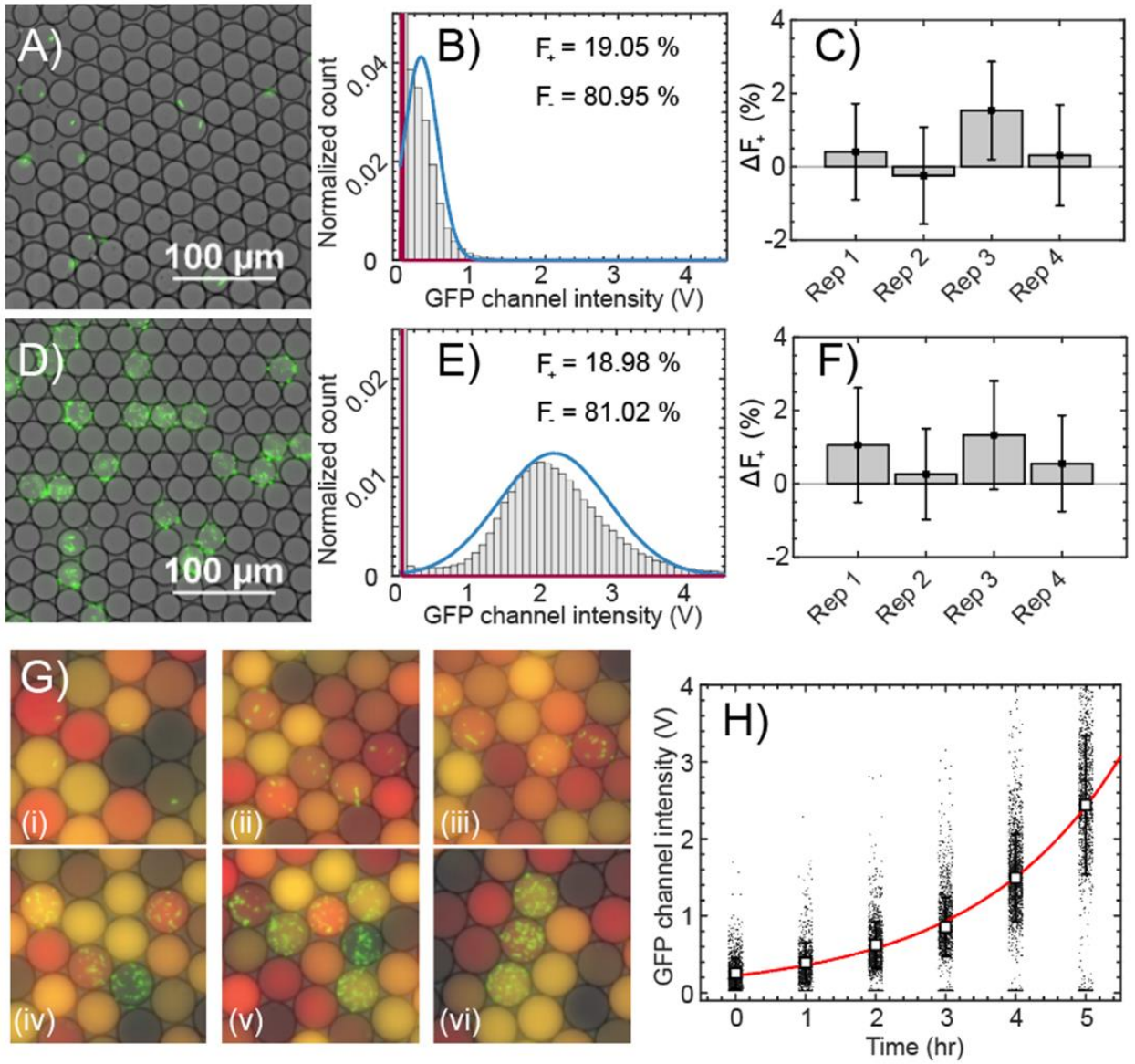

Figure 5.3. Programmatic discrimination of biotic and abiotic data. A) and D), fluorescence images from a representative growth control experiment of cell-laden droplets at time = 0 (A) and 5 (D) hours. B) And E) GFP fluorescence histograms collected during LIF of the droplets shown in A) and D), respectively. The Gaussian mixture model is drawn on top of the histograms. F_{biotic} and F_{abiotic} reported on each plot are output by the model. C) And F) error analysis of programmatic F_{biotic} counting in MATLAB. For each of 4 growth control bio reps, F_{biotic} was first enumerated in fluorescence images. Then, discrepancy between the two counting methods is reported as $\Delta F_{+} = F_{+,\text{ image}} - F_{+,\text{ GMM}}$, such that a value of 0 indicates perfect agreement between the two F_{+} counting methods. G) Fluorescence images of cell-laden drops across a 5-hour growth process in hourly

intervals. (i) – (vi) correspond to 0-5 hours, respectively. Scale bars, 100 μm. H) Droplet GFP fluorescence data from the same drops as in G). Droplet populations first had abiotic data eliminated using the gaussian mixture model program in MATLAB, then biotic data are reported.

To demonstrate the utility of this procedure, we monitored growth of *E. coli* in droplets over a 5-hour time course. In hourly intervals, we collected fluorescence images (Figure 5.3G), and detected LIF signals (Figure 5.3H) from the droplet sample. Biotic data from each hourly dataset was extracted using the GMM F_+ counting program, and plotted against time to probe for our ability to monitor exponential growth processes occurring in the droplets. Figure 5.3H shows the mean GFP fluorescence intensity of each processed dataset +/- standard deviation, with raw GFP signals jittered and plotted underneath. Exponential growth of the cells in droplets can be clearly discerned from the data, as well as growth heterogeneity. We found that the mean droplet GFP intensity is always greater than the median, indicating that the growth signal is being disproportionately affected by outlying droplets on the upper end of the growth observation range. It is possible that these outlier growth observations result from cells that over-produce GFP without over-producing biomass, but they are notable for this phenotype nonetheless. Last, we note that we detected statistically significant differences in GFP distributions between time = 0 and 1 hour (P-value $\approx 10^{-73}$, two-tailed t-test), suggesting that this procedure could be used to generate AST results with as little as 1 hour of incubation time.

Minimum inhibitory concentrations (MICs) for a multiplexed panel of antibiotics can be extracted from GFP fluorescence antibiograms.

The primary goal of AST and AMR surveillance applications is to generate a quantitative susceptibility result. The minimum inhibitory concentration (MIC) is the conventional metric for communicating the susceptibility or resistance level of an organism. There are several methods to

calculate a MIC from growth data; here, we modify the method developed by Lambert et al. (2000) [83, 91, 161]. In the Lambert method, which was developed for use on turbidity measurements from plate reader instruments, an antibiogram is generated by plotting normalized growth vs log-transformed antibiotic concentration. Then, a sigmoidal Gompertz function is fit to the antibiogram to calculate MIC. This method is capable of outputting MICs between tested conditions because of its use of a curve fitting procedure to interpolate growth data. Droplet ASTs that have implemented the Lambert method use an observed fraction of growth droplets as the normalized growth signal [83, 91]. Here, we build on these reports by using the magnitude of cellular GFP fluorescence signals from microfluidic droplets, rather than the number of growth droplets, in the Lambert method to calculate MICs.

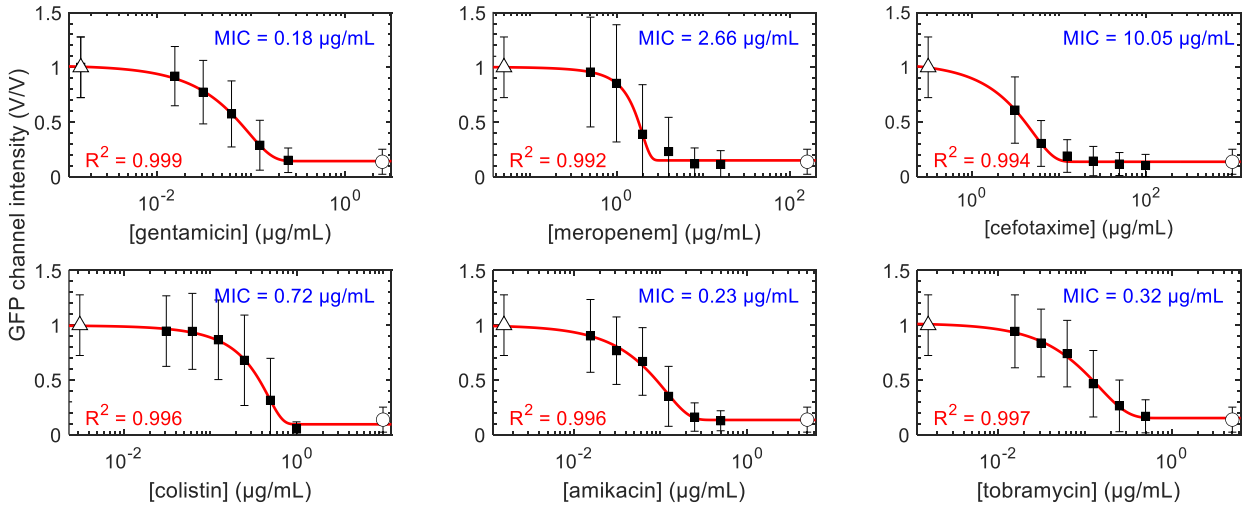

Figure 5.4. MIC calculation using the Lambert method. Biotic-only datasets are first segmented by barcode cluster, then plotted as cluster GFP mean +/- standard deviation vs log antibiotic concentration. All data are normalized to the NABC value for individual experiments. Each of the 6 antibiotics is tested in 6 concentrations (black squares). Gentamicin is present in 5 concentrations to allow room for the NABC. The NABC is shown on each plot as a white triangle, and data collected at time = 0 hours is shown as the white circle. Once the sigmoidal gompertz function is fit, the MIC is output as the x-coordinate of the intersection of the sigmoid lower asymptote and the line tangential to the inflection point.

Biotic droplet datasets are first binned according to antibiotic condition, using fluorescence barcode signals. Each antibiotic in the panel is present in 6 concentrations each; one of the antibiotics is present in only 5 concentrations, to allow room for a no-antibiotic control (NABC, Figure B.2). An antibiogram is generated for each of the antibiotics by plotting the mean GFP fluorescence intensity of its subpopulations of droplets, against log-transformed antibiotic concentration (Figure 5.4, black squares). Each antibiogram receives a data point corresponding to the NABC (Figure 5.4, white triangles). As the log transformation of 0 equals -infinity, we set the antibiotic concentration for the NABC datum equal to $1/10^{th}$ of the lowest antibiotic concentration tested for each antibiotic-specific antibiogram. We also include the mean fluorescence intensity collected from the entire droplet sample at time = 0 on our antibiograms (Figure 5.4, white circles), by assuming that data collected before any growth has occurred can be plotted in the inhibitory region of the antibiogram curve. As this datum also does not have an inherent antibiotic concentration, it is set equal to 10 times the highest antibiotic concentration tested for each antibiotic-specific antibiogram. As explained in Lambert et al., the MIC is the abscissa of the intersection of the sigmoid lower asymptote and the line tangential to the inflection point [161].

We found that the antibiogram should include data in both the inhibitory and non-inhibitory regions of the curve to produce a meaningful susceptibility result. If these regions are unpopulated, the two asymptotes of the sigmoid cannot be defined, and the results are untrustworthy. For example, in the absence of a non-inhibitory condition, a sigmoid can be solved for that has its upper asymptote in the region corresponding to [antibiotic] < 0, producing a MIC <0. Use of the NABC and time = 0 data as done here is a valuable procedural element, as these datasets function

as positive and negative control populations, respectively, and allow the sigmoidal curve asymptotes to be estimated even if the range of tested antibiotic concentrations is incorrect. Importantly, this usage of time = 0 data is only made possible because we can distinguish single cell droplets from abiotic droplets using our GMM method.

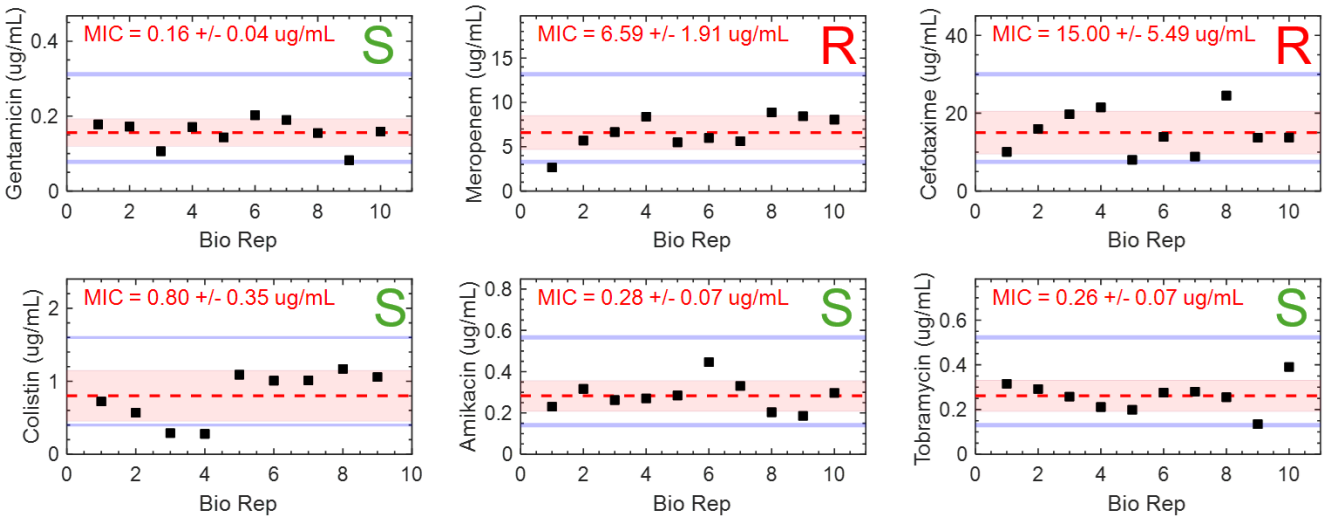

Figure 5.5. output MICs across 10 biological reps of multiplex droplet AST. Each plot is specific to one of the 6 antibiotics in the panel. Plots show output MIC vs biological rep, for 10 reps. Red dashed line, average MIC across 10 reps. Red shaded area, standard deviation of MIC across 10 reps. Blue shaded regions correspond to a two-fold change in the MIC in either direction. Susceptible/intermediate/resistant (S/I/R) classification is shown upper right of each plot, based on comparison to CLSI breakpoint values.

Calculated MICs for the panel of 6 antibiotics are shown in Figure 5.5, for 10 biological replicates of the AST experiment. The average MIC across the 10 reps, +/- standard deviation, is shown as the red dashed line and shaded region. We observed some variability about the central MIC estimate, but it is within the expected level of variability for MIC calculations. MICs measured with standard techniques have been shown to vary by as much as 2-fold from the central MIC estimate, based on biological variability and operator error [16, 162]. On each plot, blue shaded regions have been added, which correspond to 2-fold changes in either direction from the central MIC estimate. Based on our MIC results, the model organism is classified as

susceptible/intermediate/resistant (S/I/R) towards the panel of 6 antibiotics, by comparison to CLSI breakpoint values (Figure 5.5, upper right of each plot) [12]. As expected, the organism was classified as resistant toward β-lactam antibiotics, and susceptible toward aminoglycosides and colistin, a polymyxin antibiotic [163].

We performed broth microdilution AST as a reference method, to assess the validity of the results generated by our droplet-based platform. The MICs calculated by broth microdilution are tabulated in Table B.2. The two methods for estimating MIC show excellent agreement for 5 of 6 antibiotics (gentamicin, meropenem, colistin, amikacin, tobramycin). Moreover, the day-to-day variation, measured as a standard deviation, is also similar between the two methods, supporting the validity of our droplet-based AST approach. Interestingly, the MIC calculated for cefotaxime is approximately 100-fold lower as measured by broth microdilution, compared to the MIC measured in our droplet AST platform. To explore this phenomenon, we designed experiments to better characterize *E. coli* response to cefotaxime. In these experiments, multiple populations of droplets were generated, each containing single *E. coli* cells and a single cefotaxime condition, which varied between droplet populations. The individual populations were incubated off-chip and imaged by epifluorescence microscopy to visualize *E. coli* response to cefotaxime (Figure B.3). We found that at the lowest concentration of cefotaxime tested in droplets ([cefotaxime] = 0.39 μg/mL), the cells exhibited filamentous physiology, and grew to tens of microns in length without dividing. At increasing concentrations of cefotaxime, the cells begin to lyse, and dye the individual droplets green, with cellular GFP. Thus, the analysis of cefotaxime against *E. coli* represents a limitation of our platform. The filamentous response by the cells indicates susceptibility toward the antibiotic at 0.39 μg/mL, however, our platform records these droplets as having high GFP

fluorescence, and they are classified as growth signals. In the broth microdilution method, inhibition by cefotaxime can only be discerned across ~20 hours of growth, in which the OD measurement begins to increase, as the cells filament, and then eventually plateaus, when the cells lyse. We therefore hypothesize that cefotaxime may not be amenable to any rapid AST platforms, unless the readout is microscopy-based and can detect filamentation. This is because the available non-microscopy-based rapid AST readouts, including microbial light-scattering, resazurin indicator dye, and quantitative pheno-molecular readouts, will all produce a growth reading before cell lysis occurs. Indeed, in the report by Scheler et al. in which AST of *E. coli* was conducted against cefotaxime in microfluidic droplets, growth readouts were collected after overnight incubation, rather than in a rapid AST format [83]. Currently, work is ongoing in our group to assess the affects of overnight incubation on ability to discern growth from inhibition in droplets. Moreover, we hypothesize that unique, non-sigmoidal antibiograms may result from testing at cefotaxime concentrations < 0.39 μg/mL, which could be used to infer susceptibility results.

Single-cell MIC probability density functions quantify *E. coli* heteroresistance toward tested antimicrobials.

Because we assay thousands of single cells against antibiotic dilution series, heteroresistance can be assessed with the same datasets used to calculate MICs. To probe for heteroresistance in our model organism, we implement the analysis first shown by Scheler et al. (2020) to generate single-cell MIC probability density functions (scMIC PDFs). In this technique, it is assumed that a proliferating cell exposed to an antibiotic concentration = c must have a scMIC > c. A sigmoidal curve, fit to a plot of proliferating fraction vs antibiotic concentration, is then derived to produce a PDF of scMICs.

The scMIC PDFs we calculated are shown in Figure 5.6. A single curve is output from each biological rep of the experiment; the central curve shown in Figure 6 is the average of all 10 curves, and the shaded error bar is the standard deviation from averaging the curves. In red is highlighted the region on the x-axis which corresponds to the MIC estimate, +/- standard deviation. These curves show, invariably, that the population-level susceptibility discerned by the MIC, is the result of a heterogeneous population consisting of relatively many cells more susceptible than, and relatively few cells more resistant than, the MIC estimate. This finding echoes the data in Figure 5.3H, in which the average growth value is driven to some extent by a minority outlier group near the upper limit of growth observations.

To quantify heteroresistance, we adopt the criteria to define heteroresistance most common in the literature, which is the presence of a resistant subpopulation of frequency $\geq 10^{-3}$, and whose MIC is ≥8-fold that of the main, susceptible population. We define the MIC of the main susceptible population, MIC_{main}, as the most common scMIC, which is simply the abscissa of the global max of the scMIC PDF. The scMIC value indicative of heteroresistance, $scMIC^{HR}$ is therefore defined as $scMIC^{HR} \geq 8 \times MIC_{main}$, and its frequency is calculated using the formula for a probability density function (Materials and Methods, Equation (4)). Thus, where the frequency of $scMIC^{HR}$ is $\geq 10^{-3}$ for a given antibiotic, the model organism is classified as heteroresistant. Using this single-cell susceptibility modeling approach, *E. coli* was categorized as heteroresistant toward all the tested antimicrobials. We note that in a clinical application, meropenem should be classified as resistant, not heteroresistant, as heteroresistance implies the existence of a majority susceptible

population [33]. Moreover, further experimentation is required to interpret these results as they pertain to cefotaxime.

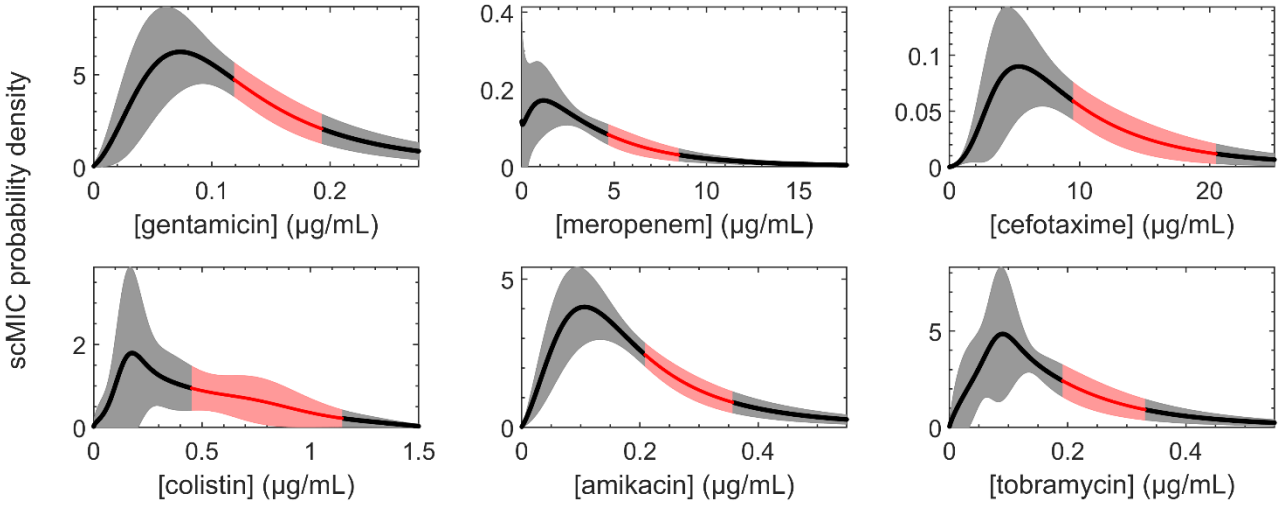

Figure 5.6. Single-cell MIC (scMIC) probability density functions (PDFs) calculated using droplet AST. Each plot shows the average scMIC PDF across 10 biological reps as the central curve, and standard deviation across biological reps as shaded error bar. For each biological rep, a single scMIC PDF is calculated by deriving a plot of proliferating fraction vs antibiotic concentration, for each of the 6 antibiotics of the panel. The red-colored region corresponds to the population-level MIC +/- standard deviation calculated in Figure 5. These curves demonstrate that the population-level behavior, discerned as a MIC, is the result of many susceptible cells and few relatively resistant cells.

Heteroresistance toward colistin has been observed in a number of *Enterobacterales* species including *E. coli.* Recent findings show that colistin heteroresistance is much more common in *Enterobacter* spp. and *Klebsiella* spp., two closely related *Enterobacterales* genera, than it is for *Escherichia* [164]. However we note that the *ampR* transcriptional regulator carried by our model organism has been shown to regulate the expression of a wide array of genes, some of which are related to non-β-lactam antibiotic resistance. Thus, the unusual observation of colistin heteroresistance in our model organism could be explained by the inclusion of the *ampR* transcriptional regulator. By contrast, heteroresistance phenotypes in *E. coli* against carbapenems

are well-established [165]. Heteroresistance toward aminoglycosides, including amikacin, gentamicin and tobramycin, has also been reported in *Enterobacterales* [166].

It is possible that the rate of heteroresistance observation in the past has been biased by relatively infrequent testing for heteroresistance. Here, we have shown a platform which makes heteroresistance testing routine. This development is imperative, as extensive validation of the relationship between heteroresistance frequency, antimicrobial therapy efficacy and clinical outcome will be required before droplet-based AST and heteroresistance assaying data can be used to guide clinical antibiotic therapy. Much attention has been paid to the scMIC as a meaningful metric of susceptibility, which is robust against inoculum effects [44]. However, clinical breakpoints have been set based on analyses of entire bacterial populations, and the switch to single-cell data in AST applications will require consideration. This switch will be made possible by first amounting massive amounts of data which can be used to demonstrate the relationship between single-cell and population-level AST data. In this latter regard, the platform we have demonstrated here is of great value, as it leverages microfluidic droplets for ultrahigh-throughput measurements of thousands of single-cell growth responses to antimicrobials.

Conclusions

The droplet-based platform described remedies several outstanding problems in the microfluidics AST community relating to multiplexing and automated analysis. We demonstrated rapid testing of tens of antibiotic conditions in microfluidic droplets, in parallel. Multiplexing of this scale has been demonstrated prior, though only by way of complicated device and experimental designs, which prohibit proliferation of the techniques. Our platform makes use of components which resemble the instrumentation of existing, wide-spread bioassays, including

microtiter plates for sample multiplexing, syringe pump-free emulsion preparation reminiscent of BioRad automated droplet generators, and photonics-based data acquisition similar to flow cytometers. Our platform has immediate room for scale-up; in an experiment not shown, we easily doubled our available barcode space by adding a third barcoding dye in two concentrations, and the new 72 barcodes showed maintained biocompatibility. Once combined with recent advances in label-free droplet AST detection such as optical fiber-based light scattering or impedance measurements, our platform will be suitable for analysis of clinical isolates. The data analysis steps we incorporated, namely biotic data identification, MIC calculation and scMIC PDF description, would all be compatible with datasets generated by these label-free techniques. In the future, we envision that clinical isolate samples could be diluted onto pre-made microtiter cards containing freeze-dried antibiotics and barcoding dyes. The multiplexed sample could be rapidly emulsified using an automatic droplet generator, and analyzed by an integrated flow-based droplet analysis unit. An all-in-one AST and heteroresistance detection platform such as this could provide drastically improved guidance to clinicians prescribing antibiotics. Moreover, a routine heteroresistance surveillance platform is paramount to the ongoing antibiotic stewardship effort.

CHAPTER 6

CONCLUSIONS AND OUTLOOK

Conclusions

The research presented in this thesis comprised three separate but related projects, during which a high-throughput, multiplexed microbial drug screening assay in microfluidic droplets was developed. The presented work contributes to the understanding of developing droplet-based single-cell assays, as well as heterogeneity in bacterial growth response to antimicrobials. Here, I will summarize the results of this work, provide context within the wider field of microfluidic AST, and comment on future work.

Chapter 3 discussed the construction and subsequent optimization of a platform for detecting multiplexed laser-induced fluorescence (LIF) signals from microfluidic droplets. Droplet LIF can be used to conduct single-cell screening assays at ultrahigh-throughput, thus facilitating biological discovery and description of cell-cell heterogeneities. However, droplet LIF presents several challenges impeding its widespread proliferation, including complicated optical equipment, droplet instability, data reliability issues, and fluorescence cross-talk. In response, we detailed robust troubleshooting and optimization procedures for addressing these issues. We outlined a robust protocol for shaping and aligning laser beams, which can be implemented by untrained personnel and uses off-the-shelf optical components. Poor beam quality can result in a number of deteriorative artefacts in LIF data, and the reported protocol should allow future experimenters to safeguard against this. Droplet instabilities, such as coalescence and droplet breakup, are another factor which negatively influence droplet LIF data quality. Fluorescence

signals from re-combined droplets can obfuscate desired assay readouts and result in uninterpretable data. In our reported methodology, we enumerated factors influencing droplet instability, as well as a number of mitigation techniques. To promote data quality, a method to encode each droplet with a fluorescent reference dye signature was developed. The reference dye signature provides a proxy measurement of droplet size, and can also be used to visualize droplet spacing and frequency in the flow channel. As a redundant safeguard against droplet instabilities, we developed a dynamic gating technique, which eliminates data of incorrect size and reference dye signature, while responding to flow variations. Moreover, we demonstrated that the droplet size, measured as droplet time inside, and fluorescence intensity have a bidirectional causal relationship. These tutorials and findings will contribute to the proliferation of droplet LIF-based methods by promoting robust, artefact-free data collection. Lastly, we detailed a method for bottom-up construction of a multiplexed growth assay using droplet LIF. The method provides an outline for future experimenters to mitigate channel cross-talk and collect reliable droplet fluorescence signals in multiple channels simultaneously, simply by modulating channel-specific detection variables.

In Chapter 4, we demonstrated rapid emulsification of a library of experimental conditions using the PIPE chip. Numerous biological assays necessitate testing of multiplexed experimental conditions in parallel, and this is typically accomplished using microtiter plates. However, translation of such parallelized assays into microfluidic droplets has proven challenging. These challenges are related to the multitude of equipment required to drive droplet formation for many conditions in parallel, as well as a method to track individual experimental conditions in droplets. The PIPE chip interfaces with a microtiter plate to rapidly emulsify the plate contents, and

eliminates the requirement for multiple pump sources to drive parallel droplet formation. Moreover, the condition contained within the droplet is tracked with a spectral barcoding method.

We showed that droplet formation is monodisperse and follows a drop scaling law [167] which can be used to predict drop size based on the pressurization of fluid sources. Moreover, we used 2-color combinations of quantum dots and fluorescent microbeads to generate droplet libraries consisting of 188 and 24 unique spectral barcodes, respectively. We showed that the dominant form of noise present in the barcode fluorescence signals is determined by the barcoding particle size. For larger (~10^0 μm diameter) colloidal particles, the dominant form of noise is the Poisson-governed discrete random loading of fluorescent barcode particles into the droplet. For particles much smaller than the microscope objective resolution, as in ~10^1 nm diameter quantum dots, the shot noise of the photodetector is the dominant form of noise. The PIPE chip simplifies experimental workflows by utilizing a single microfluidic device to quickly emulsify an entire 96-well plate into a barcoded droplet library. This innovative platform holds great value in conducting multiplexed droplet assays, particularly for assays such as drug discovery and molecular biology, where processing numerous chemical or biological reactions simultaneously is essential.

In Chapter 5, we leveraged the PIPE chip to conduct multiplexed, single-cell antimicrobial susceptibility testing (AST) in microfluidic droplets. The PIPE chip brings an important innovation for droplet AST, as multiplexing in AST is essential in allowing clinicians to deduce a best therapy route over a reasonable timeframe. With this platform, we leveraged the artificial analyte concentrating property of microfluidic droplets to conduct rapid AST which produced MICs and quantitative heteroresistance determination, concurrently in 5 hours. Our platform showed excellent agreement with the reference standard broth microdilution method, emphasizing its

potential for eventual use in clinics. As part of this platform, we demonstrated a technique to programmatically distinguish droplets laden with even a single microbial cell, from abiotic droplets. This data processing step allowed for the high-resolution description of heterogeneous growth response and growth processes in droplets, as well as enumeration of non-proliferating droplets. The ability to detect a high-resolution spectrum of growth readouts represents an advance compared to the field-standard digital droplet AST, in which the droplet growth readouts are binned binarily. Individual droplet growth readouts collected at ultrahigh-throughput were used to model the distribution of single-cell MICs (scMICs) as a probability density function [83]. This enabled estimation of heteroresistant subpopulation frequencies, which were estimated in the range of ~1-3% for gentamicin, amikacin, tobramycin and cefotaxime, ~7% for colistin, and ~47% for meropenem. While the clinical significance of heteroresistance is still a matter of some debate, the need for a method to detect heteroresistance concurrently with AST is clear. Our droplet platform represents a solution to this problem.

Outlook and Future Work

The three projects presented in this thesis share a common goal of improving the existing capabilities and scale-up potential for single-cell screening in droplet microfluidics. They accomplish this goal by (1) reporting facile methodology to construct flow-based, ultrahigh-throughput droplet assays (2) detailing a platform for parallel generation and analysis of multiplexed experimental conditions in droplets and (3) demonstrating a rapid, automated total-analysis droplet assay, where ~150,000 single cells are screened against a multiplexed panel of drugs in a single working day.

An obvious way to improve the applicability of our platform is by the accommodation of unlabeled bacterial cells, as clinical isolates will not express a fluorescent protein. The platform is capable of integration with recently reported label-free techniques to estimate bacterial viability, including the metabolism indicator dye resazurin, as well as optical fiber-based detection of microbially scattered light. Importantly, the data processing steps to identify biotic from abiotic data should be immediately applicable to datasets consisting of scattered light signals collected by optical fibers. This is because the program acts on a univariate dataset which is a composite distribution of multiple underlying subpopulations. Programmatic identification of single-celled droplets from abiotic droplets using cell-scattered light would represent a significant advance in the field. To our knowledge, optofluidic light scattering detection devices have only been used as in a digital assay where vigorous growth droplets laden with many cells are identified as positive reads, and anything else is labeled a negative read.

More broadly, it is my opinion that optofluidic light scattering devices are a relatively under-explored avenue for label-free droplet AST. Whereas viability indicators like resazurin produce an on/off viability signal, microbially-scattered light is a signal which is directly related to the amount of biomass contained within a droplet. Detection of this signal from droplets thus presents an opportunity for high-resolution measurements of bacterial growth, and possibly estimation of bacterial growth rates. AST against gram positive and negative bacteria has been demonstrated with an optical fiber device, in a digital AST format [89]. However, a demonstration of graded biomass-scattered light readouts by an optofluidic device is missing from the literature. The combination of such a device with our parallel droplet library generation and barcoding technique would produce a powerful platform for assaying clinical isolates against drug panels

with single-cell resolution. Moreover, optical fiber devices are amenable to platform integration, which will be a requirement for the proliferation of any novel AST platform.

Our platform could also be improved by increasing the number of antimicrobial conditions tested in parallel. A droplet AST platform which matches the clinical standard of 96 parallel experiments would represent a significant advance in the field. A first step in updating our platform would be to increase the available barcoding space using AlexaFluor dyes. In an experiment not shown, we easily doubled the AlexaFluor barcoding space from 36 to 72 by the inclusion of a third barcoding dye in two concentrations, and cell viability was maintained within the updated barcode space. The theoretical barcoding space from three dyes in six concentrations each is 216. Moreover, attempts to expand the barcoding space of a single dye from 6 conditions to 8 or 12, as was done for the quantum dots, could prove fruitful. Maintained cell viability in the presence of the new barcoding spaces would need to be verified, however, this is not expected to be an issue.

An expanded panel of antimicrobials would need to be tested for retention in the dispersed phase of the multiplexed emulsion sample. An experiment designed to test for this behavior from a multiplexed panel of antimicrobials was conducted in this work, and could be repeated for an expanded drug panel. However feasible, this approach to verifying droplet retention of panels of antimicrobials for use in multiplexed droplet assays could quickly become laborious, as each panel will require independent validation. Moreover, if reporter cells are used to indicate presence or absence of interdrop drug transport, it is possible that antimicrobial panels could show differential transport based on reporter cell species. Perhaps then, the droplet microfluidics drug-screening community should embrace recent advances in tuning surfactant geometry for interdrop transport mitigation [159, 160]. It has been shown that tri-block copolymer surfactants, which are the most

commonly used, mediate interdrop transport primarily by forming oil-in-water-in-oil (o/w/o) vesicular structures, as opposed to water-filled micelles [154, 159]. This behavior helps explain the dependence on water solubility, of the interdrop transport of a solute. A solution then, is to use di-block copolymer surfactants, which are incapable of vesicle bilayer structural assembly [159]. This body of work holds great promise for the future of droplet microfluidics. While the common avenue to mitigate interdrop transport is by tuning reaction components in an application-specific manner [156, 157], the proposed work based on novel surfactants seeks to eliminate the primary mechanism of interdrop transport altogether.

In the future, we envision a host of novel assays which could be developed by building on the presented body of work. The method to programmatically identify single fluorescent cells could be applied to droplet assays which do not entail microbial growth. For example, studies of dormant or persister cells [168] in droplets would rely on the detection of a single, non-proliferating cell. Moreover, the technique could be used in experiments designed to study microbial interaction networks [169] of multiple different bacterial species labeled with different fluorophores. In such an experiment, the species content of droplets could be identified with method presented in this work, and used to probe for effects on microbial growth at ultrahigh-throughput. Last, we envision that the PIPE chip platform, with improved barcoding capacity, could be used to conduct pathogen ID concurrently with AST. For example, using a panel of 72 barcoded conditions, we could accommodate an array of 36 antimicrobial conditions as demonstrated in this work, and a parallel array of 36 molecular 16S rRNA probes, which hybridize and fluoresce in a taxonomically-specific manner. In the end, the adaptation of established

biological assays into single-cell droplet-based formats will continue facilitate improvements in medical tools and research, as well as novel discoveries.

APPENDICES

APPENDIX A

APPENDIX A: SUPPLEMENTARY INFORMATION FOR CHAPTER 4: RAPID PARALLEL GENERATION OF A FLUORESCENTLY BARCODED DROP LIBRARY FROM A MICROTITER PLATE USING THE PLATE-INTERFACING PARALLEL ENCAPSULATION (PIPE) CHIP

Electronic Supplementary Material (ESI) for Lab on a Chip.

Electronic Supplementary Information

Rapid Parallel Generation of a Fluorescently Barcoded Drop Library from a Microtiter Plate Using the Plate-Interfacing Parallel Encapsulation (PIPE) Chip

Geoffrey K. Zath[1,2]‡, Ralph A. Sperling[4,5]‡, Carter W. Hoffman[1,2], Dimitri A. Bikos[1,2], Reha Abbasi[1,2], Adam R. Abate[6], David A. Weitz[4,7], Connie B. Chang[1,2,3]*

[1]Center for Biofilm Engineering, Montana State University, Bozeman, MT, USA

[2]Department of Chemical and Biological Engineering, Montana State University, Bozeman, MT, USA

[3]Department of Physiology and Biomedical Engineering, Mayo Clinic, Rochester, MN, USA

[4]Department of Physics, School of Engineering and Applied Sciences, Harvard University, Cambridge, MA, USA

[5]Fraunhofer Institute for Microengineering and Microsystems IMM, Mainz, Germany

[6]Department of Bioengineering and Therapeutic Sciences, University of California, San Francisco, CA, USA

[7]Wyss Institute for Biologically Inspired Engineering at Harvard University, Boston, MA, USA

‡ Authors contributed equally

*To whom correspondence may be addressed: Connie B. Chang, Department of Physiology and Biomedical Engineering, Mayo Clinic, 200 1st St SW, Rochester, MN 55902, conniebchang@gmail.com

Table of contents

1. PIPE Chip Fabrication

Negative master molds were fabricated upon 3-in diameter silicon wafers (University Wafer, ID# 447, test grade) using UV cross-linked SU-8 photoresist exposed through photomasks printed on high-resolution transparent plastic film (CAD Art, 20k dpi). The top (Fig. 1a, i) and middle (Fig. 1a, ii) layer negative master molds were made with SU-8 2075 (MicroChem) to create 250 μm tall channels while the bottom layer (Fig. 1a, iii) was made with SU-8 3050 (MicroChem) to create 50 μm tall channels. To create the 250 μm tall channels, a first coat of SU-8 2075 was spun at 1000 rpm for 30 s, then softbaked at 100 °C for 60 min, and resulted in a ~200 μm thick layer. The second coat of SU-8 2075 was spun at 3000 rpm for 30 s, then softbaked at 100 °C for 10 min, and resulted in a ~250 thick layer. To create the 50 μm tall channels, SU-8 3050 was spun at 3000 rpm for 30 s, then softbaked at 95 °C for 15 min. For all spin coating conditions, photoresist was initially spun at 500 rpm for 10 s to evenly coat the wafer surface. PDMS prepolymer (Sylgard 184, 10:1 mix ratio of prepolymer to curing agent) was cast onto the negative master molds and cured overnight at 65°C. The cross-linked PDMS devices were cut out using a scalpel. Via holes

and sample inlet holes were manually punched using a 0.75 mm ID biopsy punch (Harris Unicore). A larger 1.25 mm ID biopsy punch (Robbins Instruments RBP-12) was used to fit 1/16-in OD tubing (IDEX FEP tubing) to the oil inlet and 0.052-in OD tubing (Scientific Commodities PE/5) to the drop outlet port on the top layer (Fig. 1a, i) of the device. Assembly of the PIPE chip began with oxygen plasma treatment (Harrick Plasma PDC-001) of the middle (Fig. 1a, ii) and bottom (Fig. 1a, iii) PDMS layers for 30 s at medium power and 700 mTorr oxygen pressure. A thin layer of deionized (DI) water was introduced between the plasma-treated surfaces to temporarily prevent the PDMS layers from bonding during the alignment process, which was accomplished by eye. The aligned layers were immediately baked for $\geq$1 h in a 65 °C oven to dry the DI water and allow the PDMS layers to bond. The top face of the bonded two-layer device was subjected to oxygen plasma (Fig. 1a, i) of the device with the previously mentioned plasma treatment settings. DI water was introduced to prevent bonding while the top layer (Fig. 1a, i) was aligned with the previously bonded middle (Fig. 1a, ii) and bottom (Fig. 1a, iii) layers such that the via holes of the middle layer (Fig. 1a, ii) connect with their respective oil inlet and drop outlet channels. Device channels were made hydrophobic by flowing Aquapel (Pittsburgh Glass Works) through the channels of the bonded device, flushing with compressed air, and baking in a 65 °C drying oven for $\geq$1 h to complete the reaction.

2. Microbead and Quantum Dot Barcode Label Combinations

Table S1 Green and red microbead barcode concentration combinations.

#	Green microbeads (beads/μL)	Red microbeads (beads/μL)	#	Green microbeads (beads/μL)	Red microbeads (beads/μL)
1	5.1×10^5	5.1×10^5	13	2.3×10^6	2.3×10^6
2	1.3×10^6	5.1×10^5	14	3.6×10^6	2.3×10^6
3	2.3×10^6	5.1×10^5	15	5.1×10^6	2.3×10^6
4	3.6×10^6	5.1×10^5	16	5.1×10^5	3.6×10^6
5	5.1×10^6	5.1×10^5	17	1.3×10^6	3.6×10^6
6	5.1×10^5	1.3×10^6	18	2.3×10^6	3.6×10^6
7	1.3×10^6	1.3×10^6	19	3.6×10^6	3.6×10^6
8	2.3×10^6	1.3×10^6	20	5.1×10^6	3.6×10^6
9	3.6×10^6	1.3×10^6	21	5.1×10^5	5.1×10^6
10	5.1×10^6	1.3×10^6	22	1.3×10^6	5.1×10^6
11	5.1×10^5	2.3×10^6	23	2.3×10^6	5.1×10^6
12	1.3×10^6	2.3×10^6	24	3.6×10^6	5.1×10^6

Table S2 QD625 and QD705 quantum dot barcode concentration combinations.

#	QD625 (pM)	QD705 (pM)	#	QD625 (pM)	QD705 (pM)	#	QD625 (pM)	QD705 (pM)	#	QD625 (pM)	QD705 (pM)
1	1.15×10^4	1.02×10^4	49	1.15×10^4	5.76×10^3	97	1.15×10^4	2.56×10^3	145	1.15×10^4	6.40×10^2
2	9.68×10^3	1.02×10^4	50	9.68×10^3	5.76×10^3	98	9.68×10^3	2.56×10^3	146	9.68×10^3	6.40×10^2
3	8.00×10^3	1.02×10^4	51	8.00×10^3	5.76×10^3	99	8.00×10^3	2.56×10^3	147	8.00×10^3	6.40×10^2
4	6.48×10^3	1.02×10^4	52	6.48×10^3	5.76×10^3	100	6.48×10^3	2.56×10^3	148	6.48×10^3	6.40×10^2
5	5.12×10^3	1.02×10^4	53	5.12×10^3	5.76×10^3	101	5.12×10^3	2.56×10^3	149	5.12×10^3	6.40×10^2
6	3.92×10^3	1.02×10^4	54	3.92×10^3	5.76×10^3	102	3.92×10^3	2.56×10^3	150	3.92×10^3	6.40×10^2
7	2.88×10^3	1.02×10^4	55	2.88×10^3	5.76×10^3	103	2.88×10^3	2.56×10^3	151	2.88×10^3	6.40×10^2
8	2.00×10^3	1.02×10^4	56	2.00×10^3	5.76×10^3	104	2.00×10^3	2.56×10^3	152	2.00×10^3	6.40×10^2
9	1.28×10^3	1.02×10^4	57	1.28×10^3	5.76×10^3	105	1.28×10^3	2.56×10^3	153	1.28×10^3	6.40×10^2
10	7.20×10^2	1.02×10^4	58	7.20×10^2	5.76×10^3	106	7.20×10^2	2.56×10^3	154	7.20×10^2	6.40×10^2
11	3.20×10^2	1.02×10^4	59	3.20×10^2	5.76×10^3	107	3.20×10^2	2.56×10^3	155	3.20×10^2	6.40×10^2
12	8.00×10^1	1.02×10^4	60	8.00×10^1	5.76×10^3	108	8.00×10^1	2.56×10^3	156	8.00×10^1	6.40×10^2
13	1.15×10^4	9.00×10^3	61	1.15×10^4	4.84×10^3	109	1.15×10^4	1.96×10^3	157	1.15×10^4	3.60×10^2
14	9.68×10^3	9.00×10^3	62	9.68×10^3	4.84×10^3	110	9.68×10^3	1.96×10^3	158	9.68×10^3	3.60×10^2
15	8.00×10^3	9.00×10^3	63	8.00×10^3	4.84×10^3	111	8.00×10^3	1.96×10^3	159	8.00×10^3	3.60×10^2
16	6.48×10^3	9.00×10^3	64	6.48×10^3	4.84×10^3	112	6.48×10^3	1.96×10^3	160	6.48×10^3	3.60×10^2
17	5.12×10^3	9.00×10^3	65	5.12×10^3	4.84×10^3	113	5.12×10^3	1.96×10^3	161	5.12×10^3	3.60×10^2
18	3.92×10^3	9.00×10^3	66	3.92×10^3	4.84×10^3	114	3.92×10^3	1.96×10^3	162	3.92×10^3	3.60×10^2
19	2.88×10^3	9.00×10^3	67	2.88×10^3	4.84×10^3	115	2.88×10^3	1.96×10^3	163	2.88×10^3	3.60×10^2
20	2.00×10^3	9.00×10^3	68	2.00×10^3	4.84×10^3	116	2.00×10^3	1.96×10^3	164	2.00×10^3	3.60×10^2
21	1.28×10^3	9.00×10^3	69	1.28×10^3	4.84×10^3	117	1.28×10^3	1.96×10^3	165	1.28×10^3	3.60×10^2
22	7.20×10^2	9.00×10^3	70	7.20×10^2	4.84×10^3	118	7.20×10^2	1.96×10^3	166	7.20×10^2	3.60×10^2
23	3.20×10^2	9.00×10^3	71	3.20×10^2	4.84×10^3	119	3.20×10^2	1.96×10^3	167	3.20×10^2	3.60×10^2
24	8.00×10^1	9.00×10^3	72	8.00×10^1	4.84×10^3	120	8.00×10^1	1.96×10^3	168	8.00×10^1	3.60×10^2
25	1.15×10^4	7.84×10^3	73	1.15×10^4	4.00×10^3	121	1.15×10^4	1.44×10^3	169	1.15×10^4	1.60×10^2
26	9.68×10^3	7.84×10^3	74	9.68×10^3	4.00×10^3	122	9.68×10^3	1.44×10^3	170	9.68×10^3	1.60×10^2
27	8.00×10^3	7.84×10^3	75	8.00×10^3	4.00×10^3	123	8.00×10^3	1.44×10^3	171	8.00×10^3	1.60×10^2
28	6.48×10^3	7.84×10^3	76	6.48×10^3	4.00×10^3	124	6.48×10^3	1.44×10^3	172	6.48×10^3	1.60×10^2
29	5.12×10^3	7.84×10^3	77	5.12×10^3	4.00×10^3	125	5.12×10^3	1.44×10^3	173	5.12×10^3	1.60×10^2
30	3.92×10^3	7.84×10^3	78	3.92×10^3	4.00×10^3	126	3.92×10^3	1.44×10^3	174	3.92×10^3	1.60×10^2
31	2.88×10^3	7.84×10^3	79	2.88×10^3	4.00×10^3	127	2.88×10^3	1.44×10^3	175	2.88×10^3	1.60×10^2
32	2.00×10^3	7.84×10^3	80	2.00×10^3	4.00×10^3	128	2.00×10^3	1.44×10^3	176	2.00×10^3	1.60×10^2
33	1.28×10^3	7.84×10^3	81	1.28×10^3	4.00×10^3	129	1.28×10^3	1.44×10^3	177	1.28×10^3	1.60×10^2
34	7.20×10^2	7.84×10^3	82	7.20×10^2	4.00×10^3	130	7.20×10^2	1.44×10^3	178	7.20×10^2	1.60×10^2
35	3.20×10^2	7.84×10^3	83	3.20×10^2	4.00×10^3	131	3.20×10^2	1.44×10^3	179	3.20×10^2	1.60×10^2
36	8.00×10^1	7.84×10^3	84	8.00×10^1	4.00×10^3	132	8.00×10^1	1.44×10^3	180	8.00×10^1	1.60×10^2
37	1.15×10^4	6.76×10^3	85	1.15×10^4	3.24×10^3	133	1.15×10^4	1.00×10^3	181	1.15×10^4	4.00×10^1
38	9.68×10^3	6.76×10^3	86	9.68×10^3	3.24×10^3	134	9.68×10^3	1.00×10^3	182	9.68×10^3	4.00×10^1
39	8.00×10^3	6.76×10^3	87	8.00×10^3	3.24×10^3	135	8.00×10^3	1.00×10^3	183	8.00×10^3	4.00×10^1
40	6.48×10^3	6.76×10^3	88	6.48×10^3	3.24×10^3	136	6.48×10^3	1.00×10^3	184	6.48×10^3	4.00×10^1
41	5.12×10^3	6.76×10^3	89	5.12×10^3	3.24×10^3	137	5.12×10^3	1.00×10^3	185	5.12×10^3	4.00×10^1
42	3.92×10^3	6.76×10^3	90	3.92×10^3	3.24×10^3	138	3.92×10^3	1.00×10^3	186	3.92×10^3	4.00×10^1
43	2.88×10^3	6.76×10^3	91	2.88×10^3	3.24×10^3	139	2.88×10^3	1.00×10^3	187	2.88×10^3	4.00×10^1
44	2.00×10^3	6.76×10^3	92	2.00×10^3	3.24×10^3	140	2.00×10^3	1.00×10^3	188	2.00×10^3	4.00×10^1
45	1.28×10^3	6.76×10^3	93	1.28×10^3	3.24×10^3	141	1.28×10^3	1.00×10^3	189	1.28×10^3	4.00×10^1
46	7.20×10^2	6.76×10^3	94	7.20×10^2	3.24×10^3	142	7.20×10^2	1.00×10^3	190	7.20×10^2	4.00×10^1
47	3.20×10^2	6.76×10^3	95	3.20×10^2	3.24×10^3	143	3.20×10^2	1.00×10^3	191	3.20×10^2	4.00×10^1
48	8.00×10^1	6.76×10^3	96	8.00×10^1	3.24×10^3	144	8.00×10^1	1.00×10^3	192	8.00×10^1	4.00×10^1

3. PIPE Chip Drop Formation Characterization

Reynolds Number Calculation. The Reynolds number was calculated independently for the water and oil phases as $Re = \frac{\rho v d}{\mu}$ where ρ is the fluid density (0.997 g/mL for water and 1.614 g/mL for HFE 7500), v is the fluid velocity (maximum of 0.4 m/s for water and 0.9 m/s for oil), d is the hydraulic diameter ($2w_{channel}$ for a square channel, or 100 μm), and μ is the dynamic viscosity (0.881 mPa·s for water and 1.243 mPa·s for oil). A maximum Reynolds number of 45 was calculated for the water inlet channel and 58 for the oil inlet channel. For laminar flow at a low Reynolds number (Re < 60 for PIPE chip operation), a linear correlation between P and Q is expected based upon the Hagen-Poiseuille relationship ($\Delta P = \frac{8\mu l}{\pi r^4} Q$). We generated a standard curve which verifies that Q_{water}/Q_{oil} is linearly correlated with P_{water}/P_{oil} ($R^2 = 0.916$) (Fig. S1).

Convert L_{drop} to V_{drop}. To fit the data of V_{drop} as a function of Q_{water}/Q_{oil} in Fig 3c, we converted L_{drop} to V_{drop} in the drop with a scaling law,[1] which relates drop length (L_{drop}) to Q_{water}/Q_{oil} (Equation 1). The V_{drop} is converted by approximating a drop in a channel as having a capsule geometry where $V_{drop} = \frac{\pi}{4} w_{channel}^2 (L_{drop} - \frac{1}{3} w_{channel})$.

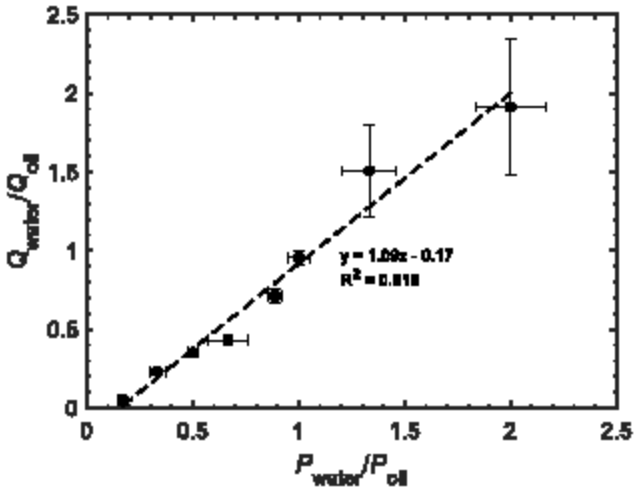

Fig. S1 Standard curve relating volumetric flowrate ratio to pressure ratio during PIPE chip operation. The relationship between the water/oil pressure ratio (P_{water}/P_{oil}) and water/oil volumetric flowrate ratio (Q_{water}/Q_{oil}) is linear. Error bars on the x-axis represent gauge error and error bars on the y-axis represent one standard deviation of volume measurements.

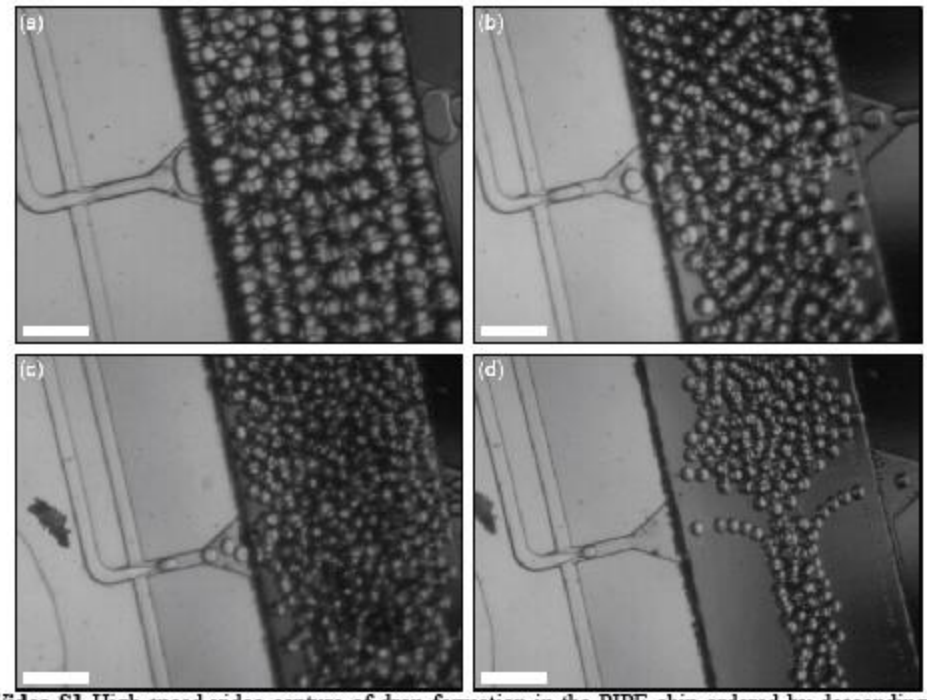

Video S1 High speed video capture of drop formation in the PIPE chip ordered by descending D_{drop}, for (a) high water pressure (■, P_{water} = 6 psig and P_{oil} = 3 psig, P_{water}/P_{oil} = 2), (b) low combined pressure (▼, P_{water} = 2 psig and P_{oil} = 3 psig, P_{water}/P_{oil} = 0.67), (c) high combined pressure (▲, P_{water} = 8 and P_{oil} = 12 psig, P_{water}/P_{oil} = 0.67), (d) and high oil pressure (♦, P_{water} = 2 psig and P_{oil} = 12 psig, P_{water}/P_{oil} = 0.17) conditions. Scale bars are 500 μm.

4. Barcoded Drop Detection

The drop fluorescence detection system for the microbead barcoded drop library consisted of a custom modified Nikon Diaphot 300 inverted microscope with two lasers, a set of dichroic mirrors and photomultiplier tubes (PMTs, Hamamatsu H10723-20).[2] The beams of the 50 mW, 473 nm laser (Suzhou Daheng Optics and Fine Mechanics Co., DHOM-W473-50mW) and the 50 mW, 405 nm laser (Changchun New Industries Optoelectronics Tech Co., MDL-III-405-50mW) were aligned together and coupled into the backport of the microscope where they were focused to a spot by the objective (40×, NA 0.60, Motic). The flowing of drops across the laser spot resulted in fluorescence detection by three PMTs split into three channels using dichroic and bandpass filters, Ch1: 445/40 nm (blue), Ch2: 525/50 nm (green), Ch3: >561 nm (red). A schematic of the drop fluorescence detection system and a detailed optical path representation are provided in Fig. S4. For bright field illumination, the light from the incandescent bulb was filtered by a 785/62 nm near-infrared (NIR) bandpass filter in order to not interfere with fluorescence detection measurements. A field programmable gate array (FPGA, National Instruments NI-7852R) was used to control the PMT gains and record fluorescence measurements using LabVIEW 2015.

The detection system for quantum dot barcoding consisted of a custom modified microscope, similar to the one described above. The beam of the laser (488 nm, 25 mW, Picarro) was coupled into the backport of the microscope and focused to a spot by the objective (40×, 0.85 NA, Leica). The light was split into three colors for fluorescent detection by using dichroic and bandpass filters for each channel, Ch1: 536/40 nm (green), Ch2: 632/22 nm (red), Ch3: 716/40 nm (far-red), and detected by a PMT for each channel.

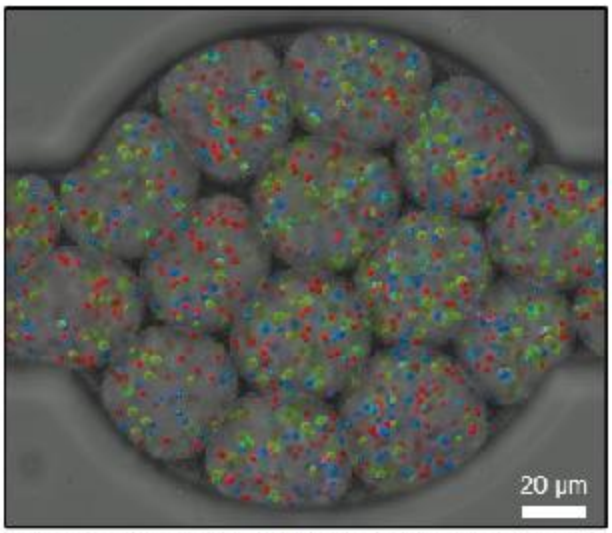

Fig. S2 Confocal image of fluorescent blue, green, and red microbeads in drops.

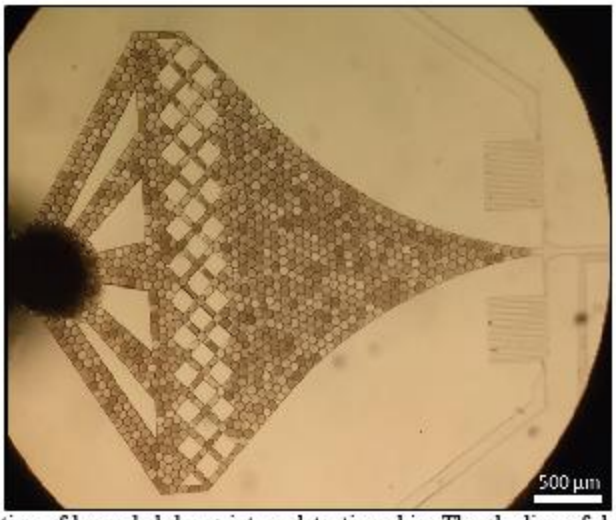

Fig. S3 Re-injection of barcoded drops into a detection chip. The shading of drops is due to the various microbead concentrations encapsulated in the drops.

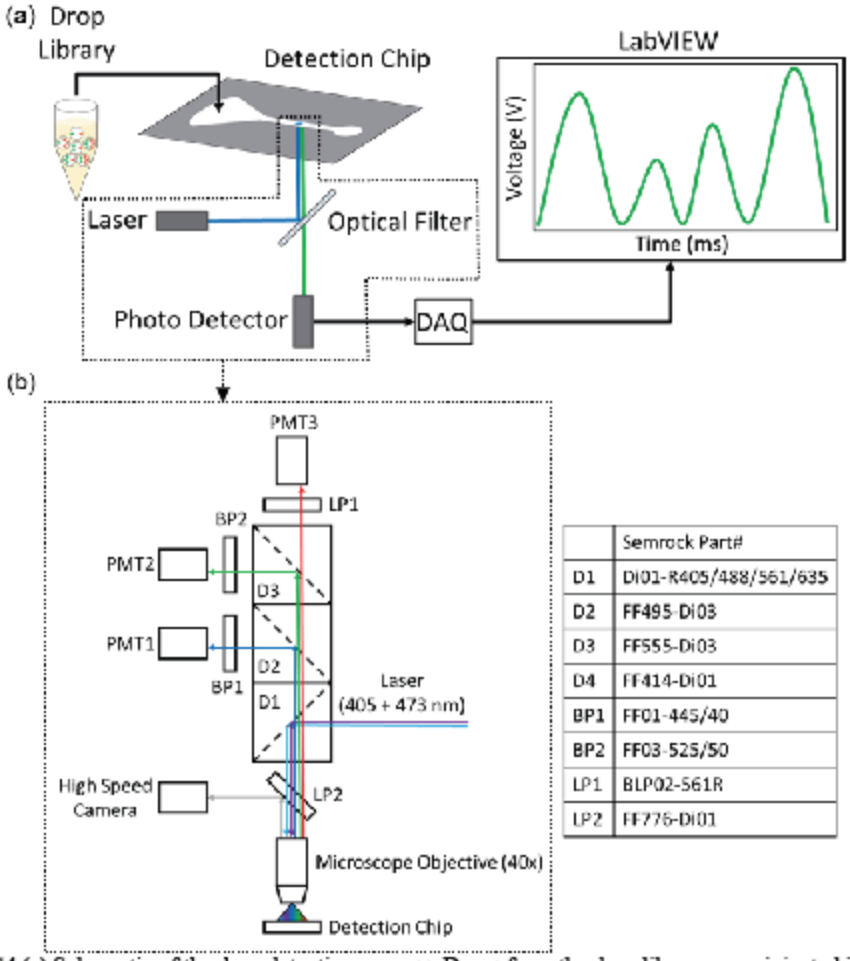

	Semrock Part#
D1	DI01-R405/488/561/635
D2	FF495-Di03
D3	FF555-Di03
D4	FF414-Di01
BP1	FF01-445/40
BP2	FF03-525/50
LP1	BLP02-561R
LP2	FF776-Di01

Fig. S4 (a) Schematic of the drop detection process. Drops from the drop library are reinjected into a detection chip mounted on the stage of a fluorescence detection microscope. The optical filter system allows laser light to be reflected towards the fluorescent barcoded drop while allowing emitted light from the drop to be detected by a photodetector in-line with the drop. The output of the photo detector is collected by a data acquisition device (DAQ) and then processed and recorded in a custom LabVIEW program. (b) Optical path for fluorescent drop detection. Coupled laser light enters the PMT stack and is reflected to the objective by the first dichroic mirror (D1). Emitted fluorescence passes through the first dichroic mirror (D1) and blue light is reflected by the second dichroic (D2), filtered by the first bandpass filter (BP1), and detected by the channel 1 PMT (PMT1). This process is repeated for green light while all red light above a wavelength of 555 nm is collected by PMT3. A 776 nm longpass filter (LP2) allows for transmitted light to be captured by a high-speed camera during fluorescent drop detection.

5. Discrimination of Discrete Signals in Barcoded Drop Libraries

Drop Library Clustering. The clustering algorithm Density-Based Spatial Clustering of Applications with Noise (DBSCAN)[3] was used to assign each drop detected to a cluster related to a specific barcode in the microbead and quantum dot barcoded drop library. DBSCAN is a density-based clustering method that groups together closely packed data points and marks outliers which lie in low-density regions as noise. Drops containing the same concentration of a fluorescence barcode should emit the same fluorescence signal, while factoring in signal noise, and will therefore create a data cluster that DBSCAN can find and tag with a specific identification code. DBSCAN uses two parameters for clustering, *minPts* defines the minimum number of data to include in a cluster and ε represents the maximum allowable distance between data in a cluster. The DBSCAN function in MATLAB was used for clustering data (introduced in MATLAB R2019a). For microbead barcoding, *minPts* was set to 50 and ε was set to 2.8×10^{-2} while for quantum dot barcoding, *minPts* was set to 25 and ε was set to 1×10^{-4}.

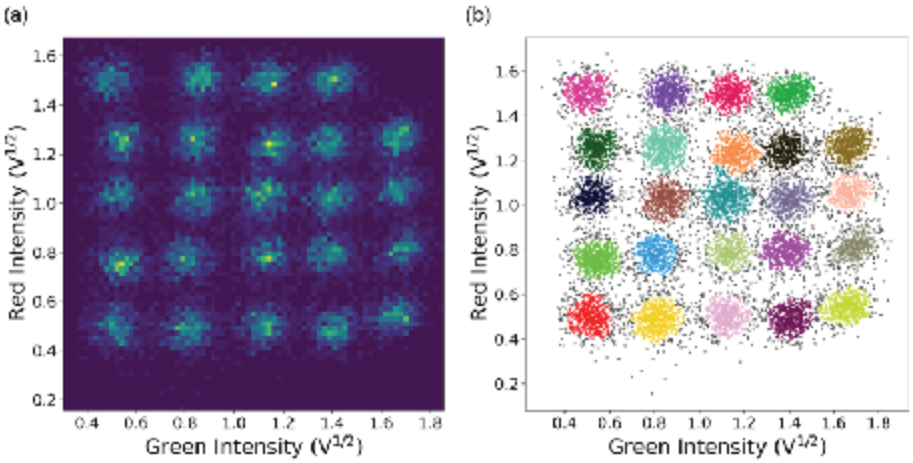

Fig. S5: Additional plots of the microbead drop library data using a (a) heatmap and (b) DBSCAN clustering where each cluster is labeled a different color and noise is shown in gray. The data was corrected for the spectral overlap here to better show the grid of barcoded clusters. To correct for the overlap, the compensation matrix [[1, -0.42], [-0.05, 1]] was applied.

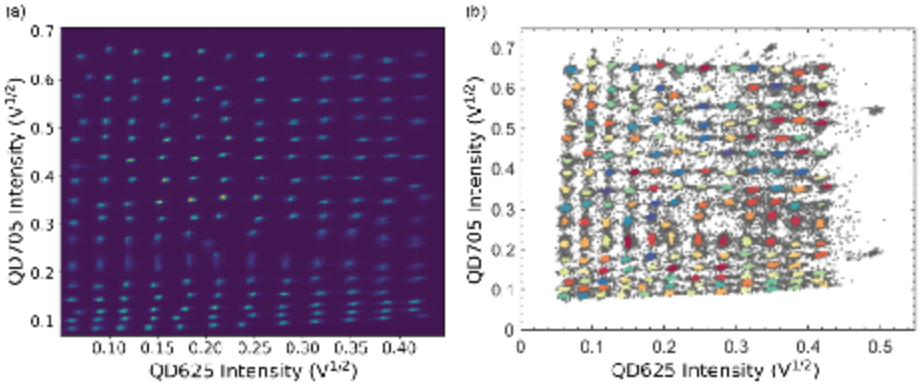

Fig. S6: Additional plots of the quantum dot drop library data using a (a) heatmap and (b) DBSCAN clustering where each cluster is labeled a different color and noise is shown in gray. Here, spectral overlap has not been corrected.

Schottky Equation. The Schottky equation adapted for PMTs with a voltage output,[4, 5] approximates shot noise and is defined here as:

$$\sigma_{\mathbf{shot}} = \sqrt{\mu_{\mathbf{itensity}} CGe\pi f_{\mathbf{3dB}}} \qquad \text{(Eq. S1)}$$

where $\sigma_{\mathbf{shot}}$ is the standard deviation of the PMT intensity measured in volts, $\mu_{\mathbf{intensity}}$ is the average measured PMT intensity in volts, C is a current to voltage conversion factor, G is the gain of the PMT (unitless), e is the fundamental charge of an electron (1.6×10^{-19} C), f_{3dB} is the 3 dB point in the PMT frequency distribution and is inversely proportional to the measurement time of the PMT. Values for C (0.1 V/μA), G across a range of control voltages, and f_{3dB} (200 kHz) are provided in the PMT spec sheet (0.1 V/μA).[6]

Calculation of Noise. The theoretical estimates of $\sigma_{particle}$ ($\sqrt{\lambda}$) are calculated for an arbitrary range of particle loading values (λ) of microbeads and quantum dots in drops. For microbeads, a range of 10^1 to 10^3 microbeads/drop is used. The number of quantum dots are calculated from the molarity, assuming each particle represents a molecule. Therefore, the particle concentration is calculated as the molarity multiplied by the drop volume (65 pl) and Avogadro's number (≈6.022 × 10^{23} mol^{-1}). A quantum dot concentration range of 1.3 × 10^0 to 1.3 × 10^5 pM is used and corresponds to a particle loading range of 5 × 10^2 to 5 × 10^6 QD/drop. For comparison with the barcode data (Fig. 4c-d, inset), the estimates of $\sigma_{particle}$ (Fig. 4c-d, inset, dashed red line) are converted from particles/drop to voltage using Fig. S7a and Fig. S7c for the microbead and quantum dot cases, respectively. The voltage ranges used for the *x*-axis are calculated by converting the range of microbead and quantum dot particles per drop to voltages using the respective standard curves in Fig. S7. The same voltage ranges are then used to calculate σ_{shot} from Eq. S1 (Fig. 4c-d, inset, dotted green line).

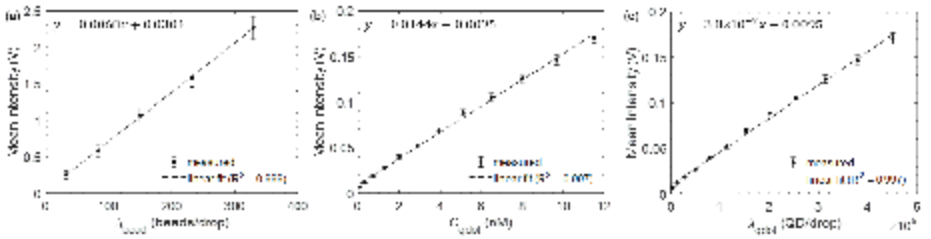

Fig. S7 Standard curves of the mean fluorescence intensity (V) versus (a) the number of microbeads per drop (λ_{bead}), (b) the concentration of quantum dots (C_{qdot}), and (c) number of quantum dots per drop (λ_{qdot}). Error bars represent one standard deviation.

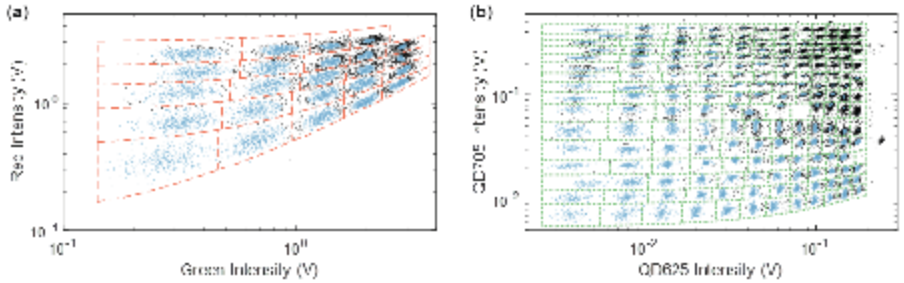

Fig. S8 Manual grouping of barcoded drop library data for (a) microbead and (b) quantum dot barcoded drops indicated by dashed red and dotted green lines, respectively.

6. Supplemental References

1. P. Garstecki, M. J. Fuerstman, H. A. Stone and G. M. Whitesides, *Lab on a Chip*, 2006, **6**, 437-446.
2. L. Mazutis, J. Gilbert, W. L. Ung, D. A. Weitz, A. D. Griffiths and J. A. Heyman, *Nature protocols*, 2013, **8**, 870-891.
3. M. Ester, H.-P. Kriegel, J. Sander and X. Xu, Portland, OR, 1996.
4. W. Schottky, *Annalen der physik*, 1918, **362**, 541-567.
5. R. L. McClain and J. C. Wright, *Journal of Chemical Education*, 2014, **91**, 1455-1457.
6. Hamamatsu, Specification sheet for H10723-20 photomultiplier tube, https://www.hamamatsu.com/resources/pdf/etd/H10723_TPMO1064E.pdf).

APPENDIX B

APPENDIX B: SUPPLEMENTAL INFORMATION FOR CHAPTER FIVE: AUTOMATED, MULTIPLEXED ANTIMICROBIAL SUSCEPTIBILITY TESTING AND QUANTITATIVE HETERORESISTANCE DETERMINATION IN MICROFLUIDIC DROPLETS

Time	P_{aq}	P_{oil}	Notes
0:00	0.5	0	
1:30	0.5	0.5	
2:30	1	1	
3:30	2	2	
4:00	2	3.5	operating pressures
4:00-6:00			equilibrate into waste
6:00-9:00			sample collection

Table B.1 PIPE chip operational protocol designed to gradually ramp to operating pressures. Time is reported as m:sec, and indicates the time at which the indicated pressures were set. All units are in PSI_g.

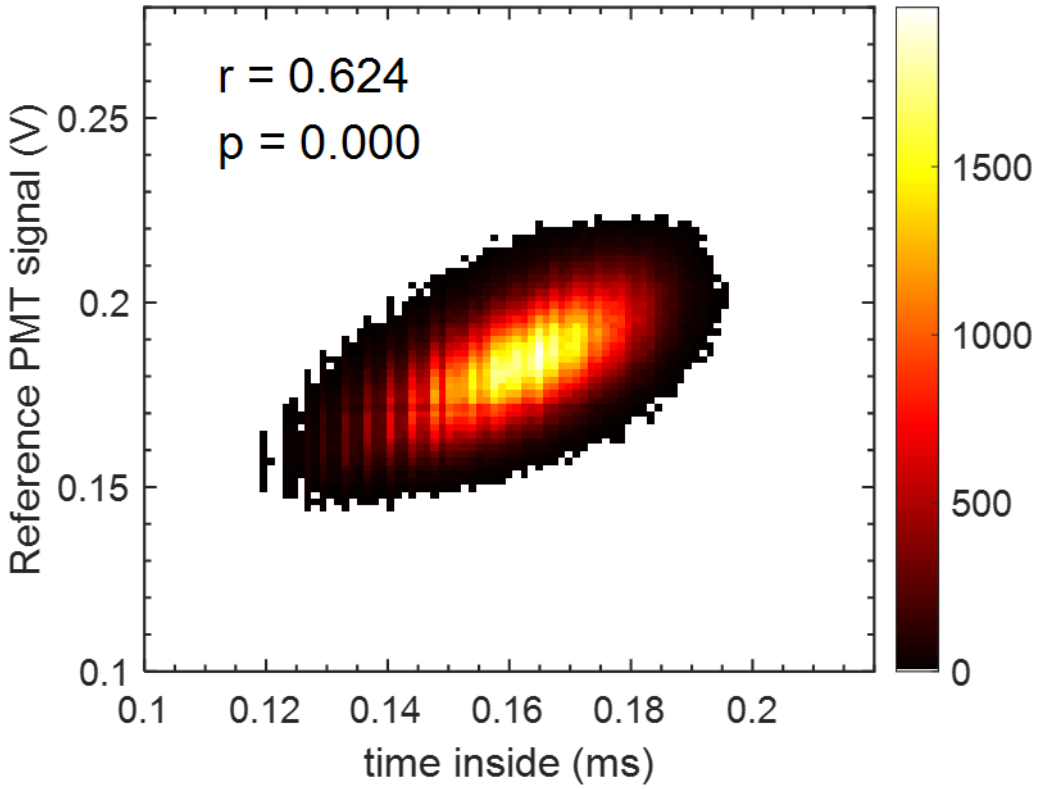

Figure B.1. Fluorescent dye intensity measured by droplet laser-induced fluorescence (LIF) correlates with droplet size. The LIF detector records a time inside measurement for each droplet, which is a residence time that the droplet spends underneath the laser. The data shown are from a single 36-plexed AST experiment, and the PMT signal corresponds to a reference dye intensity, which is a standardized signal imparted onto each droplet. We calculate a Pearson correlation coefficient, r = 0.624 with p-value = 0, indicating moderate positive correlation with statistical significance. Color bar indicates number of drops.

AlexaFluor 647 concentration

		1	2	3	4	5	6	
		0 nM	70 nM	176 nM	316 nM	492 nM	700 nM	
A	0 nM	NABC	0.0156	0.0313	0.0625	0.125	0.25	gentamicin
B	70 nM	0.5	1	2	4	8	16	meropenem
C	176 nM	0.39063	3.125	6.25	12.5	25	50	cefotaxime
D	316 nM	0.03125	0.0625	0.125	0.25	0.5	1	colistin
E	492 nM	0.01563	0.0313	0.0625	0.125	0.25	0.5	amikacin
F	700 nM	0.01563	0.0313	0.0625	0.125	0.25	0.5	tobramycin

AlexaFluor 568 concentration

Figure B.2. Microtiter plate layout for PIPE chip emulsification. Barcoding dye conditions in two channels are listed along the columns and rows.

Antimicrobial	MIC (µg / mL)	Stdv	CV (%)
Meropenem	9.03	0.812	8.99
Cefotaxime	0.13	0.003	2.31
Tobramycin	0.47	0.167	35.53
Gentamicin	0.29	0.074	25.52
Colistin	0.91	0.178	19.56
Amikacin	0.48	0.135	28.13

Table B.2 MIC estimation by reference method. Susceptibility of the model organism was assayed against the panel of antimicrobials by broth microdilution. Results shown are from 9 biological replicates.

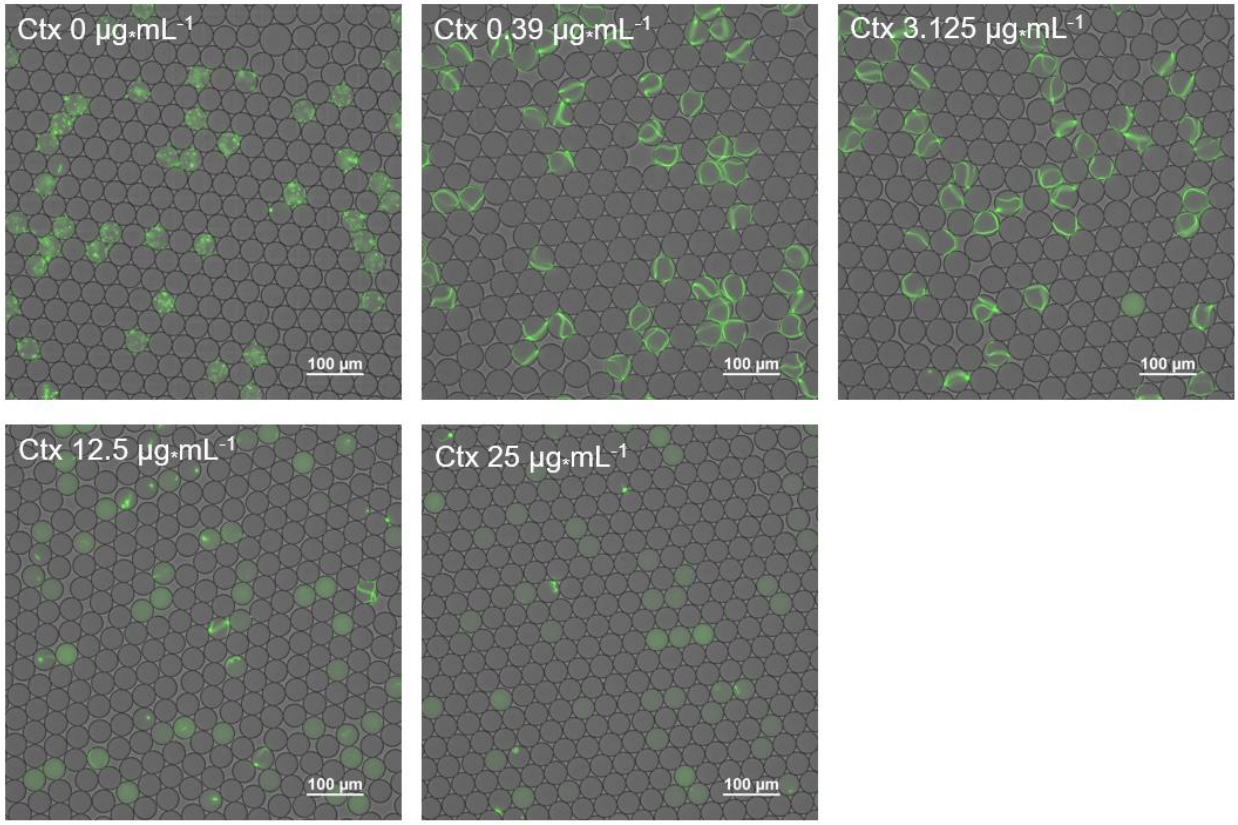

Figure B.3 Cefotaxime exposure results in filamentous physiology for *E. coli.* Fluorescence images of droplets loaded with single GFP-*E. coli* cells and variable cefotaxime condition, after 5 hour growth period. Cefotaxime condition is indicated by the text in each image. Filamentous phenotype can be observed for [cefotaxime] < 12.5 µg/mL. Cell lysis results in the droplet being dyed green by cellular GFP at [cefotaxime] ≥ 12.5 µg/mL. Ctx, cefotaxime.

REFERENCES CITED

1. Organization, W.H. *Antimicrobial Resistance*. 2023 [cited 2025; Available from: https://www.who.int/news-room/fact-sheets/detail/antimicrobial-resistance.

2. Organization, W.H., *WHO Bacterial Priority Pathogens List, 2024: bacterial pathogens of public health importance to guide research, development and strategies to prevent and control antimicrobial resistance*. 2024: Geneva.

3. Group, W.B. *Drug-Resistant Infections: A Threat to our Economic Future*. 2017; Available from: https://www.worldbank.org/en/topic/health/publication/drug-resistant-infections-a-threat-to-our-economic-future.

4. Mantravadi, P.K., et al., *The Quest for Novel Antimicrobial Compounds: Emerging Trends in Research, Development, and Technologies.* Antibiotics (Basel), 2019. **8**(1).

5. Breijyeh, Z., B. Jubeh, and R. Karaman, *Resistance of Gram-Negative Bacteria to Current Antibacterial Agents and Approaches to Resolve It.* Molecules, 2020. **25**(6).

6. Gauba, A. and K.M. Rahman, *Evaluation of Antibiotic Resistance Mechanisms in Gram-Negative Bacteria.* Antibiotics (Basel), 2023. **12**(11).

7. Nishino, K., et al., *Function and Inhibitory Mechanisms of Multidrug Efflux Pumps.* Front Microbiol, 2021. **12**: p. 737288.

8. Li, X.Z., P. Plesiat, and H. Nikaido, *The challenge of efflux-mediated antibiotic resistance in Gram-negative bacteria.* Clin Microbiol Rev, 2015. **28**(2): p. 337-418.

9. Fernandez, L. and R.E. Hancock, *Adaptive and mutational resistance: role of porins and efflux pumps in drug resistance.* Clin Microbiol Rev, 2012. **25**(4): p. 661-81.

10. Tamma, P.D., et al., *Infectious Diseases Society of America 2024 Guidance on the Treatment of Antimicrobial-Resistant Gram-Negative Infections.* Clin Infect Dis, 2024.

11. Reygaert, W.C., *An overview of the antimicrobial resistance mechanisms of bacteria.* AIMS Microbiol, 2018. **4**(3): p. 482-501.

12. James S. Lewis II, P., FIDSA, et al. *CLSI M100-ED35:2025 Performance Standards for Antimicrobial Susceptibility Testing*. 2025 [cited 2025; 35:[Available from: https://em100.edaptivedocs.net/GetDoc.aspx?doc=CLSI%20M100%20ED35:2025&scope=user.

13. Schumacher, A., et al., *In vitro antimicrobial susceptibility testing methods: agar dilution to 3D tissue-engineered models.* Eur J Clin Microbiol Infect Dis, 2018. **37**(2): p. 187-208.

14. Jorgensen, J.H. and M.J. Ferraro, *Antimicrobial susceptibility testing: a review of general principles and contemporary practices.* Clin Infect Dis, 2009. **49**(11): p. 1749-55.

15. Karlowsky, J.A.R., S. S.; Patel, J. B., *Antimicrobial Susceptibility Testing Systems.* Manual of Clinical Microbiology, 2023. **13**: p. 1-18.

16. Mouton, J.W., et al., *Variation of MIC measurements: the contribution of strain and laboratory variability to measurement precision.* J Antimicrob Chemother, 2018. **73**(9): p. 2374-2379.

17. Sabhachandani, P., et al., *Integrated microfluidic platform for rapid antimicrobial susceptibility testing and bacterial growth analysis using bead-based biosensor via fluorescence imaging.* Microchimica Acta, 2017. **184**(12): p. 4619-4628.

18. van Belkum, A., et al., *Innovative and rapid antimicrobial susceptibility testing systems.* Nat Rev Microbiol, 2020. **18**(5): p. 299-311.

19. van Belkum, A. and W.M. Dunne, Jr., *Next-generation antimicrobial susceptibility testing.* J Clin Microbiol, 2013. **51**(7): p. 2018-24.

20. Nseir, S. and P. Povoa, *Multipathogen real-time PCR system adds benefit for my patients: no.* Intensive Care Med, 2015. **41**(3): p. 531-3.

21. Nordmann, P. and L. Poirel, *Epidemiology and Diagnostics of Carbapenem Resistance in Gram-negative Bacteria.* Clin Infect Dis, 2019. **69**(Suppl 7): p. S521-S528.

22. Reszetnik, G., et al., *Next-generation rapid phenotypic antimicrobial susceptibility testing.* Nat Commun, 2024. **15**(1): p. 9719.

23. Schrader, S.M., H. Botella, and J. Vaubourgeix, *Reframing antimicrobial resistance as a continuous spectrum of manifestations.* Curr Opin Microbiol, 2023. **72**: p. 102259.

24. Sanchez-Romero, M.A. and J. Casadesus, *Contribution of phenotypic heterogeneity to adaptive antibiotic resistance.* Proc Natl Acad Sci U S A, 2014. **111**(1): p. 355-60.

25. Reyes Ruiz, L.M., C.L. Williams, and R. Tamayo, *Enhancing bacterial survival through phenotypic heterogeneity.* PLoS Pathog, 2020. **16**(5): p. e1008439.

26. Sherry, J. and E.H. Rego, *Phenotypic Heterogeneity in Pathogens.* Annu Rev Genet, 2024. **58**(1): p. 183-209.

27. Hernandez-Beltran, J.C.R., et al., *Plasmid-mediated phenotypic noise leads to transient antibiotic resistance in bacteria.* Nat Commun, 2024. **15**(1): p. 2610.

28. Cooper, G.A., et al., *The evolution of mechanisms to produce phenotypic heterogeneity in microorganisms.* Nat Commun, 2022. **13**(1): p. 195.

29. Nicoloff, H., et al., *The high prevalence of antibiotic heteroresistance in pathogenic bacteria is mainly caused by gene amplification.* Nat Microbiol, 2019. **4**(3): p. 504-514.

30. Dorman, C.J., *Variable DNA topology is an epigenetic generator of physiological heterogeneity in bacterial populations.* Mol Microbiol, 2023. **119**(1): p. 19-28.

31. Band, V.I., et al., *Antibiotic failure mediated by a resistant subpopulation in Enterobacter cloacae.* Nat Microbiol, 2016. **1**(6): p. 16053.

32. Band, V.I. and D.S. Weiss, *Heteroresistance: A cause of unexplained antibiotic treatment failure?* PLoS Pathog, 2019. **15**(6): p. e1007726.

33. Andersson, D.I., H. Nicoloff, and K. Hjort, *Mechanisms and clinical relevance of bacterial heteroresistance.* Nat Rev Microbiol, 2019. **17**(8): p. 479-496.

34. Roch, M., R. Sierra, and D.O. Andrey, *Antibiotic heteroresistance in ESKAPE pathogens, from bench to bedside.* Clin Microbiol Infect, 2023. **29**(3): p. 320-325.

35. Wootton, M., et al., *A modified population analysis profile (PAP) method to detect hetero-resistance to vancomycin in staphylococcus aureus in UK hospital.* Journal of Antimicrobial Chemotherapy, 2001. **47**: p. 399-403.

36. Satola, S.W., et al., *Comparison of detection methods for heteroresistant vancomycin-intermediate Staphylococcus aureus, with the population analysis profile method as the reference method.* J Clin Microbiol, 2011. **49**(1): p. 177-83.

37. Abe, R., et al., *Population analysis profiling: is it still the gold standard for the determination of heteroresistance in carbapenemase-producing Enterobacteriaceae?* Int J Antimicrob Agents, 2022. **60**(4): p. 106644.

38. El-Halfawy, O.M. and M.A. Valvano, *Antimicrobial heteroresistance: an emerging field in need of clarity.* Clin Microbiol Rev, 2015. **28**(1): p. 191-207.

39. Pal, A. and D.I. Andersson, *Bacteria can compensate the fitness costs of amplified resistance genes via a bypass mechanism.* Nat Commun, 2024. **15**(1): p. 2333.

40. Huh, D. and J. Paulsson, *Non-genetic heterogeneity from stochastic partitioning at cell division.* Nat Genet, 2011. **43**(2): p. 95-100.

41. Nicoloff, H., et al., *Three concurrent mechanisms generate gene copy number variation and transient antibiotic heteroresistance.* Nat Commun, 2024. **15**(1): p. 3981.

42. Lyu, F., et al., *Phenotyping antibiotic resistance with single-cell resolution for the detection of heteroresistance.* Sensors and Actuators B: Chemical, 2018. **270**: p. 396-404.

43. Osaid, M., et al., *A multiplexed nanoliter array-based microfluidic platform for quick, automatic antimicrobial susceptibility testing.* Lab Chip, 2021. **21**(11): p. 2223-2231.

44. Artemova, T., et al., *Isolated cell behavior drives the evolution of antibiotic resistance.* Mol Syst Biol, 2015. **11**(7): p. 822.

45. Hsieh, K., et al., *Combating Antimicrobial Resistance via Single-Cell Diagnostic Technologies Powered by Droplet Microfluidics.* Acc Chem Res, 2022. **55**(2): p. 123-133.

46. Wu, W., et al., *Direct single-cell antimicrobial susceptibility testing of Escherichia coli in urine using a ready-to-use 3D microwell array chip.* Lab Chip, 2023. **23**(10): p. 2399-2410.

47. Li, H., et al., *Single-cell pathogen diagnostics for combating antibiotic resistance.* Nat Rev Methods Primers, 2023. **3**.

48. Baltekin, O., et al., *Antibiotic susceptibility testing in less than 30 min using direct single-cell imaging.* Proc Natl Acad Sci U S A, 2017. **114**(34): p. 9170-9175.

49. Udekwu, K.I., et al., *Functional relationship between bacterial cell density and the efficacy of antibiotics.* J Antimicrob Chemother, 2009. **63**(4): p. 745-57.

50. Postek, W., N. Pacocha, and P. Garstecki, *Microfluidics for antibiotic susceptibility testing.* Lab Chip, 2022. **22**(19): p. 3637-3662.

51. Xia, Y. and G.M. Whitesides, *Soft Lithography.* Angew Chem Int Ed Engl, 1998. **37**(5): p. 550-575.

52. Campo, A.d. and C. Greiner, *SU-8: a photoresist for high-aspect-ratio and 3D submicron lithography.* Journal of Micromechanics and Microengineering, 2007. **17**(6): p. R81-R95.

53. Scott, S.M. and Z. Ali, *Fabrication Methods for Microfluidic Devices: An Overview.* Micromachines (Basel), 2021. **12**(3).

54. Gale, B.K., et al., *A Review of Current Methods in Microfluidic Device Fabrication and Future Commercialization Prospects.* Inventions, 2018. **3**(3).

55. Whitesides, G.M. and A.D. Stroock, *Flexible Methods for Microfluidics.* Physics Today, 2001. **54**(6): p. 42-48.

56. Stone, H.A. and S. Kim, *Microfluidics: Basic issues, applications, and challenges.* AIChE Journal, 2004. **47**(6): p. 1250-1254.

57. Liu, Y. and I. Papautsky, *Heterogeneous Immunoassay Using Channels and Droplets in a Digital Microfluidic Platform.* Micromachines (Basel), 2019. **10**(2).

58. Besanjideh, M., et al., *Simple Method for On-Demand Droplet Trapping in a Microfluidic Device Based on the Concept of Hydrodynamic Resistance.* Langmuir, 2024. **40**(18): p. 9406-9413.

59. Song, H., J.D. Tice, and R.F. Ismagilov, *A microfluidic system for controlling reaction networks in time.* Angew Chem Int Ed Engl, 2003. **42**(7): p. 768-72.

60. Jin, B.-J. and J.Y. Yoo, *Visualization of droplet merging in microchannels using micro-PIV.* Experiments in Fluids, 2011. **52**(1): p. 235-245.

61. Baret, J.C., et al., *Fluorescence-activated droplet sorting (FADS): efficient microfluidic cell sorting based on enzymatic activity.* Lab Chip, 2009. **9**(13): p. 1850-8.

62. Chung, C.H.Y., et al., *Droplet-Based Microfluidic Synthesis of Hydrogel Microparticles via Click Chemistry-Based Cross-Linking for the Controlled Release of Proteins.* ACS Appl Bio Mater, 2021. **4**(8): p. 6186-6194.

63. Agresti, J.J., et al., *Ultrahigh-throughput screening in drop-based microfluidics for directed evolution.* Proc Natl Acad Sci U S A, 2010. **107**(9): p. 4004-9.

64. Kulesa, A., et al., *Combinatorial drug discovery in nanoliter droplets.* Proc Natl Acad Sci U S A, 2018. **115**(26): p. 6685-6690.

65. Utada, A.S., et al., *Dripping, Jetting, Drops, and Wetting: The Magic of Microfluidics.* MRS Bulletin, 2011. **32**(9): p. 702-708.

66. Utada, A.S., et al., *Dripping to jetting transitions in coflowing liquid streams.* Phys Rev Lett, 2007. **99**(9): p. 094502.

67. Abate, A.R., et al., *Impact of inlet channel geometry on microfluidic drop formation.* Phys Rev E Stat Nonlin Soft Matter Phys, 2009. **80**(2 Pt 2): p. 026310.

68. Fu, T., et al., *Droplet formation and breakup dynamics in microfluidic flow-focusing devices: From dripping to jetting.* Chemical Engineering Science, 2012. **84**: p. 207-217.

69. Baroud, C.N., F. Gallaire, and R. Dangla, *Dynamics of microfluidic droplets.* Lab Chip, 2010. **10**(16): p. 2032-45.

70. Postek, W. and P. Garstecki, *Droplet Microfluidics for High-Throughput Analysis of Antibiotic Susceptibility in Bacterial Cells and Populations.* Acc Chem Res, 2022. **55**(5): p. 605-615.

71. Kaminski, T.S., O. Scheler, and P. Garstecki, *Droplet microfluidics for microbiology: techniques, applications and challenges.* Lab Chip, 2016. **16**(12): p. 2168-87.

72. Ruszczak, A., et al., *Droplet-based methods for tackling antimicrobial resistance.* Curr Opin Biotechnol, 2022. **76**: p. 102755.

73. Bartkova, S., et al., *A Guide to Biodetection in Droplets.* Anal Chem, 2024. **96**(24): p. 9745-9755.

74. Wang, Y., et al., *Cascade filtration and droplet digital detection integrated microfluidic assay enables isolating culture-free phenotypic identification of carbapenem-resistant organisms.* Biosens Bioelectron, 2023. **220**: p. 114863.

75. Jeong, Y., et al., *Color-Coded Droplets and Microscopic Image Analysis for Multiplexed Antibiotic Susceptibility Testing.* Biosensors (Basel), 2021. **11**(8).

76. Samimi, A., S. Hengoju, and M.A. Rosenbaum, *Combinatorial sample preparation platform for droplet-based applications in microbiology.* Sensors and Actuators B: Chemical, 2024. **417**.

77. Riti, J., et al., *Combining deep learning and droplet microfluidics for rapid and label-free antimicrobial susceptibility testing of colistin.* Biosens Bioelectron, 2024. **257**: p. 116301.

78. Kim, J.S., et al., *Label-free single-cell antimicrobial susceptibility testing in droplets with concentration gradient generation.* Lab Chip, 2024. **24**(24): p. 5274-5289.

79. Le Quellec, L., et al., *Measuring single-cell susceptibility to antibiotics within monoclonal bacterial populations.* PLoS One, 2024. **19**(8): p. e0303630.

80. Kang, W., et al., *Ultrafast Parallelized Microfluidic Platform for Antimicrobial Susceptibility Testing of Gram Positive and Negative Bacteria.* Anal Chem, 2019. **91**(9): p. 6242-6249.

81. Zhang, P., et al., *A Cascaded Droplet Microfluidic Platform Enables High-Throughput Single Cell Antibiotic Susceptibility Testing at Scale.* Small Methods, 2022. **6**(1): p. e2101254.

82. Yan, J.D., et al., *A Label-Free Droplet Sorting Platform Integrating Dielectrophoretic Separation for Estimating Bacterial Antimicrobial Resistance.* Biosensors (Basel), 2024. **14**(5).

83. Scheler, O., et al., *Droplet-based digital antibiotic susceptibility screen reveals single-cell clonal heteroresistance in an isogenic bacterial population.* Sci Rep, 2020. **10**(1): p. 3282.

84. Kaushik, A.M., et al., *Accelerating bacterial growth detection and antimicrobial susceptibility assessment in integrated picoliter droplet platform.* Biosens Bioelectron, 2017. **97**: p. 260-266.

85. Churski, K., et al., *Rapid screening of antibiotic toxicity in an automated microdroplet system.* Lab Chip, 2012. **12**(9): p. 1629-37.

86. Li, H., et al., *Combinatorial nanodroplet platform for screening antibiotic combinations.* Lab Chip, 2022. **22**(3): p. 621-631.

87. Kaushik, A.M., et al., *Droplet-Based Single-Cell Measurements of 16S rRNA Enable Integrated Bacteria Identification and Pheno-Molecular Antimicrobial Susceptibility Testing from Clinical Samples in 30 min.* Adv Sci (Weinh), 2021. **8**(6): p. 2003419.

88. Zhang, P., et al., *Facile syringe filter-enabled bacteria separation, enrichment, and buffer exchange for clinical isolation-free digital detection and characterization of bacterial pathogens in urine.* Analyst, 2021. **146**(8): p. 2475-2483.

89. Pacocha, N., et al., *High-Throughput Monitoring of Bacterial Cell Density in Nanoliter Droplets: Label-Free Detection of Unmodified Gram-Positive and Gram-Negative Bacteria.* Anal Chem, 2021. **93**(2): p. 843-850.

90. Liu, X., et al., *High-throughput screening of antibiotic-resistant bacteria in picodroplets.* Lab Chip, 2016. **16**(9): p. 1636-43.

91. Postek, W., et al., *Microfluidic screening of antibiotic susceptibility at a single-cell level shows the inoculum effect of cefotaxime on E. coli.* Lab Chip, 2018. **18**(23): p. 3668-3677.

92. Pacocha, N., et al., *You will know by its tail: a method for quantification of heterogeneity of bacterial populations using single-cell MIC profiling.* Lab Chip, 2022. **22**(22): p. 4317-4326.

93. Yang, D., et al., *Artificial intelligence-accelerated high-throughput screening of antibiotic combinations on a microfluidic combinatorial droplet system.* Lab Chip, 2023. **23**(18): p. 3961-3977.

94. Pratt, S.L., et al., *DropSOAC: Stabilizing Microfluidic Drops for Time-Lapse Quantification of Single-Cell Bacterial Physiology.* Front Microbiol, 2019. **10**: p. 2112.

95. Hengoju, S., et al., *Optofluidic detection setup for multi-parametric analysis of microbiological samples in droplets.* Biomicrofluidics, 2020. **14**(2): p. 024109.

96. Sklavounos, A.A., et al., *Bacterial classification and antibiotic susceptibility testing on an integrated microfluidic platform.* Lab Chip, 2021. **21**(21): p. 4208-4222.

97. Nguyen, A.V., et al., *Ladder-shaped microfluidic system for rapid antibiotic susceptibility testing.* Communications Engineering, 2023. **2**(1).

98. Avesar, J., et al., *Rapid phenotypic antimicrobial susceptibility testing using nanoliter arrays.* Proc Natl Acad Sci U S A, 2017. **114**(29): p. E5787-E5795.

99. Opalski, A.S., et al., *Combinatorial Antimicrobial Susceptibility Testing Enabled by Non-Contact Printing.* Micromachines (Basel), 2020. **11**(2).

100. Jalali, F., F. Ellett, and D. Irimia, *Rapid antibiotic sensitivity testing in microwell arrays.* Technology (Singap World Sci), 2017. **5**(2): p. 107-114.

101. Spencer, D.C., et al., *A fast impedance-based antimicrobial susceptibility test.* Nat Commun, 2020. **11**(1): p. 5328.

102. Kara, V., et al., *Microfluidic detection of movements of Escherichia coli for rapid antibiotic susceptibility testing.* Lab Chip, 2018. **18**(5): p. 743-753.

103. Gopalakrishnan, S., et al., *Rapid antimicrobial susceptibility testing using carbon screen printed electrodes in a microfluidic device.* Sci Rep, 2025. **15**(1): p. 5133.

104. Yang, Y., K. Gupta, and K.L. Ekinci, *All-electrical monitoring of bacterial antibiotic susceptibility in a microfluidic device.* Proc Natl Acad Sci U S A, 2020. **117**(20): p. 10639-10644.

105. Alonso-Tarres, C., et al., *Bacteriuria and phenotypic antimicrobial susceptibility testing in 45 min by point-of-care Sysmex PA-100 System: first clinical evaluation.* Eur J Clin Microbiol Infect Dis, 2024. **43**(8): p. 1533-1543.

106. Sujith, S., A.P. Solomon, and J.B.B. Rayappan, *Comprehensive insights into UTIs: from pathophysiology to precision diagnosis and management.* Front Cell Infect Microbiol, 2024. **14**: p. 1402941.

107. Filbrun, A.B., et al., *Rapid, label-free antibiotic susceptibility determined directly from positive blood culture.* Cytometry A, 2022. **101**(7): p. 564-576.

108. Pitt, W.G., et al., *Rapid separation of bacteria from blood-review and outlook.* Biotechnol Prog, 2016. **32**(4): p. 823-39.

109. Alves, I.P. and N.M. Reis, *Microfluidic smartphone quantitation of Escherichia coli in synthetic urine.* Biosens Bioelectron, 2019. **145**: p. 111624.

110. Cui, X., et al., *Smartphone-based rapid quantification of viable bacteria by single-cell microdroplet turbidity imaging.* Analyst, 2018. **143**(14): p. 3309-3316.

111. Parmanik, A., et al., *Current Treatment Strategies Against Multidrug-Resistant Bacteria: A Review.* Curr Microbiol, 2022. **79**(12): p. 388.

112. Choi, J., et al., *A rapid antimicrobial susceptibility test based on single-cell morphological analysis.* Sci Transl Med, 2014. **6**(267): p. 267ra174.

113. Malmberg, C., et al., *Evaluation of the Speed, Accuracy and Precision of the QuickMIC Rapid Antibiotic Susceptibility Testing Assay With Gram-Negative Bacteria in a Clinical Setting.* Front Cell Infect Microbiol, 2022. **12**: p. 758262.

114. Marschal, M., et al., *Evaluation of the Accelerate Pheno System for Fast Identification and Antimicrobial Susceptibility Testing from Positive Blood Cultures in Bloodstream Infections Caused by Gram-Negative Pathogens.* J Clin Microbiol, 2017. **55**(7): p. 2116-2126.

115. QuantaMatrix. *dRast, Direct & Rapid Antimicrobial Susceptibility Test.* 2023.

116. Biosensors, A. *LifeScale: Innovation in Phenotypic Susceptibility Testing.* . 2023; Available from: https://affinitybio.com/.

117. G., R.A., *Resistell AG - Developing Leading Rapid AST Solution.* 2023.

118. Pujol-Vila, F., R. Villa, and M. Alvarez, *Nanomechanical Sensors as a Tool for Bacteria Detection and Antibiotic Susceptibility Testing.* Frontiers in Mechanical Engineering, 2020. **6**.

119. Sciambi, A. and A.R. Abate, *Accurate microfluidic sorting of droplets at 30 kHz.* Lab Chip, 2015. **15**(1): p. 47-51.

120. Li, M., et al., *Droplet flow cytometry for single-cell analysis.* RSC Adv, 2021. **11**(34): p. 20944-20960.

121. Mazutis, L., et al., *Single-cell analysis and sorting using droplet-based microfluidics.* Nat Protoc, 2013. **8**(5): p. 870-91.

122. Schaefer, R.W., *ULTRA HIGH-THROUGHPUT FLUORESCENCE DETECTION FOR SINGLE CELL APPLICATIONS IN DROP MICROFLUIDICS*, in *Chemical and Biological Engineering*. 2016, Montana State University.

123. Janiak, F.K., et al., *Non-telecentric two-photon microscopy for 3D random access mesoscale imaging.* Nat Commun, 2022. **13**(1): p. 544.

124. Sasian, J., *Aberrations in Optical Systems*, in *Introduction to Aberrations in Optical Imaging Systems*. 2017.

125. Horiba. *What's the aberration, and why do we need to correct it?* [cited 2025; Available from: https://www.horiba.com/esp/scientific/technologies/vacuum-ultra-violet-spectroscopy/aberration/.

126. Thorlabs. *FiberPort Collimators / Couplers*. 2025; Available from: https://www.thorlabs.com/newgrouppage9.cfm?objectgroup_id=2940.

127. Chen, Y., S. Narayan, and C.S. Dutcher, *Phase-Dependent Surfactant Transport on the Microscale: Interfacial Tension and Droplet Coalescence.* Langmuir, 2020. **36**(49): p. 14904-14923.

128. UCSF. *Microdroplets: Reinjection*. 2023; Available from: https://www.abatelab.org/reinjection.

129. Niu, X., et al., *Pillar-induced droplet merging in microfluidic circuits.* Lab Chip, 2008. **8**(11): p. 1837-41.

130. Chen, C.H., et al., *Antimicrobial susceptibility testing using high surface-to-volume ratio microchannels.* Anal Chem, 2010. **82**(3): p. 1012-9.

131. Jin, J., et al., *Coalescence Processes of Droplets and Liquid Marbles.* Micromachines (Basel), 2017. **8**(11).

132. Bibette, J.M., D. C.; Witten, T. A.; Weitz, D. A., *Stability Criteria for Emulsions.* Physical Review Letters, 1992. **69**(16): p. 2439-2442.

133. Hinderink, E., et al., *Coalescence of concentrated emulsions in microfluidic constrictions through avalanches.* Sci Rep, 2025. **15**(1): p. 5720.

134. Instruments, E. *Laser Spot Size in a Microscope*. 2021; Available from: https://www.edinst.com/resource/laser-spot-size-in-a-microscope/.

135. Huebner, A., et al., *Quantitative detection of protein expression in single cells using droplet microfluidics.* Chem Commun (Camb), 2007(12): p. 1218-20.

136. Hamamatsu. *Photosensor Modules H10723 Series*. 2016; Available from: https://www.hamamatsu.com/content/dam/hamamatsu-photonics/sites/documents/99_SALES_LIBRARY/etd/H10723_TPMO1064E.pdf.

137. Zath, G.K., et al., *Rapid parallel generation of a fluorescently barcoded drop library from a microtiter plate using the plate-interfacing parallel encapsulation (PIPE) chip.* Lab Chip, 2022. **22**(23): p. 4735-4745.

138. Ester, M.K.H.-P.S., J.; Xu, X. , *A Density-Based Algorithm for Discovering Clusters in Large Spatial Databases with Noise.* Proceedings of the Second International Conference on Knowledge Discovery and Data Mining (KDD-96), 1996.

139. Gajic, I., et al., *Antimicrobial Susceptibility Testing: A Comprehensive Review of Currently Used Methods.* Antibiotics (Basel), 2022. **11**(4).

140. Holmes, A.H., et al., *Understanding the mechanisms and drivers of antimicrobial resistance.* Lancet, 2016. **387**(10014): p. 176-87.

141. Prevention, U.C.f.D.C.a. *Antimicrobial Resistance Facts and Stats*. 2025; Available from: https://www.cdc.gov/antimicrobial-resistance/data-research/facts-stats/index.html.

142. Pereira, C., et al., *The highly dynamic nature of bacterial heteroresistance impairs its clinical detection.* Commun Biol, 2021. **4**(1): p. 521.

143. Kuper, K.M., et al., *Antimicrobial susceptibility testing: a primer for clinicians.* Pharmacotherapy, 2009. **29**(11): p. 1326-43.

144. Sanka, I., et al., *Investigation of Different Free Image Analysis Software for High-Throughput Droplet Detection.* ACS Omega, 2021. **6**(35): p. 22625-22634.

145. Parsley, N.C., A.L. Smythers, and L.M. Hicks, *Implementation of Microfluidics for Antimicrobial Susceptibility Assays: Issues and Optimization Requirements.* Front Cell Infect Microbiol, 2020. **10**: p. 547177.

146. Lu, H., et al., *High throughput single cell counting in droplet-based microfluidics.* Scientific Reports, 2017. **7**(1).

147. Taylor, D., et al., *Tracking the stochastic growth of bacterial populations in microfluidic droplets.* Phys Biol, 2022. **19**(2): p. 026003.

148. Alexander, H.K. and R.C. MacLean, *Stochastic bacterial population dynamics restrict the establishment of antibiotic resistance from single cells.* Proc Natl Acad Sci U S A, 2020. **117**(32): p. 19455-19464.

149. Tebano, G., et al., *Antibiotic Treatment of Infections Caused by AmpC-Producing Enterobacterales.* Pharmacy (Basel), 2024. **12**(5).

150. Balasubramanian, D., H. Kumari, and K. Mathee, *Pseudomonas aeruginosa AmpR: an acute-chronic switch regulator.* Pathog Dis, 2015. **73**(2): p. 1-14.

151. Nakano, R., et al., *Role of AmpR in the High Expression of the Plasmid-Encoded AmpC beta-Lactamase CFE-1.* mSphere, 2017. **2**(4).

152. Tariq, F.N., et al., *The functional repertoire of AmpR in the AmpC beta-lactamase high expression and decreasing beta-lactam and aminoglycosides resistance in ESBL Citrobacter freundii.* Heliyon, 2023. **9**(9): p. e19486.

153. Romanowsky, M.B., et al., *High throughput production of single core double emulsions in a parallelized microfluidic device.* Lab Chip, 2012. **12**(4): p. 802-7.

154. Gruner, P., et al., *Controlling molecular transport in minimal emulsions.* Nat Commun, 2016. **7**: p. 10392.

155. Skhiri, Y., et al., *Dynamics of molecular transport by surfactants in emulsions.* Soft Matter, 2012. **8**(41).

156. Loveday, E.K., et al., *Screening of Additive Formulations Enables Off-Chip Drop Reverse Transcription Quantitative Polymerase Chain Reaction of Single Influenza A Virus Genomes.* Anal Chem, 2021. **93**(10): p. 4365-4373.

157. Ruszczak, A., et al., *Physicochemical Properties Predict Retention of Antibiotics in Water-in-Oil Droplets.* Anal Chem, 2023. **95**(2): p. 1574-1581.

158. Waeterschoot, J., et al., *The effects of droplet stabilization by surfactants and nanoparticles on leakage, cross-talk, droplet stability, and cell adhesion.* RSC Adv, 2024. **14**(33): p. 24115-24129.

159. Chowdhury, M.S., et al., *Dendronized fluorosurfactant for highly stable water-in-fluorinated oil emulsions with minimal inter-droplet transfer of small molecules.* Nat Commun, 2019. **10**(1): p. 4546.

160. Chowdhury, M.S., et al., *Linear triglycerol-based fluorosurfactants show high potential for droplet-microfluidics-based biochemical assays.* Soft Matter, 2021. **17**(31): p. 7260-7267.

161. Lambert, R.J. and J. Pearson, *Susceptibility testing: accurate and reproducible minimum inhibitory concentration (MIC) and non-inhibitory concentration (NIC) values.* J Appl Microbiol, 2000. **88**(5): p. 784-90.

162. Hombach, M., et al., *Relative contribution of biological variation and technical variables to zone diameter variations of disc diffusion susceptibility testing.* J Antimicrob Chemother, 2016. **71**(1): p. 141-51.

163. Pogue, J.M., et al., *Polymyxin Susceptibility Testing and Interpretive Breakpoints: Recommendations from the United States Committee on Antimicrobial Susceptibility Testing (USCAST).* Antimicrob Agents Chemother, 2020. **64**(2).

164. Band, V.I., et al., *Colistin Heteroresistance Is Largely Undetected among Carbapenem-Resistant Enterobacterales in the United States.* mBio, 2021. **12**(1).

165. Tan, K., et al., *Prevalence of the carbapenem-heteroresistant phenotype among ESBL-producing Escherichia coli and Klebsiella pneumoniae clinical isolates.* J Antimicrob Chemother, 2020. **75**(6): p. 1506-1512.

166. Band, V.I., et al., *Antibiotic combinations that exploit heteroresistance to multiple drugs effectively control infection.* Nat Microbiol, 2019. **4**(10): p. 1627-1635.

167. Garstecki, P., et al., *Formation of droplets and bubbles in a microfluidic T-junction-scaling and mechanism of break-up.* Lab Chip, 2006. **6**(3): p. 437-46.

168. Lewis, K., *Persister cells, dormancy and infectious disease.* Nat Rev Microbiol, 2007. **5**(1): p. 48-56.

169. Hsu, R.H., et al., *Microbial Interaction Network Inference in Microfluidic Droplets.* Cell Syst, 2019. **9**(3): p. 229-242 e4.